

Influence of Inter-Particle Interactions on the Performance of Cyclone Separators

Dissertation

zur Erlangung des akademischen Grades

Doktoringenieur

(Dr.-Ing.)

von **M.Sc. Oscar Lino Sgrott Júnior**

geboren am 20.05.1987, in Nova Trento – SC (Brasilien)

genehmigt durch die Fakultät für Verfahrens- und Systemtechnik
der Otto-von-Guericke-Universität Magdeburg

Promotionskommission: Prof. Dr.-Ing. Fabian Denner (Vorsitz)
Prof. Dr.-Ing. Martin Sommerfeld (Gutachter)
Prof. Dr.-Ing. Berend van Wachem (Gutachter)
Prof. Dr.-Ing. Rüdiger Schwarze (Gutachter)

eingereicht am: 14.02.2019

Promotionskolloquium am: 29.04.2019

*“Se fosse fácil achar o caminho das pedras,
tantas pedras no caminho não seria ruim.”*

Outras Frequências – Engenheiros do Hawaii

Schriftliche Erklärung

Ich erkläre hiermit, dass ich die vorliegende Arbeit ohne unzulässige Hilfe Dritter und ohne Benutzung anderer als der angegebenen Hilfsmittel angefertigt habe. Die aus fremden Quellen direkt oder indirekt übernommenen Gedanken sind als solche kenntlich gemacht.

Insbesondere habe ich nicht die Hilfe einer kommerziellen Promotionsberatung in Anspruch genommen. Dritte haben von mir weder unmittelbar noch mittelbar geldwerte Leistungen für Arbeiten erhalten, die im Zusammenhang mit dem Inhalt der vorgelegten Dissertation stehen.

Die Arbeit wurde bisher weder im Inland noch im Ausland in gleicher oder ähnlicher Form als Dissertation eingereicht und ist als Ganzes auch noch nicht veröffentlicht.

Declaration

I hereby declare that I prepared the work submitted without inadmissible assistance and without the use of any aids other than those indicated. Facts or ideas taken from other sources, either directly or indirectly have been marked as such.

In particular, I did not use the services of a commercial graduation consultation. Further I have not made payments to third parties either directly or indirectly for any work connected with the contents of the submitted dissertation.

The work has not been submitted as a dissertation either in Germany or abroad in the same or similar form and has also not been published as a whole.

14.02.2019, Halle (Saale)

Osun L. Sghoff Jr.

Preface

The present work resumes the work performed during my PhD from April 2014 up to April 2019 at the Workgroup of Multiphase Flows (MPS) at the Faculty of Process- and Systems Engineering (IVT) of the Otto-von-Guericke-Universität Magdeburg. The main goal of the present work is to further advance the numerical prediction and improve the understanding of particle separation in gas cyclones. Although the cyclone's debut happened over a century ago, many elementary phenomena are still neglected by recent works in the literature. From gas-particle interactions to inter-particle collisions with agglomerations and agglomerate breakage, there are still many elementary processes that need to be correctly addressed. Hence, the present work aims a more complete analysis on cyclone separators, presenting a discussion of what should be considered and the best methodologies to achieve reliable agreement with the experimental data. Naturally, based on the complexity of some elementary processes as agglomeration and breakage, a more simplified approach is presented. Therefore, numerical calculations based on the coupled Euler/Lagrange approach were conducted using the open source CFD code OpenFOAM, where all the models were implemented.

Zusammenfassung

Zur weiteren Verbesserung des Verständnisses der Partikeltrennung in Gaszyklonen, der Agglomeration und dem Agglomeratbruch werden in dieser Arbeit numerische Berechnungen basierend auf dem gekoppelten Euler-Lagrange Verfahren mit dem Open-Source CFD Programm OpenFOAM durchgeführt. Für die Darstellung und Problemlösung der stark anisotrop-turbulente n Struktur der Wirbelströmung in einem Gaszyklon wird LES (Large Eddy Simulation) in Kombination mit einer dynamischen Smagorinsky sub-grid-scale (SGS) genutzt. Die Auswirkungen der Partikel-Massenbeladung auf die Gasphase werden unter Hinzunahme des Effekts der Zweivegekopplung (d. h. der Einfluss der Partikel auf das Fluidströmungsfeld) berücksichtigt. Partikelagglomeration und Agglomeratbruch werden weiterhin auf der Basis des stochastischen Partikel-Partikel -Kollisionsmodell modelliert. In dieser Hinsicht ist der Effekt der Partikeldispersion durch die SGS-Turbulenz und die Wandrauigkeit bei Partikel-Wand-Kollisionen zu berücksichtigen. Zur Beschreibung des Agglomeration-Phänomens werden zwei verschiedene Ansätze untersucht. Der erste Ansatz umfasst das sogenannte Kugelmodell, welches davon ausgeht, dass der Agglomeratdurchmesser aus der Summe des Volumens der beteiligten Primärpartikel (Volumenäquivalenter Kugeldurchmesser) berechnet wird. Als zweite Herangehensweise dient das sogenannte "History Model". Dieses berücksichtigt die Agglomeratporosität, die zur Berechnung eines geeigneteren hydrodynamischen Durchmessers verwendet wird. Daraus resultiert eine bessere Vorhersagbarkeit der Bewegung neu gebildeter Agglomerate. Nach der Validierung der Modelle werden vier Fallszenarien evaluiert, um verschiedene Phänomene in Gaszyklonen zu untersuchen. Das erste Fallszenario entspricht der Gasphasenlösung, in der die Methoden zur numerischen Gittererzeugung, Turbulenzmodellierung und deren Validierung mit experimentellen Daten vorgestellt werden. Fallszenario Nummer zwei führt die Partikelverfolgung und relevante Ansätze ein, die für eine gute Darstellung der

Partikelabscheidung erforderlich sind. In einem dritten Szenario stellt ein hypothetischer Studienfall dar, wie sich die Auswirkungen von Kollisionen zwischen Partikeln und Agglomeration auf die Zyklonleistung darstellen. Abschließend werden im vierten Fallszenario alle vorherigen Analysen vereint, indem ein Zyklon mit hoher Massenbelastung analysiert wird. Zusammenfassend lässt sich die Bedeutung der untersuchten Phänomene feststellen, die aus den Ergebnissen der Fallszenarien resultiert und eine große Übereinstimmung mit den experimentellen Daten aufzeigt.

Abstract

For further improving the understanding of particle separation in gas cyclones including the effect of inter-particle collision, agglomeration and agglomerate breakage, numerical calculations based on the coupled Euler/Lagrange approach are conducted using the open source CFD code OpenFOAM. To solve the highly anisotropic turbulent structure of the swirl flow inside a cyclone separator, LES (large eddy simulations) combined with a dynamic Smagorinsky sub-grid-scale (SGS) are considered. To respect the effects of particle mass loading on the continuous phase, two-way coupling (i.e. the influence of the particles on the fluid flow field) was accounted for in the momentum equations. Solid particle agglomeration and agglomerate breakage are modelled based on the stochastic inter-particle collision model. In that respect, it is also important to consider the effect of particle dispersion by SGS turbulence and wall roughness in particle-wall collisions which eventually may also modify the particle tracking. For describing the agglomeration phenomenon, two different approaches are studied. The first one, the so-called sphere model, considers that the agglomerate diameter is calculated from the sum of the volume of the involved primary particles (volume equivalent diameter). In the second approach, the agglomeration history model allows the calculation of the agglomerate porosity, which is used to calculate a more suitable hydrodynamic diameter and therefore allows a better prediction of the motion of newly formed agglomerates. To validate the implemented models in OpenFOAM, a study based on pneumatic conveying systems is proposed. With the models validated, four main test cases are proposed to investigate different phenomena in cyclone separators. The first test case corresponds to the continuous phase solution, where the methodologies for grid generation, turbulence modelling and validation with experimental data are presented. The second one introduces the particle tracking and the relevant approaches needed for a good representation of the collection efficiency. The third test case presents a hypothetical study case considering the effect of inter-particle collisions and agglomeration on

cyclone performance, where the importance of these elementary processes consideration is expressed. Lastly, the final test case covers all previous analysis by analysing a cyclone with high mass loading, where the importance of the studied phenomena is clear due to the observed improvement of the agreement with experimental data. In summary, the significance of the investigated phenomena can be determined, which results from the good agreement with the experimental data.

Summary

1. INTRODUCTION	1
1.1 Cyclone Separators	2
1.1.1 Performance Parameters of Cyclones Separators.....	5
1.1.1.1 Collection Efficiency	5
1.1.1.2 Pressure Drop.....	6
1.1.2 Literature Overview and Problem Identification	7
1.2 Objectives of the Study.....	9
2. SUMMARY OF THE NUMERICAL APPROACH	11
2.1 Continuous Phase	11
2.1.1 Reynolds Averaged Navier-Stokes Equations (RANS).....	12
2.1.2 Large Eddy Simulation (LES).....	13
2.1.3 Pressure-Velocity Coupling	15
2.1.4 Wall Functions	15
2.2 Discrete Phase.....	16
2.2.1 Dynamic Lagrangian Time step	17
2.2.2 Semi-Unsteady Approach	18
2.2.3 Coupling between continuous and discrete phase.....	19
2.2.4 Forces Acting on the Particles.....	19
2.2.4.1 Drag Force.....	19
2.2.4.2 Gravitational Force	21
2.2.4.3 Slip-Shear Lift Force.....	21
2.2.4.4 Slip-Rotational Lift Force	21
2.2.4.5 Torque	22
2.2.5 Sub-Grid Turbulent Dispersion Model	23

2.2.5.1	Validation of the Particle Dispersion Model in Turbulent Flow	24
2.2.6	Particle Wall Collisions Considering Wall Roughness	27
2.2.7	Stochastic Inter-Particle Collision Model.....	34
2.2.7.1	Sampling of the Fictitious Collision Partner	34
2.2.7.2	Collision Probability and Impact Efficiency	36
2.2.7.3	Particle Velocity Change due to Inter-Particle Collisions.....	39
2.2.8	Agglomeration Models	44
2.2.8.1	Agglomerate Breakage	50
2.3	Final Considerations.....	51
3.	VALIDATION CASES: PNEUMATIC CONVEYING SYSTEM.....	53
3.1	Pneumatic Conveying System: Cases Configuration.....	53
3.2	Validation Case 1: Horizontal Pipe.....	56
3.3	Validation Case 2: Horizontal Pipe, Bend and Vertical Pipe.....	62
3.4	Validation Cases: Summary and Final Considerations	68
4.	RESULTS AND DISCUSSION: CYCLONE SEPARATORS.....	69
4.1	Test Case 1: Gas Flow Validation.....	70
4.2	Test Case 2: Particle Tracking and Collection Efficiency	82
4.2.1	Small Scale Laboratory-Cyclone	82
4.2.2	Stairmand Cyclone.....	89
4.3	Test Case 3: Hypothetical Study	100
4.4	Test Case 4: Cyclone with High Particle Mass Loading.....	108
4.4.1	One-, Two- and Four-Way Coupling.....	112
4.4.2	Effect of Agglomeration and Agglomerate Breakage	119
5.	CONCLUSIONS AND OUTLOOK.....	131
	NOMENCLATURE	137
	REFERENCES	141

1. INTRODUCTION

There are many industrial processes that involve processing solid materials, in which the separation of solid particles suspended in a fluid stream is related to the need for recovery of entrained material or avoiding its emission to the atmosphere. The cyclone separator is certainly one of the most used equipment in this practice. Hence, for further improving the understanding of particle separation in gas cyclones including the effect of inter-particle interaction, numerical calculations based on the coupled Euler/Lagrange approach were conducted using an open source CFD code.

This is the first of five main Chapters, where an overview on cyclone separators is presented. The identification of the problem and the main goals of this work are also presented in this section. The second Chapter presents the summary of the numerical approach, where the modelling of the continuous and discrete phase is summarized. All relevant elementary processes to the present study are also detailed. The third chapter complements the discussion started in the previous chapter through the validation of the implemented models using pneumatic conveying systems. The fourth chapter shown the main results of the present work regarding cyclone separators. As a consequence of the complex turbulent swirl flow in cyclones and the difficulty to obtain experimental data, several test cases are proposed. The first test case addresses the validation of the glass flow in cyclones and the best practices necessary for a good representation of the swirl flow in cyclones. The second test case introduces the particle tracking to the cyclone simulations, hence providing means to predict the collection efficiency. The third and fourth test cases address more complex cases, where higher mass loadings are considered, hence inter-particle collisions, agglomeration and agglomerate breakage are observed. Finally, the last main Chapter presents the summary and conclusions of this work.

1.1 Cyclone Separators

The cyclone separator is a stationary mechanical device which uses centrifugal force to separate solid particles from a carrier gas. It is widely used in the industry due to its large range of operational conditions and simplicity of construction, leading to low investment and maintenance costs. However, back in 1885 when the first patent of a cyclone separator was granted to John M. Finch in the USA (see Figure 1-a), the construction was more complex and had little resemblance with the modern geometrical characterization of a cyclone^[1]. Still, the idea of using the centrifugal force for separating particles from a gas stream was very innovative in the late 1800's, once back then the separation process relied heavily on the gravitational settling on a settling chamber.

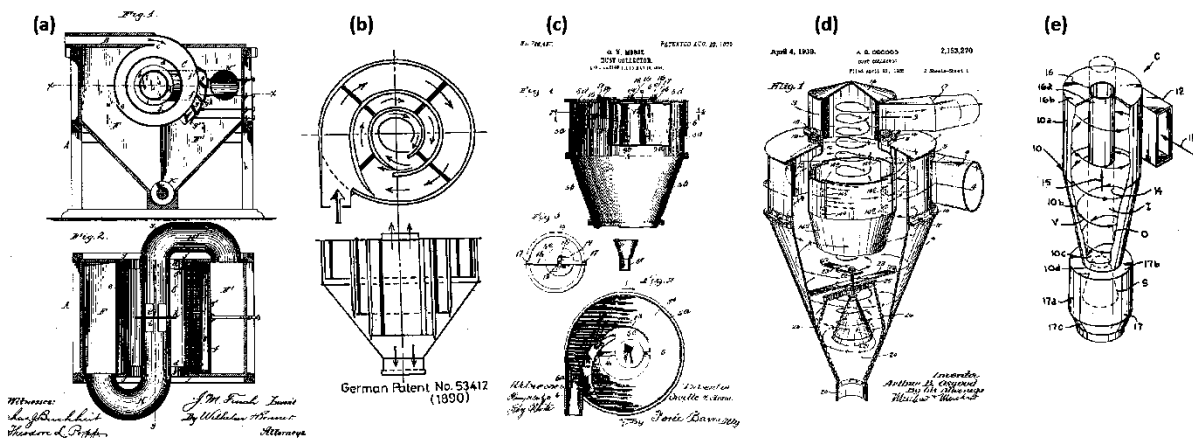


Figure 1. Geometrical evolution of the cyclone separators along the last centuries. (a) Cyclone separator patented by J. M. Finch in 1885; (b) German patent from 1890; (c) Patent by O. M. Morse in 1905; (d) Patent by A. B. Osgood in 1939; (e) Modern representation of a tangential cyclone. (source: adapted from Hoffmann and Stein^[1] and Ogawa^[2]).

A modern cyclone is composed basically by a cylindrical section over a conical section, where the gas-solid flow can be injected tangentially or axially to the cylindrical section (see Figure 2). The tangential configuration is more used due to its higher collection efficiency and simpler construction, however the axial configuration presents a more compact geometry, once flow enters at the top of the cyclone. Moreover, the axial cyclone has a lower pressure drop than the tangential cyclone, since the flow is in line with the axial direction of the cyclone. The tangential cyclone may present different inlet configurations for specific applications, where a volute or spiral inlet may be applied for a more symmetrical flow. Recently with the use of Computational Fluid Dynamics (CFD), many variations to the cyclone geometry are tested, e.g. the insertion of *deswirlers* bodies inside the vortex finder to reduce pressure drop, as studied by

Noriler et al. [3] and Misiulia et al. [4]. However, for the present work, only standard tangential cyclones are studied, where the classical designs in the literature includes two well-known geometries: the Stairmand [5] and Lapple [6] cyclones. The first one is applied when high collection efficiency is desired whereas the second is an alternative for low pressure drop. Due to the simplicity of its construction, a tangential cyclone may be characterised by eight geometrical relations, which are usually described as a function of the body diameter D_c , as shown in Figure 3.

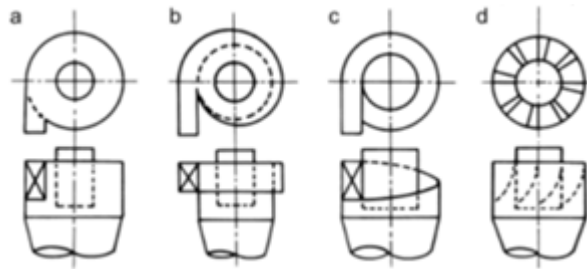


Figure 2. Different configurations of a cyclone inlet. (a) tangential; (b) tangential with volute; (c) tangential with spiral; (d) axial. Source: Dirigo and Leith [7].

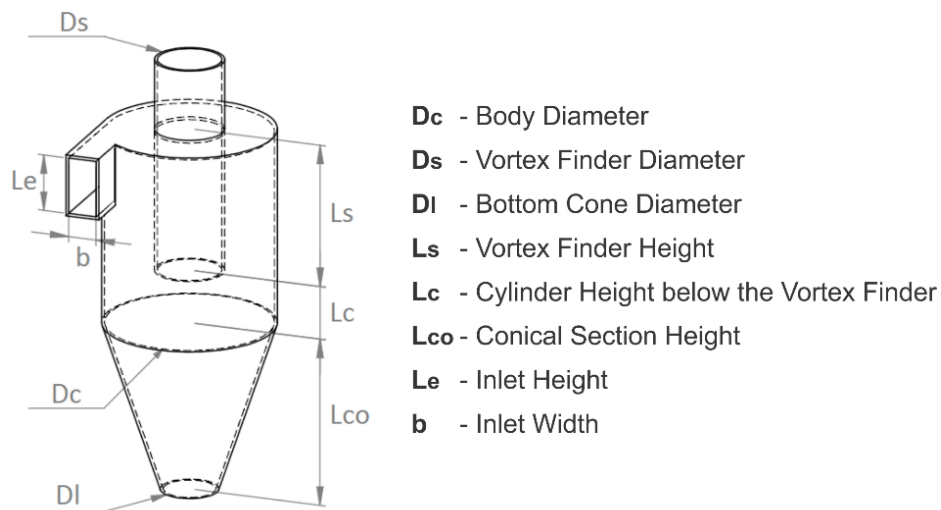


Figure 3. Geometrical parameters used to describe a standard tangential cyclone.

In a tangential cyclone, the gas-solid flow enters tangentially at the top of the cylindrical section creating a downwards vortex near the wall of the cyclone (“*outer vortex*”). At the bottom of conical section, the vortex is reversed and directed upwards at the centre of the cyclone (“*inner vortex*” or “*overflow*”), leaving the system through the axially positioned exit pipe (vortex finder) located at the top of the cyclone. An illustration of the swirl flow inside a Stairmand cyclone is shown in Figure 4, where the flow is coloured by the axial velocity values with blue representing the downwards flow and red representing the upwards flow. For a better visualization, the instantaneous (a) and averaged (b) values are presented.

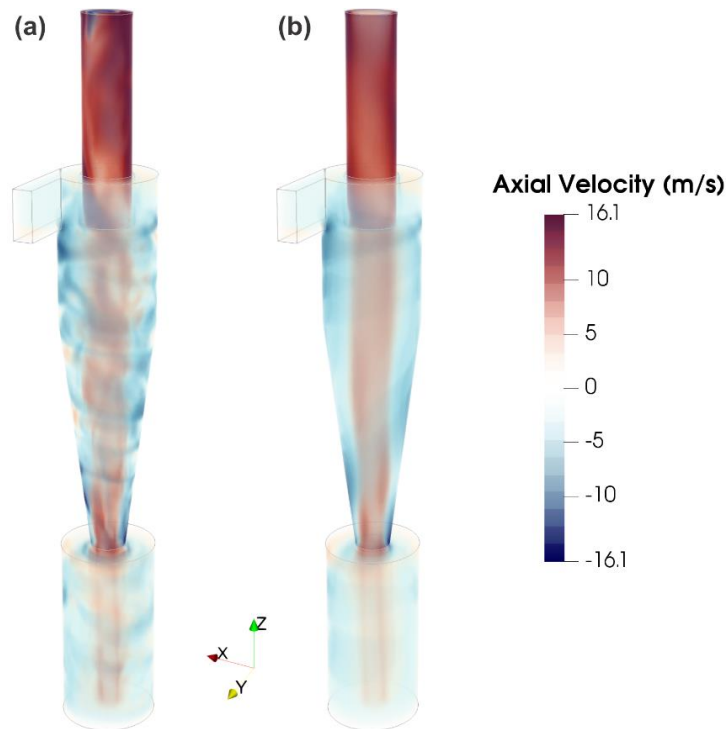


Figure 4. Representation of the swirl flow inside a high-efficiency Stairmand cyclone.
 (a) instantaneous axial velocity; (b) averaged axial velocity.

Due to the centrifugal force caused by the swirl flow, the particles move near the wall until the reversion of the vortex at the bottom of the conical section, where the particles are collected due to their inertia. Hence, the collection efficiency is higher when the particles are bigger and/or heavier. On the other hand, there are two main factors that affect negatively the collection efficiency of a cyclone. The first lies on the lack of centrifugal force, which is caused by a low tangential velocity at the body of the cyclone. In this condition, the particles in the outer vortex do not stay in the vicinity of the wall, thus being possibly dragged by the inner vortex and consequently escaping through the vortex finder. This effect may be caused by a poor design or a low gas flow, i.e. low inlet velocity. The second condition lies on the relation between the vortex finder length and inlet height (L_s and L_e respectively), where a “short circuit” may happen if both geometrical relations have similar size. That is, the particles may be dragged by the inner vortex right after they enter the body of the cyclone, not allowing the particles to be directed to the near wall region. Both problems may be solved by the application of the right operation conditions and by a proper design of the cyclone. According to Hoffmann and Stein ^[1], the downward flow in the outer part of the cyclone is critically important as it, and not gravity, is the dominant mechanism for transporting collected solids (those at the wall) out the bottom of the cyclone. In vertically oriented cyclones, gravity will assist but its influence is important only for cyclones operating at high solids-loaded conditions, for which mass loading effects are important.

1.1.1 Performance Parameters of Cyclones Separators

The design of a cyclone is a compromise between collection efficiency and pressure drop, the two major performance parameters. By increasing the flow in a cyclone, it is possible to increase its collection efficiency due to the higher tangential velocity, i.e. centrifugal force. However, this increment in the flow increases the cost of operating the cyclone, by increasing its pressure drop. Recently optimization studies have been performed to find the best balance between both parameters. Thus, manipulation of geometrical relations and operational conditions are performed by many authors with the use of CFD techniques.

1.1.1.1 Collection Efficiency

Over the last century, different empirical models were proposed to estimate the collection efficiency in cyclones, where basically two main modelling concepts are presented in the literature: the “equilibrium-orbit” models and the “time-of-flight” models. The “equilibrium-orbit” model was originally determined by Barth^[8], where the cut size is calculated as a function of the centrifugal and drag forces at a “control-surface” region. The author also predicted experimentally an “universal curve”, which could be adapted for the cut size¹ x_{50} , hence providing the collection efficiency curve as a function of size. Dirgo and Leith^[7] extended the model by regressing the experimental data from Barth^[8], hence providing the collection efficiency as function of the cut size x_{50} and particle size. On the other hand, the “time-of-flight” model was proposed originally by Rosin et al.^[9], where the time required for a particle injected at the inlet to reach the cyclone wall is accounted for. A more in-depth analysis of all the variations of the mentioned models are extensively discussed by Hoffmann and Stein^[1]. Despite relative success to predict the collection efficiency for classical cyclones, both classes of models and its hybrid successors rely heavily on empirical observation and correlations. Thus, not being suitable to predict the collection efficiency for every cyclone geometry and operational conditions. With the advent of CFD techniques and the increase of computational power, the collection efficiency of cyclones can be determined by numerical experiments.

The global collection efficiency can be calculated as the ratio of the collected mass by the injected mass of particles. According to Hoffmann and Stein^[1], it is possible to divide the mass

¹ Cut size x_{50} is the size of particle that will be removed from the cyclone with a 50 % collection efficiency. Particles larger than the cut size will be removed with a greater collection efficiency, whereas smaller particles present a lower collection efficiency.

balance of particles in a cyclone in three distinct regions: the mass injected, the mass collected and the mass escaped:

$$m_{injected} = m_{collected} + m_{escaped} \quad (1)$$

The easiest way to experimentally measure the collection efficiency is by the rate of collected and injected particles, where a constant injection is known and the collected mass can be measured. Hence, the collection efficiency as function of particle size may be determined by measuring the size distribution before injecting into the cyclone and by the collected particles. Recently, a number of authors ^[10, 11, 12] used optical sensors to measure the size distribution of particles at the injection, collection and escape regions. Thus, presenting “online” values for the collection efficiency. This second method is similar to the one applied to numerical simulations, once the distribution of particles is known in all three regions. Therefore, the collection efficiency, in dependence of particle size x can be calculated considering two different approaches as follow:

$$\eta = \frac{N(x)_{collected}}{N(x)_{injected}} = 1 - \frac{N(x)_{escaped}}{N(x)_{injected}} \quad (2)$$

$$\eta = \frac{N(x)_{collected}}{N(x)_{escaped} + N(x)_{collected}} = 1 - \frac{N(x)_{escaped}}{N(x)_{escaped} + N(x)_{collected}} \quad (3)$$

Both approaches present the same result for the collection efficiency under normal circumstances, however differences may appear if agglomeration and agglomerate breakage are considered. If the particles agglomerate inside the cyclone, a different size distribution at the collected and escaped regions are observed in comparison with the injection. Thus, differences on the collection efficiency curve as function of particle size may appear. This topic will be further discussed in the test cases when agglomeration is considered, where a comparison between both approaches is presented.

1.1.1.2 Pressure Drop

The pressure drop is a very important performance parameter, once it represents directly the energy necessary to operate the cyclone. It can be modified by the injection of particles in the cyclone, where the particle loss of momentum due to particle-wall and inter-particle interactions should be compensated by the gas flow, hence decreasing the swirl and

consequently the pressure drop. However, according to Ogawa ^[2], the most significant contribution to the pressure drop is attributed to the energy dissipation by the turbulent swirl flow. Thus, the gas flow and geometrical relations of the cyclone are the most relevant parameters influencing the pressure drop. The vortex finder diameter D_s plays a major role, once its reduction increases the swirl intensity and consecutively the pressure drop, as observed in the experimental measurements of Hoekstra ^[13] and the optimization studies of Sgrott Jr. et al. ^[14] and Luciano et al. ^[15].

As discussed for the collection efficiency, many empirical models were developed to predict the pressure drop in a cyclone. Stairmand ^[16] proposed a model that considers the wall-friction effect, however the author did not consider the effect of mass loading on the pressure drop, being this problem addressed later by Barth ^[8]. Shepherd and Lapple ^[17] and Casal and Martinez-Benet ^[18] developed models for tangential cyclones operating at low mass loading. However, for the same reasons as presented for the collection efficiency, the pressure drop in the present study is obtained via numerical simulations using CFD techniques. A further discussion about the influence of pressure drop and the best practices to its measurement in numerical calculations are presented in gas flow validation in the test cases.

1.1.2 Literature Overview and Problem Identification

Several authors analysed the effect of geometry and operational conditions on cyclone's performance parameters. Hoekstra ^[13] performed experimental measurements in a Stairmand cyclone with variations of the diameter of the vortex finder D_s , observing that when its size is reduced, the collection efficiency and the pressure drop increase. The same pattern was observed by Elsayed and Lacor ^[19] with numerical calculations using LES. Lim et al. ^[20] performed numerical calculations to study the effect of cylinder- and cone-shaped vortex finders on the collection efficiency, showing that its application does not show significant improvements regarding to the cost caused by the higher pressure drop. On the other hand, Souza et al. ^[21] and Balestrin et al. ^[22] analysed the effect of the exit pipe length and shape downstream the cyclone, being the least successful by increasing the collection efficiency. The inlet dimensions of the cyclone are also the subject of studies, as presented by Lim et al. ^[23], Bernardo et al. ^[24], Yang et al. ^[25] and Elsayed and Lacor ^[26]. The results shown that, the maximum tangential velocity in the cyclone decreases with increasing the inlet dimensions, hence decreasing the collection efficiency. By decreasing the bottom cone diameter D_s , Xiang et al. ^[10] was able to increase experimentally the collection efficiency without increasing significantly the pressure drop. Later, the same behaviour was observed by Souza et al. ^[27] using

LES simulations. Regarding to the conical section, Lee et al. [28] and Elsayed and Lacor [29] performed numerical calculations with elongated versions of the cone, where the first observed a limitation for the vortex length, causing “short circuits” between the outer- and inner-vortex, hence decreasing the collection efficiency of the cyclone. Based on these observations, many optimisation studies were conducted in the last decade in order to increase the collection efficiency or to decrease the pressure drop of cyclones. Elsayed and Lacor [30] and Safikhani et al. [31], for example, used artificial neural network and response surface methodology to optimize the geometrical relations of cyclones. Sgrott Jr. et al. [14, 32] proposed a multi-objective optimization methodology which the objective function is obtained directly from CFD simulation and the optimization problem is formulated such that the collection efficiency was maximized with a restriction for the maximum pressure drop. This methodology was extended by Luciano et al. [15], where the geometrical optimization of multi-cyclones was studied. These optimization results indicate a significant effect of the vortex finder diameter D_s , the vortex finder height L_s and the inlet dimensions on the cyclone performance.

Design improvements based on Computational Fluid Dynamics (CFD) techniques rely on accurate description of all relevant physical phenomena involved in the cyclone operation. However, most published studies neglect inter-particle collisions (four-way coupling) and many also neglect the interaction between the fluid flow and the particles (two-way coupling). It is very important to also consider the mass-loading effects in the cyclone, once the particles cause the cyclone to lose swirl and as a consequence of that, the collection efficiency may be modified, as shown numerically by Derksen et al. [33] and experimentally by Hoffmann et al. [34]. With the increasing of mass-loading, Hoffmann et al. [34] also observed that the collection efficiency is increased through inter-particle collisions. Sedrez et al. [35] observed experimentally that by increasing the mass loading, lower rates of erosion were measured on the cyclone’s walls, being this phenomenon attributed to inter-particle collisions and its consequent loss of momentum. The collection efficiency has a great sensibility regarding the particle size; thereby the larger particles are, more inertial and consequently are easier collected than the smaller ones. Through agglomeration larger particles (agglomerates) are produced, which can be easier collected due to their larger weight, improving the collection efficiency for smaller particles [36, 37, 38]. Ji et al. [11] observed experimentally that agglomeration takes place in cyclones even with extremely low particle concentrations. Haig et al. [39] studied the influence of material properties on the collection efficiency of cyclones. The authors used two different materials with similar particle material densities and observed that they present different collection efficiency curves, being this phenomenon related to the agglomeration affinity of one

of the materials. However, as stated by Lipowsky and Sommerfeld^[36], the resulting agglomerates may break and generate small particles in areas that could not be reached by those size classes under normal conditions, resulting in a decrease of the collection efficiency. Hence, for a better understanding of the particle separation in a cyclone, a more accurate representation of all relevant physical phenomena is needed.

1.2 Objectives of the Study

The main objective of the present work is to further improve the understanding of particle separation in gas cyclones by considering different particle related phenomena. For that, a solver considering the Euler/Lagrange approach is implemented in an open source code. OpenFOAM is the leading open source software for computational fluid dynamics (CFD), which is developed and maintained by individuals who contribute with their work to the project. The already large library of different applications (solvers and models) and the possibility of its modification, makes OpenFOAM the most suitable option to perform the present work. Therefore, the objectives regarding the present work may be divided in three main parts.

1. Implementation and validation of the necessary models in OpenFOAM:

Despite the large library available in OpenFOAM, the implementation of additional models is necessary, as follows:

- Euler/Lagrange solver considering interaction between the continuous and discrete phases (two-way coupling);
- Relevant forces acting on the particles and dispersion due to turbulence;
- Particle-wall collision considering wall roughness;
- Stochastic inter-particle collision model;
- Agglomeration and agglomerate breakage models;
- Additional utilities for statistical averaging and data sampling.

To verify if the implemented models are correctly representing the modelled elementary processes, a validation study on pneumatic conveying systems is proposed. Here, a comparison between the numerical results obtained with OpenFOAM and with experimental data from the literature is performed.

2. Development of methodologies and strategies for cyclone simulations:

To obtain reliable results, a suitable methodology for cyclone simulation is proposed. From numerical grid generation to collection efficiency or pressure drop calculation, different methodologies and best practices on cyclone simulation are presented.

3. Influence of particle related phenomena on cyclone performance:

The effect of the interaction between the gas and particle phases is investigated, where the presence of particles modifies the swirl flow inside the cyclone. Also the effect of inter-particle collisions is observed, where its effect on the performance parameters is studied. Finally, the effect of agglomeration and agglomerate breakage is discussed, where its presence may be beneficial or not to the improvement of the collection efficiency.

2. SUMMARY OF THE NUMERICAL APPROACH

The numerical scheme adopted to simulate the pneumatic conveying system and cyclone separators is the coupled unsteady and three-dimensional Euler/Lagrange approach. All relevant information regarding the modelling of the main phenomena involved in the present work are presented in this chapter. The summary of the numerical approach is divided in two major sections, being the first designated to the continuous phase, describing the turbulence models used in the present study as well as the coupling between the continuous and discrete phases. The second section presents all modelling related to the discrete phase, detailing the Lagrangian approach and describing all relevant forces for the present study. The turbulent dispersion model used is also presented considering a small test case for its validation. Finally, the particle-wall interaction, inter-particle interaction, agglomeration and agglomerate breakage models are detailed.

2.1 Continuous Phase

In the present study, the continuous phase is solved by two different methods: the Reynolds Averaged Navier-Stokes Equations (RANS) for the simpler flow structures; such as the pneumatic conveying systems; and the Large Eddy Simulation (LES) for the more complex and anisotropic flow structures as in the cyclone separators.

2.1.1 Reynolds Averaged Navier-Stokes Equations (RANS)

For the pneumatic conveying system, the fluid phase calculations are performed based on the Euler approach by solving the Reynolds-Averaged Navier-Stokes (RANS) equations in connection with the standard k - ε turbulence model. Since the main focus of the present work lies on the cyclone separators solution, only a short summary of the RANS equations is given. The time-dependent conservation equations for a Newtonian fluid may be written in the general form, in tensorial notation (where the comma followed by a subscript means partial derivative and summation is performed over repeated indexes), as:

$$(\rho \phi)_{,t} + (\rho U_i \phi)_{,i} = (\Gamma_{ik} \phi_{,k})_{,i} + S_\phi + S_{\phi p} \quad (4)$$

where ρ is the fluid density, U_i are the Reynolds-averaged velocity components, and Γ_{ik} is an effective transport tensor. S_ϕ summarizes the usual source terms within the continuous phase equation while $S_{\phi p}$ represents additional source terms due to phase interaction (detailed in Chapter 2.2.3). Table 1 summarises the meaning of these quantities for the variable ϕ .

<i>Table 1. Summary of terms in the general conservation equation for the different variables describing the gas phase by the k-ε turbulence model.</i>			
ϕ	Γ_{ik}		S_ϕ
1	0		0
U_j	$(\mu + \mu_T)\delta_{ik}$	$P_{,j} + (\Gamma_{jk} U_{i,k})_{,i} - (2/3\rho k + \mu_T U_{k,k})_{,j} + \rho g_j$	
k	$(\mu + \mu_T/\sigma_k)\delta_{ik}$		$P - \rho\varepsilon$
ε	$(\mu + \mu_T/\sigma_\varepsilon)\delta_{ik}$		$c_{\varepsilon 1} P \varepsilon/k - \rho c_{\varepsilon 2} \varepsilon^2/k$

where P is the mean pressure, μ is the fluid dynamic viscosity and $\mu_T = \rho C_\mu k^2/\varepsilon$ is the turbulent viscosity. k is the turbulent kinetic energy and ε is the turbulent dissipation rate.

$$P = -\rho R_{ij} U_{i,j} \quad (5)$$

$$\rho R_{ij} = \left(\frac{2}{3} \rho k + \mu_T U_{k,k} \right) \delta_{ik} - \mu_T (U_{i,j} - U_{j,i}) \quad (6)$$

$$C_\mu = 0.09 \quad \sigma_k = 1.0 \quad \sigma_\varepsilon = 1.3 \quad c_{\varepsilon 1} = 1.44 \quad c_{\varepsilon 2} = 1.92 \quad (7)$$

2.1.2 Large Eddy Simulation (LES)

Although cyclones are characterized by a simple construction, its turbulent flow is very complex, where the gas motion usually is highly turbulent, fundamentally three-dimensional and unsteady. Due to swirl, the turbulence is strongly anisotropic, and the swirling motion possesses an inherent instability^[40]. In such anisotropic flow, the tangential velocity component is approximately two orders of magnitude higher than the radial one, causing the standard k- ϵ model, for example, to severely under-predict the swirl intensity^[27]. Hoekstra et al.^[41] and Kaya and Karagoz^[42] concluded by comparing experimental and numerical data that the k- ϵ model also predicted unrealistic distributions of axial and tangential velocity, being unsuitable for a proper solution of the flow in a cyclone separator. The Reynolds Stress Turbulence Model (RSM) is capable to describe the high anisotropy of the swirling flow. However, several authors^[33, 40, 43, 44, 45] recognize the inability of the RSM to predict the higher-order statistical moments precisely, where the RMS values for the velocity profiles are considerably below observed experimental data. On the other hand, several studies^[27, 33, 40, 43, 45, 46] have already demonstrated that Large Eddy Simulations (LES) is more accurate than RANS turbulence methods in predicting the velocity profiles in cyclone separators. In LES simulations, the largest eddies are directly resolved by the numerical grid and for smaller eddies (sub-grid scale eddies), a turbulence model (sub-grid scale model) is applied. In this way, special care regarding the refinement and quality of the numerical grid is required. In LES, the instantaneous velocity u_i is decomposed into a resolvable scale filtered velocity \bar{u}_i and a sub-grid velocity \bar{u}'_i , as follow:

$$u_i = \bar{u}_i + \bar{u}'_i \quad (8)$$

The resolved velocity in the LES model is obtained by spatially filtering the governing Navier-Stokes equations, where the filtering process separates the scales (i.e. sub-grid scale, SGS) which are smaller than the grid size^[44]. By applying the filtering operation to the continuity and to the filtered Navier Stokes equations for an incompressible and Newtonian, one gets:

$$\frac{\partial \bar{u}_i}{\partial x_i} = 0 \quad (9)$$

$$\frac{\partial \bar{u}_i}{\partial t} + \frac{\partial \bar{u}_i \bar{u}_j}{\partial x_j} = -\frac{1}{\rho} \frac{\partial \bar{p}}{\partial x_i} - \frac{1}{\rho} \frac{\partial \bar{\tau}_{ij}}{\partial x_j} + \frac{\partial}{\partial x_j} \left[\nu \left(\frac{\partial \bar{u}_i}{\partial x_j} + \frac{\partial \bar{u}_j}{\partial x_i} \right) \right] + \bar{S}_{ui,p} \quad (10)$$

where the overbar denotes the filtered quantity, \bar{p} is the resolved static pressure, ν is the kinematic gas viscosity and $\bar{\mathbf{S}}_{ui,p}$ represents the additional source term due to phase interaction. The SGS stress tensor $\boldsymbol{\tau}_{ij}$ may be calculated based on the turbulent viscosity ν_T and the strain rate tensor based on the resolved scales \bar{S}_{ij} , as follow:

$$\boldsymbol{\tau}_{ij} - \frac{1}{3} \tau_{kk} \delta_{ij} = 2\nu_T \bar{S}_{ij} \quad (11)$$

$$\bar{S}_{ij} = \frac{1}{2} \left(\frac{\partial \bar{u}_i}{\partial x_j} + \frac{\partial \bar{u}_j}{\partial x_i} \right) \quad (12)$$

Here, the isotropic part of the SGS tensor $\tau_{kk} \delta_{ij}$ is not modeled and added to the resolved static pressure \bar{p} [44]. The SGS model is used to represent the effects of unresolved scales (i.e. small eddies, swirls, vortices, etc.) on the transport equations of resolved scales. The SGS stress constitute a substantial portion of the turbulent energy and need to be modelled. The first SGS model was developed by Smagorinsky [47] and it models the turbulent viscosity as:

$$\nu_T = (C_s \Delta)^2 \sqrt{2\bar{S}_{ij}\bar{S}_{ij}} \quad (13)$$

where the grid length scale $\Delta = (V_{CV})^{1/3}$ is based on the volume of the computational cell. The eddy viscosity coefficient C_s can vary according to the flow, Reynolds number, numerical grid resolution or another adimensional parameters [48, 49], making difficult to have an universal analytical value that fits well for different equipment or operational conditions. To solve such problem, Germano et al. [48] and Lilly [50] proposed a dynamic procedure where the eddy viscosity coefficient C_s is automatically computed locally for each time step, reflecting closely the real state of the flow. This is done by sampling the smallest resolved scales and using this information to model the sub-grid scales at two different filtered levels (i.e. the grid filter Δ and the test filter $\tilde{\Delta}$). Germano et al. [48] specifies that the ratio between both filters should be greater than one and is the only variable that can be adjustable in the model. The author gives the ideal ratio as $\tilde{\Delta}/\Delta = 2$. A short summary of the extended formulation used by Lilly [50] is presented as:

$$C_s = \frac{1}{2} \frac{L_{ij} M_{ij}}{M_{ij}^2} \quad (14)$$

$$M_{ij} = \tilde{\Delta}^2 |\tilde{S}| \tilde{S}_{ij} - \Delta^2 |\bar{S}| \bar{S}_{ij} \quad (15)$$

$$L_{ij} = -\widetilde{\overline{u_i u_j}} + \widetilde{u_i} \widetilde{u_j} \quad (16)$$

where the elements of L are the resolved components of the stress tensor associated with the scales of motion between the test scale and the grid scale. The overbar denotes the grid filter process whereas the overtilde denotes the test filter process. For a more detailed explanation of the filtering process, as well as the SGS model, see Smagorinsky^[47], Germano et al.^[48] and Lilly^[50]. Unfortunately, OpenFOAM 4.1 does not have the Smagorinsky model with the dynamic approach implemented in its standard version. To overcome this problem, an open source version of the turbulence model implemented by Passalacqua^[51] for OpenFOAM 2.3.1 was implemented in the newer version. Thus, for the cyclone calculations in the present study, the gas phase transport equations are solved using the Smagorinsky model with the dynamic approach.

2.1.3 Pressure-Velocity Coupling

Solving the Navier-Stokes equations requires numerical techniques for coupling the pressure and momentum quantities. This can be done in OpenFOAM by applying the SIMPLE algorithm for steady-state calculations or PISO and PIMPLE algorithms for unsteady calculations. The main advantage of the PIMPLE (merged PISO-SIMPLEC) in comparison with the PISO algorithm, is that the first allows larger Courant numbers ($Co \gg 1$) and therefore, the time step of the calculations can be increased^[52]. This advantage can be useful in cases with a complex numerical grid, where a refinement of the grid in a specific region may be necessary. Hence, the stability of the solution may be increased by using the PIMPLE algorithm without the need to reduce drastically the time step. However, one should keep in mind that the time scales should be respect in order to have a correct solution of the flow field (especially important for the LES calculations). Therefore, for the present study, the PIMPLE algorithm is applied to couple the velocity and pressure fields for all the calculations.

2.1.4 Wall Functions

Wall functions are empirical equations used to satisfy the physics of the flow in the vicinity of the wall. They bridge the region between the wall and the turbulent fully developed flow, hence providing the near-wall boundary conditions for the momentum and turbulence transport equations^[53]. By applying the wall functions approach there is no need to resolve the boundary layer, which yields to a significant reduction of the mesh size and the computational

cost. The wall functions in OpenFOAM are implemented according to Kalitzin ^[54] to ensure that they can provide the accurate result to wherever the position of the first cell. For the present study the standard wall functions present in OpenFOAM 4.1 are applied, where for the RANS cases the *kqRWallFunction*, *epsilonWallFunction* and *nutkWallFunction* are applied in the wall boundary condition for the turbulent kinematic energy k , turbulent dissipation rate ε and turbulent kinematic viscosity ν respectively. For the LES cases, *nuSgsWallFunction* (Spalart Allmaras wall function boundary condition for incompressible flows) is applied for the turbulent kinematic viscosity.

2.2 Discrete Phase

The dispersed phase is treated in the Lagrangian framework, in which each particle is time-dependent tracked through the flow domain. The particles are treated as point masses and their shape is assumed to be spherical. For the present study the mass and heat transfer are neglected. To account for the correct particle mass flow rate, the considered computational parcels represent a certain number of real particles with the same properties, which yields a computationally treatable number of parcels. Particle transport is calculated by considering all relevant forces, which include particle inertia, drag force F_D , gravitational force F_g , slip-shear force F_{ls} and slip-rotational lift force F_{lr} . The change of the angular velocity along the particle trajectory due to the viscous interaction with the fluid (i.e. torque \mathbf{T}_i) requires the solution of an additional ordinary differential equation. Hence, the complete equations of motion for the particles are given by:

$$\frac{dx_{pi}}{dt} = u_{pi} \quad (17)$$

$$m_p \frac{du_{pi}}{dt} = \sum_i \mathbf{F}_i \quad (18)$$

$$I_p \frac{d\omega_{pi}}{dt} = \mathbf{T}_i \quad (19)$$

where u_{pi} and ω_{pi} are respectively the linear and angular velocity components of the particle, x_{pi} are the particle position components, $m_p = \rho_p D_p^3 \pi / 6$ is the particle mass, $\sum_i \mathbf{F}_i$ is the sum of all forces acting on the particles, $I_p = 0.1 m_p D_p^2$ is the moment of inertia and \mathbf{T}_i is the torque acting on a rotating particle due to viscous interaction with the fluid.

To increase the accuracy of the calculations, the properties of the continuous phase (e.g. gas velocity, velocity curl, turbulent kinetic energy, turbulent dissipation rate) are obtained for to the particle position. For that, a linear interpolation of the desired properties is performed based on the information stored at the centre of the actual cell and its neighbours.

2.2.1 Dynamic Lagrangian Time step

There are many unsteady situations where the required Eulerian time step Δt_E is much larger than the expected Lagrangian time steps Δt_L ^[55]. In the present study, the Eulerian time step may be found between $\Delta t_E = [10^{-5}s, 10^{-4}s]$, while the Lagrangian time steps may lay between $\Delta t_L = [10^{-10}s, 10^{-5}s]$, depending on the equipment simulated and the type of particle considered. Larger time steps are expected for the pneumatic conveying system cases ($D_p = 15 - 85\mu m$), while smaller ones are expected for the cyclone separators with fine particles ($D_p = 0.5 - 10\mu m$). Thus, the time step used for the particle tracking calculation should be automatically adjusted along the particle trajectory by considering all relevant time scales which also are changing throughout the flow field. The considered relevant time scales in the present study are listed below:

- The time required for a particle to cross a control volume Δt_{cv} , meaning that the Eulerian time step should be small enough in order to yield a courant number being smaller than one;
- The integral Stokesian time scale of turbulence $T_L = c_T \sigma_F^2 / \varepsilon$;
- The particle response time $\tau_P = \rho_P D_P^2 / 18\mu_F$;
- The average time between binary inter-particle collisions $\tau_{coll} = 1/f_c$ (the collision frequency f_c is detailed in Chapter 2.2.7.2);

To ensure that the particle tracking is solved properly, the Lagrangian time step Δt_L must be a fraction of the minimum of the time scales detailed above. Hence, for the present cases a Lagrangian time step of 20% of the smaller relevant time scale is adopted.

$$\Delta t_L = 0.2 \min(\Delta t_{cv}, T_L, \tau_P, \tau_{coll}) \quad (20)$$

The solution of the Eulerian and Lagrangian parts is performed through a semi-unsteady approach, where the influence of the particle phase on the fluid flow is considered.

2.2.2 Semi-Unsteady Approach

Due to the complexity of the swirling flow in cyclone separators and its unsteady nature, only unsteady calculations can correctly predict this kind of flow. There are different approaches to calculate unsteady particle laden flows, where the fully unsteady approach, for example, would call for equal time steps for the flow field and for the particle tracking. In this approach, the overall time step is governed by the smaller time step of all simulated entities. Hence, the required computational effort to perform such calculations in the present study would be prohibitive, once the required Lagrangian time step $\Delta t_L = [10^{-10}s, 10^{-5}s]$ may be several orders of magnitude smaller than the Eulerian time step $\Delta t_E = [10^{-5}s, 10^{-4}s]$.

On the other hand, the computational cost can be significantly reduced by considering the semi-unsteady approach^[56]. In this approach, the Eulerian and Lagrangian parts are solved consecutively, where the flow field is solved first for one Eulerian time step. Afterwards the particles are tracked in the “frozen” flow field over length of the same Eulerian time step. Within this Eulerian time step length, the tracking of each particle is sub-divided into several Lagrangian time steps, which are dynamically calculated considering all relevant time scales (see Chapter 2.2.1). If the last Lagrangian time step calculated reaches beyond the end of the actual Eulerian time step, its value is shortened appropriately. An illustration of the semi-unsteady approach used in the present calculations is shown in Figure 5.

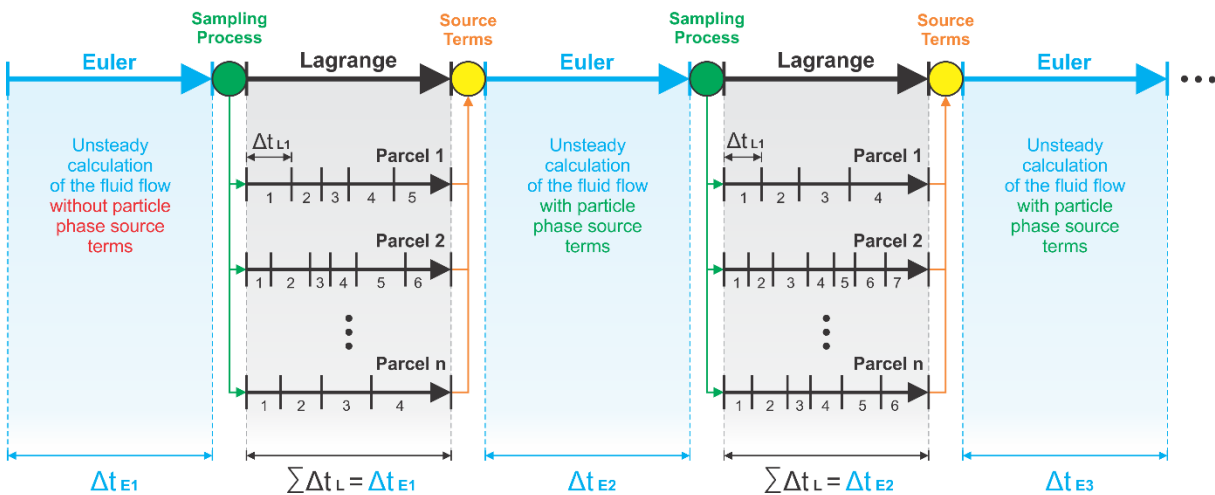


Figure 5. Representation of the semi-unsteady approach used on the present calculations. The fluid field calculated for a Eulerian time step is given to the Lagrangian part. The particles are tracked with dynamically calculated time steps in this “frozen” flow field. The calculated particle source terms are used in the calculation of the next Eulerian time step. The particle sampling used in the generation of the fictitious collision partner is performed once per Eulerian time step after the calculation of the Eulerian part and before starting the particle tracking.

2.2.3 Coupling between continuous and discrete phase

The term $\bar{\mathbf{S}}_{ui,p}$ (called $S_{\phi p}$ for the RANS simulations) represents the additional source term added to the momentum equation due to phase interaction, i.e., the influence of the particles on the fluid phase (see Sommerfeld ^[55] and Laín and Sommerfeld ^[57]). For the present study, it is not considered the influence of the particles on the turbulence properties. Hence, there are no source terms on the conservation equations for k and ε and for the RANS calculations and for the SGS on the LES calculations.

$$\bar{\mathbf{S}}_{ui,p} = -\frac{1}{V_{cv} \Delta t_E} \sum_i \sum_j (\sum \mathbf{F}_{ij} - \mathbf{F}_{G,ij}) N_i \Delta t_{L,ij} \quad (21)$$

where, V_{cv} is the cell volume, Δt_E and Δt_L are the Eulerian and Lagrangian time-steps, respectively and N_i is the number of real particles in the parcel i . The subscript j represents the Lagrangian time step of the parcel i . $\sum \mathbf{F}_{ij}$ is the sum of all forces acting on the parcel i in the Lagrangian time step j , while $\mathbf{F}_{G,ij}$ represents the gravitational force.

2.2.4 Forces Acting on the Particles

A brief overview of the considered forces acting on the particles are presented as follow.

2.2.4.1 Drag Force

Drag force dominates the particle motion in most fluid-particle systems and can be expressed for higher particle Reynolds numbers with the introduction of the drag coefficient C_D , as expressed by Crowe et al. ^[58] and Sommerfeld et al. ^[59]:

$$\mathbf{F}_D = \frac{3}{4} \frac{\rho_F m_P}{\rho_P D_P} C_D (\mathbf{U}_F - \mathbf{U}_P) |\mathbf{U}_F - \mathbf{U}_P| \quad (22)$$

where ρ_F and ρ_P are the fluid and particle density respectively, D_P is the particle diameter and \mathbf{U}_F is the fluid velocity. The drag coefficient C_D is given as a function of the particle Reynolds number Re_P .

$$Re_p = \frac{\rho_F D_P |\mathbf{U}_F - \mathbf{U}_P|}{\mu_F} \begin{cases} Re_p < 0.5 & C_D = \frac{24}{Re_p Cu} \\ 0.5 < Re_p < 1000 & C_D = \frac{24}{Re_p} (1 + 0.15 Re_p^{0.687}) \\ Re_p > 1000 & C_D \approx 0.44 \end{cases} \quad (23)$$

In the Stokes regime, which is generally valid for very small particles, e.g. $Re_p < 0.5$, the reduction of the drag coefficient may be accounted for by a correction function, so called Cunningham correlation Cu :

$$Cu = 1 + Kn (2.514 + 0.8 e^{-0.55/Kn}) \quad (24)$$

It should be noted that this correlation is only valid for $Re_p < 0.5$ and $0.1 < Kn < 1000$. Rarefaction effects should be considered if the particles are very small (e.g. nanoparticles). This phenomenon results in the reduction of the drag coefficient and may be estimated based on the ratio of mean free path of the gas molecules to the particle diameter ^[59], which is the Knudsen number Kn :

$$\lambda = \frac{\mu_F}{0.499 \overline{c_{mol}} \rho_F} \quad (25)$$

$$\overline{c_{mol}} = \sqrt{\frac{8p}{\pi \rho_F}} \quad (26)$$

$$Kn = \frac{\lambda}{D_P} \sqrt{2} \quad (27)$$

where $\overline{c_{mol}}$ is the mean relative velocity between gas molecules, λ is the mean free path of the gas molecules, μ_F is the fluid absolute viscosity and p is the system pressure. No swarm effects are accounted in the drag force, since the particles used in the present study are very small (0.5 – 85 μm) and the higher value of volume fraction is under 3%.

2.2.4.2 Gravitational Force

The gravitational force acting on the particle can be expressed as showed by Crowe et al. [58] and Sommerfeld et al. [59]:

$$\mathbf{F}_G = m_p \mathbf{g} \left(1 - \frac{\rho_F}{\rho_P}\right) \quad (28)$$

2.2.4.3 Slip-Shear Lift Force

Particles moving in a shear layer experience a transverse lift force, due to non-uniform relative velocity around the particle, resulting in a non-uniform pressure distribution. The calculation of the slip-shear lift force is based on analytical results of Saffman [60] and extended for high particle Reynolds number according to Mei [61]:

$$\mathbf{F}_{LS} = 1.615 D_p \mu_F Re_s^{1/2} c_{ls} [(\mathbf{U}_F - \mathbf{U}_P) \times \boldsymbol{\omega}_F] \quad (29)$$

where $\boldsymbol{\omega}_F = \nabla \times \mathbf{U}_F$ is the fluid rotational velocity, $Re_s = \rho_F D_p^2 |\boldsymbol{\omega}_F| / \mu_F$ is the particle Reynolds number of the shear flow and $c_{ls} = f(Re_p, Re_s) = F_{LS} / F_{LS/Saff}$ represents the ratio of the extended lift force to the Saffman force:

$$c_{ls} = \begin{cases} (1 - 0.3314 \sqrt{\beta}) e^{Re_p/10} + 0.331 \sqrt{\beta} & Re_p \leq 40 \\ 0.0524 \sqrt{\beta Re_p} & Re_p > 40 \end{cases} \quad (30)$$

with β being a parameter given by $\beta = 0.5 Re_s / Re_p$.

2.2.4.4 Slip-Rotational Lift Force

Particles may experience a lift force due to their rotation if they are not freely rotating in a flow. High particle rotation may for example be induced by particle-wall or inter-particle collisions, frequently occurring in pneumatic conveying systems. The rotation of the particle results in a deformation of the flow field around the particle, associated with a shift of the stagnation points and a transverse lift force [59]. An extension of the slip-rotation lift force for

higher particle Reynolds numbers by the introduction of a lift coefficient C_{LR} is proposed by Crowe et al. [58]:

$$\mathbf{F}_{LR} = \frac{\rho_F \pi}{2} \frac{D_P^2}{4} C_{LR} |\mathbf{U}_F - \mathbf{U}_P| \frac{\boldsymbol{\Omega} \times (\mathbf{U}_F - \mathbf{U}_P)}{|\boldsymbol{\Omega}|} \quad (31)$$

where $\boldsymbol{\Omega} = 0.5 \nabla \times \mathbf{U}_F - \boldsymbol{\omega}_P$ is the relative rotation and $\boldsymbol{\omega}_P$ is the particle rotational velocity. The lift coefficient for high particle Reynolds numbers is obtained from the following correlation introduced by Oesterlé and Bui Dinh [62].

$$C_{LR} = 0.45 + \left(\frac{Re_R}{Re_P} - 0.45 \right) \exp(-0.05684 Re_R^{0.4} Re_P^{0.3}) \quad \text{for } Re_P < 140 \quad (32)$$

where $Re_R = \rho_F D_P^2 |\boldsymbol{\Omega}| / \mu_F$ is the Reynolds number of particle rotation.

2.2.4.5 Torque

The torque acting on a rotating particle due to the interaction with the fluid for a three-dimensional flow and for high Reynolds numbers can be defined as:

$$\mathbf{T}_i = \frac{\rho_F}{2} \left(\frac{D_P}{2} \right)^5 C_R |\boldsymbol{\Omega}| \boldsymbol{\Omega} \quad (33)$$

The rotational coefficient C_R can be defined for small values of Reynolds number of particle rotation ($Re_R \leq 32$) according to Rubinow and Keller [63]. For higher values ($32 < Re_R < 1000$) it can be described according to the numerical simulations of Dennis et al. [64] and experimental data of Sawatzki [65]:

$$C_R = \frac{64\pi}{Re_R} \quad \text{for } Re_R \leq 32 \quad (34)$$

$$C_R = \frac{12.9}{Re_R^{0.5}} + \frac{128.4}{Re_R} \quad \text{for } 32 < Re_R < 1000 \quad (35)$$

2.2.5 Sub-Grid Turbulent Dispersion Model

The sub-grid turbulent particle dispersion is calculated using the isotropic Langevin model proposed by Sommerfeld et al. ^[66] and extended for LES simulations by Lipowsky and Sommerfeld ^[56]. In this modelling approach the new fluctuating fluid velocity seen by the particle at the next location is determined using a correlated and a random part, both depending on Lagrangian and Eulerian correlation functions:

$$\dot{u}_i^{n+1} = R_{P,i}(\Delta t_L, \Delta r) \dot{u}_i^n + \sigma_F \sqrt{1 - R_{P,i}^2(\Delta t_L, \Delta r)} \xi_i \quad (36)$$

where the superscripts denote the time step and the subscripts the spatial component. Δt_L is the Lagrangian time step and Δr is the spatial separation between the virtual fluid element and the particle during the time Δt_L . The SGS turbulence may be considered to be isotropic so that σ_F represents the rms value of the fluid velocity fluctuation and ξ_i denote a Gaussian distribution with zero mean and unit variance. The first term on the right hand side of the equation represents the correlated part, the second term the random contribution to the velocity fluctuation and the last term represents the drift correction for the transverse velocities fluctuations ^[66]. The correlation functions $R_{P,i}(\Delta t_L, \Delta r)$ have Lagrangian and Eulerian components:

$$R_{P,i}(\Delta t_L, \Delta r) = R_L(\Delta t_L) R_{E,ij}(\Delta r) \quad (37)$$

The Lagrangian correlation describes the instantaneous velocity fluctuation along the way of a virtual fluid element and depends on the Lagrangian integral time scale:

$$R_L(\Delta t_L) = \exp\left(-\frac{\Delta t_L}{T_L}\right) \quad (38)$$

On the other hand, the Eulerian correlation reflects the deviation of the particle trajectory from the path of the virtual fluid element, the so-called crossing trajectory effect:

$$R_{E,ij}(\Delta r) = \{f(\Delta r) - g(\Delta r)\} \frac{\Delta r_i \Delta r_j}{|\Delta \mathbf{r}|^2} + g(\Delta r) \delta_{ij} \quad (39)$$

where $f(\Delta r)$ and $g(\Delta r)$ are the longitudinal and transverse two-point correlation functions ^[66]. ^[67]. The required integral time scale $T_L = c_T \sigma_F^2 / \varepsilon_{SGS}$ and the turbulent length scale of

turbulence $L_E = c_L \sigma_F T_L$ are estimated with $\sigma_F = \sqrt{2/3 k_{SGS}}$ and the constants $c_T = 0.24$ and $c_L = 3.0$. From the LES results it is possible to estimate the unresolved turbulent kinetic energy k_{SGS} and the dissipation rate ε_{SGS} , reconstructed base on the approximations introduced by Lilly [68].

$$k_{SGS} = \frac{\mu_{t,c}^2}{\rho_F^2 (0.094 \Delta)^2} \quad (40)$$

$$\varepsilon_{SGS} = \frac{C_\varepsilon k_{SGS}^{3/2}}{\Delta} \quad (41)$$

with the dissipation constant selected as $C_\varepsilon = 0.7$ [69].

2.2.5.1 Validation of the Particle Dispersion Model in Turbulent Flow

The performance of the implemented turbulent dispersion model is validated using the experiments from Snyder and Lumley [70], where the dispersion of solid particles from a point source in grid generated turbulence are examined. The wind tunnel has a square cross section of 400 mm by 400 mm and the mean air velocity is 6.55 m/s (see Figure 6).

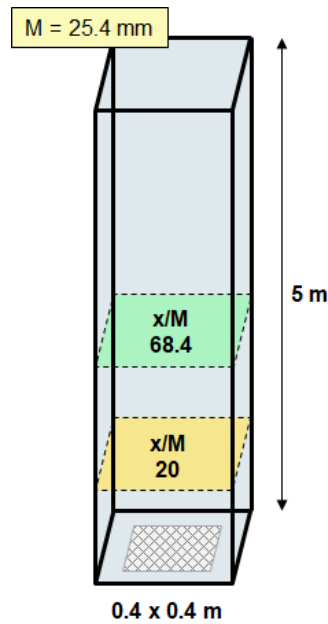


Figure 6. Representation of the Snyder and Lumley [70] experiment.

The flow field was not calculated; however, the values are obtained according to the correlations specified by the authors. The mean fluctuating components in the stream wise and

lateral directions along the wind tunnel (coordinate x) can be determined from correlations of the form:

$$\frac{U^2}{u'^2} = a_u \left(\frac{x}{M} + b_u \right) \quad \frac{U^2}{v'^2} = a_v \left(\frac{x}{M} + b_v \right) \quad (42)$$

here M is the grid spacing which was 25.4 mm in both cases. The constants a_u , b_u , a_v and b_v for both test cases are summarised in Table 2.

<i>Table 2. Constants for the determination of the mean fluctuating components for the experiments of Snyder and Lumley^[70].</i>				
U [m/s]	au	bu	av	bv
6.55	42.4	-16.0	39.4	-12.0

For this test case, the turbulent kinetic energy (k) and the dissipation rate (ε) are determined from:

$$k = \frac{1}{2} (\overline{u^2} + 2 \overline{v^2}) \quad (43)$$

$$\varepsilon = \frac{U^3}{2M} \left(\frac{1}{a_u \left(\frac{x}{M} + b_u \right)^2} + \frac{2}{a_v \left(\frac{x}{M} + b_v \right)^2} \right) \quad (44)$$

For the calculation of particle dispersion all the flow properties are prescribed along the wind tunnel for the considered test cases. In the experiments a vertically upward directed flow is considered. A total of 5000 particles are injected through a small pipe with the mean stream wise velocity of the air at the location $x/M = 20$. At the injection the particle's fluctuation velocity is sampled from a Gaussian distribution with 0 mean and 0.5 m/s variance. Three particles with different size and densities were used, which consequently have different response times as summarized in Table 3.

<i>Table 3. Particle properties used in the experiments of Snyder and Lumley^[70].</i>			
Particle Material	Particle diameter [mm]	Particle density [kg/m ³]	Stokesian response Time [ms]
hollow glass	46.5	260	1.7
corn pollen	87.0	1000	20.0
glass beads	87.0	2500	45.0

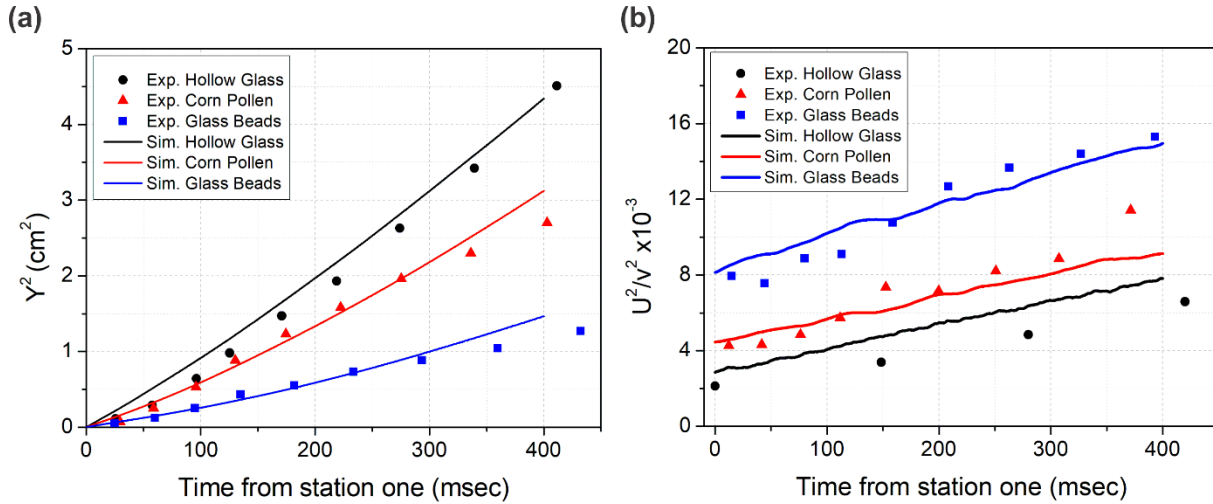


Figure 7. Particle dispersion (a) and particle velocity decay (b). Where the symbols are the experimental data obtained by Snyder and Lumley [70] and the lines are the results obtained with the implemented model in OpenFOAM.

The measurements of particle dispersion (i.e. mean square displacement) and particle velocities are performed for various locations downstream of $x/M = 68.4$. The particle dispersion (Figure 7-a) is given by the variance of the radial position [m^2] in a coordinate system where the main flow direction is in the positive axial (x) direction and the gravity force is in the negative axial (x) direction. As expected, the lighter the particle, the larger is the dispersion, as can be observed for the hollow glass particles. Hence, a good agreement with the experimental data is observed, being possible to prescribe well the dispersion for both lighter and heavier particles. The same good agreement is presented for the velocity decay (Figure 7-b). Here, the larger is the particle, larger is the velocity decay, once the larger/heavier particle presents a smaller velocity fluctuation in comparison with the smaller/lighter ones. Overall, the implemented model presents a good agreement with experimental data and therefore it is used in the calculations presented in this document.

2.2.6 Particle Wall Collisions Considering Wall Roughness

Particle-wall interaction affects directly the particle transport behaviour in confined systems such as pneumatic conveying, fluidized beds, cyclone separators and others. In pneumatic conveying systems, for example, the momentum loss of a particle caused by an inelastic wall collision results in the re-acceleration of the particle by the fluid after rebound. Hence, momentum is transferred from the fluid phase to accelerate the particle causing the additional pressure loss ^[71]. This pressure loss depends on the average wall collision frequency or mean free path between subsequent particle-wall collisions. According to Sommerfeld et al. ^[59], the wall collision frequency is mainly determined by the particle mass loading, dimensions of the confinement, particle response time or response distance, conveying velocity, turbulence intensity, particle shape and wall roughness.

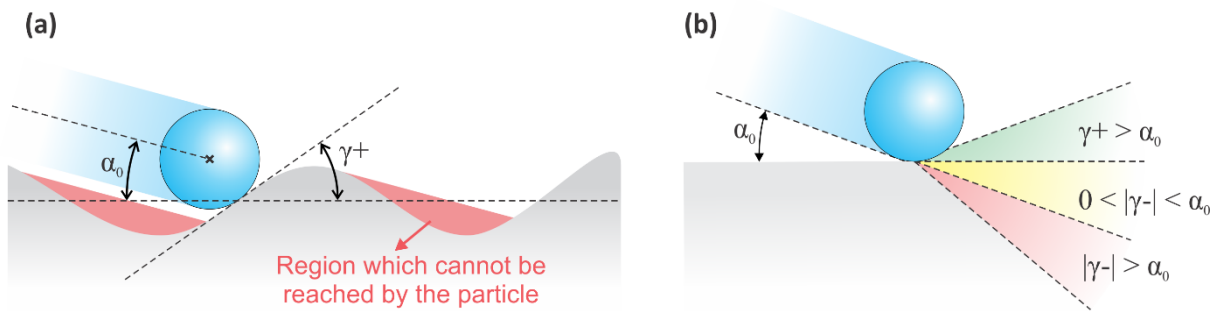


Figure 8. Illustration of the shadow effect for small impact angles. (a) Visual representation of the lee side of a roughness structure and (b) three possible regimes for the shadow effect.

In industrial equipment, e.g. pneumatic conveying lines, steel is commonly used as construction material, which has a mean roughness height between 20 and 50 μm , depending on the way of manufacture. Therefore, the wall collision process for small particles (i.e. $< 100 \mu\text{m}$) may be strongly affected by the wall roughness, since small particles are able to experience the details of the roughness structure (see Figure 8-a). Several experimental studies ^[71, 72, 73] have shown that wall roughness has a considerable impact on the particle wall collision process. Experimental studies of Sommerfeld and Huber ^[71] also revealed that the roughness angle distribution may be represented by a normal distribution function. Thus, appropriate modelling of such collisional process is important.

The implemented model is based on studies of Sommerfeld and Huber ^[71] and assumes that the particle impact angle α_1 is composed of the particle trajectory angle α_0 plus a stochastic contribution due to the wall roughness (Equation (45)). The stochastic contribution is sampled

from a Gaussian distribution ξ with mean zero and a standard deviation of one. The value of the roughness angle $\Delta\gamma$ depends mainly on the structure of wall roughness and particle size.

$$\alpha_1 = \alpha_0 + \Delta\gamma\xi \quad (45)$$

The associated shadow effect (Figure 8-b) for a small impact angle, results in a shift of the effective roughness angle distribution towards positive values since the particles are not able to reach the lee-side of the roughness structures. Since the particle cannot hit the lee-side its probability to hit a front side of a roughness structure becomes larger. From Figure 8-b three possible regimes can be identified:

1. A collision between a particle and a roughness structure is not possible for $|\gamma_-| > \alpha_0$. This means that $f(\alpha_0, \gamma) = 0$. Red region on the Figure 8-b.
2. The probability of a particle to hit a roughness structure in the interval of $0 < |\gamma_-| < \alpha_0$ is $f(\alpha_0, \gamma) = \frac{\sin(\alpha_0 + \gamma_-)}{\sin(\alpha_0)}$. Yellow region on the Figure 8-b.
3. The particle will hit a roughness structure with positive inclination, $\gamma_+ > 0$, with the probability equal to $f(\alpha_0, \gamma) = \frac{\sin(\alpha_0 + \gamma_+)}{\sin(\alpha_0)}$. Green region on the Figure 8-b.

Since an unrealistic collision occurs if a negative roughness angle with an absolute value greater than α_0 is sampled (first regime), the sampled roughness angle is multiplied by the following function:

$$f(\alpha_0, \gamma) = \frac{\sin(\alpha_0 + \gamma)}{\sin \alpha_0} \quad (46)$$

Equation (46) automatically shifts the distribution function towards positive values. This method leads to the following effective distribution function of the wall roughness inclination seen by the particle:

$$P_{eff}(\alpha_0, \Delta\gamma, \gamma) = P(\Delta\gamma, \gamma) f(\alpha_0, \gamma) = \frac{1}{\sqrt{2\pi\gamma^2}} \exp\left(-\frac{\gamma^2}{2\Delta\gamma^2}\right) \frac{\sin(\alpha_0 + \gamma)}{\sin(\alpha_0)} \quad (47)$$

The effective roughness angle distribution due to the shadow effect is plotted in Figure 9 for different impact angles ($\alpha_0 = 2.5, 5, 12.5$ and 32.5°) with a standard deviation of the roughness angle $\Delta\gamma$ of 6.5° . One can observe that with the increase of the impact angle α_0 , the shadow effect is reduced. Hence, the effective roughness angle distribution approaches the shape of a normal distribution.

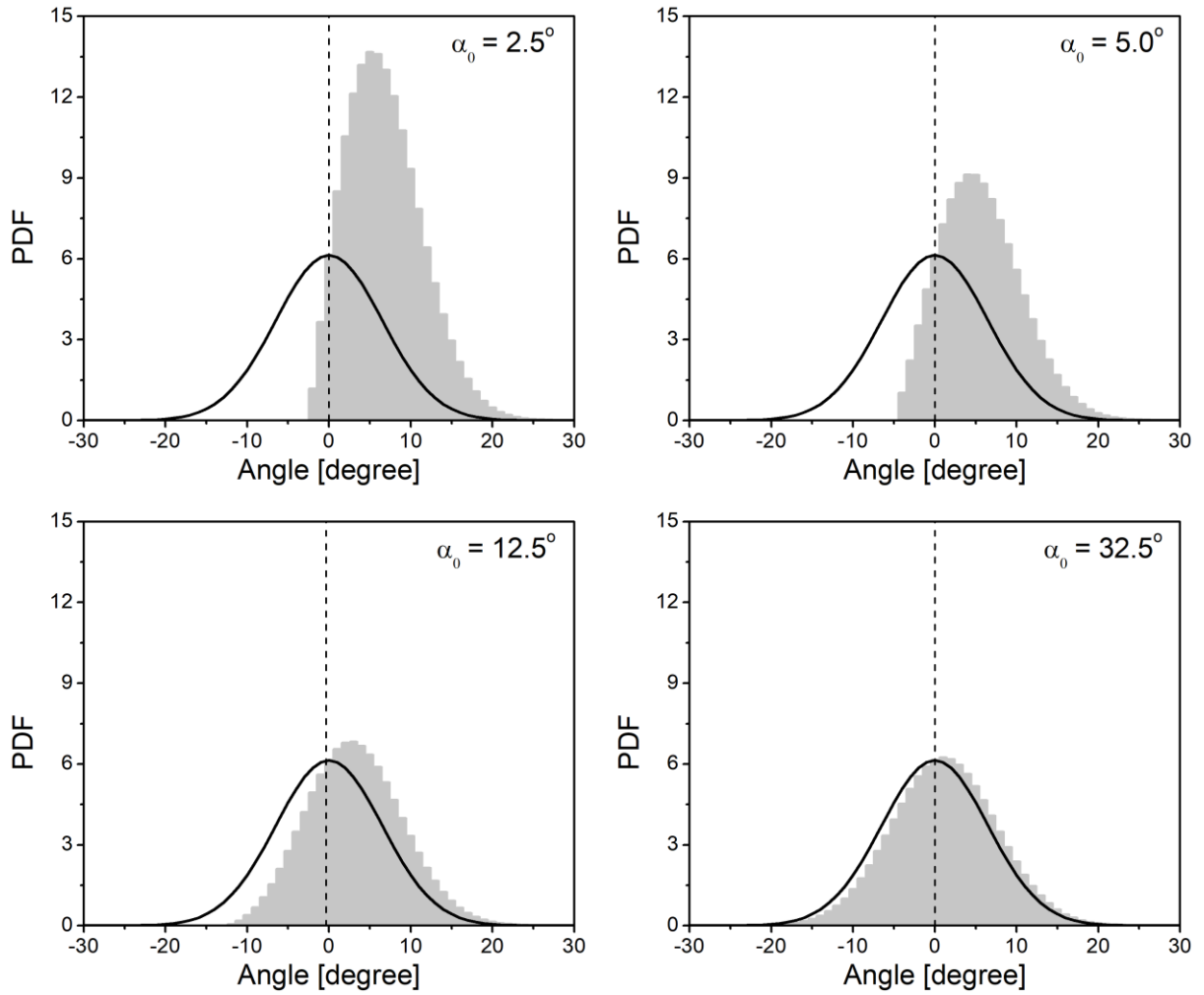


Figure 9. Modification of the roughness angle distribution due to the shadow effect for four different impact angles ($\alpha_0 = 2.5, 5, 12.5$ and 32.5°) and a standard deviation of the roughness angle $\Delta\gamma=6.5^\circ$. Where the lines represent the normal distribution and the bars represent the distribution modified by the shadow effect.

The roughness is considered to be three-dimensional, therefore two different roughness angles are required. With both roughness angles sampled, it is possible to perform a matrix rotation to readjust the velocity components accordingly to the modified orientation to the wall due to the roughness, as observed in Figure 10 for the lateral and top views.

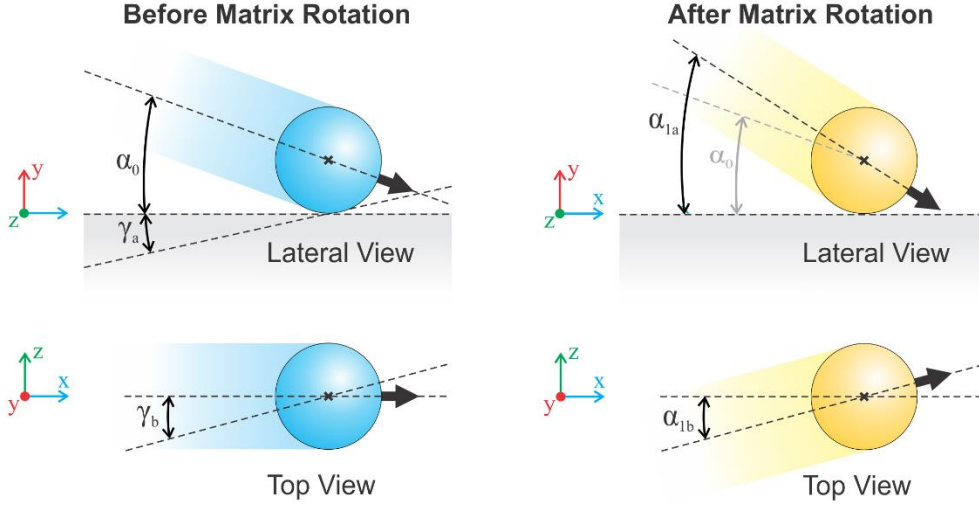


Figure 10. Matrix rotation to readjust the velocity components in order to consider the roughness contribution to the impact angle.

With the velocity components adjusted to considering the roughness angle, it is possible to calculate the change of velocity due to the collision to the wall. The changes in the particle velocity are calculated considering the so-called hard sphere model. This approach does not consider the particle deformation during the collision process explicitly. Hence, the new three-dimensional translational and angular velocity components are calculated considering a sliding or a non-sliding collision in relation to a virtual wall inclined by the roughness angle. The set of equations that describe the change in the particle translational and angular velocity for a sliding or a non-sliding collision are obtained by the solution of the momentum equation together with the Coulombs law of friction. Thus, an inelastic collision is comprehended of a compression and a recovery period, which are characterized by three types of collision:

- **Type 1:** the particle stops sliding in the compression period;
- **Type 2:** the particle stops sliding in the recovery period;
- **Type 3:** the particle slides during the whole collision process.

The types 1 and 2 correspond to a non-sliding collision while the type 3 correspond to a sliding collision. A **non-sliding** collision occurs when the following relation is satisfied:

$$|u_{R1}| \leq \frac{7}{2} \mu_0 (1 + e) v_{p1} \quad (48)$$

where μ_0 is the static coefficient of friction, e is the normal coefficient of restitution and u_{R1} is the velocity of the particle surface in relation to the contact point. The latter is calculated by:

$$u_{R1} = \sqrt{\left(u_{P1} - \frac{D_P}{2} \omega_{P1}^z\right)^2 + \left(w_{P1} + \frac{D_P}{2} \omega_{P1}^x\right)^2} \quad (49)$$

If Equation (48) is not satisfied, a sliding collision occurs. Equation (50) summarizes the equations that describe the change in the particle translational and angular velocities after the collision process considering a sliding and non-sliding collision. In these set of equations, u_{P2} , v_{P2} , and w_{P2} are the translational velocity components in the x-, y- and z-direction and ω_{P2}^x , ω_{P2}^y , and ω_{P2}^z are the angular velocity components of the particle in the coordinate system illustrated in Figure 11.

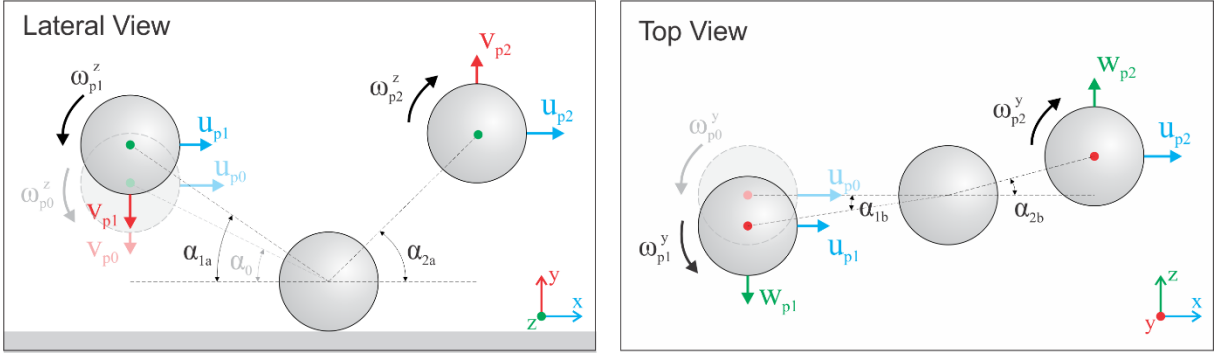


Figure 11. Definition of the velocity components before impact and after rebound.

Non-sliding collision

$$u_{P2} = \frac{5}{7} \left(u_{P1} - \frac{D_P}{5} \omega_{P1}^z \right)$$

$$v_{P2} = -e v_{P1}$$

$$w_{P2} = \frac{5}{7} \left(w_{P1} + \frac{D_P}{5} \omega_{P1}^x \right)$$

$$\omega_{P2}^x = \frac{2 w_{P2}}{D_P}$$

$$\omega_{P2}^y = \omega_{P1}^y$$

$$\omega_{P2}^z = -\frac{2 u_{P2}}{D_P}$$

Sliding collision

$$u_{P2} = u_{P1} + \mu_d \epsilon_x (1 + e) v_{P1}$$

$$v_{P2} = -e v_{P1}$$

$$w_{P2} = w_{P1} + \mu_d \epsilon_z (1 + e) v_{P1}$$

$$\omega_{P2}^x = \omega_{P1}^x - 5 \mu_d \epsilon_z (1 + e) \frac{v_{P1}}{D_P}$$

$$\omega_{P2}^y = \omega_{P1}^y$$

$$\omega_{P2}^z = \omega_{P1}^z + 5 \mu_d \epsilon_x (1 + e) \frac{v_{P1}}{D_P}$$

(50)

The terms ϵ_z and ϵ_x are the factors indicating the proportion of velocity in each component direction and are calculate as expressed in Equation (51).

$$\epsilon_x^2 + \epsilon_z^2 = 1 \quad \left\{ \begin{array}{l} \epsilon_x = \left(\frac{u_{P1} - \frac{D_P}{2} \omega_{P1}^z}{u_{R1}} \right) \\ \epsilon_z = \left(\frac{w_{P1} + \frac{D_P}{2} \omega_{P1}^x}{u_{R1}} \right) \end{array} \right. \quad (51)$$

Based on the experiments of Sommerfeld and Huber ^[71], one can express for spherical particles the dynamic coefficient of friction μ_d and the coefficient of restitution e as a function of the impact angle α_1 (expressed in degrees) as ^[57]:

$$e = \max\{0.7, 1 - 0.0136 \alpha_1\} \quad (52)$$

$$\mu_d = \max\{0.15, 0.5 - 0.0175 \alpha_1\} \quad (53)$$

It is important to highlight, that during the collision process, many particles may leave the wall with an angle close to zero. It means that many particles may not leave the region close to wall and return to flow as expected. In this perspective, Konan et al. ^[74] proposed a stochastic approach to account for the multiple rebound effects during the interaction of particles with rough walls. In this approach particles may collide with other rough structures with a certain probability when the rebound angle from the first collision is greater than zero. The higher the resultant angle from the first collision, the smaller is the probability of the particle to collide with another roughness structure. According to Konan et al. ^[74] the probability to occur only one rebound resulting from the first collision of the particle is represented by the following condition:

$$P = \begin{cases} \tanh\left(1.5 \frac{\alpha_2}{\Delta\gamma}\right) & \text{if } \alpha_2 \geq 0 \\ 0 & \text{if } \alpha_2 \leq 0 \end{cases} \quad (54)$$

where α_2 is the rebound angle of the particle and the $\Delta\gamma$ is standard deviation of the wall roughness structure. A new particle-wall interaction takes place if the probability becomes smaller than a uniform random number in the range of 0 and 1. In the case of a new particle-wall collision, a new wall roughness angle is sampled. Once the presented particle-wall collision model has several steps and may be complicated to understand, a simplified algorithm of the model is presented in Figure 12.

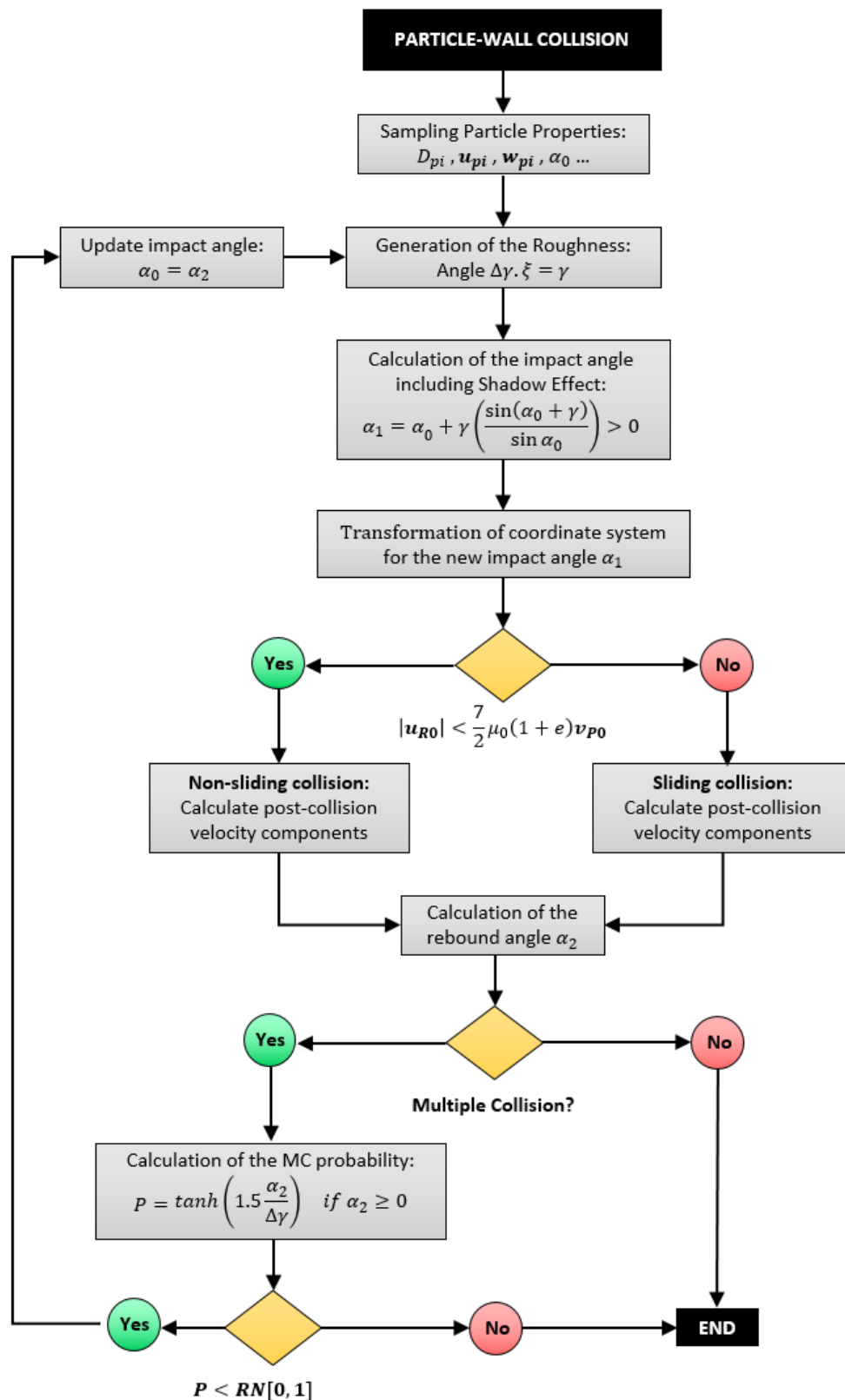


Figure 12. Simplified algorithm of the particle-wall collision model implemented in OpenFOAM 4.1.

2.2.7 Stochastic Inter-Particle Collision Model

The stochastic inter-particle collision model relies on the generation of fictitious collision partners and the calculation of the collision probability according to kinetic theory^[75]. The main advantage of this model is that no information is required on the actual position and direction of motion of the surrounding real particles (i.e. deterministic model). Instead the fictitious collision partner is sampled through the local distribution of particle properties made up for each control volume. With this approach it is possible to represent the inter-particle collision phenomenon with a lower computation effort in comparison with the deterministic model. In the next sections the sampling of the fictitious collision partner, the calculation of the collision probability and the particle velocity change due the inter-particle collision are explained in detail.

2.2.7.1 Sampling of the Fictitious Collision Partner

The sampling of the fictitious particle requires information on the local particle properties for each control volume of the entire computational domain. These local particle properties are updated after every Eulerian time step (i.e. before the particle tracking), allowing its temporal evolution and consequently a correct prediction for unsteady processes. The update of the local particle properties is executed only once per Eulerian time step to save computational effort, since this process corresponds to the major computational cost of the present model. An illustration of the sampling process is shown in Figure 13.

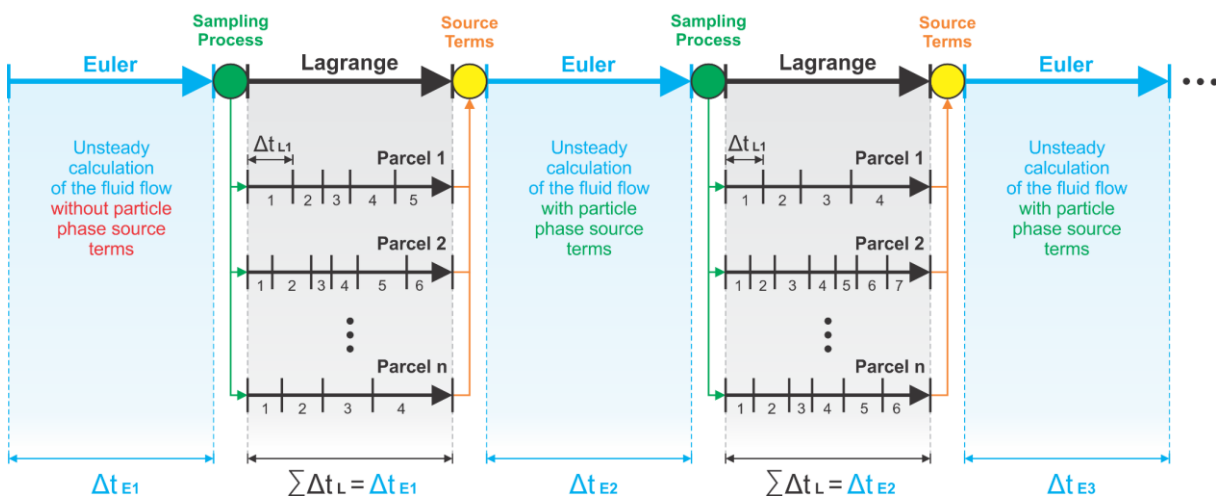


Figure 13. Illustration of the sampling process for the fictitious collision partner, where the local particle properties are updated after every Eulerian time step and before the particle tracking.

Thus, a new fictitious collision partner is sampled based on the local particle properties for every Lagrangian time step of every parcel tracked. If a class density distribution is used, the probability for each class corresponds to the relative number concentrations. The velocity of the fictitious particle \mathbf{U}_{Pj} is composed by the local mean velocity $\bar{\mathbf{U}}_{P,cv}$ and its fluctuating velocity \mathbf{U}'_{Pj} , which is based on a correlation with the real particle and a Gaussian velocity distribution with the local rms-value. Since there is no specific correlation for the angular velocity shift, an averaged value correlated to the class size is attributed to the fictitious particle.

$$\mathbf{U}_{Pj} = \bar{\mathbf{U}}_{P,cv} + \mathbf{U}'_{Pj} \quad (55)$$

$$\mathbf{U}'_{Pj} = R(St) \mathbf{U}'_{Pi} + \sigma_{P,cv} \sqrt{1 - R(St)^2} \xi \quad (56)$$

where $\sigma_{P,cv}$ is the local rms value of the particle velocity in the control volume, \mathbf{U}'_{Pi} is the fluctuating velocity of the real particle and ξ is a Gaussian random number with zero mean and a standard deviation of one. The subscript i and j denote the real and the fictitious particle respectively.

One can observe that the sampled fluctuating velocity components of the fictitious particle are composed by a correlated (first term of the right-hand side) and a random contribution (second term of the right-hand side). By increasing the Stokes number, the correlated contribution is decreased, while the random contribution is increased accordingly. The correlation function on the Stokes number $R(St)$ is proposed by Sommerfeld^[75] and was found by comparing model calculations with LES results, as follow:

$$R(St) = \exp(-0.55 St^{0.4}) \quad (57)$$

The degree to which the particle fluctuating velocities are correlated depends on their response to the turbulence fluctuations, which can be characterized by the turbulent Stokes number St , i.e. the ratio of the particle response time τ_P to the relevant time scale of turbulence τ_t .

$$St = \frac{\tau_P}{\tau_t} = \frac{\tau_P}{T_L} \quad (58)$$

$$\tau_P = \frac{\rho_{Pi} D_{Pi}^2}{18 \mu_F f_D} \quad (59)$$

$$f_D = \frac{C_D Re_P}{24} \quad (60)$$

where $T_L = c_T \sigma_F^2 / \varepsilon$ is the integral time scale and the turbulent length scale of turbulence $L_E = c_L \sigma_F T_L$ are estimated with $\sigma_F = \sqrt{2/3 k}$ and the constants $c_T = 0.24$ and $c_L = 3.0$. Once the sampling of all particle properties is concluded, it is possible to create the collision partner for every real particle and their respective collision probability.

2.2.7.2 Collision Probability and Impact Efficiency

After sampling the fictitious partner, the next step in the collision model is the determination of the inter-particle collision probability P_{coll} , which depends mainly on the particle concentration, particle size and fluctuating motion of particles. It can be calculated as the product of collision frequency f_c and the particle tracking time step Δt . Collision events of one particle with another can happen only inside a collision cylinder which is defined by the cross-sectional area $\frac{\pi}{4} (D_{Pi} + D_{Pj})^2$ and the length $|\mathbf{U}_{Pi} - \mathbf{U}_{Pj}| \Delta t_L$. Multiplying the collision cylinder by the number of particles² over the volume of the specific control volume n_p / V_{cell} , one can have the collision probability between the considered particle and the surrounding particles as showed in equation (61).

$$P_{coll} = f_c \Delta t = \frac{\pi}{4} (D_{Pi} + D_{Pj})^2 |\mathbf{U}_{Pi} - \mathbf{U}_{Pj}| \frac{n_p}{V_{cell}} \Delta t_L \quad (61)$$

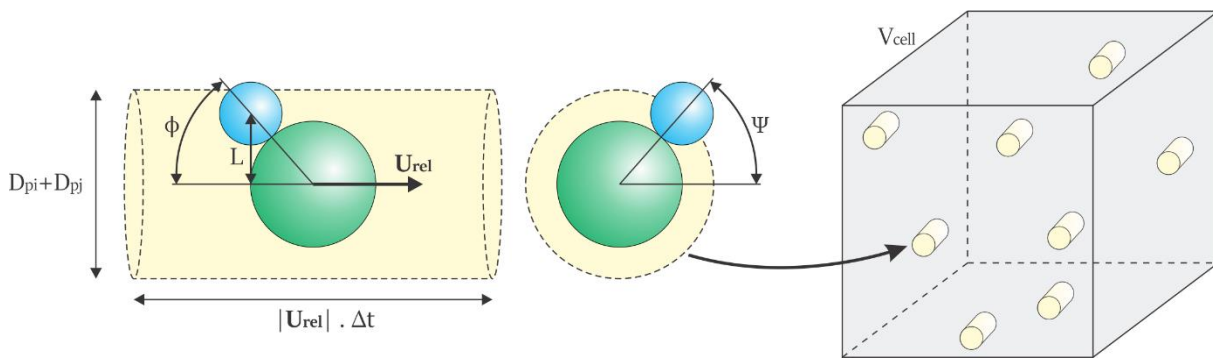


Figure 14. Illustration of the collision cylinder (left), collision cross-sectional area (middle) and collision probability (right).

² If a particle size distribution is considered, n_p should be the number concentration of all particle fractions, since the fictitious particle is sampled from the size distribution which already accounts for the probability if a particle being in a certain size interval.

To obtain the collision fictitious point of impact, the collision calculation is done in a coordinate system where the real particle is stationary, so that the axis of the collision cylinder is aligned with the relative velocity vector (Figure 15-a). The non-dimensional radial location of the collision point in the cross-section of the collision cylinder (lateral non-dimensional displacement L_a) is obtained stochastically by generating two uniform random numbers XX and ZZ in the range $[0, 1]$. Hence, the angle of impact $\phi = \arcsin(L)$ can be determined by the lateral displacement. The orientation of the collision plane in the cross-section of the collision cylinder (i.e. the angle Ψ , Figure 15-c) is randomly sampled from a uniform distribution in the range $[0 < \Psi < 2\pi]$.

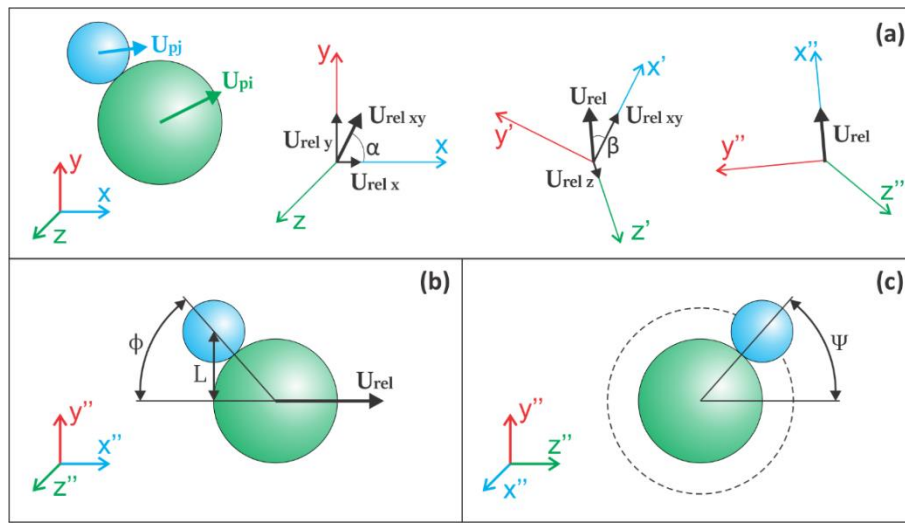


Figure 15. Transformation of the coordinate system in order to align the relative velocity with the axis of the collision cylinder (a) and to obtain the point of impact (b, c).

$$L_a = \sqrt{XX^2 + ZZ^2} \quad \text{with } L_a < 1 \quad (62)$$

$$L = \frac{L_a(D_{PC} + D_{PS})}{2} \quad (63)$$

Considering a particle size distribution leads to the possibility of small particles colliding with much larger ones (collector particle), requires the impact efficiency (Figure 16) to be accounted for. This elementary process implies that the smaller particle might move around the collector particle with the relative flow yielding a reduced collision probability. In this specific configuration, the larger particle is always the stationary one and the velocity components are transformed accordingly.

$$\text{if } (D_{Pi} > D_{Pj}) \begin{cases} D_{PC} = D_{Pi} \\ D_{PS} = D_{Pj} \end{cases} \quad \text{if } (D_{Pi} < D_{Pj}) \begin{cases} D_{PC} = D_{Pj} \\ D_{PS} = D_{Pi} \end{cases} \quad (64)$$

where the subscript Pc and Ps designate the collector and the small particle respectively. The impact efficiency^[75] is actually the ratio of the circular cross-section with radius Y_c to the cross-section of the collision cylinder, from where the small particle might come and still hit the collector particle (Figure 16). It is also possible to correlate the impact efficiency through a function of relative Stokes number $St_{Rel,i}$, namely the ratio of the small particle response time to the time needed to pass the collector. This correlation was developed by Schuch and Loeffler^[76] for different Reynolds numbers of the collector particle, expressing the radial distance Y_c in Equation (65) and the collection efficiency in Equation (66).

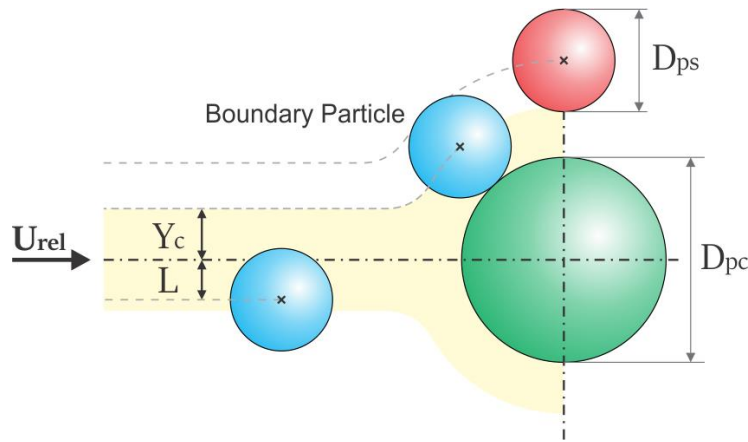


Figure 16. Representation of the impact efficiency for a small particle interacting with a stationary collector (green particle), where the blue particles represent the colliding particles and the red one represents the particles that missed the collision.

$$Y_c = \frac{D_{Pc} + D_{Ps}}{2} \sqrt{\left(\frac{St_{Rel,i}}{St_{Rel,i} + a}\right)^b} \quad (65)$$

$$\eta_P = \left(\frac{2 Y_c}{D_{Pc} + D_{Ps}}\right)^2 = \left(\frac{St_{Rel,i}}{St_{Rel,i} + a}\right)^b \quad (66)$$

where L is the lateral displacement, D_{Pc} is the diameter of the collector particle, D_{Ps} is the diameter of the smaller particle, XX and ZZ are random numbers with range $[0, 1]$, η_P is the impact efficiency, Y_c is the radial distance and a and b are constants for the impact efficiency correlation proposed by Schuch and Loeffler^[76] (see Table 4). The relative Stokes number $St_{Rel,i}$ can be expressed as:

$$St_{Rel,i} = \frac{\rho_P |\mathbf{U}_{Pc} - \mathbf{U}_{Ps}| D_{Ps}^2}{18 \mu f_D D_{Pc}} \quad (67)$$

$$f_D = \frac{C_d Re_{PC}}{24} \quad (68)$$

$$Re_{PC} = \frac{\rho_F D_{PC} |\mathbf{U}_F - \mathbf{U}_{Ps}|}{\mu_F} \quad (69)$$

<i>Table 4. Constants for the impact efficiency correlation proposed by Schuch and Loeffler^[76].</i>		
	<i>a</i>	<i>b</i>
$Re_{PC} < 1$	0.65	3.7
$1 < Re_{PC} < 20$	1.24	1.95
$20 < Re_{PC} < 40$	1.03	2.07
$40 < Re_{PC} < 80$	0.506	1.84
$Re_{PC} > 80$	0.25	2.0

Finally, an inter-particle collision only takes place when a random number RN obtained from a uniform distribution with interval $[0,1]$ is smaller than the calculated collision probability P_{coll} and the lateral displacement L is smaller than the radial distance of the boundary particle trajectory Y_c .

$$if \begin{cases} RN < P_{coll} \\ L < Y_c \end{cases} = collision \quad (70)$$

2.2.7.3 Particle Velocity Change due to Inter-Particle Collisions

The change of linear and angular velocity components can be calculated by solving the momentum equations in connection with Coulomb's law of friction. It is also considered that only binary collisions happens and the deformation of the particles during the collision process is not considered explicitly (hard sphere model). The relative velocity components at the point of contact (u_R u_{Ry} u_{Rz}) are determined with the relative linear velocity components and the angular velocity components of the real and fictitious particle, as:

$$u_R = \sqrt{u_{Ry}^2 + u_{Rz}^2}$$

$$u_{Ry} = v_{P1} + \frac{D_{Pi}}{2} \omega_{P1,i}^z + \frac{D_{Pj}}{2} \omega_{P1,j}^z \quad (71)$$

$$u_{Rz} = w_{P1} - \frac{D_{Pi}}{2} \omega_{P1,i}^y - \frac{D_{Pj}}{2} \omega_{P1,j}^y$$

where $(u_{P1} \ v_{P1} \ w_{P1})$ are the relative linear velocity components and $(\omega_{P1}^x \ \omega_{P1}^y \ \omega_{P1}^z)$ are the angular velocity components. The subscript i and j denote the real and the fictitious particle respectively, where the subscript 1 denotes impact and 2 rebound. One should keep in mind that these velocity components are already converted to the transformed coordinate system. Therefore, the impulsive force in the direction of the collision J_x can be calculated as follow:

$$J_x = -(1 + e) u_{P1} \frac{m_{Pi} m_{Pj}}{m_{Pi} + m_{Pj}} \quad (72)$$

where e is the restitution coefficient and m_p is the particle mass. By applying Coulomb's law of friction, a condition for non-sliding (rolling) collision as a function of the static coefficient of friction μ_0 can be obtained:

$$|u_R| < \frac{7}{2} \mu_0 (1 + e) |u_{P1}| \quad (73)$$

The components of the impulsive force J_y and J_z are dependent on the type of collision. For a non-sliding collision, they can be calculated as shown in Equation (74). For a sliding collision, the components of the impulsive force are dependent on the dynamic coefficient of friction μ_d , as expressed in Equation (75).

Non-sliding Collision

$$\begin{cases} J_y = -\frac{2}{7} u_{Ry} \frac{m_{Pi} m_{Pj}}{m_{Pi} + m_{Pj}} \\ J_z = -\frac{2}{7} u_{Rz} \frac{m_{Pi} m_{Pj}}{m_{Pi} + m_{Pj}} \end{cases} \quad (74)$$

Sliding Collision

$$\begin{cases} J_y = -\mu_d \frac{u_{Ry}}{u_R} |J_x| \\ J_z = -\mu_d \frac{u_{Rz}}{u_R} |J_x| \end{cases} \quad (75)$$

The following equations calculate the new relative linear (Equation (76)) and angular (Equation (77)) velocity components for both particles (real and fictitious) in terms of the relative velocity before collision.

Real Particle

$$\begin{cases} u_{P2,i} = u_{P1,i} + \frac{J_x}{m_{Pi}} \\ v_{P2,i} = v_{P1,i} + \frac{J_y}{m_{Pi}} \\ w_{P2,i} = w_{P1,i} + \frac{J_z}{m_{Pi}} \end{cases}$$

Fictitious Particle

$$\begin{cases} u_{P2,j} = -\frac{J_x}{m_{Pj}} \\ v_{P2,j} = -\frac{J_y}{m_{Pj}} \\ w_{P2,j} = -\frac{J_z}{m_{Pj}} \end{cases} \quad (76)$$

Real Particle

$$\begin{cases} \omega_{P2,i}^x = \omega_{P1,i}^x \\ \omega_{P2,i}^y = \omega_{P1,i}^y - \frac{5 J_z}{m_{Pi} D_{Pi}} \\ \omega_{P2,i}^z = \omega_{P1,i}^z + \frac{5 J_y}{m_{Pi} D_{Pi}} \end{cases}$$

Fictitious Particle

$$\begin{cases} \omega_{P2,j}^x = \omega_{P1,j}^x \\ \omega_{P2,j}^y = \omega_{P1,j}^y + \frac{5 J_z}{m_{Pj} D_{Pj}} \\ \omega_{P2,j}^z = \omega_{P1,j}^z - \frac{5 J_y}{m_{Pj} D_{Pj}} \end{cases} \quad (77)$$

The subscript i and j denote the real and the fictitious particle respectively, where the subscript 1 denotes impact and 2 rebound velocity components. Once the new relative velocities are obtained, they need to be re-transformed into the original coordinate system and added to the velocity of the real particle to consider the changing of momentum due to the inter-particle collision.

Finally, to better understand the implementation process, the structure of the algorithm is presented. Figure 17 shown the first part of the algorithm necessary to create the properties of the fictitious partner and to verify if a collision will take place. The initial blue steps presented in Figure 17 are executed once per Eulerian time step, while the grey ones are executed every Lagrangian time step, as explained in the sampling process in Chapter 2.2.7.1. In Figure 18 details the second part of the algorithm, where the inter-particle collision is already confirmed ($RN < P_{coll}$ and $L < Y_c$). This part of the model treats the change of velocity of the particles after the collision and the possibility of an agglomeration takes place. The agglomeration model, as well as the possibility of breakage of the created agglomerate are presented in the next sections.

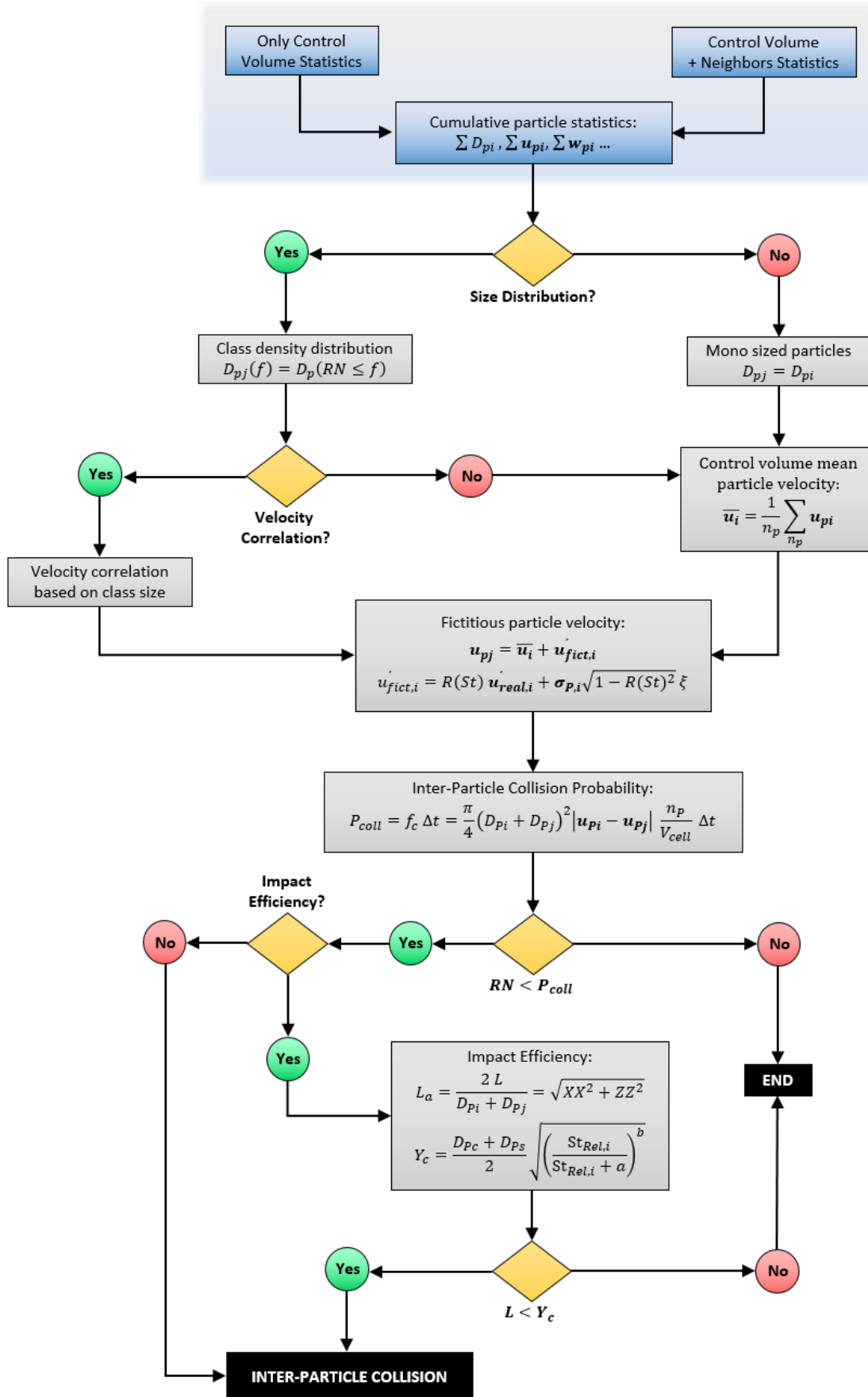


Figure 17. Stochastic inter-particle collision model algorithm (part one).

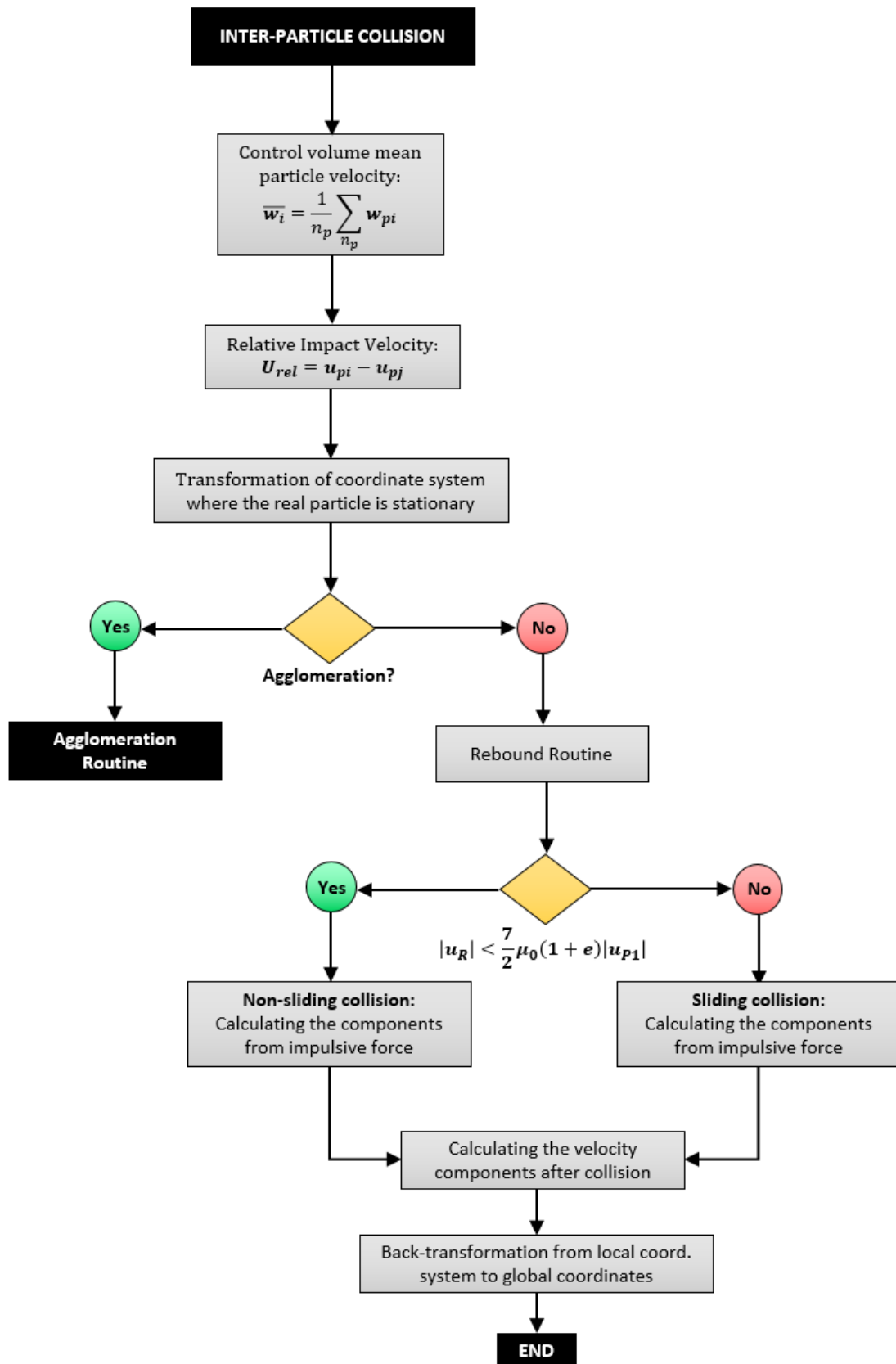


Figure 18. Stochastic inter-particle collision model algorithm (part two).

2.2.8 Agglomeration Models

The agglomeration of solid particles in gas or liquid flows is a common elementary process in numerous technical and industrial processes. An agglomerate consists of a number of primary particles being bound together by an adhesive force, resulting in different forms, such as compact or complex structures involving dendrites. Agglomeration may be desired for diverse industrial processes, as in the case of particle separation in cyclones, where the bigger particles are easier to collect. Hence, a proper modelling of the agglomeration phenomenon should be considered. According to Sommerfeld and Stübing ^[38], the four main steps of agglomeration modelling are:

1. Detection of a possible collision between two particles;
2. Determination of the collision point by accounting for the impact efficiency;
3. Decision whether particles are sticking together or being rebound;
4. Description of the resulting agglomerate size (or structure) and the resultant velocity after collision.

The first two steps are accounted for by the collision probability and impact efficiency calculation in the stochastic inter-particle collision model, while the last two steps are presented as follow. In a gas-particle system, e.g. pneumatic conveying systems and cyclones, the most relevant adhesion force is the van der Waals molecular interaction force. Electrostatic forces are not important unless contact charging of particles is employed, while contact forces through liquid adsorption layers around the particle are only important if the considered process is very humid and vapour may adsorb on the particle surface ^[38]. Since for the present study only dry and insulating particles are considered, the van der Waals is the only adhesion force considered for particle agglomeration. The criterion for agglomeration of dry particles is obtained by comparing the kinetic energy of the primary particle before the inter-particle collision E_{ki} , with the possible rebound kinetic energy E_{kr} , the dissipated energy E_d and the energy due to van der Waals attraction ΔE_{vdW} ^[77], as follow:

$$E_{ki} = E_{kr} + E_d + \Delta E_{vdW} \quad (78)$$

An agglomeration can only take place if there is not kinetic energy available for the rebound ($E_{kr} = 0$), while the relative kinetic energy E_{ki} may be determine as a function of the

relative velocity. By assuming that the deformation of both particles during the collision is very small compared to the particles size, the van der Waals energy for separation of two planar surfaces is obtained from the adhesion force per area (i.e. adhesion pressure) and deformation area $A_d = \pi D_{ps} h_{ps}$. Therefore, a summary of the formulation of the agglomeration criterion [38, 77, 78] is expressed as follow:

$$E_{kr} = 0 \quad (79)$$

$$E_{ki} = \frac{\pi}{12} \rho_p D_{ps}^3 |\mathbf{U}_{Rel}|^2 \quad (80)$$

$$\Delta E_{vdW} = \frac{H A_d}{12 \pi z_0^2} \quad (81)$$

$$E_d = \frac{\pi}{2} p_c (D_{ps} h_{ps}^2 + D_{pc} h_{pc}^2) = (1 - k_r^2) E_{ki} \quad (82)$$

$$h_{ps} = D_{ps} |\mathbf{U}_{Rel}| \sqrt{\frac{(1 - k_r^2) \rho_p}{6 p_c (1 + D_{ps}/D_{pc})}} \quad (83)$$

where D_{ps} is the smaller (moving) particle, D_{pc} is the collector particle, H is the Hamacker constant, z_0 is the minimum contact distance between the particles, h_{ps} is the particle deformation depth, k_r is the energy restitution ratio and p_c is the yield pressure.

Thus, by combining the above equations, is possible to determine the critical velocity U_{crit} . As shown by Hiller [77], if the relative velocity between the two colliding particles before the impact is less than a critical velocity U_{crit} , the restitution energy after the impact will not surpass the van der Waals energy between the particles, thus creating an agglomerate [78] with conditions expressed by:

$$U_{crit} = \frac{\sqrt{1 - k_r^2}}{k_r^2} \cdot \frac{H}{\pi D_{ps} z_0^2 \sqrt{6 p_c \rho_p (1 + D_{ps}/D_{pc})}} \quad (84)$$

$$|\mathbf{U}_{Rel}| \cos(\phi) \leq U_{crit} \quad (85)$$

where $|\mathbf{U}_{Rel}|$ is the modulus of the relative velocity, $\phi = \arcsin(L)$ is the impact angle and ρ_p is the density of the primary particle. The parameters used to calculate the critical impact velocity in Equation (84) are summarized in Table 5.

<i>Table 5. Particle adhesion properties for calculating the critical impact velocity Sommerfeld and Stübing^[38].</i>		
Hamacker constant	H	$5 \times 10^{-19} \text{ J}$
Energy restitution ratio	k_r	0.7
Minimum contact distance	z_0	$4 \times 10^{-10} \text{ m}$
Yield pressure	p_c	$5 \times 10^9 \text{ Pa}$

In case the normal component of the relative velocity $|\mathbf{U}_{Rel}| \cos(\phi)$ is larger than the critical velocity U_{crit} , a rebound is calculated using the impulse equations in connection with Coulomb's law of friction^[36], otherwise an agglomeration will take place. Thus, the adhesive force F_b of the newly created bond between the particles is calculated as proposed by Lipowsky and Sommerfeld^[36].

$$F_b = \frac{H}{12 z_0^2} \left(\frac{D_{ps} D_{pc}}{D_{ps} + D_{pc}} \right) \quad (86)$$

To represent the agglomeration phenomenon, two different approaches are tested. The first one, so called sphere model, considers that the agglomerate's diameter is calculated from the sum of the volume of all involved primary particles. So far, most agglomeration models used in Euler/Lagrange calculations assumed that the agglomerate behaves like a volume equivalent sphere, with the exception of the recent works of Breuer and Almohammed^[79, 80], where the agglomerate is considered to have an inertia-equivalent diameter (gyration diameter) or alternatively a closed-packed sphere diameter. The sphere model has been tested and validated by Ho and Sommerfeld^[78] for homogeneous isotropic turbulence, a plane shear layer^[78, 81] and a gas cyclone^[37]. The second agglomeration model tested is the history model proposed by Lipowsky and Sommerfeld^[36]. The pore volume between two primary particles (Figure 19, blue region) is calculated as the volume of a truncated cone minus two spherical caps (Figure 19, red region), as summarized in Equation (90).

$$h = (D_{pc} D_{ps}) / (D_{pc} + D_{ps}) \quad (87)$$

$$\alpha = \arcsin(|r_1 - r_2| / (r_1 + r_2)) \quad (88)$$

$$r_{ci} = \cos(\alpha) \cdot r_i \quad (89)$$

$$V_{Pore} = \frac{2h\pi}{3} \cdot (r_{c1}^2 + r_{c1} \cdot r_{c2} + r_{c2}^2) - \frac{h^2\pi}{3} \cdot (3r_1 + 3r_2 - 2h) \quad (90)$$

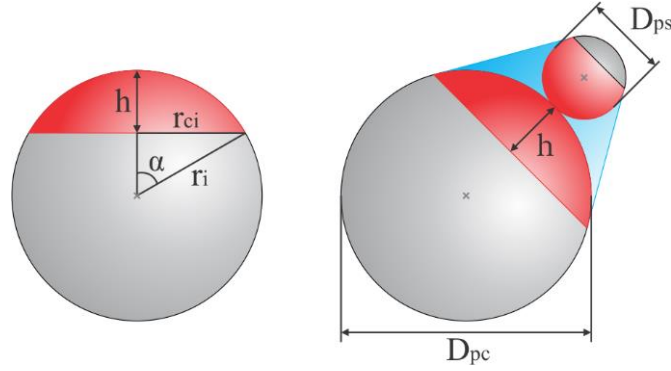


Figure 19. Example of a spherical cap (left) and a binary primary particle agglomeration (right), where the pore volume between two primary particles (blue) is calculated as the volume of a truncated cone minus two spherical caps (red) of the primary particles.

With the pore volume one can calculate the total agglomerate volume, the porosity and its new density, being these properties required for considering the real size of the agglomerate in the particle tracking (i.e. all resistance coefficients of the agglomerate). With the new agglomerate volume, the diameter of the porous sphere is obtained which is also used further in the particle tracking and in the calculation of the correct collision cross-section. Hence, if a new inter-particle collision takes place with the formed agglomerate, the agglomerate properties as size (cross-section), density and porosity are considered, making possible a further particle agglomeration to the agglomerate. A summary of the main differences between both studied agglomeration models is presented in Table 6.

<i>Table 6. Agglomerate properties calculated for the two different models.</i>		
	Sphere Model	History Model
Volume [m ³]	$V_{Ag} = V_{pc} + V_{ps}$	$V_{Ag} = V_{pc} + V_{ps} + V_{pore}$
Volume Equivalent Diameter [m]	$D_{Ag} = \sqrt[3]{\frac{6}{\pi} V_{Ag}}$	$D_{Ag} = \sqrt[3]{\frac{6}{\pi} V_{Ag}}$
Porosity [-]	$\varepsilon_V = 0$	$\varepsilon_V = V_{pore} / V_{Ag}$
Density [kg/m ³]	$\rho_{Ag} = \rho_p$	$\rho_{Ag} = \rho_p (1 - \varepsilon_V)$

If an agglomeration takes place, the primary particle increases in size and consequently in mass. Considering computational parcels means, that all the particles represented by this parcel also agglomerate and increase in size and mass. Thus, the particle represents a number of agglomerates equal to the number of initial primary particles. To conserve the parcel total mass, i.e., the sum of the masses of all the particles that the parcel represents, it is necessary to close the balance by decreasing the initial number of primary particles represented by the parcel.

Even with the increase in size, this effect will have an influence on the further relevant local collision probability. Hence, agglomeration reduces the total number density of particles/agglomerates in the control volume.

A short comparison between the two used agglomeration models is presented as follow, where 15 primary particles with size of $12\ \mu\text{m}$ and density of $1,000\ \text{kg/m}^3$ are consecutively agglomerated. Figure 20 shown the evolution of the agglomerate size, porosity and density within the increase of the number of primary particles in the agglomerate. The larger size for the agglomerate produced by the History model is noticeable, where an increment of around 36% in size in comparison with the one produced by the Sphere model is observed (40.41 and $29.59\ \mu\text{m}$ respectively). However, within the increase in size, the porosity also increases, consequently reducing the agglomerate density. Thus, with the History model effectively larger porous agglomerates are produced yielding higher aerodynamic drag in comparison with the agglomerates produced by the Sphere model. This difference may play a major role in the collection efficiency prediction, once the larger and porous agglomerate may be easier dragged by the inner vortex of the cyclone and directed to the escape region. An illustrative comparison of both agglomerates formed from 15 primary particles is shown in Figure 21.

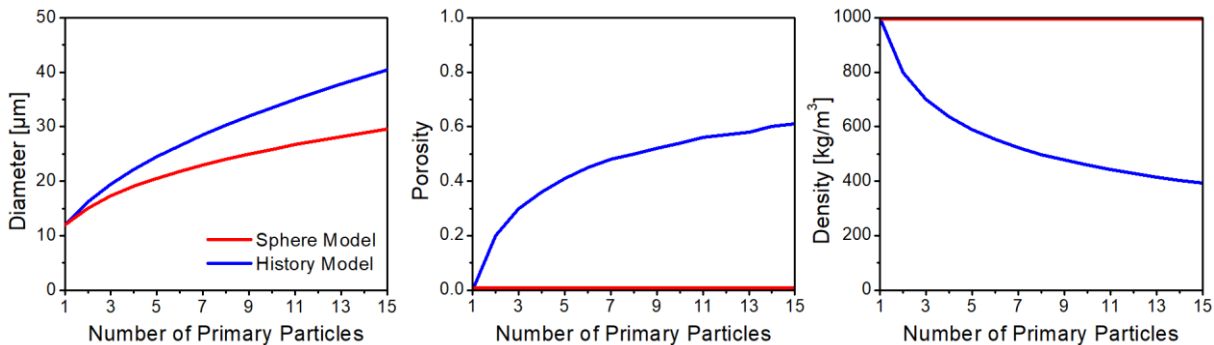


Figure 20. Comparison between the Sphere model (red lines) and the History model (blue lines) for a consecutive agglomeration of 15 primary particles with size of $12\ \mu\text{m}$ and density of $1,000\ \text{kg/m}^3$. Evolution of agglomerate size (left), porosity (middle) and density (right).

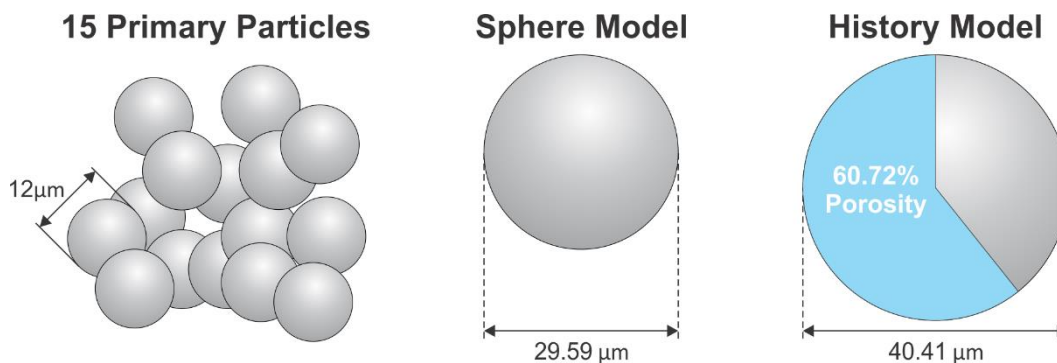


Figure 21. Visual comparison between the Sphere model and the History model for a consecutive agglomeration of 15 primary particles with size of $12\ \mu\text{m}$ and density of $1,000\ \text{kg/m}^3$.

Stübing^[82] considered a more complex agglomeration model, where the structure of the agglomerate is stored, hence allowing the calculation of fractal dimension, and gyration diameter. The author performed a numerical experiment with an isotropic turbulence box with dimensions of 0.2 x 0.2 x 0.2 m, where 10,000 particles are randomly distributed inside the computational domain at the beginning of the calculations. A volume fraction of particles in the order of 1×10^{-3} is assumed and the initial particle velocity was drawn from a normal velocity distribution. The used particles have a size distribution with a mean value of 12 μm and density of 1,000 kg/m^3 . The particles are tracked inside the system for 5 seconds, where the growth due to agglomeration and further properties were analysed. On the other hand, the results obtained with the proposed models are calculated by the consecutive agglomeration of 60 primary particles with fixed size of 12 μm . Hence, a short comparison between the agglomerate properties obtained with the presented models and the numerical calculations of Stübing^[82] is shown in Figure 22. Despite the simplicity of the History model, the correlated evolution of the size and porosity of the agglomerate by the number of primary particles present a remarkable agreement with the calculations from Stübing^[82]. The wide distribution of agglomerate sizes and porosity observed by Stübing^[82] are related to size distribution used, hence allowing a fluctuation of those properties for a same number of primary particles.

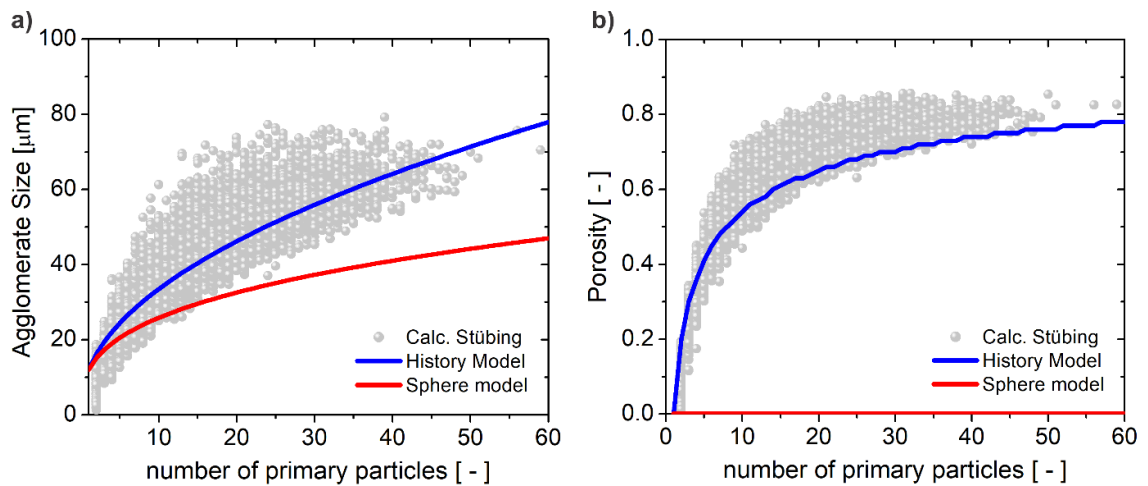


Figure 22. Correlation between primary particle numbers in the agglomerate size (a) and porosity (b). The points represent the numerical calculation of Stübing [38, 82] and the lines are the results for the History (blue) and Sphere (red) models.

Finally, if an agglomeration event is considered, the resultant velocity of the agglomerate U_{Ag} is calculated. Hence, the conservation of the agglomerate momentum is expressed as:

$$U_{Ag} = \frac{U_{P1} m_{P1} + U_{P2} m_{P2}}{m_{P1} + m_{P2}} \quad (91)$$

2.2.8.1 Agglomerate Breakage

Once an agglomerate is formed, it is possible that the same may break due to a subsequent collision with another primary particle or with the equipment walls. An agglomerate breakage may also take place due to inertia stress, rotary stress and turbulent stresses (shear and impaction) ^[83], among several others. However, due to the complexity of the studied system and the lack of experimental data regarding agglomeration and agglomerate breakage in cyclone separators, a simpler approach for the breakup phenomenon is adopted.

Once for the present study only dry and insulating particles are considered and the van der Waals is the only adhesion force considered for particle agglomeration, an agglomerate may break if the impact force, i.e. due to agglomerate-wall or agglomerate-particle collision, is higher than the adhesive force F_b . From Newton's second law of motion, is possible to determine the impact force between the agglomerate and the wall $F_{A.W.}$ as:

$$F_{A.W.} = \frac{|\mathbf{v}_{Ag} - \mathbf{v}_{Wall}| m_{Ag}}{\Delta t_L} \quad (92)$$

where m_{Ag} is the agglomerate mass and Δt_L is the Lagrangian time step. \mathbf{v}_{Ag} and \mathbf{v}_{Wall} are the normal velocity components of the agglomerate and wall respectively. For the present study, no moving walls are considered, hence $\mathbf{v}_{Wall} = (0,0,0)$.

The impact force from an agglomerate-particle collision $F_{A.P.}$ may be calculated direct through the impulsive forces J calculated in the stochastic inter-particle collision model, as follow:

$$F_{A.P.} = \frac{|J_x + J_y + J_z|}{\Delta t_L} \quad (93)$$

Thus, if the impact forces due to agglomerate-wall $F_{A.W.}$ or agglomerate-particle $F_{A.P.}$ collision are higher than the adhesive force F_b , the agglomerate will break.

$$\begin{aligned} &\textit{Agglomerate Breakage takes place if:} \\ &F_{A.W.} > F_b \text{ or } F_{A.P.} > F_b \end{aligned} \quad (94)$$

Since the proposed agglomeration models do not store the structure of the agglomerate with the specific information of each primary particle, an alternative method is adopted.

Therefore, if a breakage event takes place, the last agglomerated particle is removed from the agglomerate. If the history model is considered, the porosity is also modified by removing the porous contribution of the removed particle, hence correcting the density of the agglomerate. Agglomeration and agglomerate breakage are very complicated topics, which would demand a specific work for its proper study. Therefore, the simplified approaches adopted are justified by the inherent complexity encountered in cyclone separators. Once the importance of such phenomena for a better separation prediction is proved, a more detailed modelling is demanded.

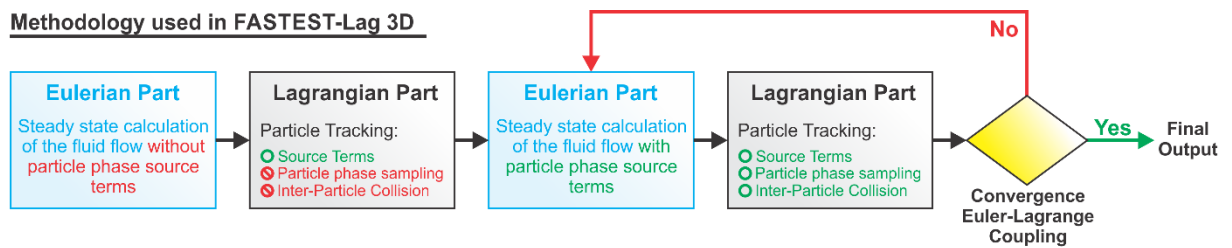
2.3 Final Considerations

The first goal of the present work is to implement and validate the presented models in the open source code OpenFOAM 4.1, despite the availability of those models on the code *FASTEST Lag-3D*. This decision was made considering that *FASTEST Lag-3D* does not allow parallel calculations, therefore requiring longer computational times to perform the calculations. A second reason for this choice is based on the number of users and the constant updates that OpenFOAM offers, which is not observed for *FASTEST Lag-3D*, where only a handful of people still uses the software and no updates are offered. On the other hand, OpenFOAM presents a large worldwide community and a continually expanded library of models and applications.

Another important reason lies in the difficulty of *FASTEST Lag-3D* to solve unsteady calculations for the continuous phase (when coupling with the discrete phase). Lipowsky and Sommerfeld^[56] proposed a solution for this problem by adopting a semi-unsteady approach, however this method presents a high computational cost and demands further validation. Thus, the steady approach according to Laín and Sommerfeld^[84] and Sommerfeld and Laín^[85] is mainly applied, where the converged solution of the coupled two-phase flow system in the solver *FASTEST Lag-3D* is obtained by successive solution of the Eulerian and Lagrangian parts, respectively. Initially, the continuous phase is calculated without the dispersed phase source terms until the convergence of the solution is achieved. Thereafter, the particles are tracked through the flow field and the source terms are sampled for every control volume. From the second Eulerian calculation, the source terms of the dispersed phase are introduced and the continuous phase is solved again until its convergence. This procedure is repeated several times until the total convergence of the calculation (the authors specify between 25-35 coupling iterations). On the other hand, it is possible to solve unsteady calculations in OpenFOAM through the semi-unsteady approach (see Chapter 2.2.2), considering two and four-way

coupling, where for every time step solved for the continuous phase, a subsequent tracking of the particles is calculated until it reaches the same time as the continuous phase. By the end of the tracking, the source terms are considered for the next time step of the continuous phase. Thus, a temporal evolution of the process can be observed, allowing the observation of transient and unstable processes, as in the case of particle separation in cyclones. An illustration of both methodologies is shown in Figure 23.

Methodology used in FASTEST-Lag 3D



Methodology used in OpenFOAM

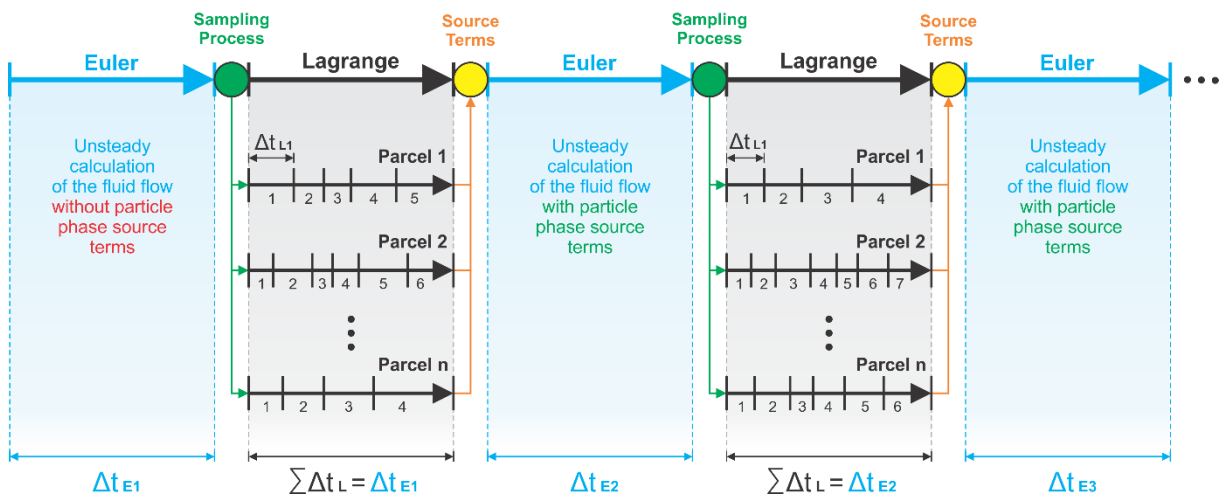


Figure 23. Comparison between the different approaches for the coupled Euler-Lagrange calculation according to FASTEST-Lag-3D (steady approach) and OpenFOAM (semi-unsteady approach).

3. VALIDATION CASES: PNEUMATIC CONVEYING SYSTEM

To validate the implemented particle-wall collision and stochastic inter-particle collision models, two different pneumatic conveying systems are studied. The first system corresponds to a horizontal pipe, where the gravitational settling plays a major role for the particle behaviour, being the particle-wall and inter-particle collisions responsible for the dispersion of particles in the system. The second system corresponds to a pipe with a horizontal section, being followed by a 90° bend with a vertical section. Here the importance of the consideration of the inter-particle interactions is even more pronounced due to the high concentration of particles on the outer bend due to inertial effects. The computational results obtained in the open source code OpenFOAM 4.1 are compared with experimental measurements of Huber and Sommerfeld^[86,87] and also with computational results obtained with *FASTEST Lag-3D* by Laín and Sommerfeld^[84] and Sommerfeld and Laín^[85]. It is important to highlight that the purpose of these studies is to validate the implementation, as well as the reliability of OpenFOAM is performing such calculations.

3.1 Pneumatic Conveying System: Cases Configuration

Two different pneumatic conveying systems are used in order to validate the implemented models in OpenFOAM 4.1, as summarized in Table 7. Both systems have the same pipe diameter of 0.15 m and a total pipe length around 10.6 m, where the first system is characterized only by a horizontal section and the second system by a horizontal-bend-vertical sections. For

both cases, three-dimensional transient numerical computations are performed using the Euler/Lagrange approach with the standard k- ϵ turbulence model accounting for two-way coupling. The time-step used for the continuous phase is fixed in 1×10^{-4} s for both cases, satisfying the condition of a maximum courant number smaller than unity. Particle transport is calculated by considering all relevant forces (including drag force, gravity, torque, slip-shear and slip-rotation lift forces) and particle dispersion due to turbulence. The time step for the particle tracking is chosen to be 20% of the smallest of all local relevant time scales, such as particle relaxation time, the integral time scale of turbulence and the mean inter-particle collision time. The material of both pipe walls is stainless steel, which is characterized by a high roughness, therefore being used the rms value of the roughness angle distribution of $\Delta\gamma = 10^\circ$, as used by Laín and Sommerfeld^[84]. Since inelastic collisions are considered, the restitution coefficient ϵ and friction coefficient μ_d are calculated based on the impact angle as presented by the Equations (52) and (53) respectively.

Table 7. Configuration of the pneumatic conveying systems for the validation cases.		
	Validation Case 1: Horizontal pipe	Validation Case 2: Horizontal-bend-vertical pipe
Pipe Diameter (D)	0.15 m	0.15 m
Inlet Velocity (U_{av})	27 m/s	27 m/s
Euler. Time-Step (Δt_E)	1×10^{-4} s	1×10^{-4} s
Mass Loading (η)	0.7	0.3
Wall Roughness ($\Delta\gamma$)	10°	10°
Injected Parcels	600,000	600,000
Particles/Parcel	$\sim 4,700$	$\sim 2,000$
Grid Size	$\sim 1,000,000$ elements	$\sim 950,000$ elements

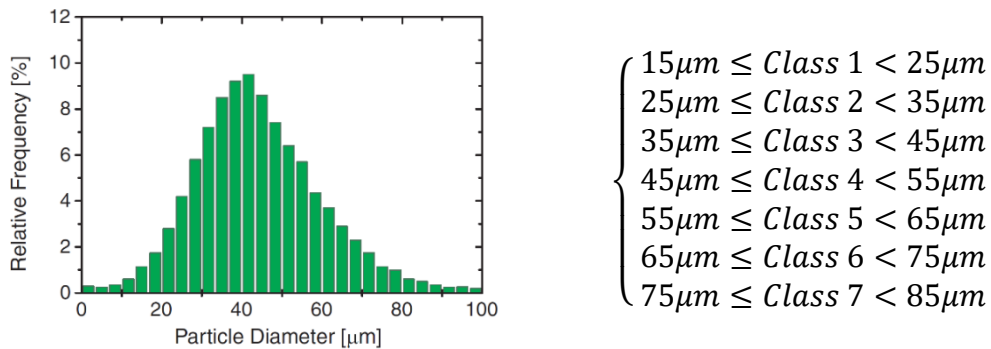


Figure 24. Size distribution of the spherical glass beads used in the experiments of Huber and Sommerfeld^[86, 87].

The used mean conveying velocities is 27 m/s ($Re = 270,000$), the gas density is 1.2 kg/m^3 and the dynamic viscosity is $18 \times 10^{-6} \text{ kg m}^{-1} \text{ s}^{-1}$. The particle phase consists of glass beads having a density of $2,500 \text{ kg/m}^3$ and a size distribution composed by 7 classes ranging from 15 to 85 μm (Figure 24). The particle sizes are sampled from a continuous cumulative distribution,

yielding also a variation of particle size within the size class. In order to represent the particle phase, 600,000 parcels/s are continuously injected during all the calculation. The particle injection velocities are sampled from a Gaussian distribution with fixed mean and rms velocities. The particle mean velocity is the same as the bulk gas velocity, i.e. 27 m/s, in the stream-wise direction and zero in the transverse components. The particle velocity fluctuation at the injection is calculated through the rms value of 3% of the gas bulk velocity for the three velocity components. For all three angular velocity components a mean of zero and standard deviation of 1000 s^{-1} are assumed. For the gas phase a no-slip boundary condition is applied to the pipe walls and a pressure outlet is attributed to the exit pipe boundary condition. Wall functions are applied in order to solve the turbulence properties in the near wall region, therefore not demanding extra refinement near the wall for its proper solution. Seeking the highest grid quality, it was decided to use only structured grid with hexahedral elements, i.e. avoiding the use of automatic generated grids with quad-dominant elements or tetrahedral elements, which may require a larger number of elements in order to avoid numerical diffusivity. Therefore, the numerical grid for all pneumatic conveying systems were generated using ANSYS® ICEM CFD by using an o-grid blocking structure. It is important to point out, that the numerical grid of the present pneumatic conveying systems have a higher refinement closer to the wall, which is not necessarily required for an improvement of the solution. Yet, this is necessary to obtain a better resolution for the averaged data, once the averaging system implemented uses the grid resolution as a spatial resolution for storing purposes.

To observe the effect of the implemented models on the particle behaviour, six different configurations are proposed for every validation case. The first three configurations consider only two-way coupling and have different approaches for the particle-wall interaction, while the last three consider four-way coupling (i.e. inter-particle collisions), as follow:

1. Two-way coupling with smooth wall ($\Delta\gamma = 0^\circ$);
2. Two-way coupling with rough wall ($\Delta\gamma = 10^\circ$);
3. Two-way coupling with rough wall ($\Delta\gamma = 10^\circ$) and multiple collisions;
4. Four-way coupling with smooth wall ($\Delta\gamma = 0^\circ$);
5. Four -way coupling with rough wall ($\Delta\gamma = 10^\circ$);
6. Four -way coupling with rough wall ($\Delta\gamma = 10^\circ$) and multiple collisions.

Finally, for all proposed cases, first only the single-phase flow is solved until it reaches its pseudo-steady state. The residence time for the continuous phase is around 0.4 s and it was observed that within 1 s, the solution was already in the pseudo-steady state. At 1 s the particles

begin to be injected continuously until the end of the solution at 5 s. To minimize statistical errors, the averaging is performed during at last four residence times, totalizing the last 2 s of simulation.

3.2 Validation Case 1: Horizontal Pipe

The first validation case is composed by a horizontal pipe 10.6 m long with a diameter of 0.15 m (Figure 25) and a mean conveying velocity of 27 m/s. A structured grid with around 1,000,000 hexahedral control volumes is used, being this resolution adequate to produce grid-independent results. The mass loading used in this test case is $\eta = 0.7$ (around 600,000 parcels/s with around 4,700 particles/parcel). Vertical profiles of particle properties are measured at a distance of 8 m downstream the inlet, where it can be compared with experimental data obtained by Huber and Sommerfeld ^[87] and calculations using *FASTEST Lag-3D* by Laín and Sommerfeld ^[84]. Huber and Sommerfeld ^[86, 87] provided only results for the properties of the solid phase, e.g. mean velocity and its fluctuation, particle mean diameter and particle mass flux. However, an extended analysis using complementary data is presented.

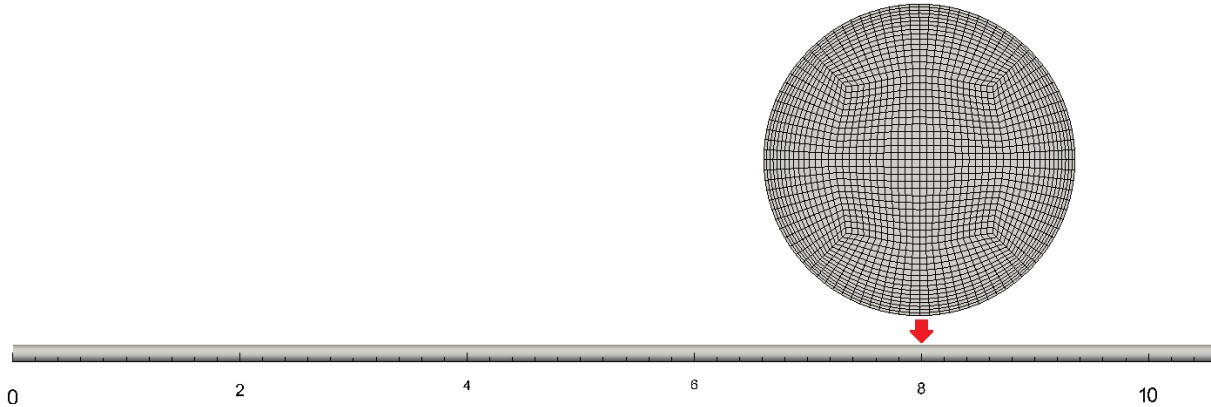


Figure 25. Computational grid for the horizontal pipe used in the first validation case.

Figure 26 shown the comparison between the experimental data and the numerical computations for the stream-wise particle velocity and its fluctuation at the distance of 8 m downstream the inlet. For a better visualization, the two (Figure 26-a) and four-way (Figure 26-b) coupling calculations are presented side by side. When considering only two-way coupling, it is not possible to have a good agreement with the experimental data, presenting a deformation on the velocity profile with an under-prediction of the stream-wise mean velocity close to the bottom of the pipe. As stated by Laín and Sommerfeld ^[84], the pipe diameter is relatively large and the particles are not very inertial, being their behaviour influenced by the gas turbulence to

a large extent. Therefore, the dispersion of particles caused by particle-wall collisions considering roughness is not that pronounced for this specific case. On the other hand, the calculations considering four-way coupling present a very good agreement with the experimental data, showing that the inter-particle collisions play a major role on the particle dispersion. However, even for the four-way coupling calculations, an under-prediction of the stream-wise particle fluctuating velocity is observed, which can be related to the application of the isotropic $k-\varepsilon$ turbulence model. Nevertheless, the shape of the fluctuating velocity profiles resembles the experimental data, where the fluctuation is higher in the near wall region due to the particle-wall collisions. Such behaviour was not observed by Laín and Sommerfeld^[84], where they obtained a good agreement in terms of intensity value, however the increment of dispersion near the walls was not observed.

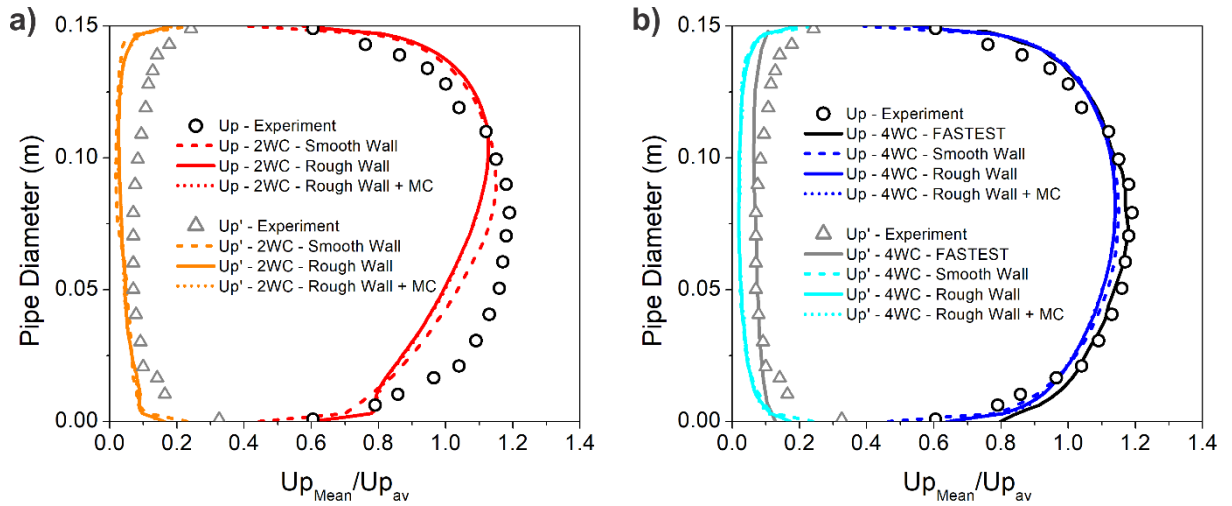


Figure 26. Mean and rms normalized particle velocity profiles at 8 m downstream the inlet. $U_{av} = 27$ m/s, $\eta = 0.7$, $\Delta\gamma = 10^\circ$. (a) two-way coupling and (b) four-way coupling solutions.

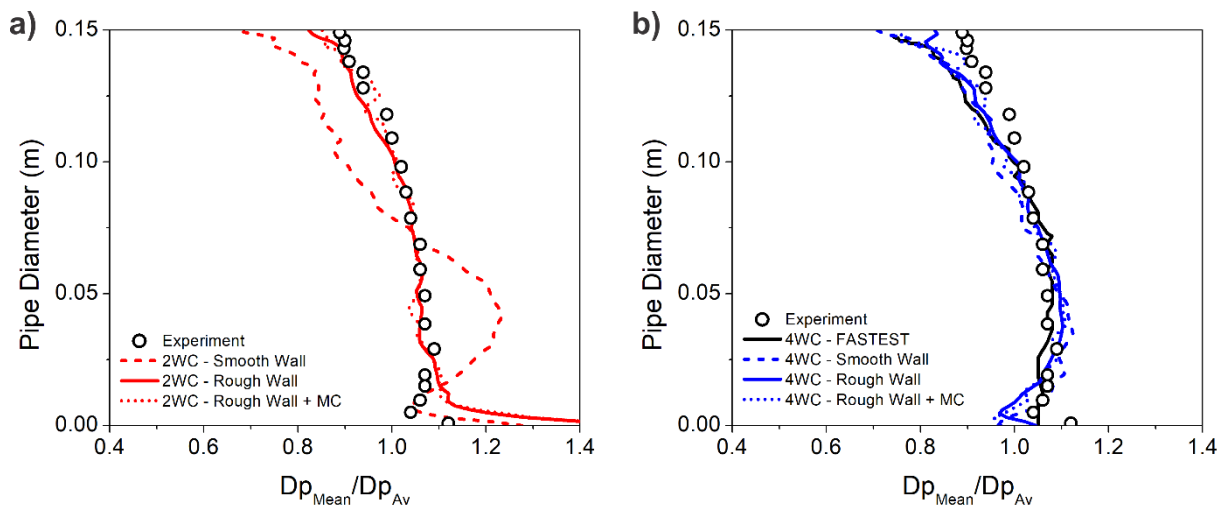


Figure 27. Profiles of normalized particle number mean diameter at 8 m downstream the inlet. $U_{av} = 27$ m/s, $\eta = 0.7$, $\Delta\gamma = 10^\circ$. (a) two-way coupling and (b) four-way coupling solutions.

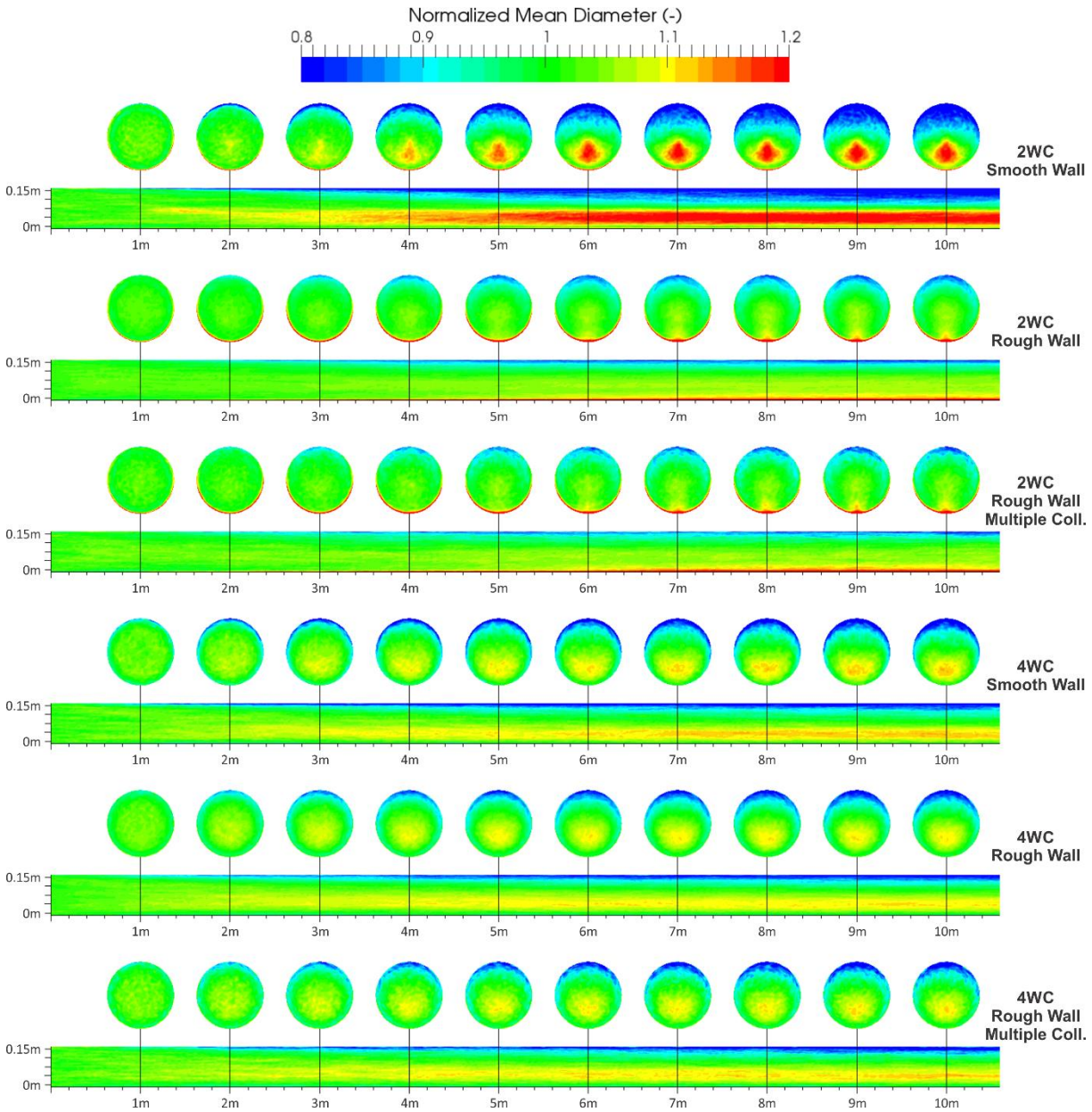


Figure 28. Development of cross-sectional distributions of normalized particle mean diameter. The cross-sections are scaled up five times for better visualization. $U_{av} = 27 \text{ m/s}$, $\eta = 0.7$, $\Delta\gamma = 10^\circ$.

When analysing the profiles of particle mean diameter (Figure 27), one can observe the concentration of larger particles at the bottom of the pipe due to the gravitational settling. The dispersive effect of the wall roughness can be noticed in the two-way coupling calculations, while the smooth wall calculation presents a higher intensity of gravitational settling. On the other hand, the four-way coupling calculations presented a good agreement with the experimental data and the calculations performed by Laín and Sommerfeld^[84] using *FASTEST Lag-3D*. The gravitational settling of particles inside the horizontal pipe can be also observed on the contour maps of the cross-sectional distributions of normalized particle mean diameter in Figure 28. Here the dispersion caused by the inter-particle collisions is clearly noticed,

presenting a slightly improvement when the wall roughness is considered. However, a significant difference between the calculations using rough walls with and without multiple collisions cannot be observed.

The gravitational settling of the particles can also be observed in the profiles of normalized particle mass flux (Figure 29). When considering four-way coupling, the profile of particle mass flux peak is slightly shifted upwards, however its shape and intensity resembles the one obtained experimentally by Huber and Sommerfeld [86, 87]. Differently, the two-way coupling calculations present a completely different shape and magnitude for the particle mass flux profiles, not being suitable for a good representation of the particle behaviour. This behaviour is also noted in the development of cross-sectional distributions of particle concentration in Figure 30. One can observe the higher concentration of particles closer to the bottom of the pipe when considering only two-way coupling, being the higher intensity attributed to the smooth wall. With inter-particle collisions the particle concentration is shifted in the direction to the core of the pipe.

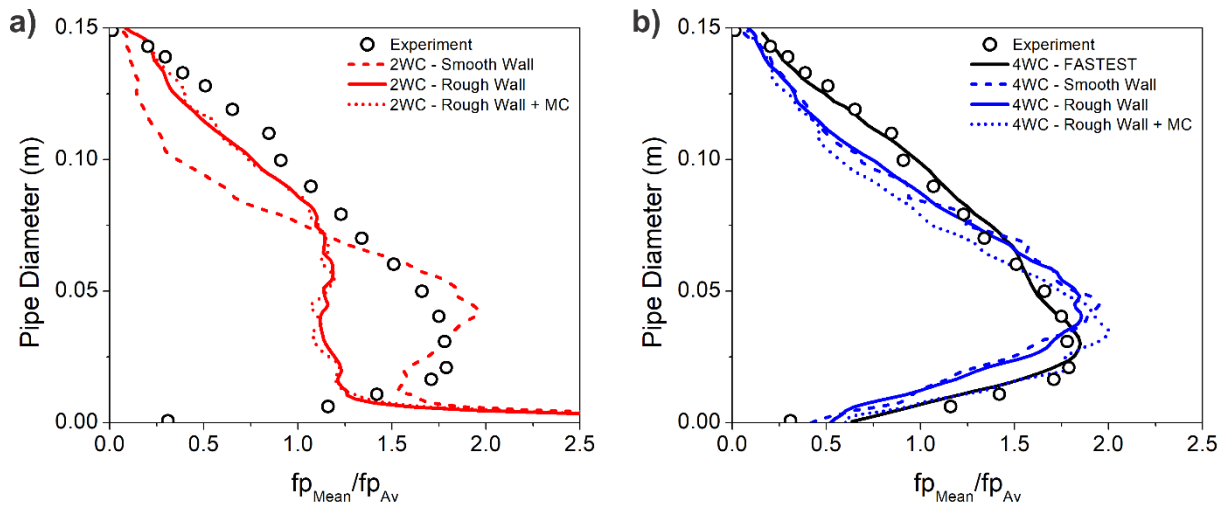


Figure 29. Profiles of normalized particle mass flux at 8 m downstream the inlet. $U_{av} = 27$ m/s, $\eta = 0.7$, $\Delta\gamma = 10^\circ$. (a) two-way coupling and (b) four-way coupling solutions. The mass flux is normalized by the inlet mass flux.

As expected, when analysing the particle-wall collision frequency in Figure 31-a, one can notice that the higher intensity is presented by the cases considering smooth wall. Here the two-way coupling case presents a particle-wall collision frequency almost twice as higher than the four-way coupling counterpart. Surprisingly, all cases considering wall roughness (two-way coupling and four-way coupling) present a relatively similar intensity of particle-wall collision frequency along the whole pipe, with the multiple collision cases presenting a slightly increased value. When considering wall roughness, the four-way coupling cases present a higher particle

wall collision frequency in comparison to the two-way coupling ones. Probably caused due to the inter-particle collisions in the near wall region, causing a shielding effect that consequently redirects particles towards the wall.

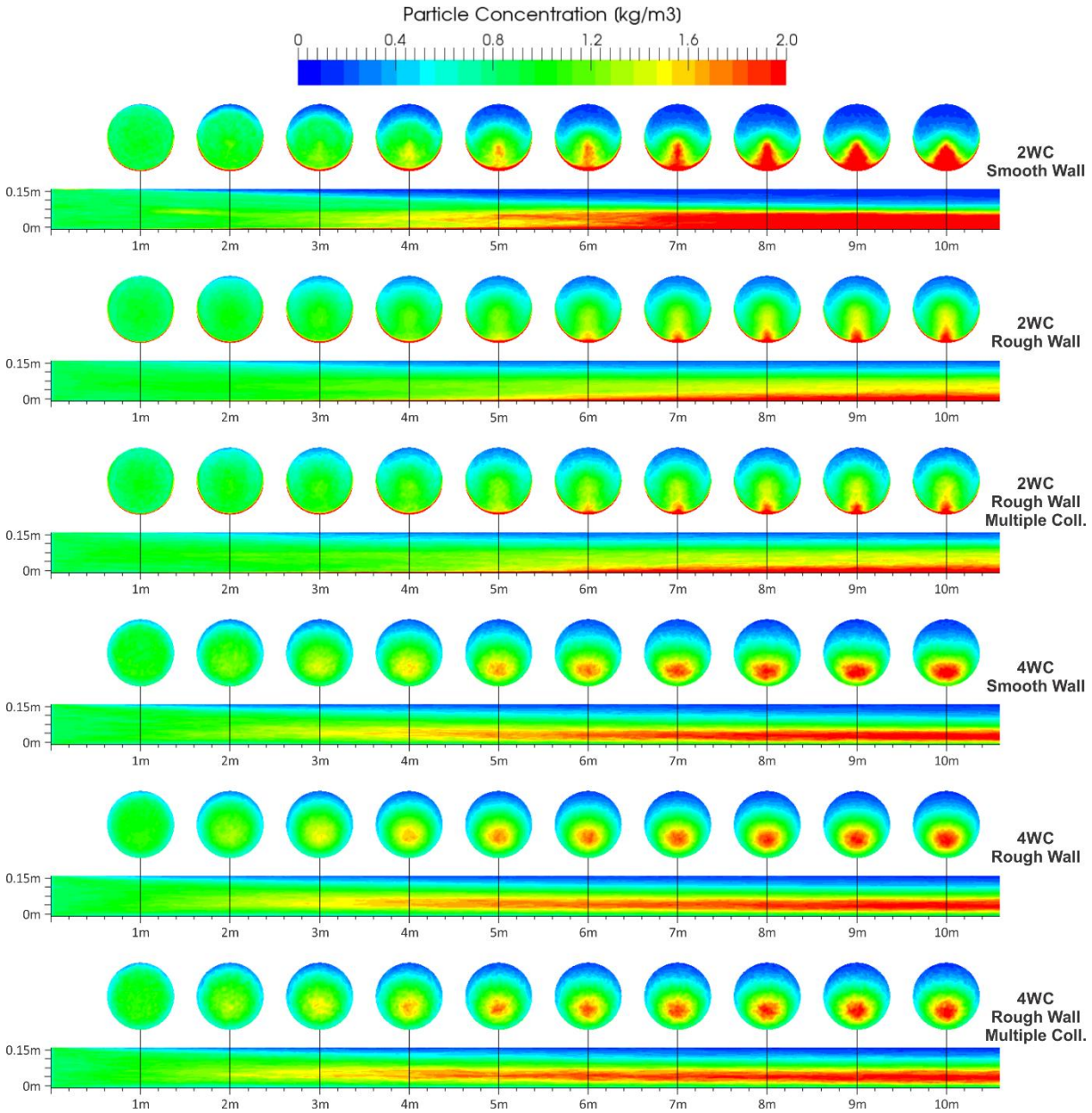


Figure 30. Development of cross-sectional distributions of averaged particle concentration. The cross-sections are scaled up five times for better visualization. $U_{av} = 27$ m/s, $\eta = 0.7$, $\Delta\gamma = 10^\circ$.

The same phenomenon is noticeable in the contours of inter-particle collision frequency in Figure 32, where the higher intensity is located middle-bottom part of the pipe. By analysing the evolution of the inter-particle collision frequency along the pipe length Figure 31-b, it is clear that the multiple collision does not affect significantly the inter-particle interactions, presenting almost the same intensity as in the case using only rough wall. Differently, the smooth wall presents a higher value due to the higher concentration of particles that stay in the

near wall region due to the lack of dispersion. Another evidence that inter-particle collisions are more relevant to the particle dispersion than the particle-wall collisions lies in its higher frequency, being the frequency of first several times higher than the second one.

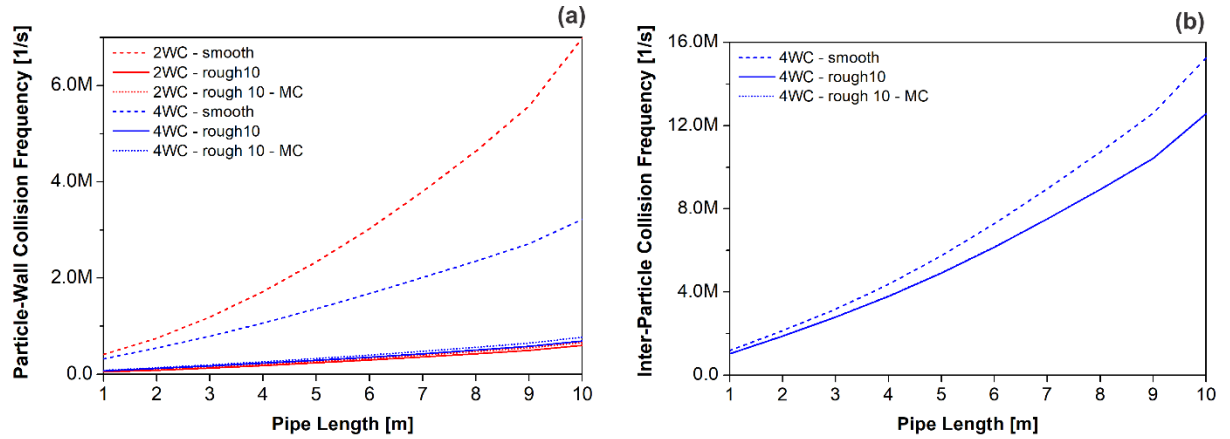


Figure 31. Evolution of the cumulative (a) particle-wall collision frequency and (b) inter-particle collision frequency along the horizontal pipe length. $U_{av} = 27$ m/s, $\eta = 0.7$, $\Delta\gamma = 10^\circ$. Every parcel-wall collision corresponds to a total of 4,700 particle-wall collisions.

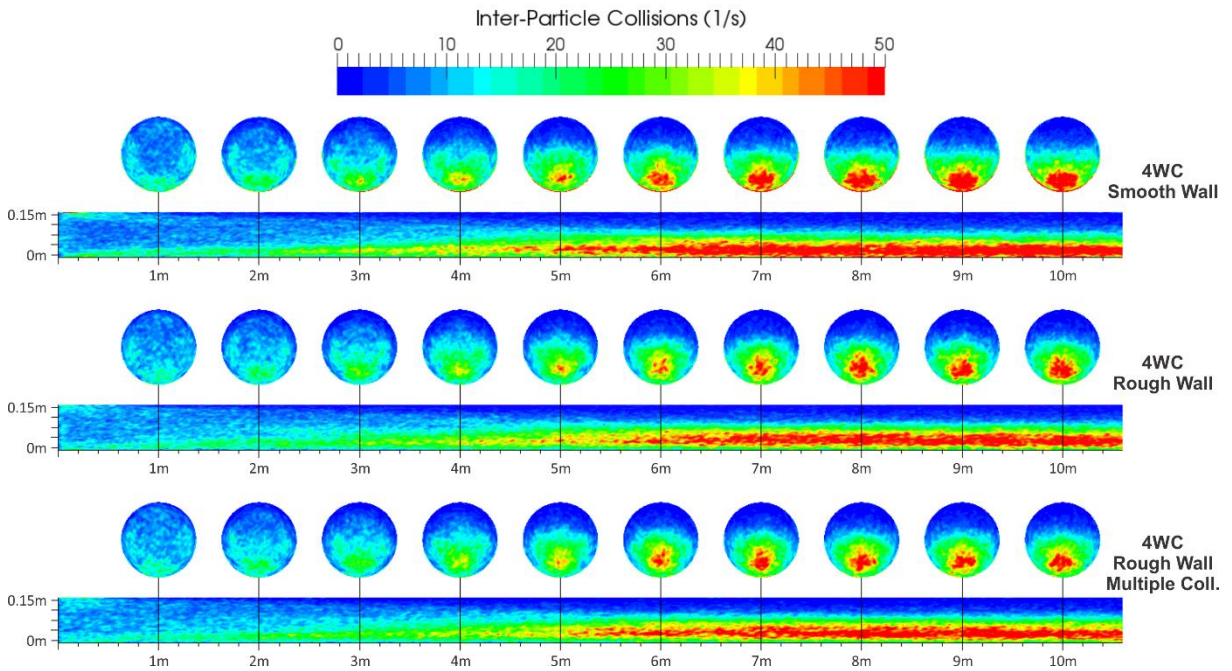


Figure 32. Development of cross-sectional distributions of inter-particle collision frequency. The cross-sections are scaled up five times for better visualization. $U_{av} = 27$ m/s, $\eta = 0.7$, $\Delta\gamma = 10^\circ$.

Despite slightly differences among the experimental data, *FASTEST Lag-3D* and the present calculations, one can affirm that a good agreement is achieved and the particle behaviour in the horizontal pneumatic conveying can be described properly. A further investigation for a pipe with horizontal-bend-vertical section is presented in the next test chapter.

3.3 Validation Case 2: Horizontal Pipe, Bend and Vertical Pipe

The second validation case is composed by a pipe with a diameter of 0.15 m, a 5 m horizontal section, a 90° bend ($R_{\text{bend}} = 2.54D = 0.381$ m) and 5 m of vertical section (Figure 33), which is widely discussed by Laín and Sommerfeld ^[84]. A structured grid with around 950,000 hexahedral control volumes is used in the present test case. As mentioned before, the grid is refined near the walls to improve also the resolution of the averaged data, once it is stored using the same spatial resolution as the one from the numerical grid. The fluid and particle properties are the same as used in the horizontal pipe, however in this specific test case the particle mass loading used is $\eta = 0.3$ (around 600,000 parcels/s with 2,000 particles/parcel).

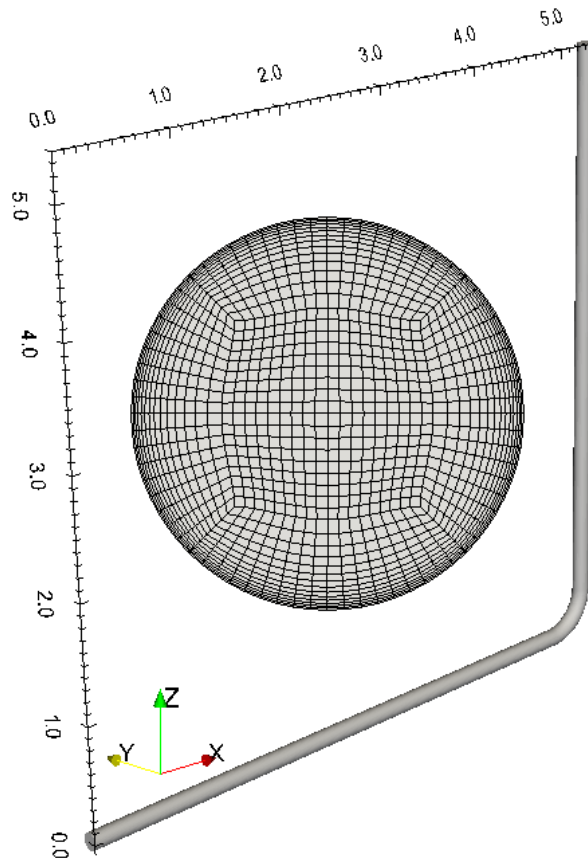


Figure 33. Computational grid used in the test case with horizontal pipe, bend and vertical pipe (pipe diameter $D = 150$ mm, bend radius 2.54 pipe diameter).

The validation of the computations is based on horizontal profiles of the particle phase properties measured in the vertical pipe at distances of 0.3, 1.3 and 4.3 m from the bend exit obtained by Huber and Sommerfeld ^[86, 87]. To better visualize the influence of the different approaches used, cross-sectional planes of particle concentration, volume fraction and inter-particle collision frequency are also presented. The same setups of cases used in the previous validation case are applied, with three wall treatment variations for the two-way and four-way

coupling calculations. The air and the particles are injected in the horizontal pipe and leave the system through the end of the vertical pipe. The gravitational force is considered in the negative z direction, e.g. opposite direction of the flow in the vertical section of the pipe.

According to Laín and Sommerfeld^[84], the two-phase flow in the bend is characterized by segregation of the mixture, being the particles accumulated at the outer wall of the bend due to inertial effects. Consequently, rather dense ropes of particles are formed in that region leading to locally high particle concentrations which support the occurrence of inter-particle collisions. Hence, the degree of particle accumulation at the bend outer wall depends strongly on wall roughness and inter-particle collision. When entering the bend, particles are driven towards the bend outer wall mainly due inertia, rebounding back to the core region of the pipe. The intensity of this rebound is related to the roughness of the wall, where higher roughness leads to a larger rebound angle. It implies that the averaged rebound angle becomes larger than the impact angle, resulting in an average transfer of wall parallel particle momentum towards the transverse components. In the present cases with a relatively high roughness ($\Delta\gamma = 10^\circ$), the particles are distributed over a large portion of the cross-section, although a more or less dense rope is formed at the outer wall of the bend exit. Figure 34 shown the development of the cross-sectional distributions of particle concentration for all calculated cases. The horizontal section of the pipe is not shown, once the main scope of the analysis lies on the bend and the downstream vertical section. However, the first plane at the left bottom represents the end of the horizontal section and the entrance of the bend. Here at the distance of 5 m to the inlet, the particles are more dispersed in comparison with the former horizontal case, because of the influence of the bend on the gas flow, hence shifting the gas flow upwards and therefore decreasing the gravitational settling. As observed for the first validation case, the calculations without inter-particle collisions present a higher rate of particle concentration at the bottom of the pipe. When considering only two-way coupling and smooth wall, a higher concentration of particles on the outer side of the bend and consequently on the right side of the vertical pipe up to the exit is observed. By considering two-way coupling with wall roughness, the rope of concentrated particles is dispersed across the entire cross section about 1 meter downstream the bend exit, despite presenting higher concentration closer to the wall. In this case, the motion of particles near the wall is governed mainly by the roughness of the wall, once higher rebound angles will make easier for the particles to leave the wall region. On the other hand, considering inter-particle collisions will lead to the occurrence of the shielding effect³.

³ i.e. even if a particle rebounds with a higher rebound angle, it is possible that this particle will collide with another one and as a result of this collision will be redirected to the wall

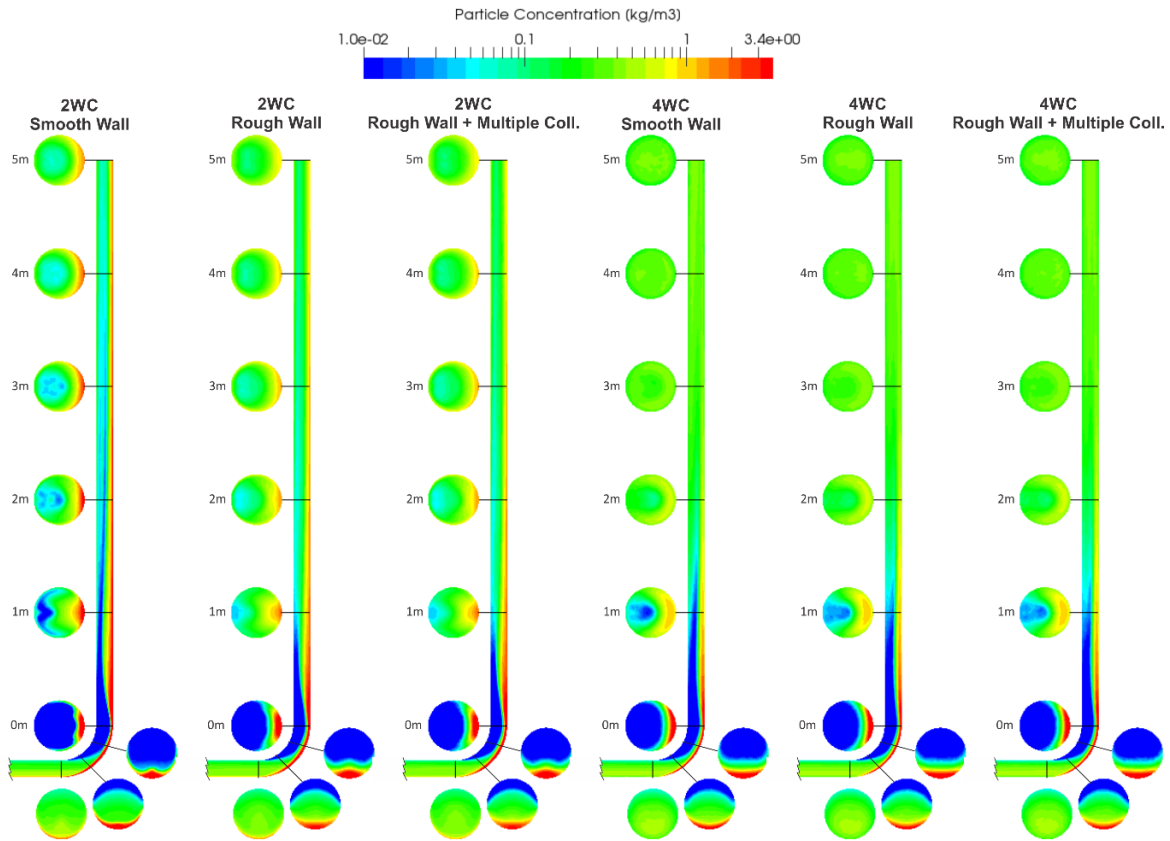


Figure 34. Development of cross-sectional distributions of averaged particle concentration. $U_{av} = 27$ m/s, $\eta = 0.3$, $\Delta\gamma = 10^\circ$.

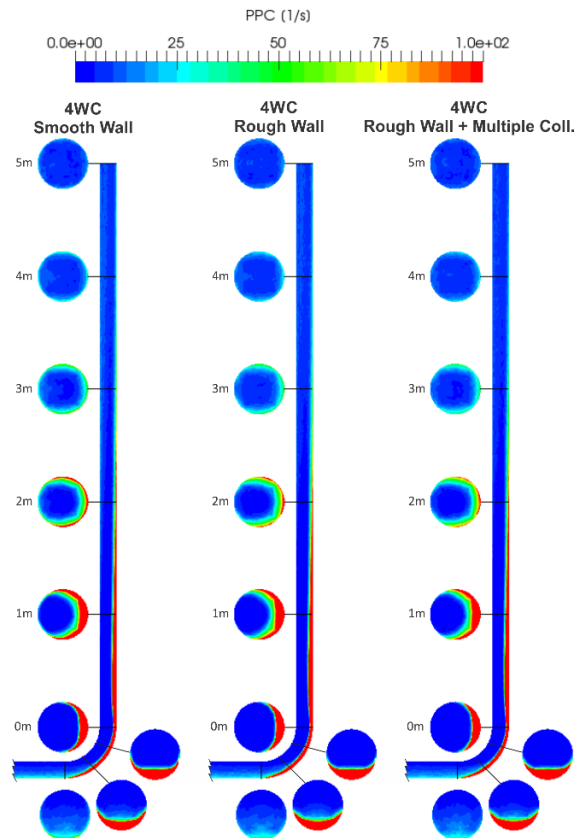


Figure 35. Development of cross-sectional distributions of inter-particle collision frequency. $U_{av} = 27$ m/s, $\eta = 0.3$, $\Delta\gamma = 10^\circ$.

Regions with higher particle concentration have a higher probability of inter-particle collisions (see Figure 35), in this way making the region of the outer wall of the bend highly susceptible to the shielding effect. Because of this effect, the rope of concentrated particles is wider around the bend outer wall and presents a larger region with lower particle concentration (see cross section 1 m downstream the bend exit). After 2 meters downstream the bend exit, one can observe that the cases considering four-way coupling present a better distribution of the particles in comparison with the two-way coupling ones. As observed for the previous case, the rough wall with multiple collision does present only a small difference in comparison with the case without it.

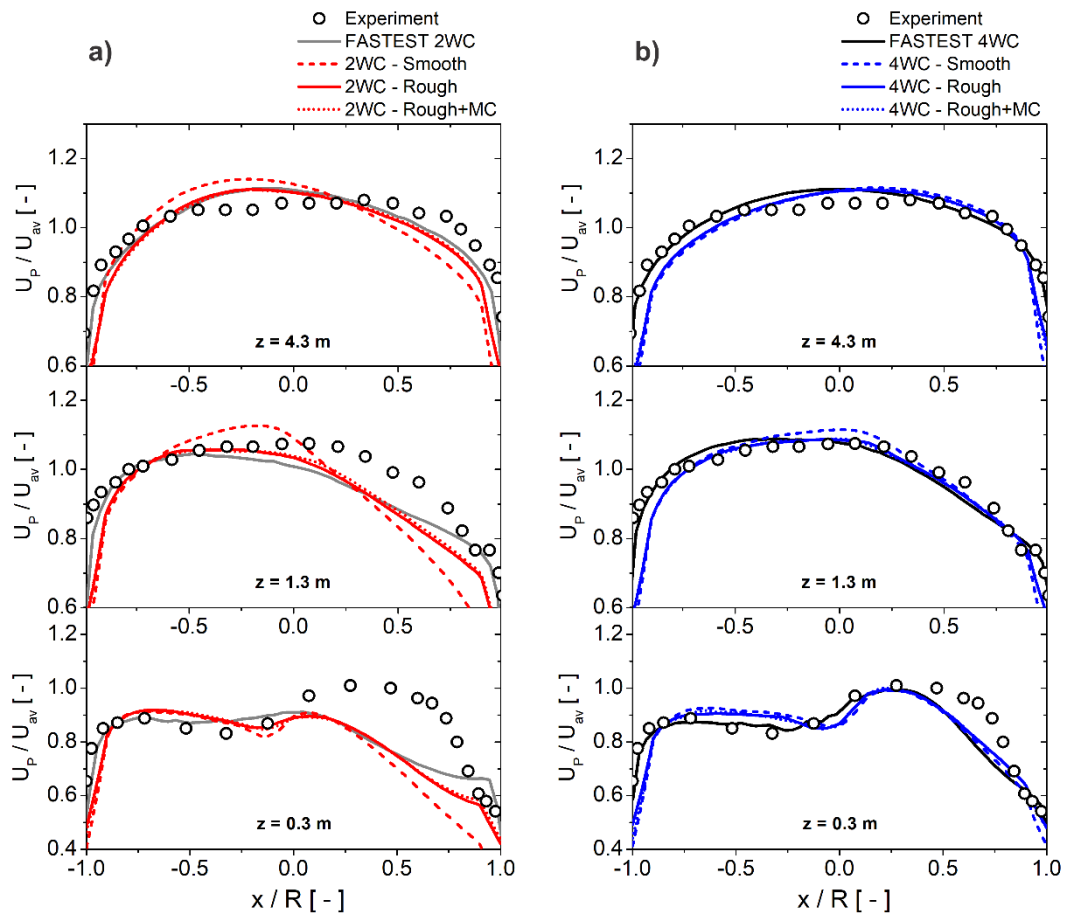


Figure 36. Calculated normalized particle mean velocity in the vertical pipe at cross-sections ($z = 0.3$, 1.3 and 4.3 m) from the bend exit. $U_{av} = 27$ m/s, $\eta = 0.3$, $\Delta\gamma = 10^\circ$. (a) two-way coupling and (b) four-way coupling solutions.

The comparison of the calculations for particle mean velocity, normalized by the inlet bulk velocity (i.e. 27 m/s), with the experimental measurements are shown in Figure 36. The inner wall of the bend is on the left-hand side of the graphics ($x/R = -1$). The velocity profiles observed in the experiments are well reproduced by the four-way coupling calculations, presenting similar results as the ones obtained by Laín and Sommerfeld^[84] using *FASTEST*

Lag-3D. A slightly under-prediction can be identified in the bend outer wall for the cross-section $z = 0.3$ m, however this behaviour is even more pronounced for the cases that neglect the inter-particle collisions, pointing the importance in considering such phenomenon. One possible reason for this under-prediction on the outer side of the bend can be related to the wider dust rope, as can be noticed in Figure 37-b. Nonetheless, the mass flux profiles for the cross-sections at $z = 1.3$ and 4.3 m are fitting remarkably the experimental data, predicting well the particles recovery after the bend and its re-dispersion in the vertical pipe. Here it is possible to affirm that in the present calculations considering inter-particle collisions, a higher particle dispersion is obtained, when comparing with the two-way coupling calculations.

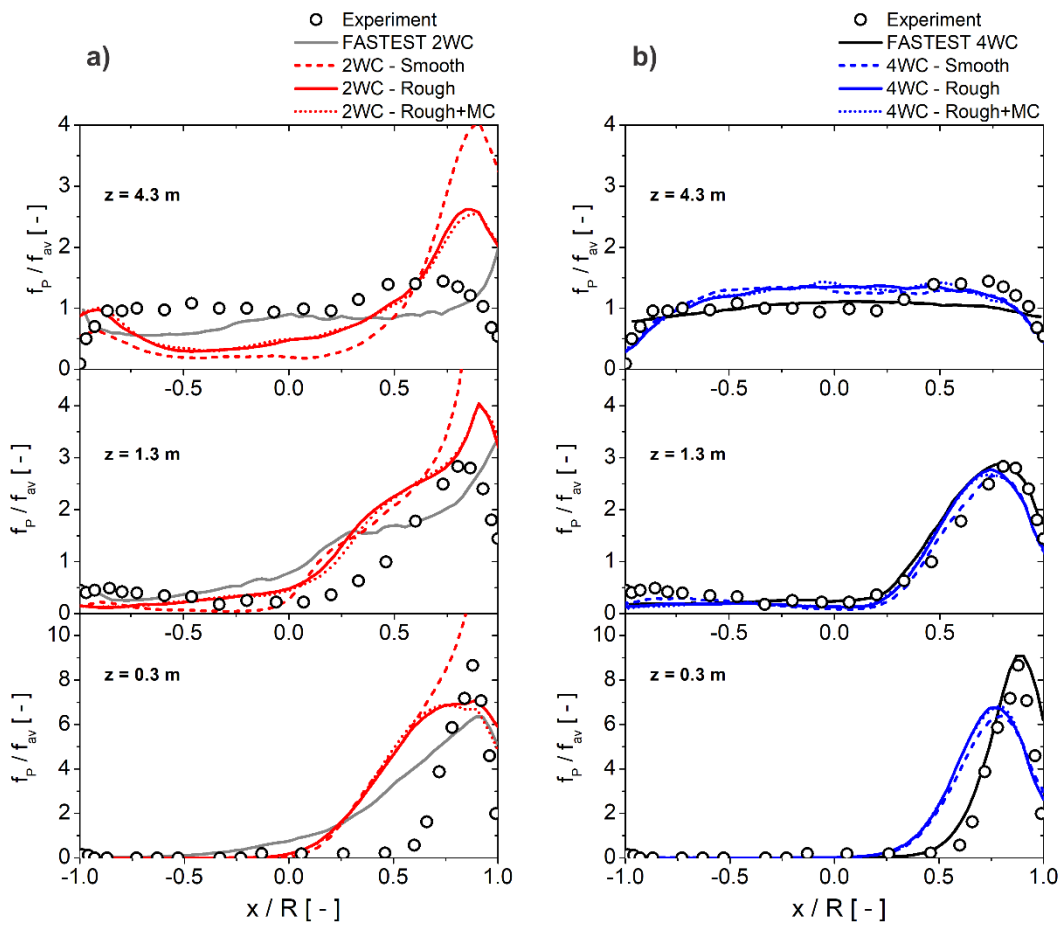


Figure 37. Calculated normalized particle mean mass flux in the vertical pipe at cross-sections ($z = 0.3, 1.3$ and 4.3 m) from the bend exit. $U_{av} = 27$ m/s, $\eta = 0.3$, $\Delta\gamma = 10^\circ$. (a) two-way coupling and (b) four-way coupling solutions. The mass flux is normalized by the inlet mass flux.

Like the experiments, the calculations considering inter-particle collisions shown particle size segregation downstream of the bend, where larger (more inertial) particles are forced towards the outer wall of the bend due to centrifugal effects. Hence, in the first two cross-sections ($z = 0.3$ and 1.3 m) a larger mean diameter (see Figure 38) is found on the right side of the pipe. However, in the first cross-section ($z = 0.3$ m) the number mean diameter is

overestimated in the core region of the pipe, almost similar to the results obtained by Laín and Sommerfeld ^[84] using *FASTEST Lag-3D*. At the second cross-section ($z = 1.3$ m) an underestimation is observed at the left side of the pipe (inner wall), while at the third cross-section ($z = 4.3$ m) has a good agreement. Overall, the general trends in the profiles of particle mean number diameter are predicted well and the agreement of all calculated particle properties are following the same level of prediction as the ones obtained by Laín and Sommerfeld ^[84] using *FASTEST Lag-3D*.

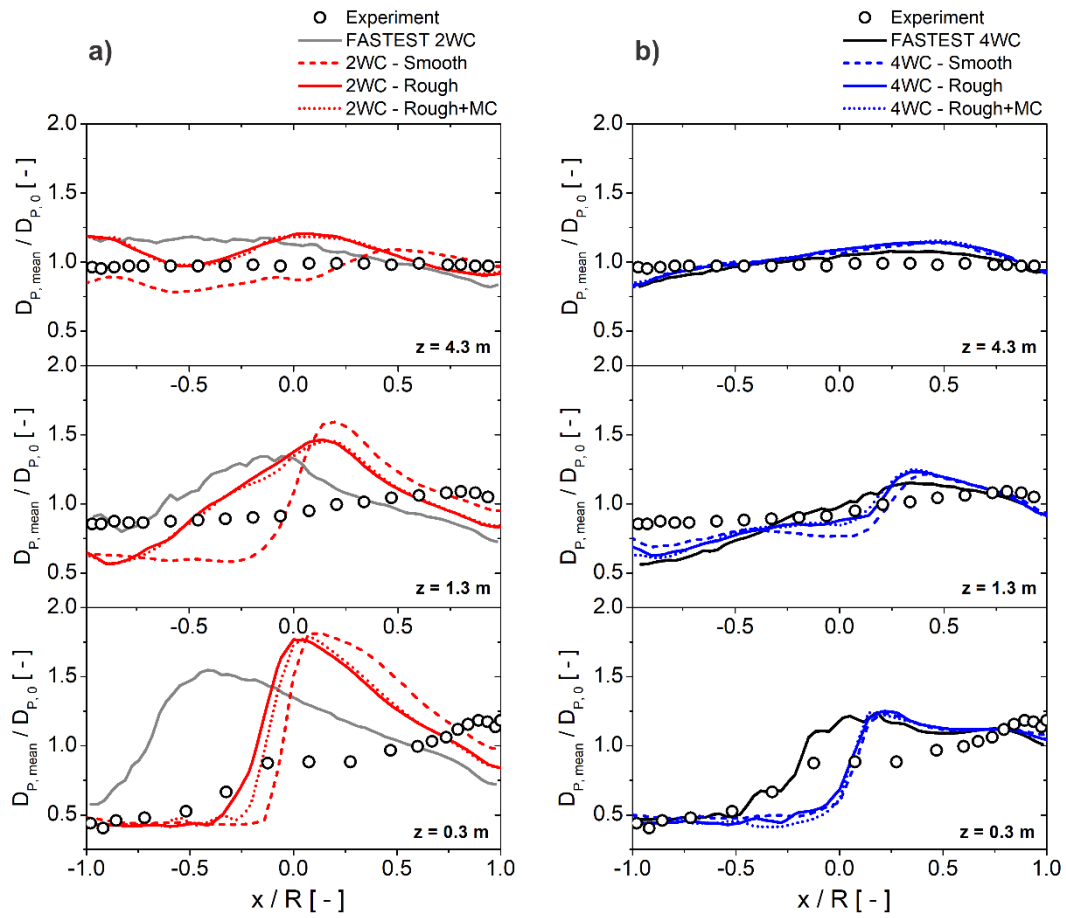


Figure 38. Calculated normalized particle mean number diameter in the vertical pipe at cross-sections ($z = 0.3, 1.3$ and 4.3 m) from the bend exit. $U_{av} = 27$ m/s, $\eta = 0.3$, $\Delta\gamma = 10^\circ$. (a) two-way coupling and (b) four-way coupling solutions.

3.4 Validation Cases: Summary and Final Considerations

The main goal of this chapter is to validate the two major models that were implemented in OpenFOAM 4.1, i.e. particle-wall collision model considering wall roughness and stochastic inter-particle collision model. The structure of particle-laden flows in two different pneumatic conveying systems has been numerically analysed. Thus, the computational results obtained in OpenFOAM are compared with experimental measurements of Huber and Sommerfeld^[86, 87] and also with computational results obtained with *FASTEST Lag-3D* by Laín and Sommerfeld^[84]. The cases are solved by applying the Euler/Lagrange approach in combination with the standard k- ϵ turbulence model. To model the discrete phase, all relevant elementary processes are considered, e.g. relevant forces acting on the particles, particle turbulent dispersion, wall roughness and inter-particle collisions.

The comparison of the present calculations with the experimental data showed a very good agreement for both validation cases. It was demonstrated that particle-wall collisions respecting the wall roughness, as well as the inter-particle collisions have a great impact on particle behaviour. In the horizontal pipe, when neglecting the roughness of the wall and the interaction between particles, the dispersion of the particle concentration could not overcome the gravitational settling, thus creating a higher concentration of particle near the bottom wall. Such effect is avoided by assuming the roughness of the wall and the interaction between particles, having the second a greater relevance for the dispersion of particles in the system. The segregation effects cause by the change of flow direction in the bend and the accumulation of particles at the outer bend wall due to inertial effects and the shielding effect is also observed in the present calculations for the second validation case. Here, a good agreement for the velocity profiles, as well as the mass flux is observed, were the dispersion of particles in the vertical pipe downstream the bend is observed. Hence, based on the good agreement obtained with the calculations performed with OpenFOAM 4.1 for the pneumatic conveying systems, the present code with the implemented models is used to calculate the swirl flow in cyclones.

4. RESULTS AND DISCUSSION: CYCLONE SEPARATORS

Despite the wide use of cyclones in the industry and its intensive study and optimization over the last century, it is rare to find in the literature experimental data for the performance parameters and velocity profiles for the same geometrical/experimental setup. Hoekstra ^[13], for example, may be the only exception, since he obtained experimental results for the gas flow field, collection efficiency and pressure drop for a high efficiency Stairmand cyclone ^[5]. On the other hand, many authors as Ji et al. ^[11], Haig et al. ^[39] and Huang et al. ^[12], obtained experimentally only collection efficiency curves for different operational conditions and particle properties. Once the performance parameters, e.g. collection efficiency and pressure drop, are directly related to the intensity of the velocity profiles, an important information is missing for a thorough analysis. Thus, for a detailed analysis on cyclone's performance parameters considering different approaches and phenomena, several separate test cases with different geometries and operational conditions are analysed. Every test case approaches a different relevant characteristic of the cyclone separators and they offer cumulative knowledge that can be carried for the subsequent test cases, e.g. numerical grid generation, appropriate turbulence models and methodologies for measuring the collection efficiency and pressure drop.

The first test case is based on the experimental data of Hoekstra ^[13] and is the step stone for a proper evaluation of the most appropriate turbulence model and approaches necessary for describing the complex anisotropic flow in cyclones. Since all cyclones studied are tangential, this test case is also used as a reference for the numerical grid generation and all its

specifications that should be respected for all other subsequent geometries. The second test case corresponds to the evaluation of the collection efficiency methodology and it is based on the experimental data obtained by Hoekstra^[13] and Xiang et al.^[10]. Here, three variations of a Stairmand cyclone are evaluated, as well as three variations of a small laboratory-cyclone. With the flow field verified in the first test case and the collection efficiency methodology validated in the second one, the third test case corresponds to a hypothetical test case based also on the high efficiency Stairmand studied by Hoekstra^[13]. A constant particle size distribution is injected in the cyclone and the impact of different approaches and phenomena are analysed. Finally, the fourth and last test case is based on the experimental data of Huang et al.^[12]. Here it is studied the impact of the mass loading on the cyclone's performance, as well as the importance of the inter-particle phenomena on its prediction.

4.1 Test Case 1: Gas Flow Validation

According to Freitas^[88], there are three different types of uncertainty that can influence numerical predictions: (a) input uncertainty, (b) model uncertainty and (c) grid/numerical uncertainty. Among the three types of uncertainties, the first two can be eliminated by a more precise definition of the input parameters and a better choice of the used models (e.g. model validation). As explained in the Chapter 2.1.2, the most suitable turbulence model to predict the unsteady and turbulent swirl flow in cyclones is the Large Eddy Simulations (LES) combined with the dynamic Smagorinsky sub-grid model. The third uncertainty, i.e. grid uncertainty, can be reduced by a proper grid generation and quantified by means of grid dependence analysis. Therefore, the first step to validate the gas flow solution is to verify if the numerical grid is independent of the refinement of the grid. When experimental data is not available for comparison with the calculations, it is possible to determine the independence of the grid through the GCI (*Grid Convergence Index*) method proposed by Roache^[89] and applied to cyclones by Sgrott et al.^[14], Balestrin et al.^[22] and Luciano et al.^[15]. However, for the present study, the validation of the gas flow field relies on the direct comparison of velocity profiles and its fluctuations with the experimental data obtained with LDA (*Laser Doppler Anemometry*) by Hoekstra^[13], hence not requiring the uncertainty quantification through the GCI method.

Seeking the highest grid quality possible, only structured grids with hexahedral elements are considered, i.e. avoiding the use of automatic generated grids with quad-dominant elements or tetrahedral elements, which may require a larger number of elements to avoid numerical diffusivity. To generate the structured grid with only hexahedral elements, a blocking of the

Stairmand cyclone is generated in the software ANSYS® ICEM CFD, as shown in Figure 39. The complexity of the blocking structure is noticeable, where three concentric “o-grids” are necessary to represent the vortex-finder (two for the inner and outer walls of the vortex-finder and the third for the its core, as observed on the right side of Figure 39). Despite the tangential entrance, the blocking structure is completely symmetrical, thus allowing the extrapolation of the blocking methodology of the present Stairmand cyclone to further cyclones geometries. That is, if the used blocking with the same ratio of refinement can predict well the swirl flow in the Stairmand cyclone, a numerical grid for a different tangential cyclone geometry following the same methodology and resolution should follow the same level of accuracy.

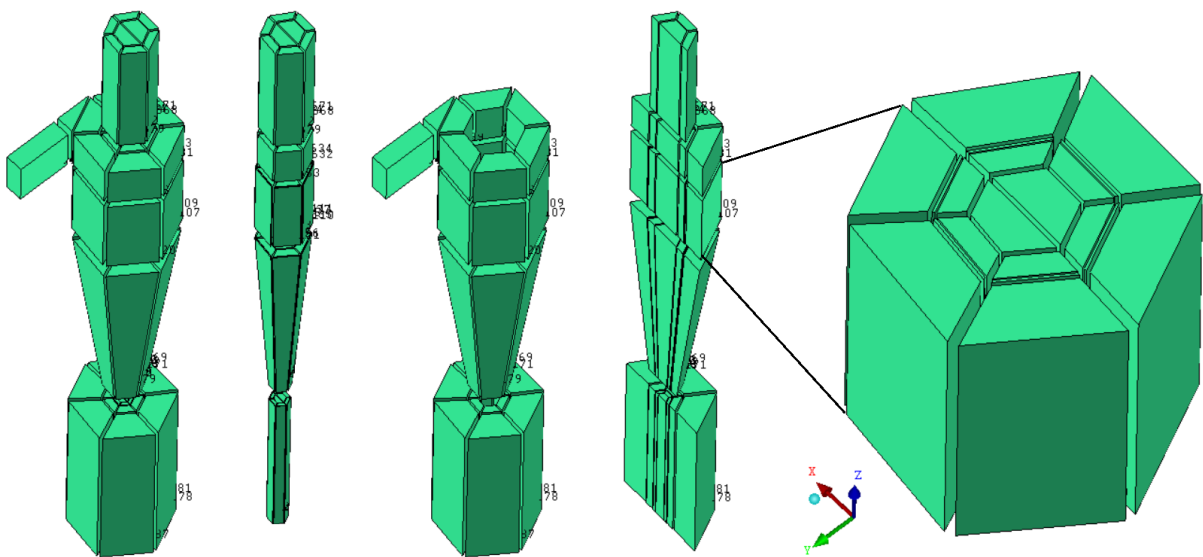


Figure 39. Illustration of the blocking division for the Stairmand cyclone with dust collector bin to generate a structured grid with hexahedral elements. The blocking and meshing process are executed in the software ANSYS® ICEM CFD.

The grid independence test is performed with two numerical grids, having the coarser grid 830,000 and the refined one 1,300,000 hexahedral elements, as shown in Figure 40. The grid size increment for the refined mesh is obtained by increasing the refinement ratio by the order of around 15% of the coarser one, i.e. increase ~15% number of elements in x , y and z directions. A fixed time-step of 1×10^{-5} s is used in the calculations, resulting in an average courant number smaller than unity. For both numerical grids, the gas flow is calculated until the solution reaches its pseudo-steady state using Large Eddy Simulations (LES) combined with the dynamic Smagorinsky sub-grid model and the PIMPLE algorithm for the velocity-pressure coupling (see Chapter 2.1.2 and 2.1.3). A no-slip boundary condition is applied to the cyclone walls and a pressure outlet is attributed to the exit at the end of the vortex-finder boundary

condition. Wall functions are applied in order to solve the turbulence properties in the near wall region. Once the gas phase reaches its pseudo-steady state, the averaging process is started.

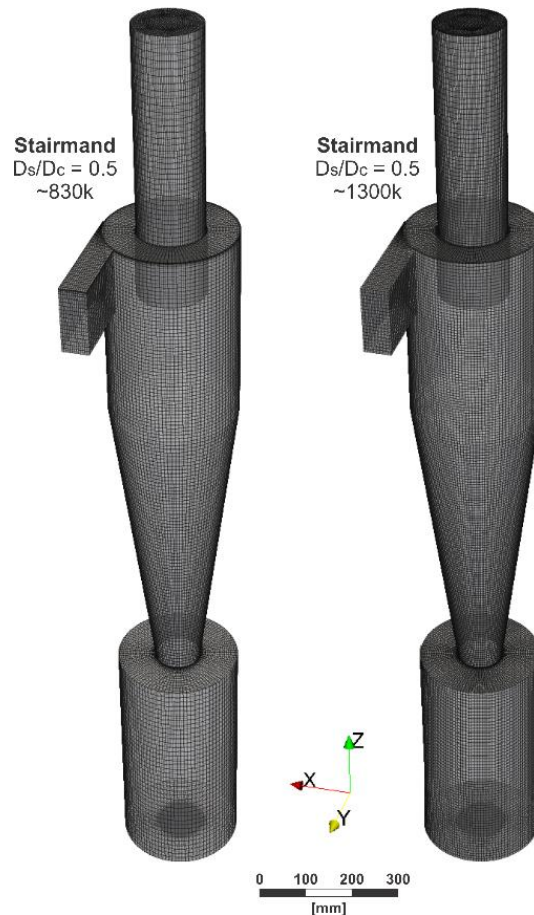


Figure 40. Structured grids used in the grid independence test for a high efficiency Stairmand cyclone with body diameter $D_c = 0.29$ m and vortex-finder $D_s = 0.145$ m. Where to the left is the coarser grid with around 830,000 elements and to the right is the refined grid with around 1,300,000 elements.

A superficial gas flow velocity at the inlet U_{in} of 16.1 m/s was prescribed, yielding a Reynolds number of around 280,000 at the body of the cyclone ($Re_{Dc} = \rho_g U_{in} D_c / \mu_g$), corresponding to the experimental data obtained by Hoekstra^[13] and later simulated by Derksen^[46]. The continuous phase is air with constant density of 1.1147 kg/m³ and a dynamic viscosity of 18.587 10⁻⁶ N s/m². To check if the solution already reached the pseudo-steady state, the intensity of the tangential velocity component is monitored in two mirrored points at the radial position of $R/D_c = 0.3$ at the axial distance from the cyclone roof of $z = 0.75 D_c$, as shown in Figure 41. Those points correspond to the extremities of the vortex core diameter, which is usually defined by the radial position of the maximum tangential velocity (see yellow points in Figure 42). To minimize statistical errors, the averaging of the continuous phase properties are performed during at least five residence times, totalizing around 3 seconds of simulation (already in the pseudo-steady state), corresponding to 300,000 time steps.

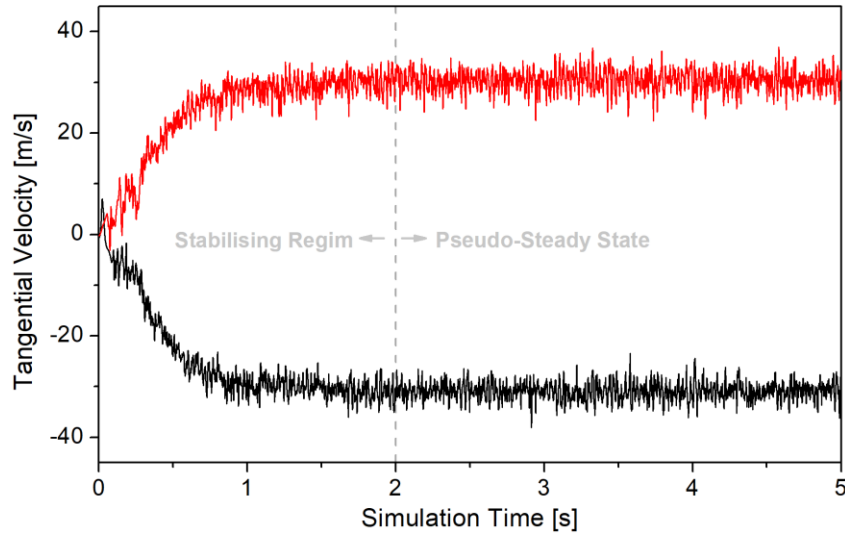


Figure 41. Evolution of the tangential velocity intensity at mirrored points at the radial position of $R/D_c = 0.3$ and axial distance from the cyclone roof of $z = 0.75 D_c$.

Dimensionless Geometrical Relations			
[m]	Geo 1	Geo 2	Geo 3
D_c	1	1	1
D_s	0.5	0.4	0.3
D_l	0.37	0.37	0.37
L_s	0.5	0.5	0.5
L_c	1	1	1
L_{co}	2.5	2.5	2.5
L_e	0.5	0.5	0.5
b	0.2	0.2	0.2

Geometrical Relations			
[m]	Geo 1	Geo 2	Geo 3
D_c	0.290	0.290	0.290
D_s	0.145	0.116	0.087
D_l	0.107	0.107	0.107
L_s	0.145	0.145	0.145
L_c	0.290	0.290	0.290
L_{co}	0.725	0.725	0.725
L_e	0.145	0.145	0.145
b	0.058	0.058	0.058

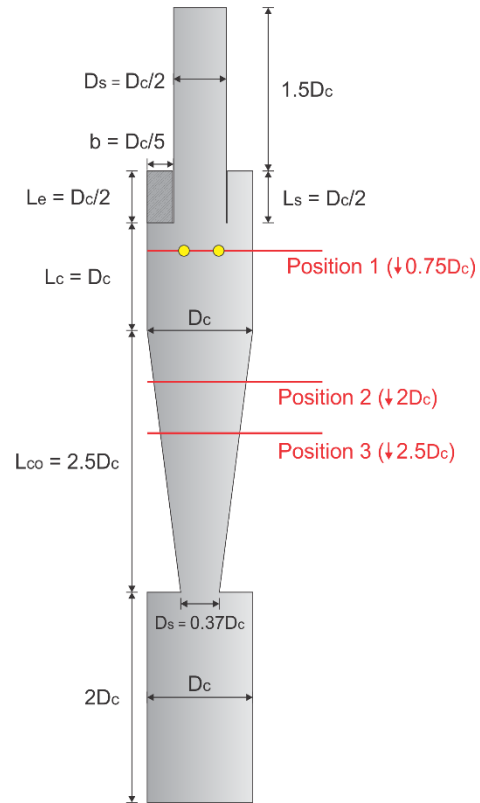


Figure 42. Main geometrical relations of the high efficiency Stairmand cyclone and its variations used in the experiments from Hoekstra^[13]. Where Geo 1 represents the standard Stairmand cyclone with a vortex-finder diameter of 50% of the cyclone's body diameter.

The radial profiles for the average and RMS tangential and axial velocity components are compared in three positions along the cyclone axis. These positions can be described as the distance from the cyclone roof, as: Position 1: $0.75 D_c = 0.2175$ m; Position 2: $2 D_c = 0.58$ m and Position 3: $2.5 D_c = 0.725$ m. The tangential velocity has the strongest effect on the particle motion and its good prediction is very important, since it directly affects the accuracy of the

collection efficiency through the exerted centrifugal force. The normalized average and RMS tangential velocity profiles at the three positions (see Figure 42) for the gas flow in the high efficiency Stairmand cyclone are shown in Figure 43. All velocity profiles are normalized by the inlet velocity U_{in} of 16.1 m/s. The profiles of average tangential velocity show a remarkable agreement with the experimental data, being possible to represent very well the intensity of the peaks of tangential velocity.

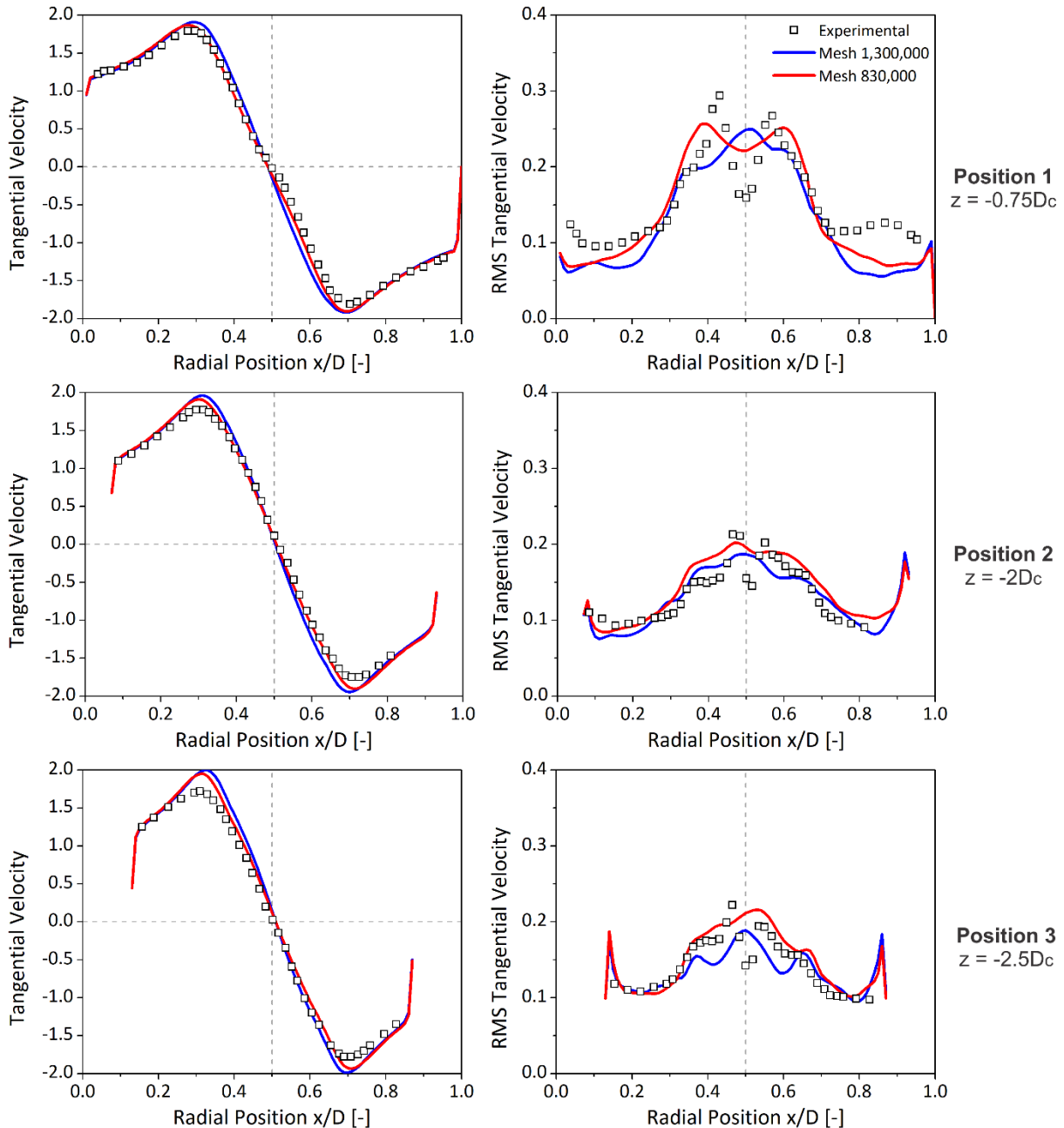


Figure 43. Normalized (by the inlet velocity) mean and RMS tangential velocity profiles at three positions for the single-phase flow in a high efficiency Stairmand cyclone with $Re_{in} = 280,000$. The symbols represent the experimental data from Hoekstra^[13], the red and blue lines the numerical results for the coarser and finer mesh respectively.

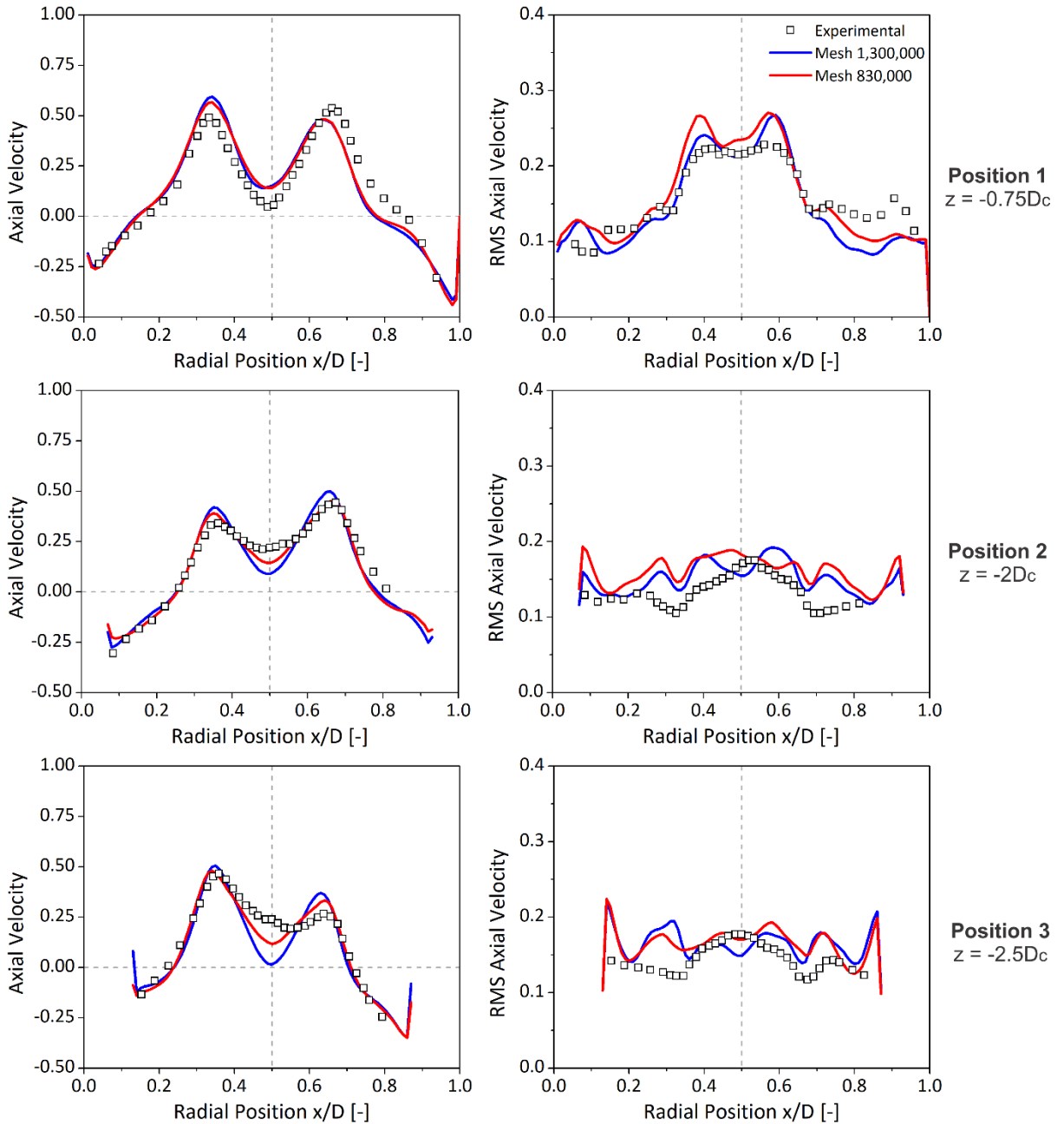


Figure 44. Normalized (by the inlet velocity) mean and RMS axial velocity profiles at three positions for the single-phase flow in a high efficiency Stairmand cyclone with $Re_{in} = 280,000$. The symbols represent the experimental data from Hoekstra^[13], the red and blue lines the numerical results for the coarser and finer mesh respectively.

Even though the RMS values for the tangential velocity present an overall good agreement with the experimental data, the local minimum near the centre of the cyclone is missed. Hoekstra^[13] made all velocity measurements using *Laser Doppler Anemometry* (LDA) technique, where the measured properties are obtained through the use of tracer particles. Once the centre of the cyclone is known to be a region with low particle concentration, one could assume that the rate of data acquisition for this specific region would have a lower acquisition rate as the one obtained with the numerical calculations (for the continuous phase is the same

rate as its time step, 1×10^{-5} s). As stated by Hoekstra ^[13], a point of concern for the LDA measurements in cyclone separators is whether there will be tracer particles present in the vortex core, and whether the tangential velocity component can be measured accurately. The particles tend to move away from the vortex core centre, which implies that low data rates will be obtained in this region. Hence, it is possible to assume that the numerical predictions may be able to observe the swirl fluctuations in a rate that the experimental data is not capable of.

Besides the tangential velocity, the axial velocity plays a major role for the transport of particles in the near wall region moving downwards to the collector bin and also in the core of the cyclone, where fine particle may be carried with the flow upward to the vortex finder. As observed for the tangential velocity, a good agreement is also achieved for the gas phase axial velocity and its fluctuation (Figure 44), indicating that the setup of the validation case, as well as the selected SGS-turbulence model is appropriate. It is important to highlight the accuracy of the dynamic LES model used which allows to accurately reproducing the swirling flow in cyclones. Even considering the inherent difficulties in solving a swirling flow with such a high Reynolds number, both meshes yielded quite similar results, indicating that for the gas phase, the mesh independence was reached on the whole. Once the refined mesh demanded around 50% more computational time than the coarser one and not presented substantial increment to the results, all further simulations are calculated with a numerical grid with the same ratio of refinement as used for the coarser grid. As observed by Derksen ^[46], the dust collector bin should be considered to realistically model the flow in a cyclone, once its absence increases the intensity of the swirl and therefore overestimates the intensity of the velocity profiles. Hence, if the experimental data is obtained with a dust collector bin attached to the cyclone, the same should also be considered to avoid errors.

With the methodology for the blocking and the refinement rate defined, it is possible to test if its application for geometrical variations of the Stairmand cyclone result in the same level of agreement with the experimental data. The presented geometries were modified by reducing the diameter of the vortex finder, where three different vortex finders were used with a diameter of 0.145, 0.116 and 0.087 m, corresponding to a ratio D_s/D_c of 0.5, 0.4 and 0.3, respectively. The numerical grid of the three geometrical variations of the Stairmand cyclone are shown in Figure 45. Unfortunately Hoekstra ^[13] provides for the three geometries only the velocity profiles at the axial Position 1 ($z = -0.75 D_c$), however a comparison with the measured pressure drop is available for different inlet velocities.

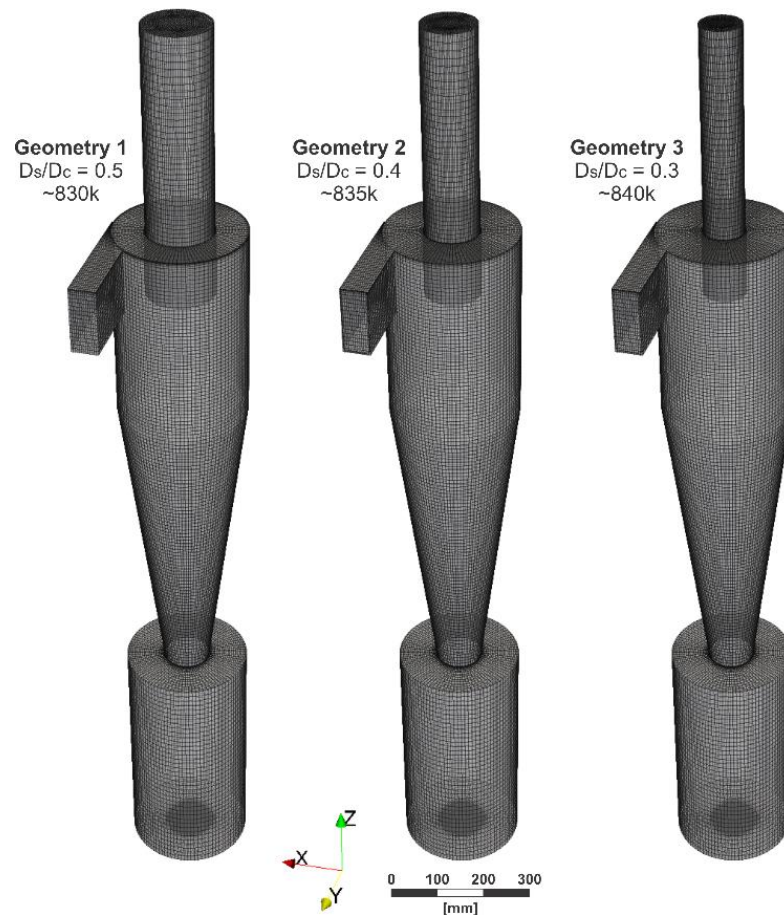


Figure 45. Structured grids of the three geometrical variations of the Stairmand cyclone with body diameter $D_c = 0.29$ m used in the experiments from Hoekstra ^[13].

The normalized average and RMS tangential and axial velocity profiles at Position 1 ($z = -0.75 D_c$) for the gas flow in a high efficiency Stairmand cyclone are shown in Figure 46 and Figure 47, respectively. Both the tangential and axial velocity profiles show a small but significant axi-asymmetry with due respect to the cyclone's centreline. The main reason for this behaviour, according to Hoekstra ^[13], lies on the relative close location of the measurement region to the tangential inlet section, and its axi-symmetric injection of the gas. The profiles of tangential velocity differ strongly with respect to the size of the vortex-finder, where its diameter reduction results in a sharp increase of the maximum tangential velocity as a result of decreasing the vortex core size. The maximum tangential velocity increases from around 1.9 to almost 3 times the inlet velocity due to the reduction of the vortex finder diameter from $0.5 D_c$ to $0.3 D_c$ respectively.

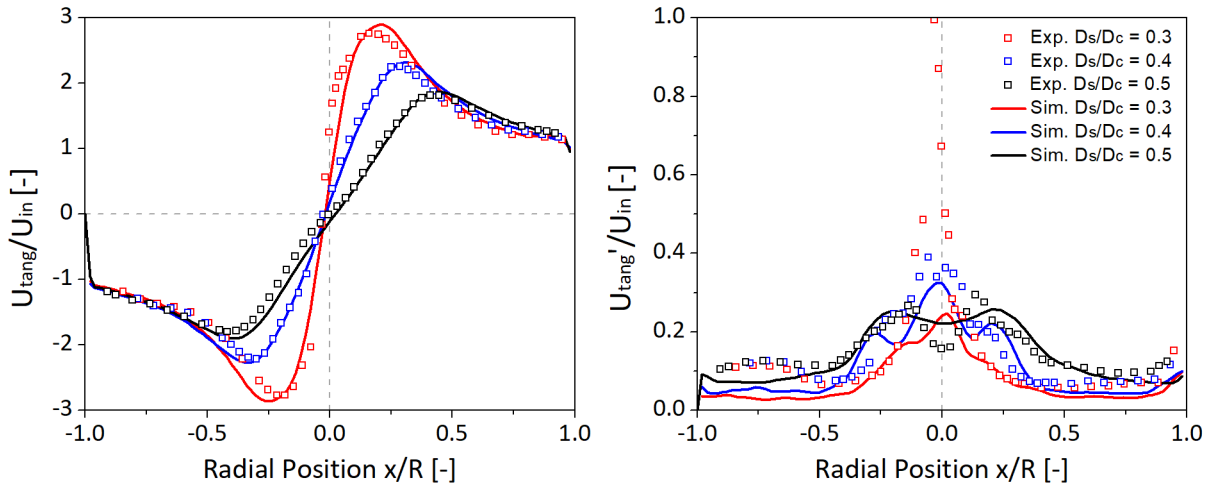


Figure 46. Normalized (by the inlet velocity 16.1 m/s) mean and RMS tangential velocity profiles at Position 1 ($z = -0.75D_c$) for the single-phase flow in a high efficiency Stairmand cyclone with $Re_{in} = 280,000$. The symbols represent the experimental data from Hoekstra^[13] and the lines the numerical results for the three geometric variations.

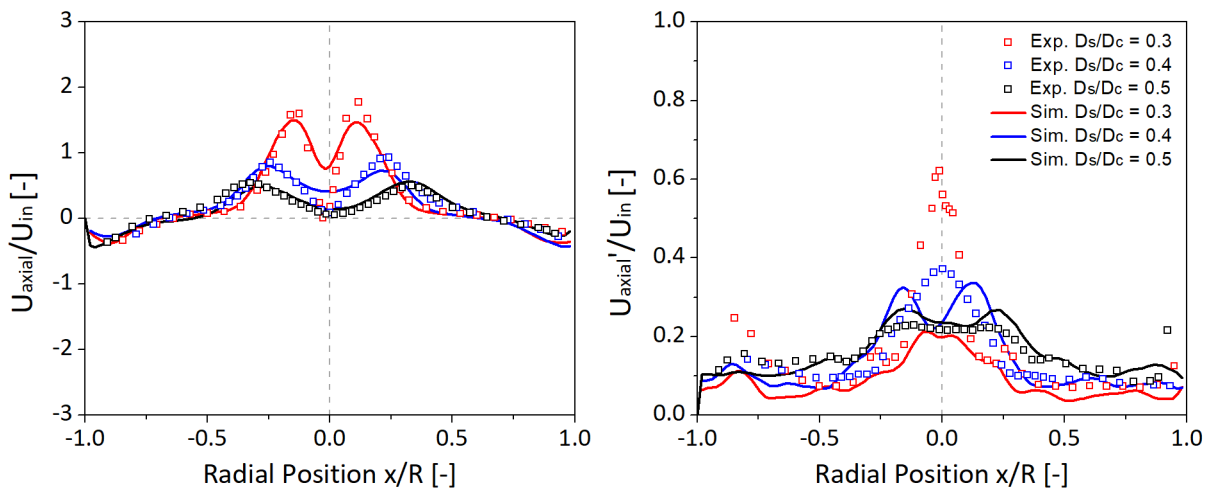


Figure 47. Normalized (by the inlet velocity 16.1 m/s) mean and RMS axial velocity profiles at Position 1 ($z = -0.75D_c$) for the single-phase flow in a high efficiency Stairmand cyclone with $Re_{in} = 280,000$. The symbols represent the experimental data from Hoekstra^[13] and the lines the numerical results for the three geometric variations.

From the axial velocity profiles is possible to observe the reverse-flow of the cyclone. The flow is directed downwards near the cyclone's wall, while in the central region the axial velocity is directed upwards, towards the exit through the vortex finder. The upward directed flow exhibits the axial velocity maximum for all three geometrical variations, where its vortex core size is normally smaller than the vortex finder diameter. As observed for the tangential velocity, due to the reduction of the vortex finder diameter, the maximum of axial velocity increases significantly to conserve the mass flow that should leave the cyclone.

For both tangential and axial averaged velocity profiles a remarkable agreement with the experimental data is observed. For the velocity fluctuations small differences are noticed,

however one should keep in mind the problem related to the measurements in the core region where low tracer concentrations are met. Overall, a good representation of the gas flow inside the three geometrical variations of the Stairmand cyclone are accomplished. Lastly, the comparison of the experimental values of pressure drop for the three geometries are compared with the numerical results for different gas velocity at the inlet. Hoekstra ^[13] estimated the pressure drop by measuring the static pressure difference between two pressure taps inserted in the cyclone wall. The first tap was located at half the inlet height of the tangential inlet and the second at the exit pipe wall ($z = D_c/2 = 0.145 \text{ m}$), as shown in Figure 48. Fortunately, Hoekstra ^[13] provided the exact position where the pressure should be measured, once its value can change substantially with the exit pipe position.

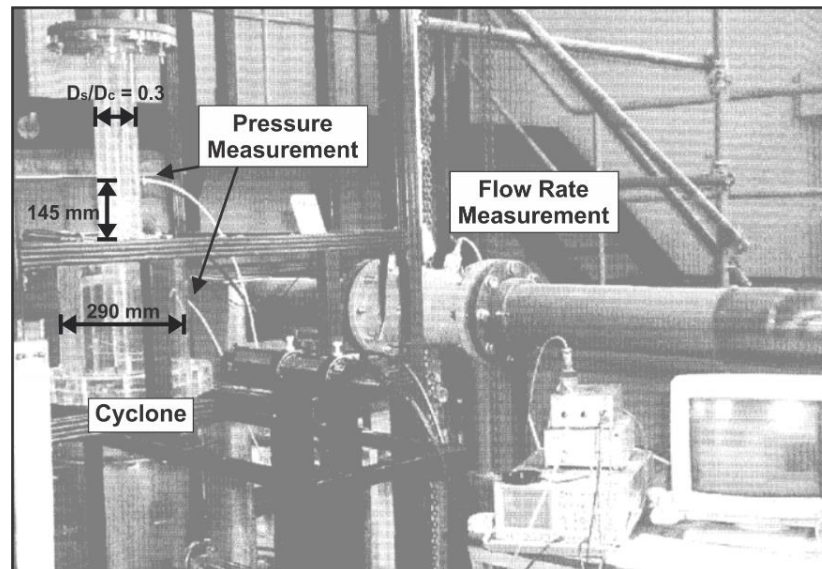


Figure 48. Experimental set-up used for the measurements in the Stairmand cyclone. Detail for the measurement regions for the pressure drop. Source: Adapted from Hoekstra ^[13].

Figure 49 shown the evolution of the pressure inside the cyclone geometry and it is divided in three parts. The first part to the left shown the contours of averaged pressure for different cross sections of the cyclone, where it is noticeable the low pressure region created by the upwards flow in the core of the cyclone. The middle graph represents the radial profiles of pressure for the inlet and the outlet pipe at the axial distances of 1, 20 and 40 cm to the cyclone's roof. The observed profiles for the inlet are constant, while the outlet pressure profiles are changing accordingly to the radial and axial position. The axial differences are mainly caused by the used boundary condition of zero relative pressure at the outlet. Thus, the correct measurement position is very important for a good estimation of the pressure drop, once there are static pressure variations within the axial position, as shown in the right graph of the Figure 49 for a centre line and another near the wall.

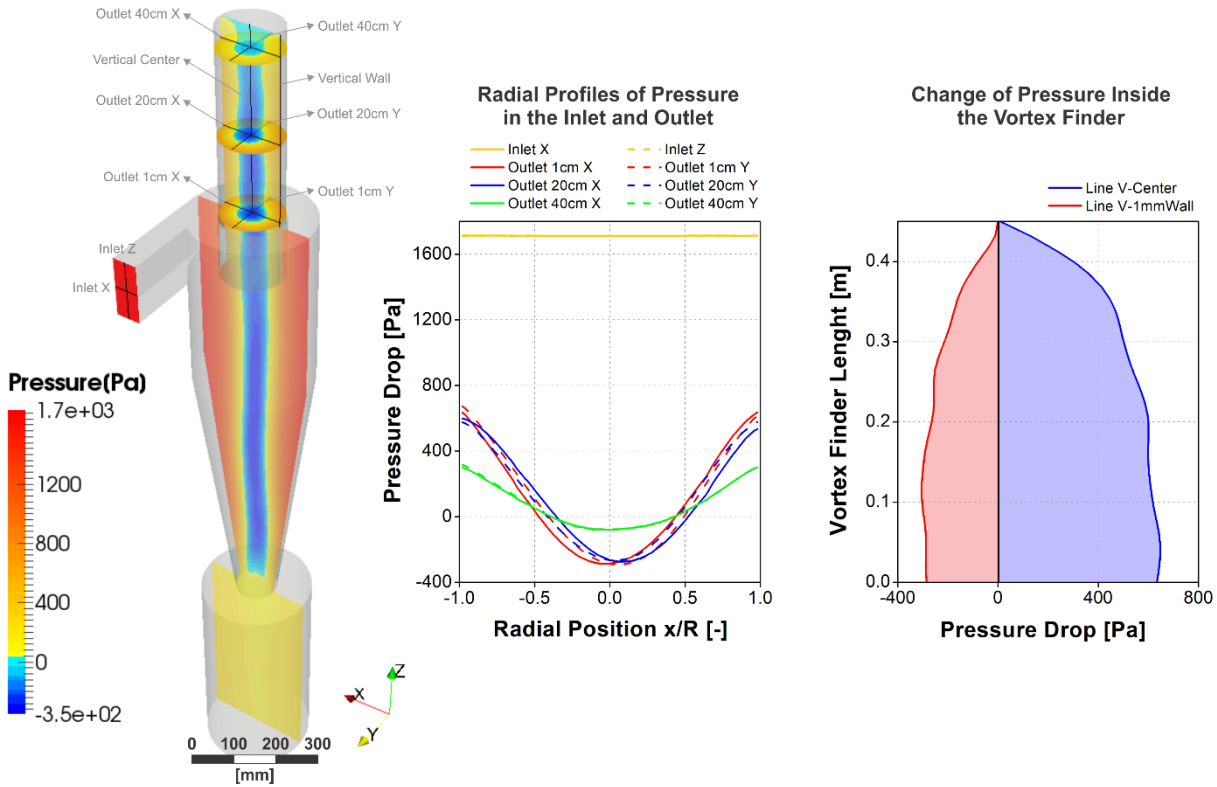


Figure 49. Evolution of the pressure inside the Stairmand cyclone with $D_s/D_c = 0.5$ and inlet velocity of 20 m/s. The left side shown the contour maps of averaged pressure in different cross-sections of the cyclone; the middle graph shown the radial profiles of pressure drop in the inlet/outlet regions and to the right is the change of pressure inside the vortex finder.

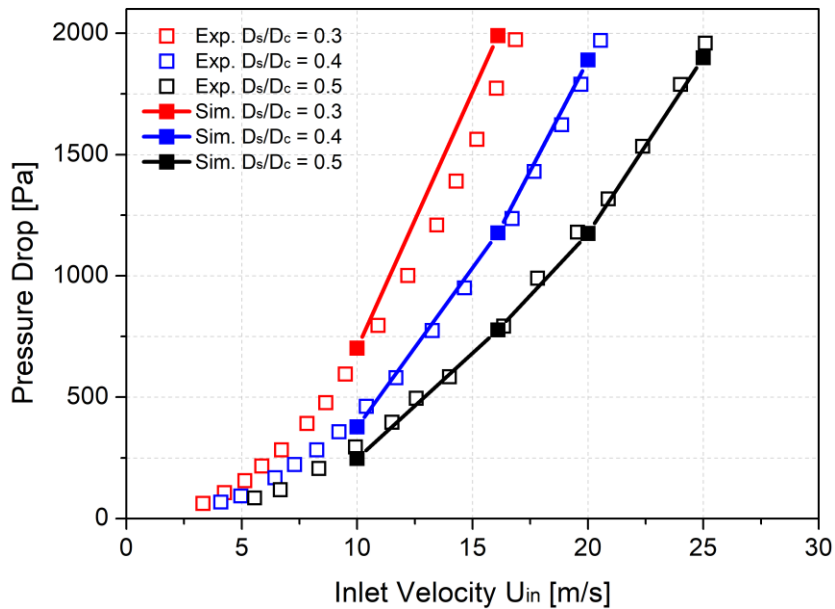


Figure 50. Pressure drop evolution as function of the inlet velocity for the three geometrical variations of the Stairmand cyclone with body diameter $D_c = 0.29$ m. The symbols represent the experimental data from Hoekstra^[13] and the lines the numerical results for the three geometric variations.

Finally, Figure 50 shown the evolution of the pressure drop as function of the inlet velocity for the three geometrical variations of the Stairmand cyclone. By considering the static pressure at the exact position as experimentally measured, it is possible to obtain an outstanding agreement with the experimental data. As expected, by reducing the diameter of the vortex finder, an increase of the pressure drop is observed due to the higher tangential and axial velocities. With a good agreement regarding the velocity profiles and the pressure drop, it is possible to affirm that the used turbulence model, as well as all the numerical set-up and grid generation are suitable to represent the turbulent swirl flow in cyclone separators. Therefore, a further investigation on the particle behaviour inside cyclones and the consequentially curves of collection efficiency are studied.

4.2 Test Case 2: Particle Tracking and Collection Efficiency

To test the appropriate approach for the particle tracking in cyclones and the methodology for the collection efficiency calculation, two different cyclones are studied in this test case. The first cyclone corresponds to a small scale laboratory-cyclone studied by Xiang et al. ^[10], where the influence of the bottom cone diameter D_1 on the performance parameters is investigated. For this case, only one-way coupling calculations are considered, resulting in a simpler configuration to start the two-phase studies. The second cyclone corresponds to the previously studied Stairmand cyclone from Hoekstra ^[13] with the three variations of the vortex finder diameter D_s (see Figure 42). Here it is possible to explore a more complex configuration, where two-way coupling calculations are performed to test the collection efficiency methodology accuracy for different rates of parcels injected in the system.

4.2.1 Small Scale Laboratory-Cyclone

Xiang et al. ^[10] studied the effect of cone dimension on the cyclone performance by experimentally testing three variations of the bottom cone diameter D_1 in small scale laboratory-cyclones. The cyclones have a body diameter of 0.031 m and are constructed out of glass. The geometrical relations for the three cyclones are shown in Figure 51. The numerical grids used in the present study case follow the same methodology as proposed in the previous Chapter, being constituted of only structured hexahedral elements, as shown in Figure 52. Unfortunately it is not clear if Xiang et al. ^[10] made use of a dust collector bin at the bottom cone of the cyclone to collect the particles. Hence, no bins are considered in the present test case once its inclusion may modify the swirl flow inside the cyclone.

Four different gas flow rates are tested, e.g. 30, 40, 50 and 60 L/min, resulting in a superficial velocity at the inlet of the cyclone of 8, 10.67, 13.33 and 16 m/s respectively. Air at ambient temperature is considered with constant density of 1.205 kg/m^3 and a dynamic viscosity of $18.2 \cdot 10^{-6} \text{ N s/m}^2$. A fixed time-step of $1 \times 10^{-5} \text{ s}$ is used for the continuous phase, resulting in an average courant number smaller than unity. For all different geometries and gas flows, the gas is calculated until the solution reaches its pseudo-steady state using Large Eddy Simulations (LES) combined with the dynamic Smagorinsky sub-grid model and the PIMPLE algorithm for the velocity-pressure coupling (see Chapter 2.1.2 and 2.1.3). Thereafter, it is possible to start the averaging of the continuous phase properties and the particle tracking. A no-slip boundary condition is applied to the cyclone walls and a pressure outlet is attributed to the exit at the end of the vortex-finder boundary condition. Wall functions are applied in order to solve the

turbulence properties in the near wall region. A short summary of the cases configuration is shown in Table 8.

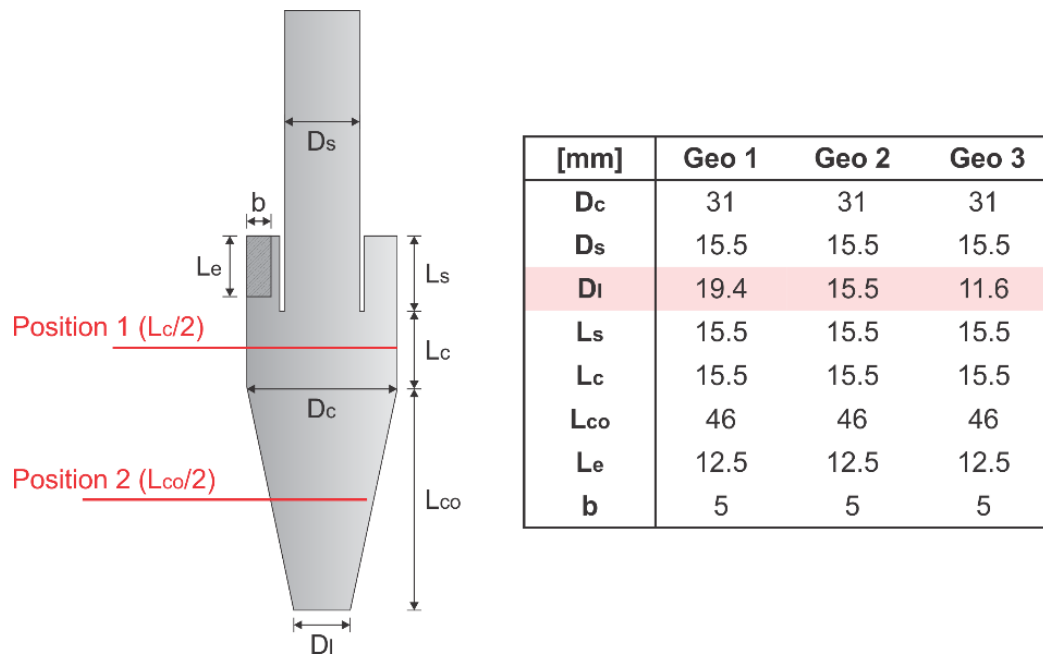


Figure 51. Main geometrical relations of the three small scale laboratory-cyclones used in the experiments from Xiang et al. ^[10]. For the three used geometries, only the bottom cone diameter D_i is modified.

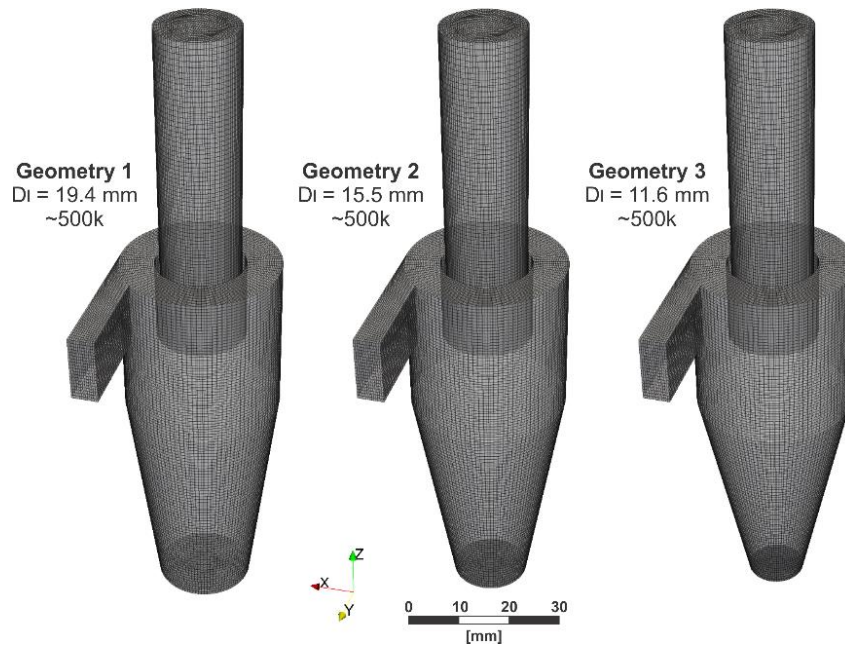


Figure 52. Structured grids of the three small scale laboratory-cyclones with body diameter $D_c = 0.031$ m with around 500,000 hexahedral elements each.

<i>Table 8. Configuration of the small-scale laboratory cyclone used in the second test case.</i>		
Geometrical Properties		
Cyclone Body Diameter	D_c	0.031 m
Bottom Cone Diameter	D_l	0.0194, 0.0155 and 0.0116 m
Grid Size	-	~ 500,000 elements
Wall Roughness	$\Delta\gamma$	-
Gas Properties		
Inlet Velocity	U_{in}	8, 10.67, 13.33 and 16 m/s
Gas Flow	Q_{in}	30, 40, 50 and 60 L/min
Density	ρ_g	1.205 kg/m ³
Dynamic Viscosity	μ_g	18.2 10 ⁻⁶ N s/m ²
Euler. Time-Step	Δt_E	1x10 ⁻⁵ s
Particles Properties		
Inlet Velocity	$U_{p,in}$	10.67, 13.33 and 16 m/s
RMS Inlet Velocity	$U_{p,in}'$	3 %
Angular Velocity	σ_ω	1,000 s ⁻¹
Mass Loading	η	-
Particle Density	ρ_p	1,050 kg/m ³
Particle Size	D_p	0.5 - 6 μ m
Parcels Rate	-	300,000 parcels/s
Particles/Parcel	-	1

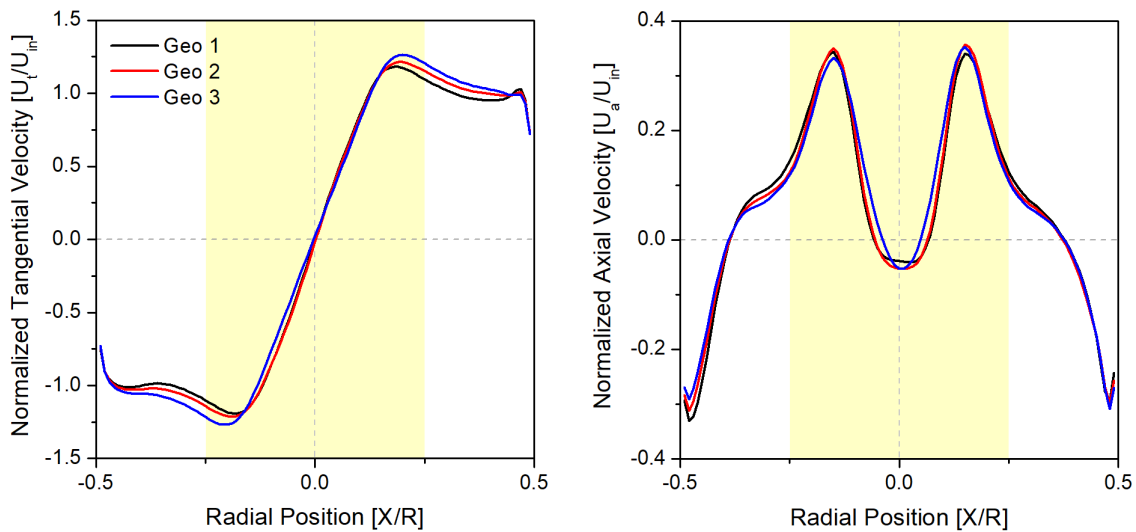


Figure 53. Normalized (by the inlet velocity 10.67 m/s) mean tangential (left) and axial (right) velocity profiles at the axial Position 1 ($L/2$) for the single-phase flow in the small scale laboratory-cyclone used by Xiang et al. ^[10]. The yellow area represents the diameter of the vortex finder D_s .

Despite the research group from Xiang et al. ^[10] have presented other studies including the effect of vortex finder shapes ^[20] and the effect of double inlets ^[23] on the collection efficiency, velocity profiles are not presented. Thus, to observe the changes in the flow caused by the geometrical modifications, numerical profiles of mean tangential and axial velocities for the cylindrical and conical sections are shown in Figure 53 and Figure 54, respectively. The

exact axial position of the measurements is shown in Figure 51. By analysing the velocity profiles for the cylindrical section, one can assume that the change of the bottom cone diameter does not induce a significant increase of the mean tangential and axial velocity. For the conical section, despite a change on the form of the profiles is caused by the constriction of the cross section of the cone, almost the same velocity intensity is observed for all three geometries.

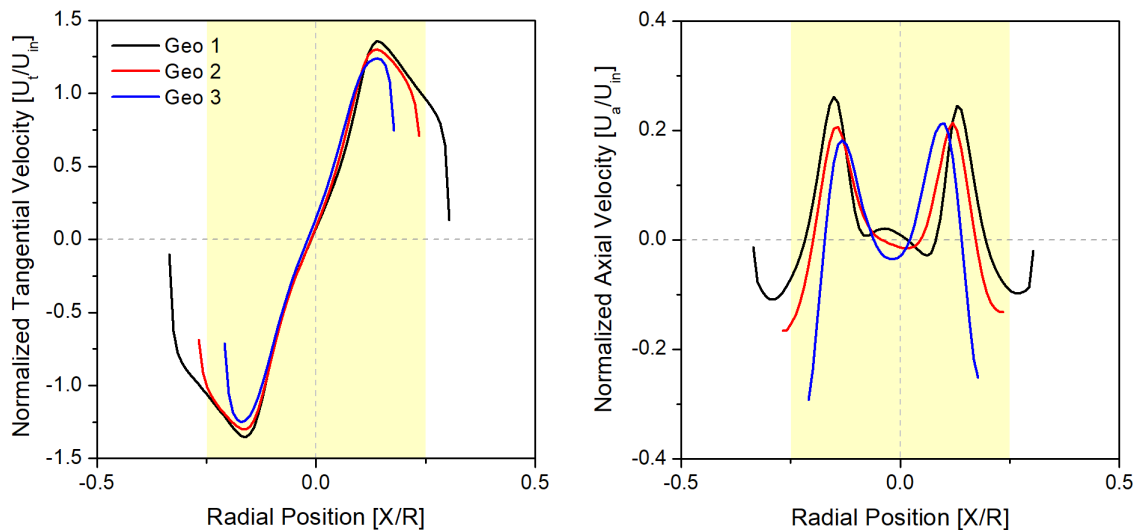


Figure 54. Normalized (by the inlet velocity 10.67 m/s) mean tangential (left) and axial (right) velocity profiles at the axial Position 2 ($L_c/2$) for the single-phase flow in the small scale laboratory-cyclone used by Xiang et al. ^[10]. The yellow area represents the diameter of the vortex finder D_s .

Once the velocity profiles did not change substantially due to the geometrical modifications, one can expect that the pressure drop for the same gas flow should be in the same magnitude for all geometries. Fortunately, Xiang et al. ^[10] provided the values of pressure drop for all geometries and gas flow rates studied. The exact position of the measurements is not described, however the comparison with the numerical data is made by measuring the static pressure at half length of the inlet and at half length of the exit pipe. Figure 55 shows the evolution of the measured (full bars) and calculated (dashed bars) pressure drop as function of the gas flow rate. As expected, for the same flow rate only small differences are observed among the three geometries, being the geometry 3 the one with higher values of pressure drop (same as observed for the velocity profiles). Overall, the numerical calculations present a higher value of pressure drop, possibly indicating that the used measurement region is not appropriate. Another cause for the differences among the experimental and numerical results can be related to the absence of the dust collector bin in the calculations, once the same can dissipate the swirl flow intensity and therefore reduce the pressure drop. For the gas flow rate of 60 L/min a strange pattern is observed for the experimental data, where the third geometry present a higher value in comparison with the other two, being this behaviour not observed in the simulations. Based

on the comparison of the pressure drop results, it is possible to affirm that a good agreement with the experimental data is observed, proving that the numerical grid generation and the models/approaches used in the simulations are appropriated.

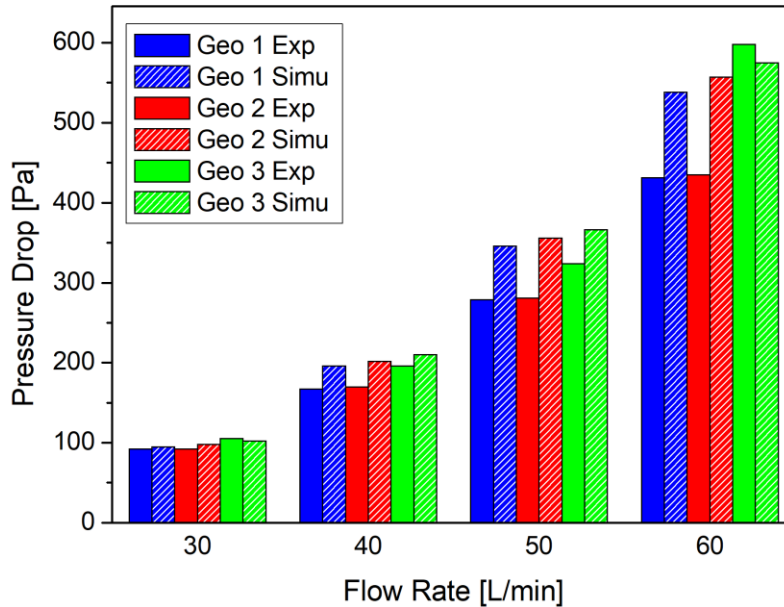


Figure 55. Evolution of the pressure drop as function of the flow rate. The full bars represent the experiments from Xiang et al. ^[10] while the dashed ones represent the present numerical results.

The final analysis and main scope of this test case is regarding the particle tracking and consequently the calculation of the collection efficiency. Xiang et al. ^[10] performed all measurements using monodisperse polystyrene latex (PSL) particles with a density of 1,050 kg/m³, where an atomizer was used to generate particles with size in the range from 0.5 to 8.1 μm . However, no information regarding the particle mass loading is specified by the author, expressing only that the system was diluted. Based on the supposedly low mass loading, small Stokes number and relaxation time for the generated particles (see Table 9), one can assume that the particles are not influencing the continuous phase significantly. Therefore, only one-way coupling calculations are been considered for the present test case, i.e. no gas-particle or inter-particle interactions are considered. Hence, for the numerical calculations a size distribution composed by 12 classes uniformly sampled ranging from 0.5 to 6 μm is applied. Once one-way coupling is considered, a single injection of 300,000 particles (25,000 particles of each size class) with velocities sampled from normal distributions with fixed mean and RMS velocities are applied. The mean particle velocity at injection is the bulk gas velocity, in the stream-wise direction and zero in the transverse components, and the RMS value is 3 % of the gas bulk velocity for the three velocity components. The three angular velocity components for the particles at the injection were assumed with a mean of zero and standard deviation of 1,000

1/s. Since the cyclone used by Xiang et al. ^[10] is made of glass, no wall-roughness is considered for the specific test case. However, inelastic collisions are considered, where the restitution coefficient ε and friction coefficient μ_d are calculated [57] based on the impact angle as presented by the Equations (52) and (53) respectively.

Table 9. Relaxation time and Stokes number calculated by the inlet velocity for the particles used in the test case.

D_p (μm)	Particle Relaxation Time (μs)	30 L/min	40 L/min	50 L/min	60 L/min
		8 m/s	10.67 m/s	13.33 m/s	16 m/s
		Particle Stokes Number	Particle Stokes Number	Particle Stokes Number	Particle Stokes Number
0.5	0.80	2.07×10^{-4}	2.75×10^{-4}	3.44×10^{-4}	4.13×10^{-4}
1.0	3.21	8.26×10^{-4}	1.10×10^{-3}	1.38×10^{-3}	1.65×10^{-3}
1.5	7.21	1.86×10^{-3}	2.48×10^{-3}	3.10×10^{-3}	3.72×10^{-3}
2.0	12.82	3.30×10^{-3}	4.41×10^{-3}	5.51×10^{-3}	6.61×10^{-3}
2.5	20.03	5.16×10^{-3}	6.88×10^{-3}	8.61×10^{-3}	1.03×10^{-2}
3.0	28.85	7.44×10^{-3}	9.91×10^{-3}	1.24×10^{-2}	1.49×10^{-2}
3.5	39.26	1.01×10^{-2}	1.35×10^{-2}	1.69×10^{-2}	2.02×10^{-2}
4.0	51.28	1.32×10^{-2}	1.76×10^{-2}	2.20×10^{-2}	2.64×10^{-2}
4.5	64.90	1.67×10^{-2}	2.23×10^{-2}	2.79×10^{-2}	3.35×10^{-2}
5.0	80.13	2.07×10^{-2}	2.75×10^{-2}	3.44×10^{-2}	4.13×10^{-2}
5.5	96.96	2.50×10^{-2}	3.33×10^{-2}	4.17×10^{-2}	5.00×10^{-2}
6.0	115.38	2.97×10^{-2}	3.97×10^{-2}	4.96×10^{-2}	5.95×10^{-2}

Particle transport is calculated by considering all relevant forces (e.g. particle inertia, drag, gravity, slip-shear force, slip-rotational lift force and torque) and turbulence dispersion. Despite the particle inertia and drag force are the most significant forces acting on the particles in a cyclone separator, the further forces are also considered due to the wide range of operational conditions studied and its low demanding computational effort. It is important to highlight that, particles are injected only when the gas flow already reached its pseudo-steady state condition, being both phases solved simultaneously afterwards. A particle escapes the system if it touches the outlet surface located at the top of the cyclone, while it is collected if it touches the bottom cone surface. All particles are tracked simultaneously until at least 95 % of the particles have left the cyclone, i.e. the sum of all particles collected and escaped. Hence, the collection efficiency, or grade efficiency, in dependence of particle size x can be calculated considering the number of particles that escaped the cyclone and the ones collected as follow:

$$\eta = 1 - \frac{N(x)_{\text{escaped}}}{N(x)_{\text{escaped}} + N(x)_{\text{collected}}} \quad (95)$$

The collection efficiency curves were obtained as a function of particle size for different gas flow rates and geometries, as shown in Figure 56. As observed by Xiang et al. ^[10], the collection efficiency increases by increasing the gas flow rate, i.e. consequently increasing the tangential velocity and centrifugal force. Additionally, a slightly increment to the collection efficiency can be attributed to the reduction of the bottom cone diameter D_1 , where the geometry 3 presents the sharpest curves of collection efficiency in comparison with the others.

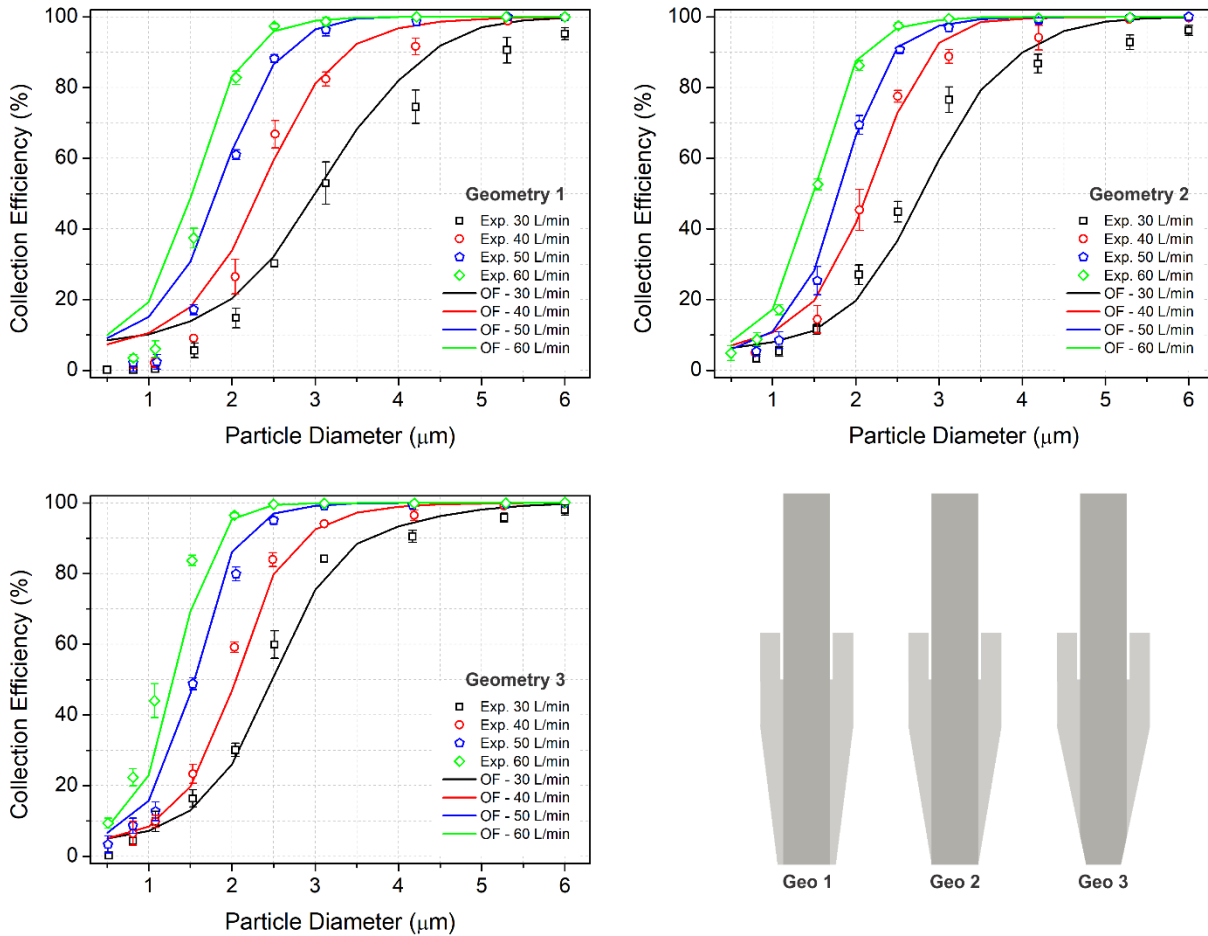


Figure 56. Collection efficiency curves in function of particle size for the three geometries used in the calculations. The symbols represent the experimental data of Xiang et al. ^[10] and the lines represent the present numerical results.

By analysing the numerical results for the geometry 1, particles smaller than $2 \mu\text{m}$ do not present a good agreement with the experimental data. The observed overestimation of the collection efficiency can be explained by the nature of the geometry and the boundary conditions used to calculate the collection efficiency. As shown in Figure 56, the bottom cone diameter D_1 is bigger than the vortex finder D_s for the geometry 1, allowing the particles to be collected without interacting with the vortex core (usually smaller than the vortex finder diameter D_s). Once the smaller particles are normally dragged by the vortex core and directed

through the exit pipe, the lack of this interaction increases artificially its collection rate. This phenomenon is also observable by analysing the profiles of axial velocity in the conical section in Figure 54, where geometry 1 shows a larger region with negative axial velocity. This problem could be solved by a more complete representation of the experimental set-up, with the extension pipe or collector bin downstream the conical section. However, an overall good agreement with the experimental results is observed, where the collection efficiency increases with the flow rate and the curves present the usual sigmoid-shape ^[1].

4.2.2 Stairmand Cyclone

The second cyclone studied in this test case is based on the experiments of Hoekstra ^[13] using a high efficiency Stairmand cyclone ^[5] with the three geometrical variations (see Figure 42). The Stairmand cyclone is modified by reducing its vortex finder diameter, e.g. 0.145, 0.116 and 0.087 m, corresponding to a ratio D_s/D_c of 0.5, 0.4 and 0.3, respectively. The structured numerical grids used for this study are the same used in the previous test case (Figure 45), where every geometry corresponds to around 830,000 hexahedral elements. Three different gas velocities are tested, e.g. 10, 20 and 30 m/s, yielding a Reynolds number at the body of the cyclone of around 1.74×10^5 , 3.48×10^5 and 5.22×10^5 respectively. The continuous phase was treated as air with constant density of 1.1147 kg/m^3 and a dynamic viscosity of $18.587 \cdot 10^{-6} \text{ N s/m}^2$. All the simulations for the flow field are performed with a fixed time-step of $1 \times 10^{-5} \text{ s}$, resulting in an average courant number smaller than unity. As specified for the previous cases, the gas is calculated until the solution reaches its pseudo-steady state using Large Eddy Simulations (LES) combined with the dynamic Smagorinsky sub-grid model and the PIMPLE algorithm for the velocity-pressure coupling (see Chapter 2.1.2 and 2.1.3). A no-slip boundary condition is applied to the cyclone walls and a pressure outlet is attributed to the exit at the end of the vortex-finder boundary condition. Wall functions are applied in order to solve the turbulence properties in the near wall region.

The particles used by Hoekstra ^[13] to measure the collection efficiency are made of calcium carbonate (CaCO_3), with a density of $2,740 \text{ kg/m}^3$. For the numerical calculations, a size distribution composed by 12 classes ranging from 0.5 to 20 μm (Table 10) is used. The injected particles have velocities sampled from a normal distribution with fixed mean and RMS velocities. The mean particle velocity at injection is the bulk gas velocity, i.e. 10, 20 or 30 m/s, in the stream-wise direction and zero in the transverse components, and the RMS value is 3 % of the gas bulk velocity for the three velocity components. The angular velocity components for the particles at the injection were assumed with a mean of zero and standard deviation of

1,000 1/s. Particle transport is calculated by considering all relevant forces (e.g. particle inertia, drag, gravity, slip-shear force, slip-rotational lift force and torque) and turbulence dispersion. As specified for the previous case, no wall-roughness is considered once the cyclone used by Hoekstra ^[13] is constructed of acrylic (Poly(methyl methacrylate) / PMMA), which presents a smooth surface. Hence, to represent the particle-wall collisions, inelastic collisions are considered, where the restitution coefficient ϵ and friction coefficient μ_d are calculated based on the impact angle as presented by the Equations (52) and (53) respectively. The general configuration of the present cases using the Stairmand cyclone are summarized in Table 11.

Table 10. Size distribution of the Calcium Carbonate (CaCO₃) particles used in the simulations.

D_p (μm)	Cumulative Fraction (%)	Fraction (%)
0.50	5.57	5.57
0.75	10.02	4.46
1.00	15.18	5.16
1.50	24.10	8.92
2.00	32.36	8.26
2.50	39.45	7.09
3.00	44.84	5.39
4.00	54.80	9.95
6.00	67.61	12.82
8.00	80.48	12.86
10.00	88.84	8.37
20.00	100.00	11.16

Table 11. General configuration of the Stairmand Cyclone used in the second test case.

Geometrical Properties		
Cyclone Body Diameter	D _c	0.290 m
Vortex Finder Diameter	D _s	0.145, 0.116 and 0.087 m
Grid Size	-	~ 830,000 elements
Wall Roughness	Δγ	-
Gas Properties		
Inlet Velocity	U _{in}	10, 20 and 30 m/s
Density	ρ _g	1.1147 kg/m ³
Dynamic Viscosity	μ _g	18.587 10 ⁻⁶ N s/m ²
Euler. Time-Step	Δt _E	1x10 ⁻⁵ s
Particles Properties		
Inlet Velocity	U _{p,in}	10, 20 and 30 m/s
RMS Inlet Velocity	U _{p,in} '	3 %
Angular Velocity	σ _ω	1,000 s ⁻¹
Mass Loading	η	2.8 x 10 ⁻³ kg particles / kg air
Particle Density	ρ _p	2,740 kg/m ³
Particle Size	D _p	0.5 - 20 μm
Parcels Rate	-	500,000 parcels/s
Particles/Parcel	-	~ 338, 677 and 1015

The mass loading of particles at the inlet used by Hoekstra ^[13] have a constant value of $2.8 \times 10^{-3} \text{ kg}_{\text{ particles}} / \text{kg}_{\text{ air}}$ for all cases. Hence, to account for the correct particle mass flow rate, the considered computational parcels represent a certain number of real particles with the same properties, which yields a computationally treatable number of parcels. The exact number of parcels necessary to have a good statistical reliability is difficult to determine without testing. Thus, a preliminary test considering four different rates of parcels conserving the mass loading for the standard Stairmand cyclone ($D_s/D_c = 0.5$) with gas flow velocity of 20 m/s is proposed, as detailed in Table 12. Despite the low mass loading, two-way coupling calculations are considered, once it is not easy to previously determine how the particles will affect the gas flow. Therefore, a continuous injection of particles is demanded to simulate the two-phase flow measured by Hoekstra ^[13]. Hence, the injection of particles only starts when the gas flow is already developed, being it injected continuously until the end of the calculation. The measurement of particle properties (e.g. particle concentration, collection efficiency) is initiated only after the number of parcels inside the cyclone is stable, i.e. the gas-solid flow reaches its pseudo-steady state.

Table 12. Configuration of the cases considering different rates of parcels.

Geometry (D_s/D_c)	Velocity (m/s)	Mass Loading ($\text{kg}_{\text{ particles}} / \text{kg}_{\text{ air}}$)	Rate of Parcels (1/s)	Number of Particles per Parcel
0.5	20	2.8×10^{-3}	250,000	1,354
0.5	20	2.8×10^{-3}	500,000	677
0.5	20	2.8×10^{-3}	1,000,000	388
0.5	20	2.8×10^{-3}	2,000,000	169

The influence of the number of parcels on the continuous phase is investigated through the temporal evolution of tangential velocity in two opposite points at radial position of $R/D_c = 0.3$ and axial distance from the cyclone roof of $z = 0.75 D_c$, as shown in Figure 57. The position of these points correspond to the extremities of the vortex core diameter, i.e. at the radial position where the maximum tangential velocity is observed. For the specific configuration, the injection of particles starts at 1 s, from where they are injected continuously up to the end of the simulation. Figure 57-a shown the instantaneous values of tangential velocity from the start of the injection through 2 s of simulation time.

At the beginning of the calculation, no difference among the cases is observed due to the lack of particles inside the body of cyclone. Hence, the fluctuations of the instantaneous tangential velocity are a product of turbulence and the unsteady nature of the swirl flow in cyclones. Around 1.1 s the particles already entered the body of the cyclone, where their impact on the continuous phase is noticeable.

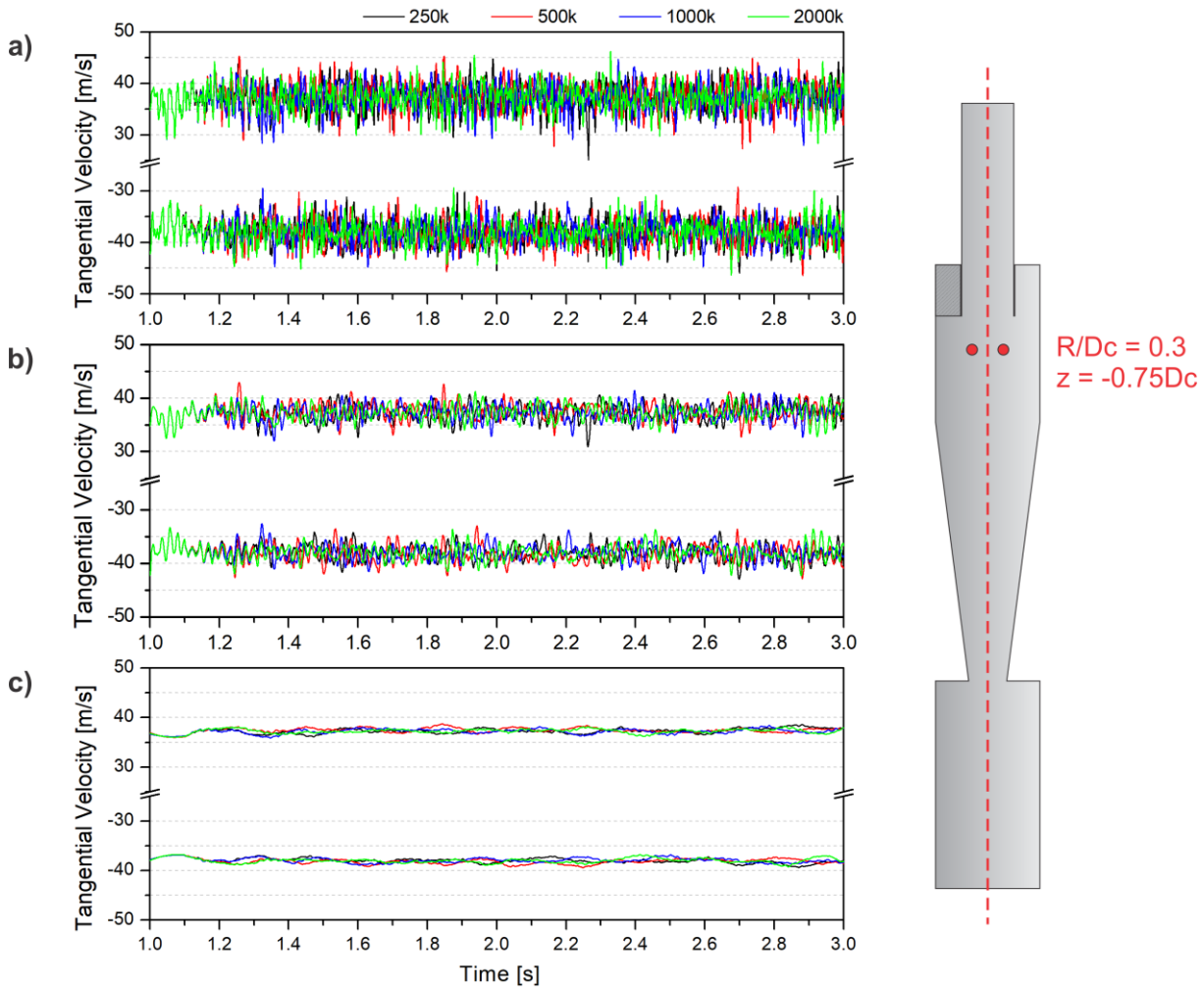


Figure 57. Temporal evolution of tangential velocity in two opposite points at radial position of $R/D_c = 0.3$ and axial distance from the cyclone roof of $z = 0.75 D_c$. Where: (a) Instantaneous values; (b) smoothed values with an interval of 1×10^{-3} ; (c) smoothed values with an interval of 1×10^{-1} .

Despite the observed differences among the fluctuations of instantaneous tangential velocity, a similar intensity is observed for all four cases. This similarity is easier to notice by applying a smoothing function to the instantaneous values. The applied Savitzky-Golay filter method^[90] performs a local polynomial regression around each point, and creates a new, smoothed value for each data point. The Savitzky-Golay filter method performs a local polynomial regression around each point, and creates a new, smoothed value for each data point. This method is superior to adjacent averaging because it tends to preserve features of the data, such as peak height and width, which can be "washed out" by adjacent averaging^[91]. To increase the smoothness of the result, one can increase the number of data points used in each local regression, i.e. the interval of time. For the specific case, two intervals of time are used, e.g. 1×10^{-3} and 1×10^{-1} s. The smoothed temporal evolution of the tangential velocity (Figure 57-b-c) shown that despite the difference on the oscillation, the same magnitude is observed for all cases. The same is observed regarding to the pressure drop, where only a slightly difference

among the cases is observed. For the present configuration, e.g. Stairmand cyclone with $D_s/D_c = 0.5$ and velocity of 20 m/s, a pressure drop around 1,230 Pa has been measured by Hoekstra^[13] for the pure gas. The author identified a slightly reduction of pressure drop with the presence of particles, however the data was not presented. For the numerical results, the pure gas case presented an averaged pressure drop of 1,180 Pa, where the four cases presented a slightly reduced value of around 1,150 Pa (250k: 1,156 Pa; 500k: 1,157 Pa; 1000k: 1147 Pa; 2000k: 1137 Pa), not showing a significant difference among the different rates of parcels.

Once a dust collector bin is considered in the present case, a different approach for the collection efficiency methodology is necessary. The time needed for a particle to touch the bottom of the collector bin would require three to four times longer simulation times, resulting in an unpractical computational cost. To optimize the computational effort needed in the calculations, all particles that enter the dust collector bin (Figure 58, green region) are considered collected and are not further tracked. The particles escape if they are inside the vortex finder and above the cyclone's roof (red region). Hence, the collection efficiency, or grade efficiency, in dependence of particle size x is calculated considering the number of particles that escaped the cyclone and the ones collected in the bin (Figure 58), as expressed in Equation (95).

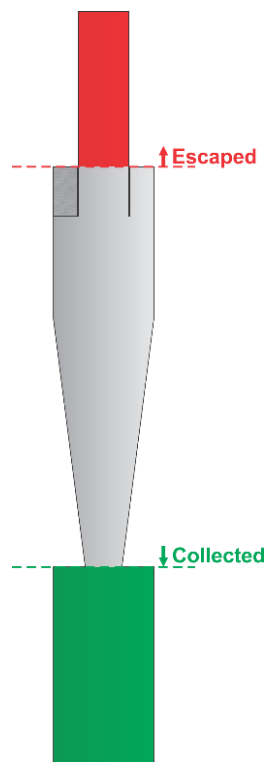


Figure 58. Methodology used to calculate the collection efficiency for a Stairmand cyclone with dust collector bin. The red region represents the region where the particles are considered as escaped whereas the green represents the regions where the particles are collected.

With the methodology for the collection efficiency defined, the further analysis regarding particle tracking are discussed. Figure 59 shows the temporal evolution of the number of parcels inside the cyclone normalized by the rate of parcels. The stabilizing regime corresponds to the beginning of the injection, where the number of parcels increases, until the number of parcels inside the cyclone is constant, e.g. the pseudo-steady state is reached. In this stage, the amount of parcels inject is the same as the number of parcels leaving the cyclone through collection or escape. A different oscillation of the number of parcels is observed among the different parcel rates, however the normalized amount of parcels inside the cyclone is virtually the same. After the gas-solid flow reaches the pseudo-steady state, the averaging of the particle properties as particle concentration and collection efficiency is conducted. Colour graphs of the distribution of averaged particle concentration within the cyclone body are shown in Figure 60. Since the dust rope oscillate spatially, a short averaging time is necessary to preserve its structure. Hence, a short averaging time of 0.1 s is adopted, starting at simulation time 2.2 s for all cases. The dust rope of higher particle concentration is well defined and spaced, following the swirling flow moving downward the cyclone outer wall towards the dust bin. The shape and the same number of revolutions is observed for all cases with minor differences. The differences on the averaged contours of particle concentration were expected, since the mass of a parcel for the case with lower parcel rate (250,000 parcels/s) is eight times smaller than the case with higher parcel rate (2,000,000 parcels/s).

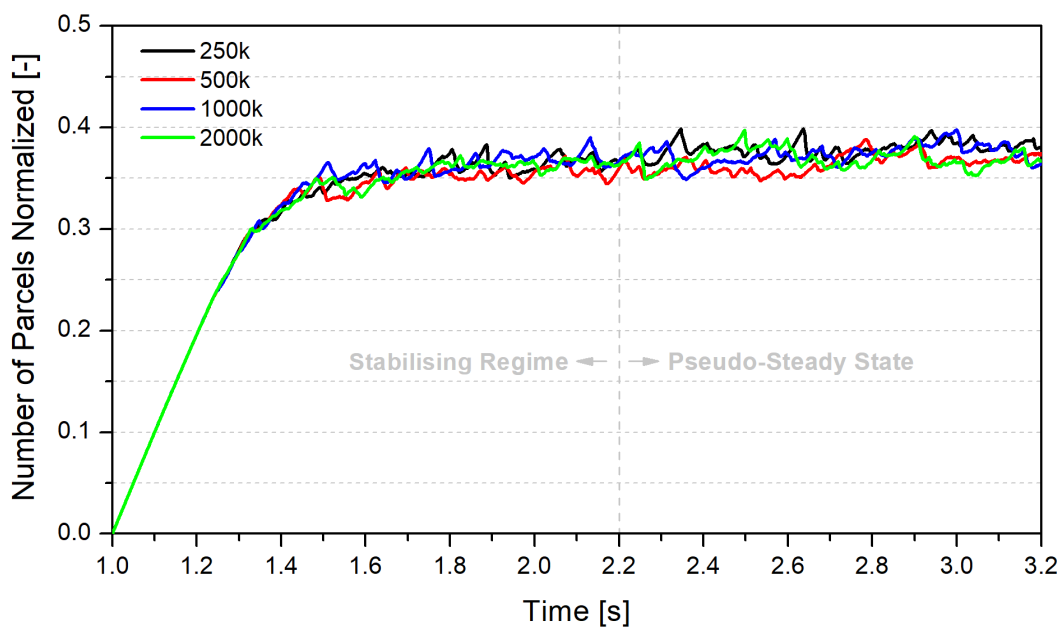


Figure 59. Temporal evolution of the number of parcels inside the cyclone. The values are normalized by the rate of parcels per second. Two-way coupling is considered for all cases.

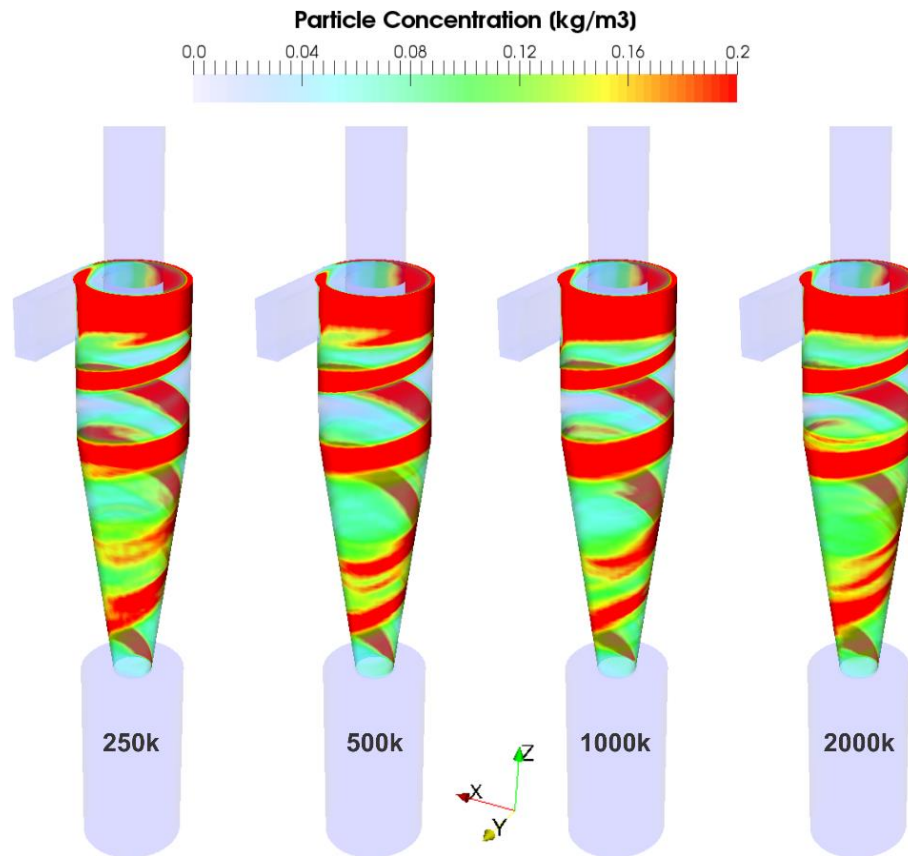


Figure 60. Colour graphs of the distribution of averaged particle concentration within the cyclone body, colour scale shown on top in $[\text{kg}/\text{m}^3]$. The averaging time is fixed at 0.1 s to preserve the rope structure. Two-way coupling is considered for all cases.

To better observe this effect, the temporal evolution of the particle concentration at four different radial distances to the cyclone wall is shown in Figure 61. The temporal evolution of particle concentration (normalized by the inlet value) is observed in four different positions near the cyclone wall, e.g. 0.5, 1, 2 and 3 mm to the wall. The axial distance of the points from the cyclone roof is $z = 0.75 D_c$, corresponding to more or less the middle of the dust rope located under the tangential inlet. This is an interesting region to analyse, because of its high particle concentration. However, even in such a region with high averaged particle concentration, low instantaneous values are observed. Hence, for better visualization, the same smoothing function as used for the temporal evolution of the tangential velocity is applied with an interval of $1 \times 10^{-3} \text{ s}$. As expected, the nearer to the wall, the higher are the values of particle concentration for all cases, due to the centrifugal force pushing the particles to the wall. However, for the case with the lower rate of parcels (250,000 parcels/s), significant higher intensities for the peaks of particle concentration are observed. On the other hand, the case with 500,000 parcels/s presented the peaks with the same magnitude as presented by the cases with higher parcel rates, indicating that this rate of parcels may be sufficient for a more precise prediction.

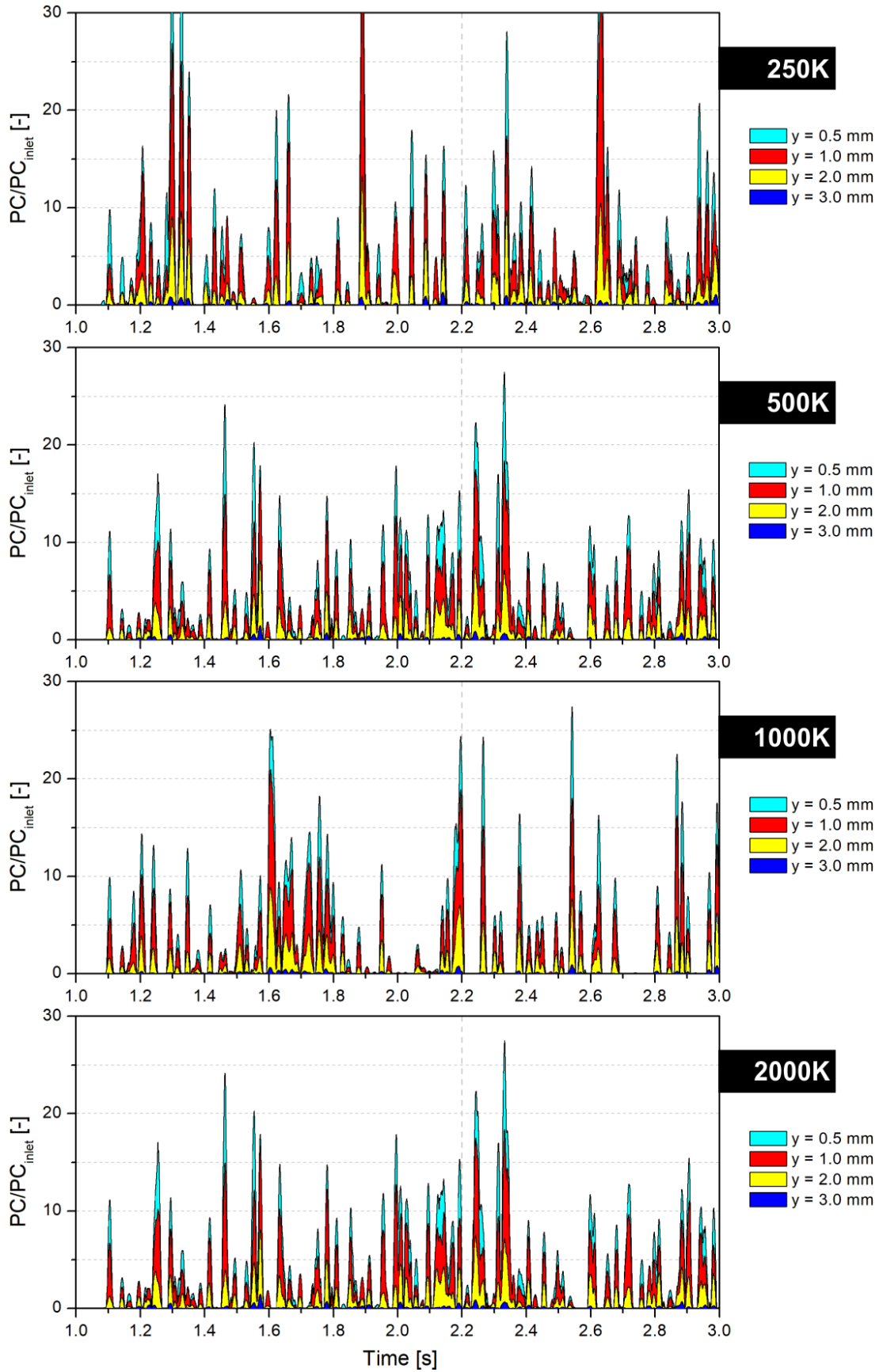


Figure 61. Temporal evolution of the normalized (by the inlet value) particle concentration at four different radial distances to the cyclone wall (0.5, 1, 2 and 3 mm). The axial distance from the cyclone roof $z = 0.75 D_c$ (see Figure 57). Two-way coupling is considered for all cases.

As mentioned, the collection efficiency starts to be calculated only after the gas-solid flow solution reached its pseudo-steady state (see Figure 59). Despite the unsteady nature of the cyclone, if the presented methodology is followed, with around two residence times of simulation time (1 s of simulation time for the present cases) it is possible to have a good convergence of the collection efficiency curve, as shown in Figure 62.

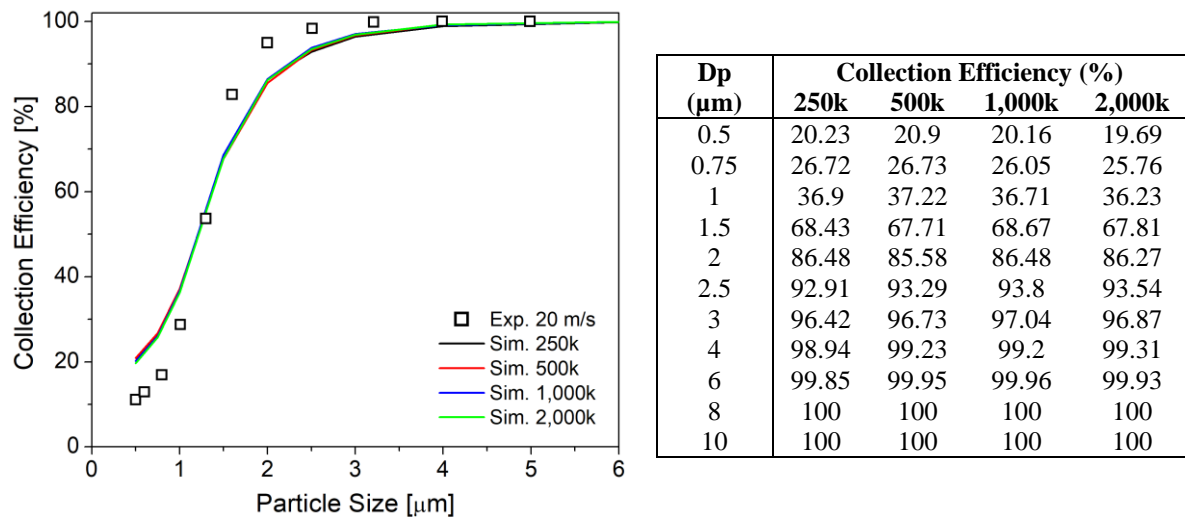


Figure 62. Collection efficiency curves for a Stairmand cyclone with $D_s/D_c = 0.5$ and gas velocity of 20 m/s for four different rates of parcels. Two-way coupling is considered for all cases.

An overall good agreement with the measurements of Hoekstra^[13] is achieved, indicating that the used rate of parcels is adequate for the collection efficiency calculation. As observed, the different rates did not affect significantly the gas flow, presenting some differences only regarding local values of particle concentration. However, for higher mass loading the rate of parcels should be increased to increase the reliability of the statistical sampling. Therefore, for the further evaluation of the collection efficiency calculation in the three geometrical variations of the Stairmand cyclone, the parcels rate of 500,000 parcels/s is used.

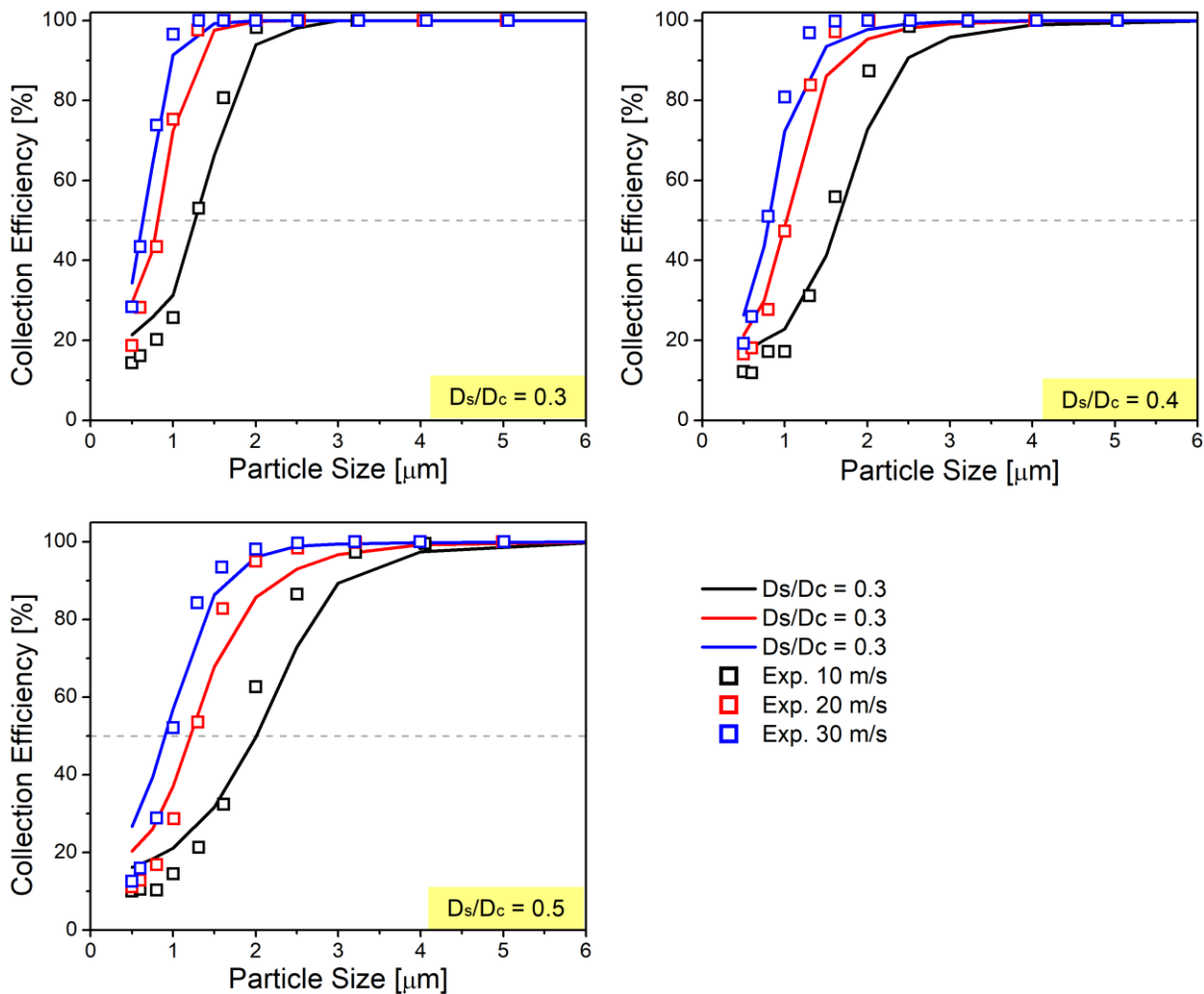


Figure 63. Collection efficiency curves for the three geometrical variations of the Stairmand cyclone with body diameter $D_c = 0.29$ m and three gas velocities (10, 20 and 30 m/s). Two-way coupling is considered for all cases.

Figure 63 shown the collection efficiency curves for the three geometrical variations of the Stairmand cyclone, e.g. $D_s/D_c = 0.3$, 0.4 and 0.5, with inlet velocities of 10, 20 and 30 m/s. As observed for the previous test case, where the reduction of the cone bottom diameter D_1 resulted in a sharper collection efficiency curve, the same trend applies for the reduction of the vortex finder diameter D_s . However, in the present case the increment of collection efficiency is much higher as presented previously. As shown in the optimization study of Sgrott Jr. et al. [14], the bottom cone diameter D_1 does not impact substantially on the collection efficiency of a cyclone in comparison with the vortex finder diameter D_s or the inlet area ($L_e \times b$). By decreasing the diameter of the vortex finder D_s , the tangential velocity is increased due to the constriction of the vortex core, while the reduction of the inlet area increases the inlet velocity, consequently also increasing the tangential velocity. Despite the increment of axial velocity in the upwards direction with the constriction of the vortex finder, the higher intensity of tangential velocity keep the particles in the vicinity of the wall, therefore allowing contact with the inner

vortex. Even if a particle has been directed upwards to the outlet, it is possible that the particle will leave the ascending region due to the tangential velocity pushing it back towards the wall direction. This behaviour is shown in Figure 64, where the normalized tangential and axial velocity profiles for the three geometries are positioned over the size of the vortex finder, represented by a coloured background. Despite small differences between the measurements of collection efficiency made by Hoekstra ^[13] and the present calculations, a good agreement is observed. The trends and shape of the curves with respect to the inlet velocity and vortex finder diameter are well represented. The slightly over-prediction of collection efficiency for the smaller particles may be related to the methodology used for its calculation, once the particles are considered collected if they enter the dust collector bin. Hence, not allowing the particle to be carried upwards with the ascending flow of the inner vortex.

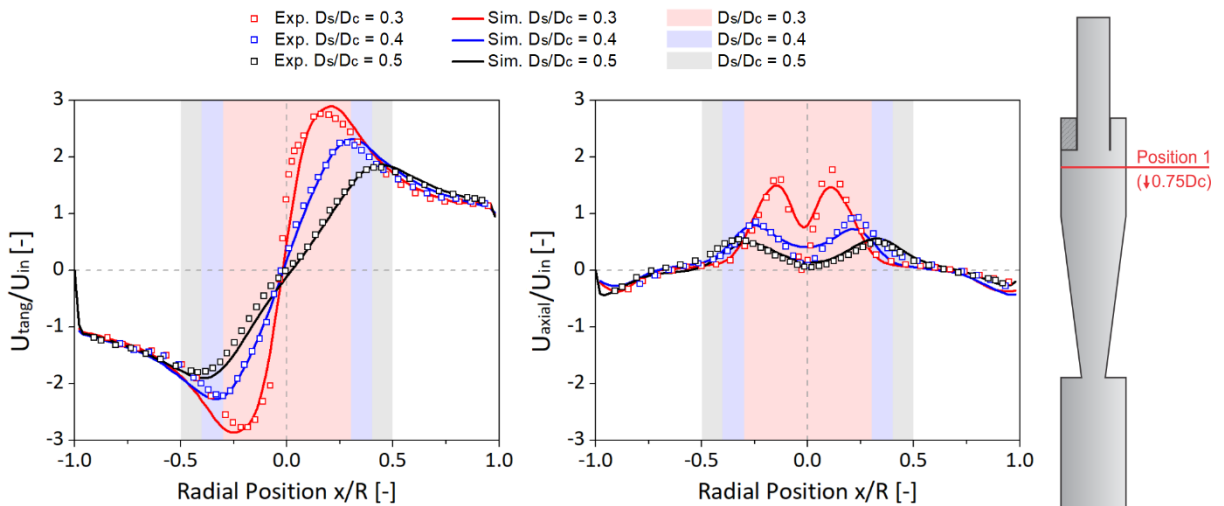


Figure 64. Normalized (by the inlet velocity 16.1 m/s) mean tangential (left) and axial (right) velocity profiles at Position 1 ($z = -0.75D_c$) for the single-phase flow in a high efficiency Stairmand cyclone with $Re_{in} = 280,000$. The symbols represent the experimental data from Hoekstra ^[13] and the lines the numerical results for the three geometric variations. Two-way coupling is considered for all cases.

Finally, based on the presented results regarding the gas flow with the good prediction of velocity profiles and pressure drop with the additionally good representation of the collection efficiency curves, it is possible to affirm that the complete approach proposed for cyclone simulation is appropriate and can be extended for further analysis involving higher mass loading and consequent inter-particle interactions.

4.3 Test Case 3: Hypothetical Study

To investigate the effect of inter-particle collisions and agglomeration on the performance of a cyclone separator, a hypothetical study is proposed ^[92] based on the experimental data obtained by Hoekstra ^[13] for a high efficiency Stairmand cyclone ^[5]. The geometrical dimensions (Geo 1: $D_s/D_c = 0.5$, Figure 42) and the numerical grid (Figure 45) used in the present test case are the same as the ones used in the previous two test cases for a Stairmand cyclone. A superficial gas flow velocity at the inlet U_{in} of 16.1 m/s was prescribed, yielding a Reynolds number of around 280,000 at the body of the cyclone. The continuous phase was treated as air with constant density of 1.1147 kg/m³ and a dynamic viscosity of 18.587 10⁻⁶ N s/m². All the simulations for the flow field are performed with a fixed time-step of 1x10⁻⁵ s, resulting in an average courant number smaller than unity. As described in the previous test cases, the gas flow is calculated until the solution reaches its pseudo-steady state using Large Eddy Simulations (LES) combined with the dynamic Smagorinsky sub-grid model and the PIMPLE algorithm for the velocity-pressure coupling (see Chapter 2.1.2 and 2.1.3). A no-slip boundary condition is applied to the cyclone walls and a pressure outlet is attributed to the exit at the end of the vortex-finder boundary condition, while wall functions are applied to solve the turbulence properties in the near wall region.

The particle phase has a density of 1,000 kg/m³ and a size distribution composed by 12 classes uniformly sampled ranging from 0.5 to 60 μ m. An injection rate of 500,000 parcels/s (around 41,000 parcels of each size class) with velocities sampled from normal distributions with fixed mean and RMS velocities are used. The mean particle velocity at injection is the bulk gas velocity, i.e. 16.1 m/s, in the stream-wise direction and zero in the transverse components, and the RMS value is 3 % of the gas bulk velocity (i.e. 0.483 m/s) for the three velocity components. The three angular velocity components for the particles at the injection were assumed with a mean of zero and standard deviation of 1,000 1/s. A mass loading of 0.1 kg particles / kg air is considered in order to observe its effect on the cyclone's performance. Particle transport is calculated by considering all relevant forces (e.g. particle inertia, drag, gravity, slip-shear force, slip-rotational lift force and torque) and turbulence dispersion. The injection of particles starts when the gas phase reaches its pseudo-steady state. Thereafter, the particles are injected continuously in the system at a rate of 500,000 parcels/s, which eventually yielded in a stabilized situation about 280,000 parcels moving simultaneously in the system. The gas-particle flow calculations imply a sequential calculation of the gas flow field (Eulerian part with fixed time step $\Delta t_E = 1.0 \times 10^{-5}$ s) including coupling terms and the particle phase

(Lagrangian part) with generally considerably smaller time steps being dynamically adapted along the trajectories ^[38]. Only after both fluid and particle phase reach the pseudo-steady state, the calculation of the collection efficiency and the averaging of the results are performed. A short summary of the hypothetical cases configuration is shown in Table 13.

<i>Table 13. Configuration of the Stairmand Cyclone used in the third test case.</i>		
Geometrical Properties		
Cyclone Body Diameter	D_c	0.290 m
Vortex Finder Diameter	D_s	0.145 m
Grid Size	-	~ 830,000 elements
Wall Roughness	$\Delta\gamma$	10°
Gas Properties		
Inlet Velocity	U_{in}	16.1 m/s
Density	ρ_g	1.1147 kg/m ³
Dynamic Viscosity	μ_g	18.587 10^{-6} N s/m ²
Euler. Time-Step	Δt_E	1×10^{-5} s
Particles Properties		
Inlet Velocity	$U_{p,in}$	16.1 m/s
RMS Inlet Velocity	$U_{p,in}'$	3 % (0.483 m/s)
Angular Velocity	σ_ω	1,000 s ⁻¹
Mass Loading	η	0.1 kg particles / kg air
Particle Density	ρ_p	1,000 kg/m ³
Particle Size	D_p	0.5 - 60 μ m
Parcels Rate	-	500,000 parcels/s
Particles/Parcel	-	~ 41,000

To investigate the effects of mass loading, inter-particle collisions and agglomeration on the performance of the cyclones, five study cases are considered:

1. one-way coupling;
2. two-way coupling;
3. four-way coupling;
4. four-way coupling with agglomeration (sphere model);
5. four-way coupling with agglomeration (history model).

The first analysis can be made through the averaged distribution of particle concentration, as shown in Figure 65. The averaged contours were obtained by an averaging the particle concentration during 0.3 s and were started at the simulation time of 2.2 s for all cases. For the one-way coupling calculation, the averaging is not available, once the case was calculated through one single injection to save computational effort. One can observe that when considering only two-way coupling, the dust rope of higher particle concentration is well

defined and spaced, following the swirling flow moving downward the cyclone outer wall towards the dust bin. The same behaviour is not observed in the four-way coupling case, where the dust ropes are moved out in the conical section of the cyclone. This happens because the particles are colliding with each other, resulting in a change of their momentum and trajectory which causes the dispersion of particles out of the initial dense rope regions. Considering the agglomeration models, the dust rope behaviour is partially recovered and its appearance is somewhat between the cases with two and four-way coupling. Due to the decrease in particle number density through agglomeration the inter-particle collision probability also reduces, whereby decreasing the particle dispersion effect observed in the four-way coupling case. This effect is observed in the distribution of inter-particle collision rate, as shown in Figure 66.

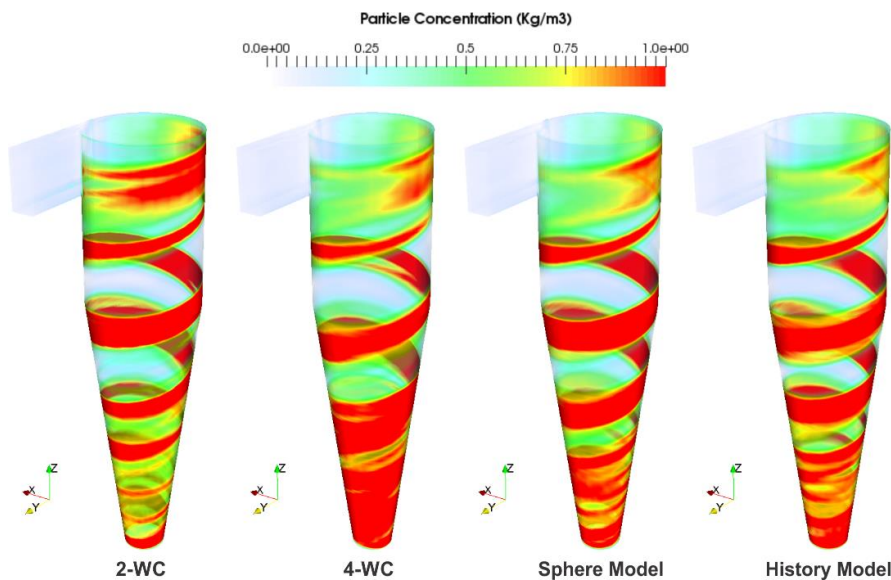


Figure 65. Colour graphs of the distribution of averaged particle concentration within the cyclone body, colour scale shown on top in $[\text{kg}/\text{m}^3]$. The averaging process starts at the simulation time of 2.2 s with a fixed duration of 0.3 s.

When considering agglomeration models, the total inter-particle collision rate in the entire cyclone drops to almost half of the value in four-way coupling ($\sim 99 \times 10^6/\text{s}$ for four-way coupling, $\sim 50 \times 10^6/\text{s}$ for sphere model and $\sim 53 \times 10^6/\text{s}$ for history model), because of the reduction of the particle number density in the control volumes (Figure 66). The cases with agglomeration models show the strongest reduction of inter-particle collision rate in the conical section of the cyclone, which can be related to the higher agglomeration rate found in this region (Figure 67). The values of the mean relative velocity (i.e. between particle classes) are lower in the conical section because in this region the particles already lost momentum due to numerous particle-wall collisions. The reduction of the mean relative velocity between particles reduces the collision probability and at the same time increases the agglomeration probability of the

particle. Another interesting aspect to highlight is the slightly higher inter-particle collision rate obtained for the history model in comparison with the sphere model. Considering the same number of primary particles, an agglomerate created with the history model will yield larger particles in comparison with the sphere model, because of the consideration of porosity. This effect increases naturally the collision cross-section, see Equation (61). Consequently, the history model also presents a higher agglomeration rate than the sphere model.

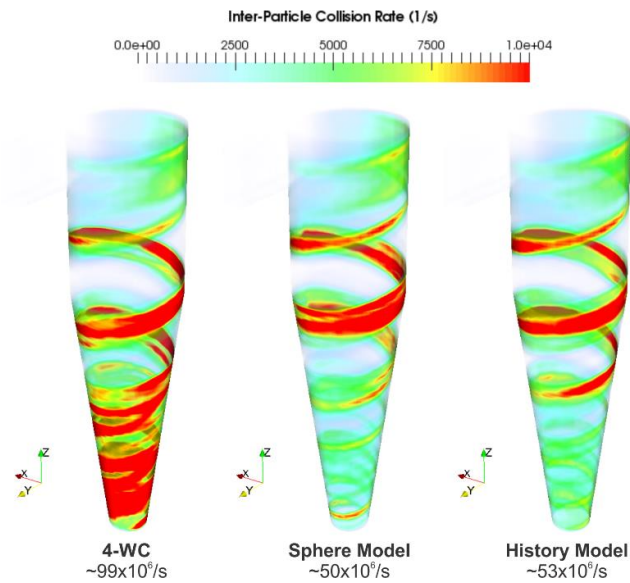


Figure 66. Colour graphs of the distribution of averaged inter-particle collision rate within the cyclone body, colour scale shown on top in [1/s]; the text below the graphs indicates the number of inter-particle collisions. The averaging process starts at the simulation time of 2.2 s with a fixed duration of 0.3 s.

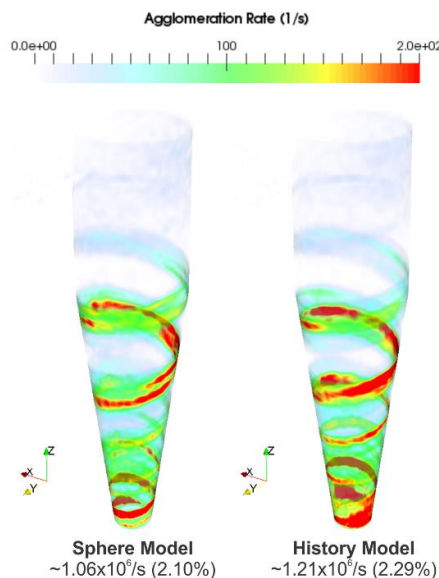


Figure 67. Colour graphs of the distribution of averaged agglomeration rate within the cyclone body, colour scale shown on top in [1/s]; the text below the graphs indicates the number of agglomerations and the agglomeration rate in terms of the total number of collisions. The averaging process starts at the simulation time of 2.2 s with a fixed duration of 0.3 s.

The pressure drop is one of the most important performance parameters in a cyclone and it is directly related to the operational costs of the equipment. Derksen et al ^[33] observed that even for moderate mass-loading of 0.05 and 0.1, the gas flow field changes significantly as a result of the presence of solid particles in the flow (two-way coupling). In strongly swirling flows, the tangential is the most expressive velocity component and is the one that is strongest modified by the presence of particles on the flow, as observed in Figure 68. Inter-particle collisions are naturally not causing directly a momentum loss for the particle-phase, but the wall collision rate is modified if inter-particle collisions are occurring in the vicinity of walls as demonstrated by Sommerfeld and Laín ^[85]. Consequently, momentum from the fluid flow is transferred to the particles for re-acceleration, causing eventually a reduction of the swirl. Hence, the reduced swirl directly reduces the wall friction and therefore the pressure drop. For the case considering only one-way coupling, a pressure drop of 900 Pa is found, being significantly reduced for the two and four-way coupling cases to 840 Pa and 820 Pa, respectively. The cases with agglomeration do not yield significant differences in relation with the case considering four-way coupling (i.e. only inter-particle collisions).

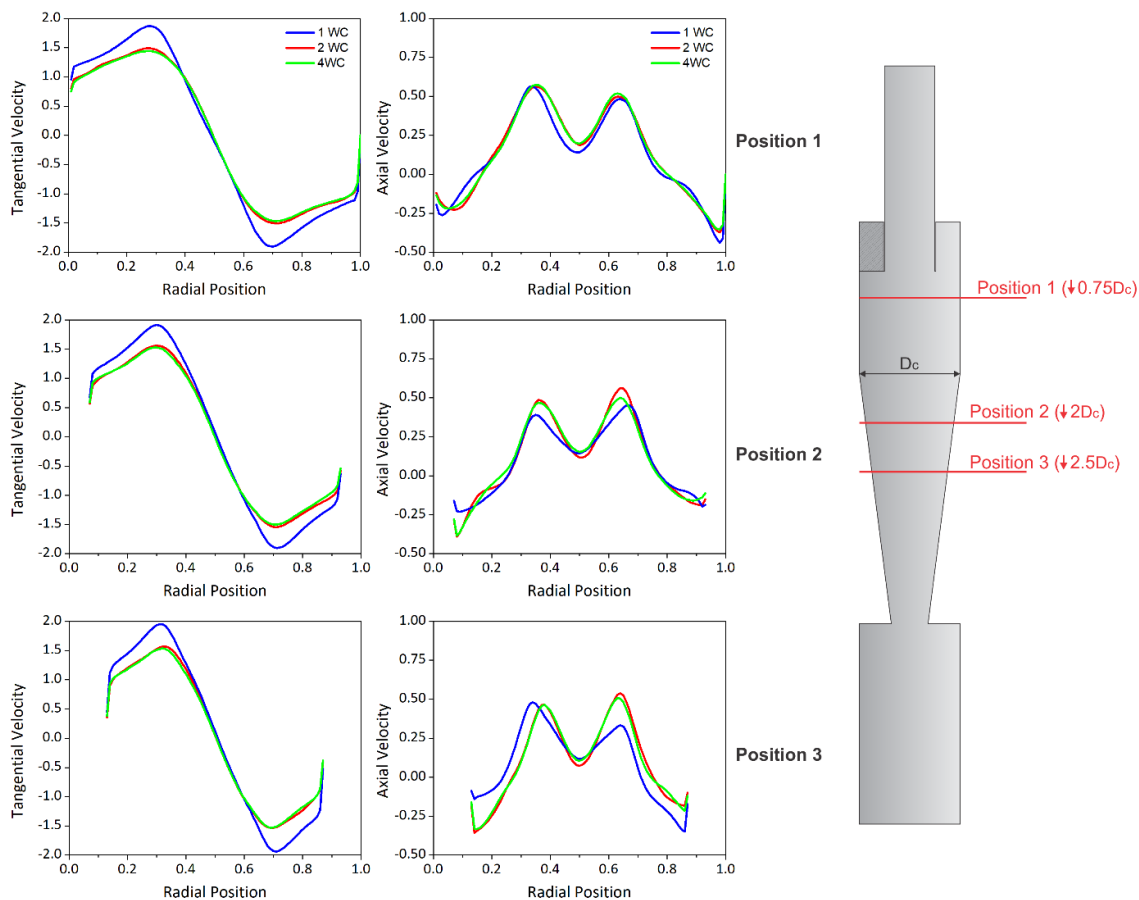


Figure 68. Normalized averaged tangential (left) and axial (right) velocity profiles of the gas phase at three positions in a high efficiency Stairmand cyclone with $Re_{in} = 280,000$, comparing the single-phase flow (1 WC) with two-way coupled (2 WC) and four-way coupled (4 WC) calculations.

The change of swirl and pressure drop magnitude has strong effects on the collection efficiency prediction, as observed in Figure 69. The same approach for the collection efficiency methodology as presented for the previous Stairmand cyclone is applied to the present test case. Thus, all particles that enter the dust collector bin (Figure 58 – page 93, green region) are considered collected and are not further tracked. The particles escape if they are inside the vortex finder and above the cyclone's roof (red region). Once agglomeration is considered in the present case, a problem related to the change of particle size is identified. In the previous cases, the collection efficiency is calculated in dependence of particle size x considering the number of particles that escaped the cyclone and the ones collected in the bin, as expressed in Equation (96). However, as previously discussed in the Chapter 1.1.1.1, one can also calculate the collection efficiency by means of the injected and escaped particles, as shown in Equation (97).

$$\eta = 1 - \frac{N(x)_{escaped}}{N(x)_{escaped} + N(x)_{collected}} \quad (96)$$

$$\eta = 1 - \frac{N(x)_{escaped}}{N(x)_{injected}} \quad (97)$$

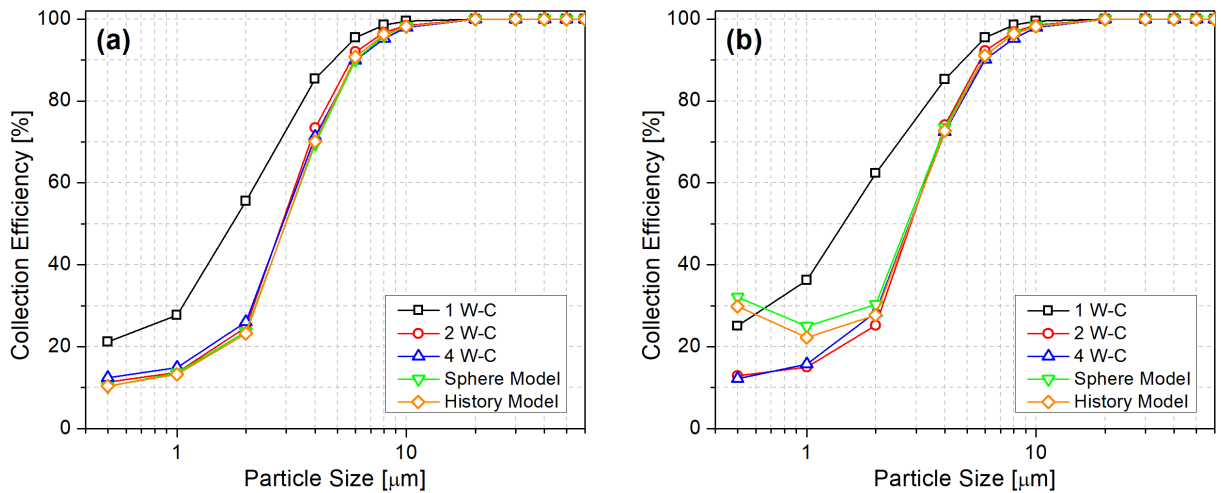


Figure 69. Collection efficiency obtained for all five study cases for particle size classes ranging from 0.5 to 10 μm . (a) collection efficiency calculated with Equation (96); (b) collection efficiency calculated with Equation (97).

As mentioned before, under normal circumstances, both equations should provide the same collection efficiency, as observed for the one-, two- and four-way coupling calculations in Figure 69, where only slightly differences between both approaches are observed. These differences are mainly caused by the short simulation times, once longer times would lessen the

statistical errors. Despite the used methodology only calculates the collection efficiency after the gas-solid suspension reached its pseudo-steady state, there are still particles that present longer residence times in comparison with its counterparts, hence modifying the collection curve. Hence, the rate of escaped by collected (Equation (96)) is preferable, since the collection efficiency is calculated without considering the “accumulated” particles inside the cyclone. However, independent of the approach considered, it is clear that the case considering only one-way coupling overestimates completely the collection efficiency for the smaller particles. The particles receive more momentum from the gas flow and as a consequence of that (i.e. centrifuging effect) remain closer to the wall and are hardly dragged by the inner-vortex towards the vortex finder. On the other hand, two and four-way coupling simulations present very similar results for the collection efficiency for all particle size classes, with the four-way coupling presenting slightly higher values.

By considering agglomeration, the change of size distribution modifies the curves of collection efficiency for the Sphere and History models. By using the Equation (96), one observes that the collection efficiency for the agglomeration models is slightly lower in comparison with the two- and four way-coupling (see Figure 69-a). At first glance, this behaviour seems inconsistent, once the increase in particle size should result in higher collection efficiency values. Nevertheless, when two particles agglomerate, they may increase in size up to the point to not be considered in the same class size anymore. Thus, if this agglomerate is collected, the collection efficiency would be accounted for the class size of the agglomerate and not the one of the primary particle. On the other hand, by considering the escaped and injected particles, i.e. Equation (97), the reduction of smaller particles due to agglomeration in comparison with the injected distribution clearly show the increase of collection efficiency (see Figure 69-b). Here, one can observe a remarkable increase of collection efficiency for the smaller-sized particles (i.e. 0.5 and 1 μm) when considering agglomeration. This is of course associated with the fact that small particles are preferably captured by larger particles or agglomerates and hence separated. This is mainly associated with the stronger adhesion energy of very small particles as seen in Equation (84). Another interesting phenomenon is that for the same particle size (Figure 69-b), the sphere model yields slightly higher collection efficiency than the more realistic history model for all particle size classes. This is resulting from the smaller agglomerate size (volume equivalent sphere) produced by the sphere model and hence the lower aerodynamic drag. With the history model effectively larger porous agglomerates are produced yielding higher aerodynamic drag whereby agglomerates may easier escape through the overflow pipe. This effect is relevant; although the agglomeration rate is slightly lower in

the sphere model (Figure 67). Unfortunately, there is no experimental data in order to validate the results of collection efficiency; however this study is interesting to analyse the possible effects that different approaches have in modelling and simulation of cyclone separators.

4.4 Test Case 4: Cyclone with High Particle Mass Loading

Huang et al.^[12] studied the effect of particle mass loading on the performance of a cyclone separator with body diameter of 0.0723 m, where the collection efficiency and pressure drop were experimentally measured. Because of the high particle mass loading used in the experiments, it is possible to observe the effect of one-, two- and four-way coupling on the cyclone performance. Four-way coupling calculations with agglomeration (sphere and history approach) and agglomerate breakage are also considered. Since the authors used a dust collector bin in the experiments, the same is considered in the numerical geometry and grid, as shown in Figure 70. The used structured mesh was generated using the same methodology as presented in the previous test cases and is formed by around 720,000 hexahedral elements.

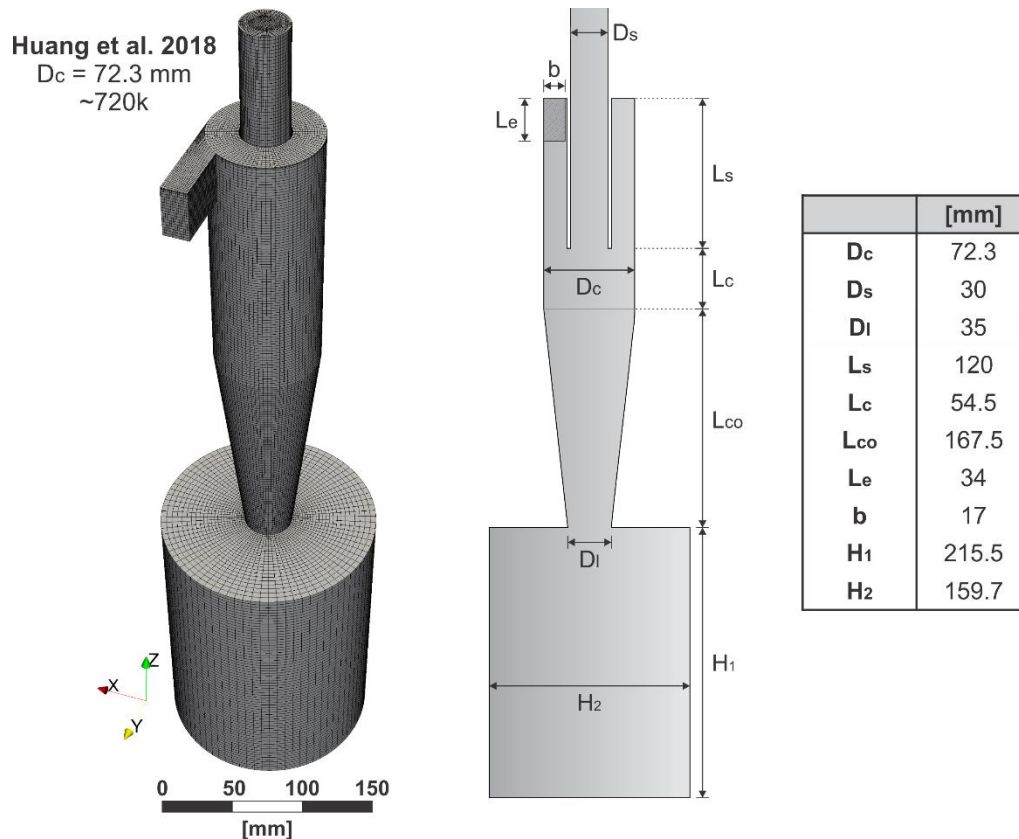


Figure 70. Structured grid and main geometrical relations of the cyclone used in the experiments from Huang et al.^[12]. For the three used geometries, only the bottom cone diameter D_l is modified.

A superficial gas flow velocity at the inlet U_{in} of 15 m/s was prescribed, yielding a Reynolds number of around 72,000 at the body of the cyclone ($Re_{Dc} = \rho_g U_{in} D_c / \mu_g$). The continuous phase was treated as air with constant density of 1.205 kg/m³ and a dynamic viscosity of 18.2 $\cdot 10^{-6}$ N s/m². All the simulations for the flow field are performed with a fixed time-step of $1 \cdot 10^{-5}$ s, resulting in an average courant number smaller than unity. The gas flow

is calculated until the solution reaches its pseudo-steady state using Large Eddy Simulations (LES) combined with the dynamic Smagorinsky sub-grid model and the PIMPLE algorithm for the velocity-pressure coupling (see Chapter 2.1.2 and 2.1.3). A no-slip boundary condition is applied to the cyclone walls and a pressure outlet is attributed to the exit at the end of the vortex-finder boundary condition, while wall functions are applied to solve the turbulence properties in the near wall region.

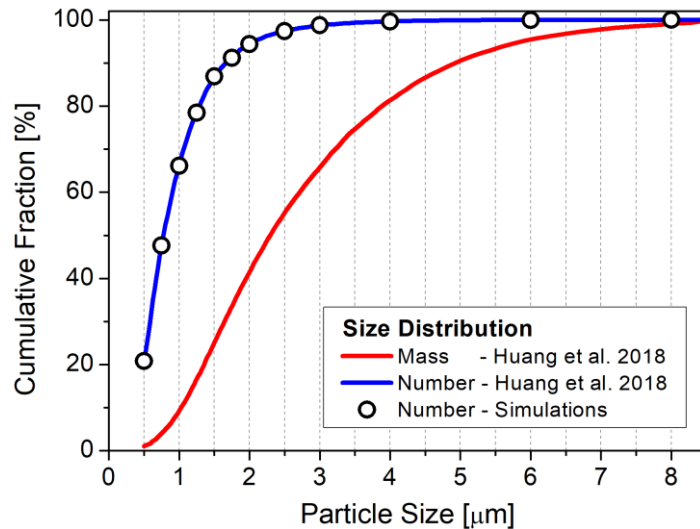


Figure 71. Particle cumulative size distribution used in the experiments of Huang et al.^[12]. Where the lines are the measured curves and the points represent the 12 size classes used in the calculations.

Class	Mean Size (μm)	Cumulative Fraction (%)	Fraction (%)
1	0.50	20.81	20.81
2	0.75	47.60	26.79
3	1.00	66.12	18.53
4	1.25	78.44	12.32
5	1.50	86.88	8.44
6	1.75	91.17	4.29
7	2.00	94.40	3.23
8	2.50	97.38	2.98
9	3.00	98.73	1.35
10	4.00	99.64	0.90
11	6.00	99.97	0.34
12	8.00	100.00	0.03

The particles used by Huang et al.^[12] are Kanto Loan Powders (No. 11, JIZ 8901) with a density of $2,900 \text{ kg/m}^3$. The authors presented a mass based size distribution, which was converted to 12 classes number based ranging from 0.5 to $8 \mu\text{m}$ for the simulations, as shown in Figure 71 and Table 14. An injection rate of 1,000,000 parcels/s (around 182,000 particles per parcel) with velocities sampled from normal distributions with fixed mean and RMS

velocities are used. The mean particle velocity at injection is the bulk gas velocity, i.e. 15 m/s, in the stream-wise direction and zero in the transverse components, and the RMS value is 3 % of the gas bulk velocity (i.e. 0.45 m/s) for the three velocity components. The three angular velocity components for the particles at the injection were assumed with a mean of zero and standard deviation of 1,000 1/s. A mass loading of $0.1153 \text{ kg}_{\text{particles}} / \text{m}^3_{\text{air}}$ is considered in order to observe its effect on the cyclone's performance. Particle transport is calculated by considering all relevant forces (e.g. particle inertia, drag, gravity, slip-shear force, slip-rotational lift force and torque) and turbulence dispersion. A short summary of the present test case configuration is shown in Table 15.

<i>Table 15. Configuration of the Cyclone used in the fourth test case.</i>		
Geometrical Properties		
Cyclone Body Diameter	D_c	0.0723 m
Grid Size	-	~ 720,000 elements
Wall Roughness	$\Delta\gamma$	10°
Gas Properties		
Inlet Velocity	U_{in}	15 m/s
Density	ρ_g	1.205 kg/m^3
Dynamic Viscosity	μ_g	$18.2 \cdot 10^{-6} \text{ N s/m}^2$
Euler. Time-Step	Δt_E	$1 \times 10^{-5} \text{ s}$
Particles Properties		
Inlet Velocity	$U_{p,in}$	15 m/s
RMS Inlet Velocity	$U_{p,in}^?$	3 % (0.45 m/s)
Angular Velocity	σ_ω	$1,000 \text{ s}^{-1}$
Mass Loading	η	$0.1153 \text{ kg}_{\text{particles}} / \text{m}^3_{\text{air}}$
Particle Density	ρ_p	$2,900 \text{ kg/m}^3$
Particle Size	D_p	0.5 - 8 μm (Figure 71)
Parcels Rate	-	1,000,000 parcels/s
Particles/Parcel	-	~182,000

The cyclone is constructed out of stainless steel, which is characterized by a high roughness, therefore being used the rms value of the roughness angle distribution of $\Delta\gamma = 10^\circ$, as used by Laín and Sommerfeld ^[84]. As described in the previous test cases, the injection of particles starts when the gas phase reaches its pseudo-steady state. Thereafter, the particles are injected continuously in the system at a rate of 1,000,000 parcels/s, which eventually yielded in a stabilized situation about 200,000 parcels moving simultaneously in the system. The gas-particle flow calculations imply a sequential calculation of the gas flow field (Eulerian part with fixed time step $\Delta t_E = 1.0 \times 10^{-5} \text{ s}$) including coupling terms and the particle phase (Lagrangian part) with generally considerably smaller time steps being dynamically adapted along the trajectories. Only after both fluid and particle phases reach the pseudo-steady state (around 2 s

of simulation time), the calculation of the collection efficiency and the averaging of the properties are performed.

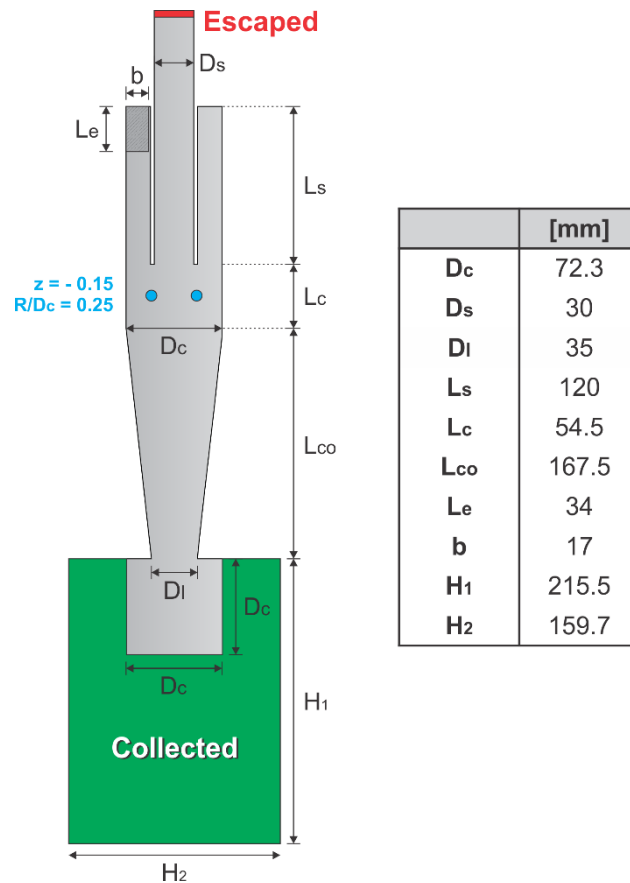


Figure 72. Methodology used to calculate the collection efficiency. The red region represents the region where the particles are considered as escaped whereas the green represents the regions where the particles are collected.

For the present test case, a slightly different methodology for the collection efficiency is applied. During the preliminary tests, an overestimated curve was obtained by assuming that all particles that enter the dust collector bin are considered collected (methodology used in the test cases 2 and 3). Due to the combination of relative low inlet velocity and high mass loading, a high rate of particles captured by the inner-vortex is observed at the upper part of the dust collector bin. To avoid the elevated computational cost to track the particles in the whole dust collector bin, a new methodology is proposed, where an extension of the tracked area is considered. Based on the preliminary tests, there is no significant improvement of the results with a region with diameter and height bigger than the cyclone's body diameter. Hence, these dimensions are used as standard for all calculations, as shown in Figure 72. Thus, all particles that enter the dust collector bin and are outside the extended region (Figure 72, green region) are considered collected and are not further tracked. The particles escape if they are inside the

vortex finder and close to the pipe exit (red region). Hence, the collection efficiency is calculated as in the previous cases (Equation (98)), i.e. by means of the escaped and collected particles. Once agglomeration is also considered, a comparison between the calculation using the agglomerate diameter and the diameter of the original primary particle are compared.

$$\eta = 1 - \frac{N(x)_{escaped}}{N(x)_{escaped} + N(x)_{collected}} \quad (98)$$

Therefore, to investigate the effects of mass loading, inter-particle collisions, agglomeration and agglomerate breakage on the cyclone's performance, seven case configurations are considered:

1. one-way coupling;
2. two-way coupling;
3. four-way coupling;
4. four-way coupling with agglomeration (sphere model);
5. four-way coupling with agglomeration (history model);
6. four-way coupling with agglomeration (sphere model) and agglomerate breakage;
7. four-way coupling with agglomeration (history model) and agglomerate breakage.

4.4.1 One-, Two- and Four-Way Coupling

A first analysis is made comparing the calculations considering one-, two- and four-way coupling, aiming a better understanding of the elementary processes required for a better prediction of the separation process in cyclones. Thus, a classification of dispersed two-phase flows with regard to the importance of interaction mechanisms according to Elgobashi ^[93] is presented. The author distinguishes the regimes between dilute and dense two-phase flows as a function of the particle volume fraction, as follow:

- **One-way coupling:** Dilute system with particle volume fraction smaller than 1×10^{-6} . The gas and particles do not interact with each other.
- **Two-way coupling:** Dilute system with particle volume fraction between 1×10^{-6} and 1×10^{-3} . The gas and particles interact with each other.
- **Four-way coupling:** Dense system with particle volume fraction higher than 1×10^{-3} . Interaction between gas and particles and inter-particles is considered.

Despite the relative high mass loading of $0.1153 \text{ kg}_{\text{particles}} / \text{m}^3_{\text{air}}$, the present case has a particle volume fraction at the inlet of the cyclone of around 4×10^{-5} . Hence, the application of two-way coupling would be sufficient for the specific case. However, as observed in the previous cases, a higher volume fraction of particles is observed in the vicinity of the cylinder and conical sections walls ($> 1 \times 10^{-3}$), where inter-particle interactions may play a major role in the particle tracking. Thus, an analysis based on the differences among the cases considering one-, two- and four-way coupling are presented.

The temporal evolution of the tangential velocity component (see Figure 73) is monitored at two mirrored points at the radial position of $R/D_c = 0.25$ at the axial distance from the cyclone roof of $z = -0.15$ (show in Figure 72). Those points correspond to the extremities of the vortex core diameter, which is usually defined by the radial position of the maximum tangential velocity. The left-hand side of the Figure 73 represents the temporal evolution of the tangential velocity for the gas flow, from the beginning of the simulation up to the beginning of the particle injection. For the gas-particle flow, one-, two- and four-way coupling are tested. The effect of the particle mass-loading on the gas flow is observed for the two- and four-way coupling, where a decrease of tangential velocity intensity occurs with the injection of particles. The gas flow loses momentum to compensate the particle momentum loss due to particle-wall or inter-particle collisions, thus decreasing the swirl, as observed numerically by Derksen et al. ^[33] and experimentally by Hoffmann et al. ^[34]. On the other hand, the one-way coupling calculation did not present a change on the intensity of the swirl, once the gas flow and particles do not interact with each other.

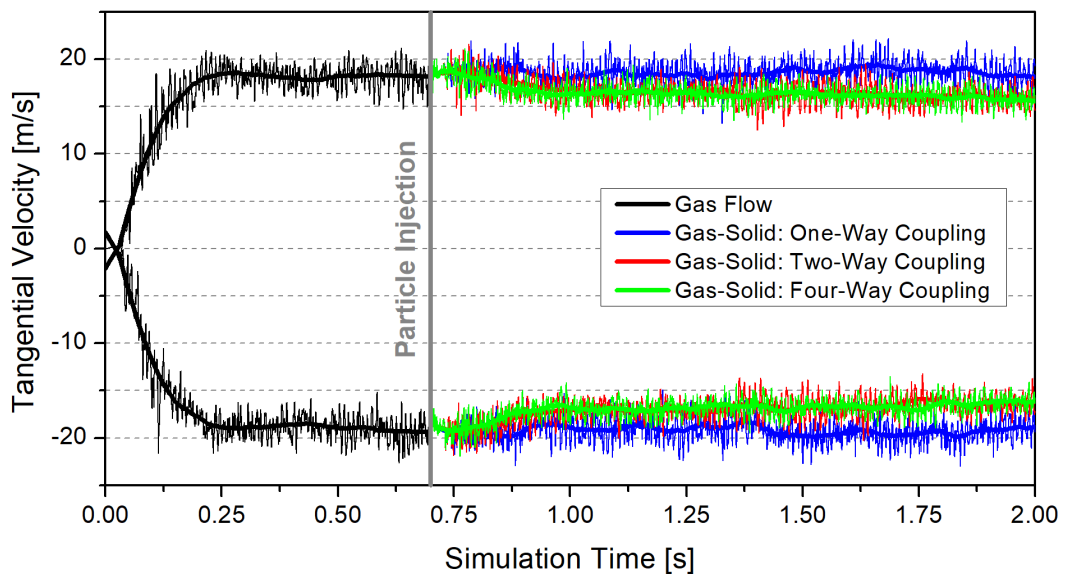


Figure 73. Temporal evolution of the gas tangential velocity component at mirrored points at the radial position of $R/D_c = 0.25$ and axial distance from the cyclone roof of $z = -0.15$.

Unfortunately, Huang et al. ^[12] did not measured velocity profiles for the present cyclone, hence a direct comparison between the experiments and numerical calculations is not possible. However, a short analysis based on the pressure drop comparison is available. The authors obtained a pressured drop of around 610 Pa by measuring the difference between the static pressure at the inlet and exit pipe without particles in the system. Since the specific location of the measurements was not informed, the numerical measurements of static pressure were performed at half height of the inlet and outlet pipe. Therefore, the numerical calculations presented a pressure drop of around 630 Pa for the gas phase flow, as well as for the one-way coupling case, presenting a good agreement with the experimental data. For the two- and four way coupling cases, a pressure drop around 575 and 560 Pa was calculated respectively, indicating that the gas loss of swirl caused by the particles affected the pressure drop.

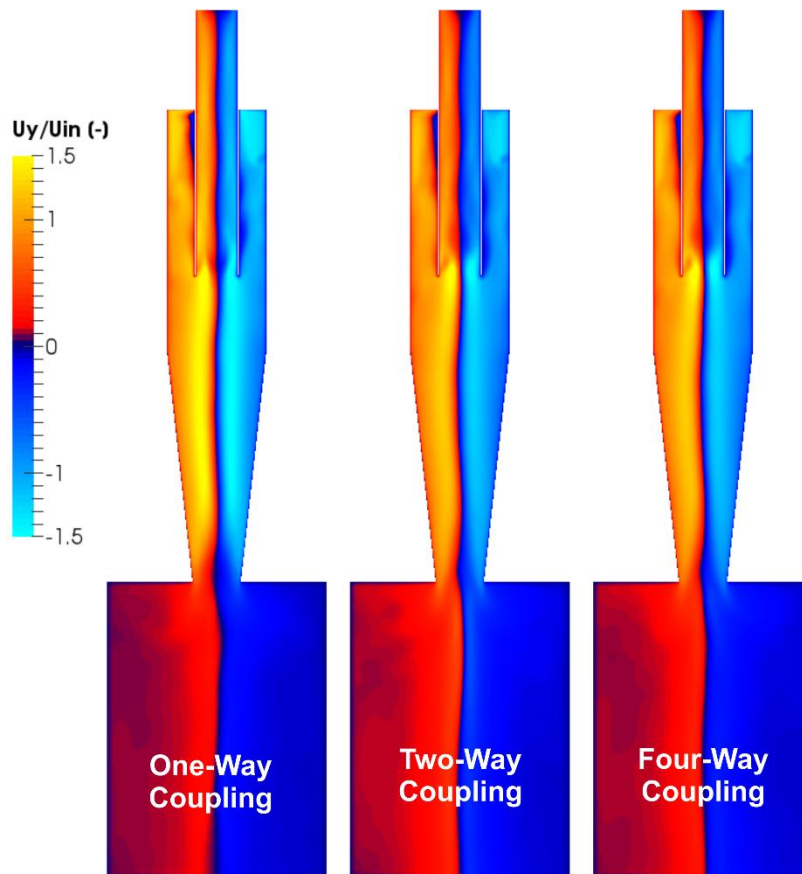


Figure 74. Colour graphs of the averaged tangential velocity normalized by the inlet value (15 m/s) at a cross-section located at the centre of the cyclone. Averaged values between 2 and 2.5 s of simulation time.

Based on the higher tangential velocity and consequently higher swirl intensity (see Figure 74), one would conclude that the one-way coupling case would present a higher collection efficiency in comparison with the two- and four-way coupling cases. With a higher

centrifugal force acting on the particles, it is expected that the particles stay in the vicinity of the wall. Hence, avoiding contact with the inner vortex and consequently increasing the collection efficiency, as observed in the previous test cases and the literature. However, due to a combination of higher mass loading and low inlet velocity, a different scenario is observed for the present study case, as shown in Figure 75.

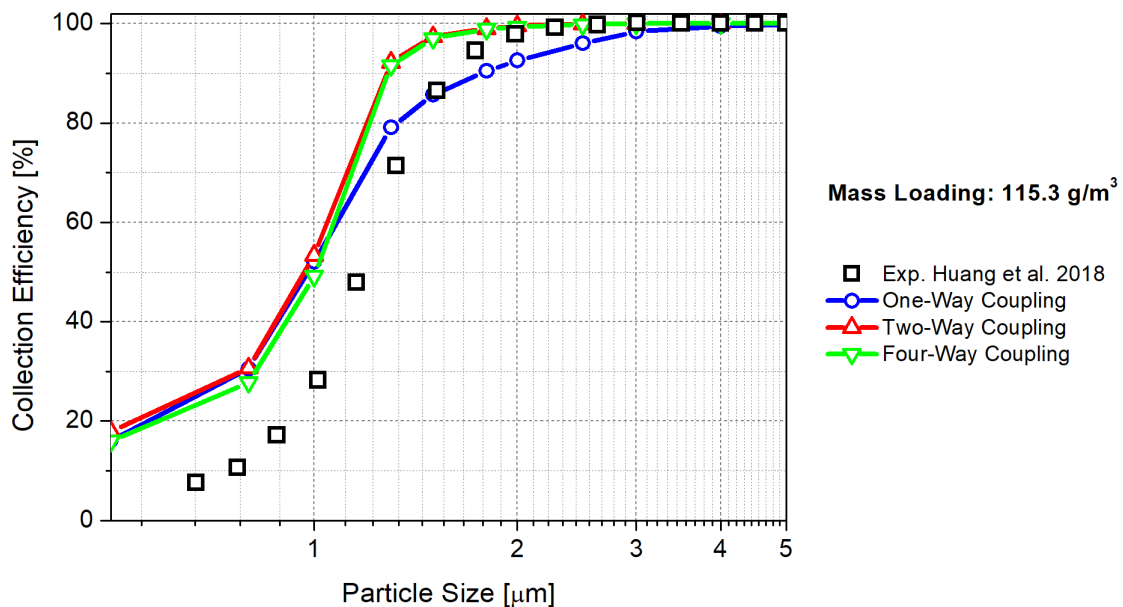


Figure 75. Comparison of the measured collection efficiency (symbols) and the numerical results (lines) for the one-, two- and four-way coupling cases. The collection efficiency is calculated during 1 s between the simulation times of 2 and 3 s.

For the smaller size classes, a similar collection efficiency is observed for all three simulation conditions. The four-way coupling presents slightly lower values due to the inter-particle collisions, where particles may be conducted away from the vicinity of the wall. This effect is less observable for bigger particles, once they are more inertial and are quickly redirected to the near wall region. Although the two- and four-way coupling calculations present an overestimation of the collection efficiency for the smaller particles in comparison with the measurements of Huang et al. [12], the sigmoid-shape of the curve follows the experimental data. The same is not observed for the one-way coupling case, where the inclination of the curve is different and an underestimation of the collection efficiency is observed for particles between 1 and 3 μm . The cause of this underestimation of collection efficiency values may be explained by observing the averaged particle concentration, as shown in Figure 76. A normalized isosurface is created with values of averaged particle concentration higher than 0.1 ($\text{PC}/\text{PC}_{\text{in}} > 0.1$), hence allowing the visualisation of its three-dimensional structure. The averaged particle concentration was obtained by an averaging the particle concentration during 0.5 s and were

started at the simulation time of 2 s for all cases. A short circuit is noticeable in all three cases, where particles leave the vicinity of the cylinder wall and are dragged by the inner vortex to the vortex finder. Between the two- and four-way coupling cases, a slightly elevated concentration is observed on the last, probably due to the inter-particle collisions directing particles away from the wall vicinity. The same pattern is observed at the bottom of the conical section, where once again the four-way coupling present a higher particle concentration at the centre in comparison with the two-way coupling. On the other hand, a completely different particle concentration pattern is obtained for the one-way coupling calculation, where a higher and wider intensity is observed in all measured regions of the cyclone, as shown in Figure 77.

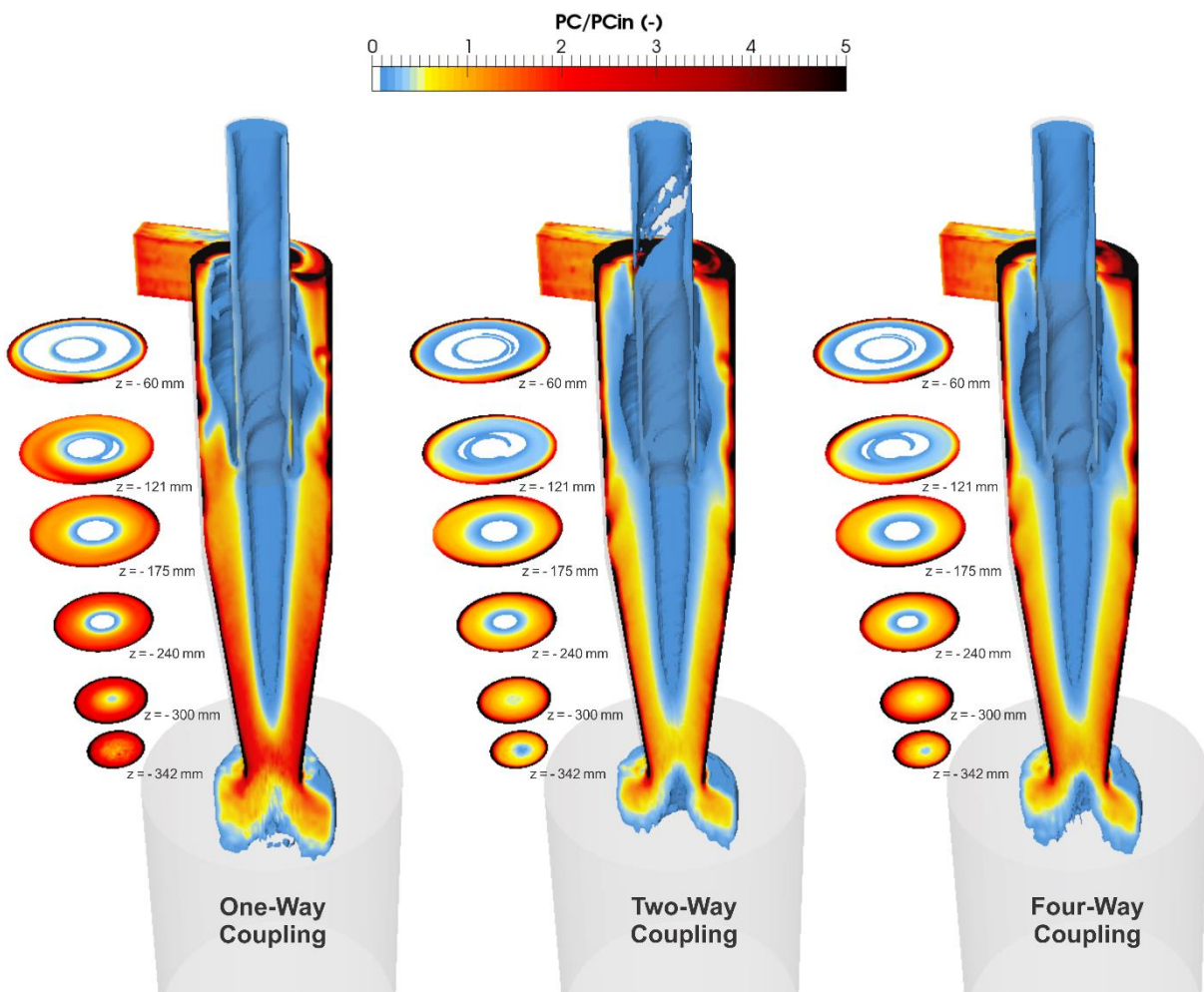


Figure 76. Half cross-section of the averaged particle concentration normalized by the inlet value ($PC_{in} = 115.3 \text{ g/m}^3$). To represent it three-dimensionally, the isosurface of particle concentration is generated with values higher than $PC/PC_{in} > 0.1$. The averaging process starts at the simulation time of 2 s with a fixed duration of 0.5 s.

The higher concentration closer to the “mouth” of the vortex finder ($z = -121 \text{ mm}$) presented by the one-way coupling case is the main reason for the underestimation of collection efficiency. Thus, the particles are easily dragged by the inner-vortex. Due to the gas-particle

interaction, the two- and four-way coupling calculations are changing the structure of the flow, creating a constriction for the gas flow in the cylindrical section around the vortex finder ($z < L_S$). Hence, a higher concentration of particles in the vicinity of the wall is observed in comparison with the one-way coupling case. An overall higher particle concentration for the one-way coupling case at the central regions of the cyclone is observed for the six profiles shown in Figure 77.

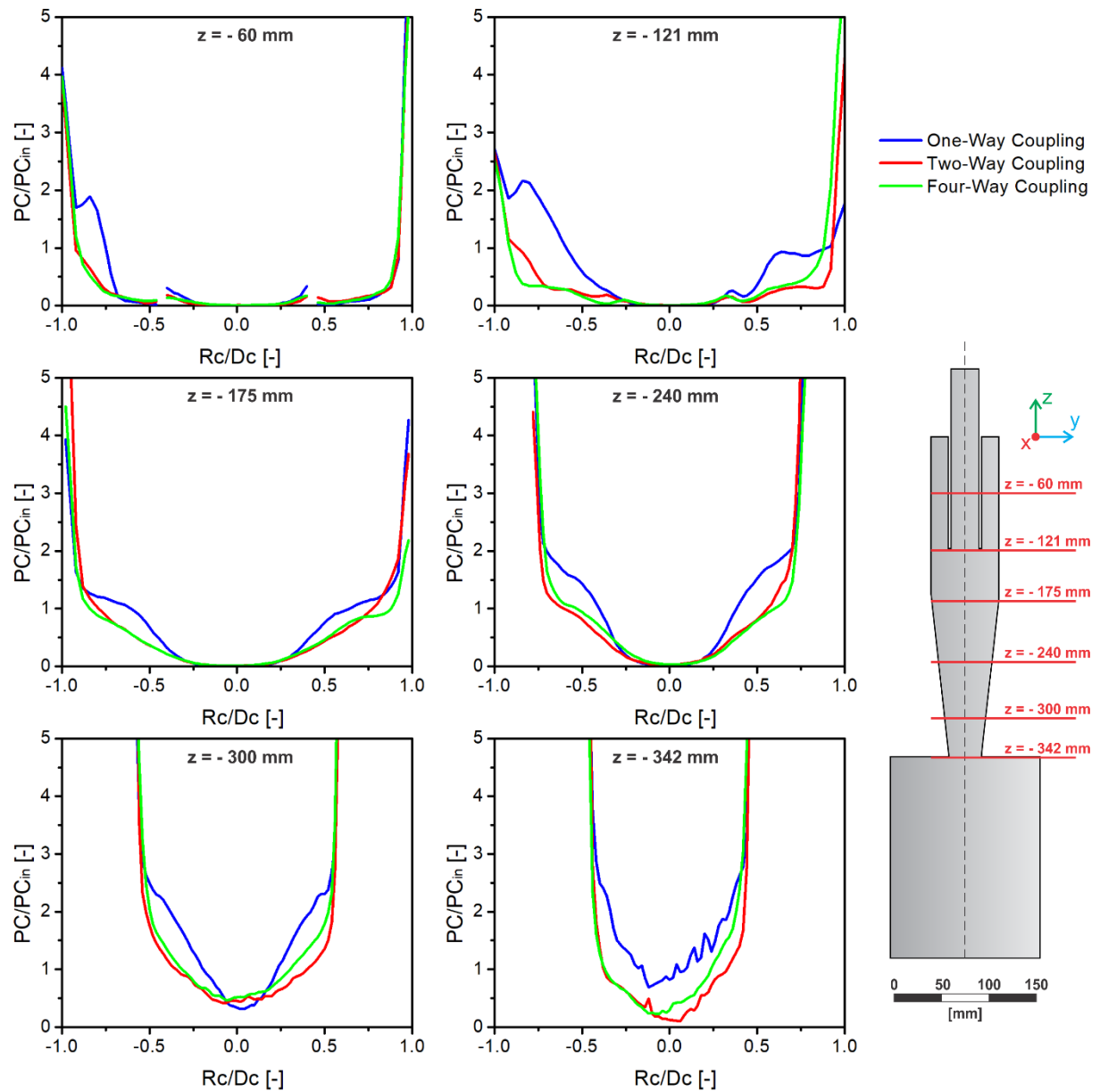


Figure 77. Profiles of averaged particle concentration normalized by the inlet value (115.3 g/m^3) at six axial distances from the top of the cyclone for one-, two- and four-way coupling cases. The averaging process starts at the simulation time of 2 s with a fixed duration of 0.5 s.

Another interesting analysis is done with respect to the averaged particle size distribution in the cyclone (Figure 78), where four different regions are measured: the inlet corresponding

to the injected distribution; the collected and escaped size distributions; and the current size distribution of all particles inside the cyclone. Overall, a similar pattern is observed for all three cases, being the present analysis more interesting when the agglomeration and agglomerate breakage are considered. Generally, the size distribution of the current particles inside the cyclone follows the distribution of the injection with minor differences due to higher/lower particle residence times. On the other hand, the size distribution of the escaped particles is remarkably shifted to the left, i.e. higher ratio for the smaller particles, while the size distribution of the collected particles is slightly shifted to the right, indicating that bigger particles are easily collected.

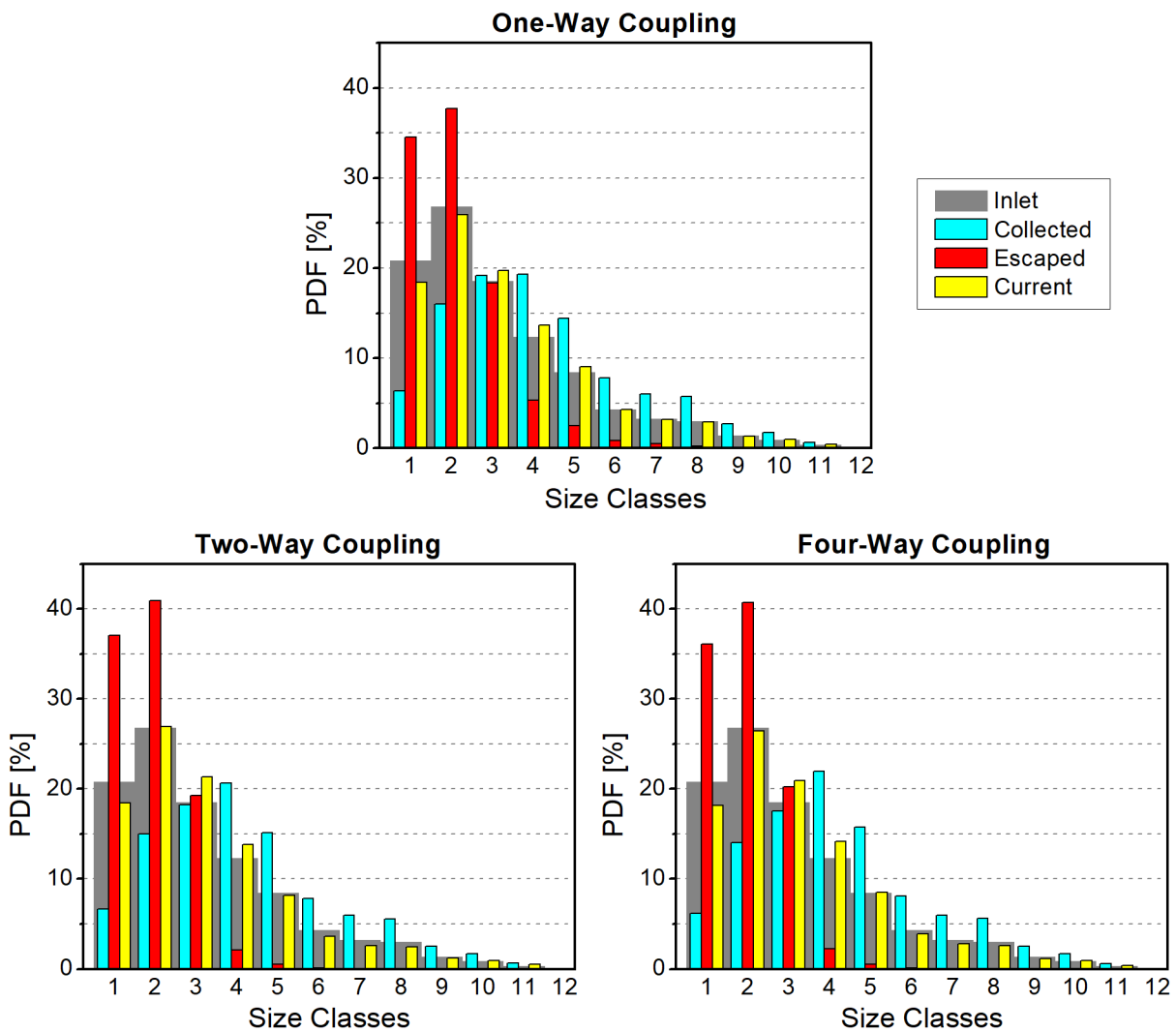


Figure 78. Averaged particle size distribution (number based) for the one-, two- and four-way coupling cases. The grey bars represent the distribution at injection, the cyan the collected, the red the escaped and the yellow the current distribution inside the cyclone. The averaged values are calculated during 1 s between the simulation times of 2 and 3 s.

The ratio of current particles corresponding to the smaller size class (Class 1: $0.5 \mu\text{m}$) presents a lower value in comparison with the injected distribution, indicating that this size class has a smaller residence time. This behaviour indicates that this size class may be experiencing more often a short circuit and leaving the system prematurely. When analysing the size distribution of the escaped particles, it is noticeable that the two- and four way coupling present higher rates for the smaller particles in comparison with the one-way coupling. On the other hand, the one-way coupling case presents a higher ratio of escaped particles for the intermediate class sizes (Classes 4 - 7: $1.25 - 2 \mu\text{m}$), thus explaining the underestimation of collection efficiency obtained for these size classes.

4.4.2 Effect of Agglomeration and Agglomerate Breakage

When considering agglomeration and agglomerate breakage, a similar behaviour regarding the fluid flow is observed in comparison with the four-way coupling, where a pressure drop of the same magnitude is determined, e.g. around 560 Pa . As shown previously for the one-, two- and four-way coupling, the same isosurface with values of averaged particle concentration higher than 0.1 ($PC/PC_{in} > 0.1$) is presented in Figure 79.

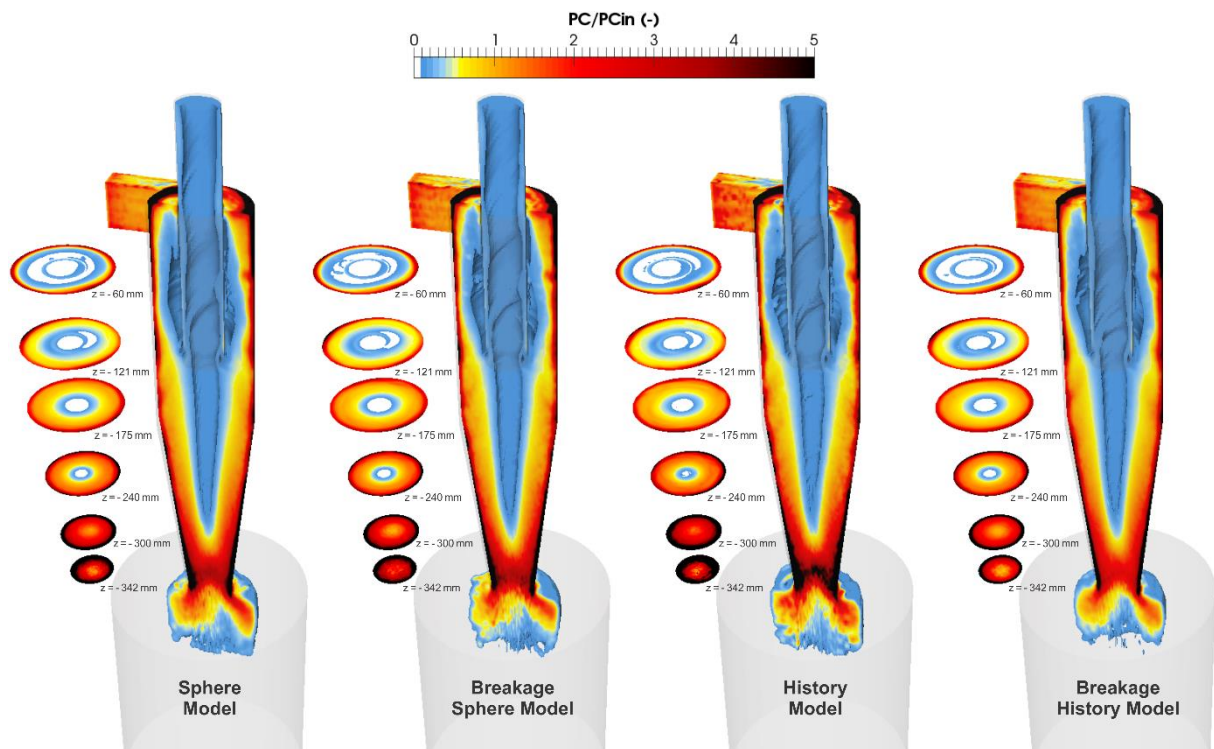


Figure 79. Half cross-section of the averaged particle concentration normalized by the inlet value ($PC_{in} = 115.3 \text{ g/m}^3$). To represent it three-dimensionally, the isosurface of particle concentration is generated with values higher than $PC/PC_{in} > 0.1$. The averaging process starts at the simulation time of 2 s with a fixed duration of 0.5 s .

As observed for the previous cases, a short circuit is also noticeable in all four cases considering agglomeration and agglomerate breakage, where particles are dragged from the outer to the inner vortex in the cylindrical section. A higher averaged particle concentration dislocated towards the centre of the cyclone is observed in comparison with the four-way coupling case. This pattern is easier to observe in Figure 80, where the profiles of averaged particle concentration at six axial distances from the cyclone top are presented. Therefore, comparative to the four-way coupling case, a higher profile of particle concentration is observed downstream of the vortex finder ($z > -121$ mm) for all cases considering agglomeration.

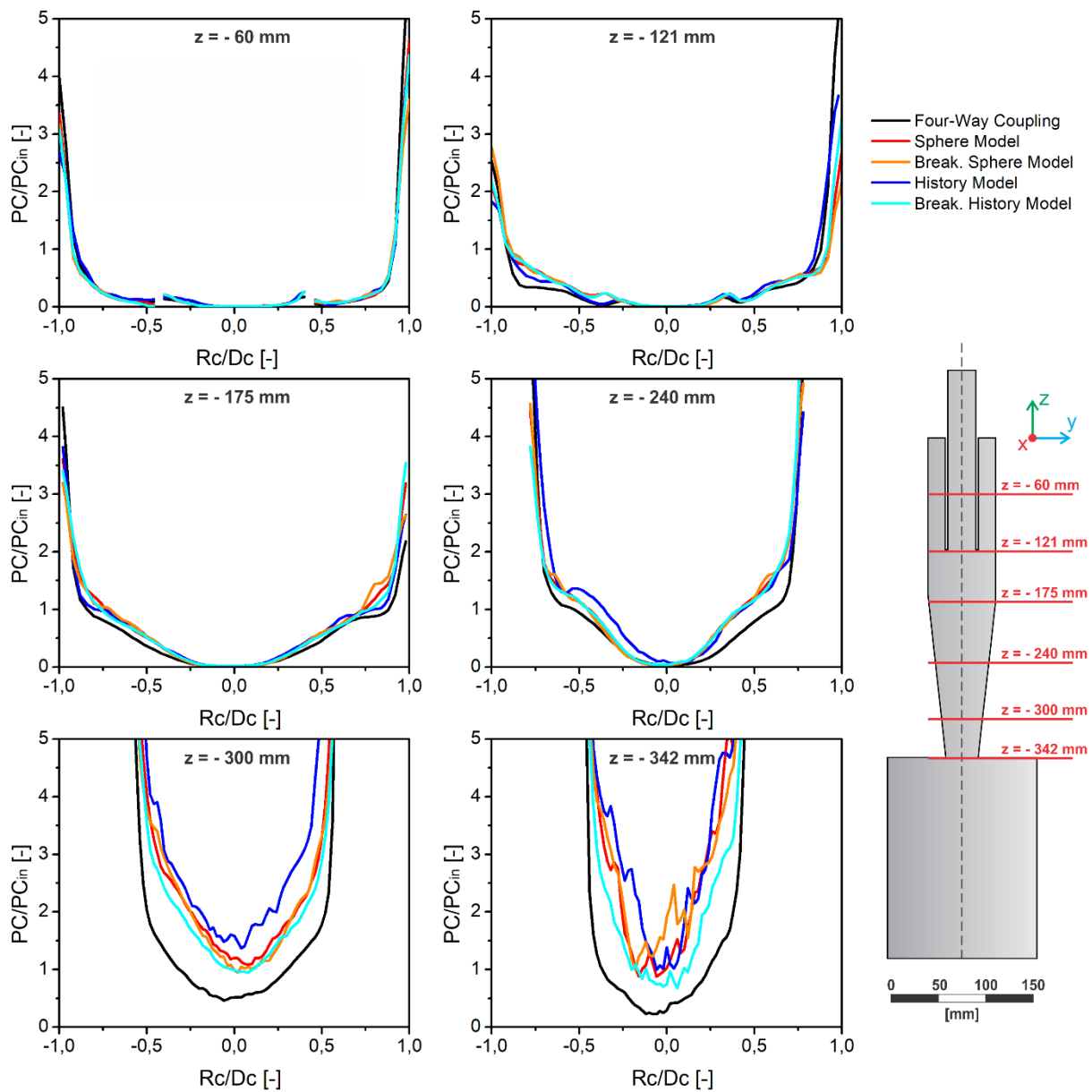


Figure 80. Profiles of averaged particle concentration normalized by the inlet value (115.3 g/m^3) at six axial distances from the top of the cyclone for the four-way coupling, agglomeration and agglomerate breakage cases. The averaging process starts at the simulation time of 2 s with a fixed duration of 0.5 s.

The higher values of averaged particle concentration observed at the conical section may be attributed to the inter-particle collisions, where a higher inter-particle collision frequency is observed for the agglomeration and agglomerate breakage cases, as shown in Figure 82. This behaviour contradicts the observed on the previous test case, where the four-way coupling presented higher values of inter-particle collision frequency in comparison with the agglomeration ones. However, in the previous case an uniform and larger particle size distribution was used (particles up to $60\ \mu\text{m}$), where smaller particles are more likely to stick to larger collector particles, hence reducing the number of particles in the numerical parcel. Consequently, the increase in size was not able to compensate the decrease in population, resulting in a decrease of collision probability. On the other hand, for the current cases, a particle size distribution composed by a narrow range of small particles is applied, presenting a significant increase in size without a huge impact on the number of particles per parcel, as observed previously.

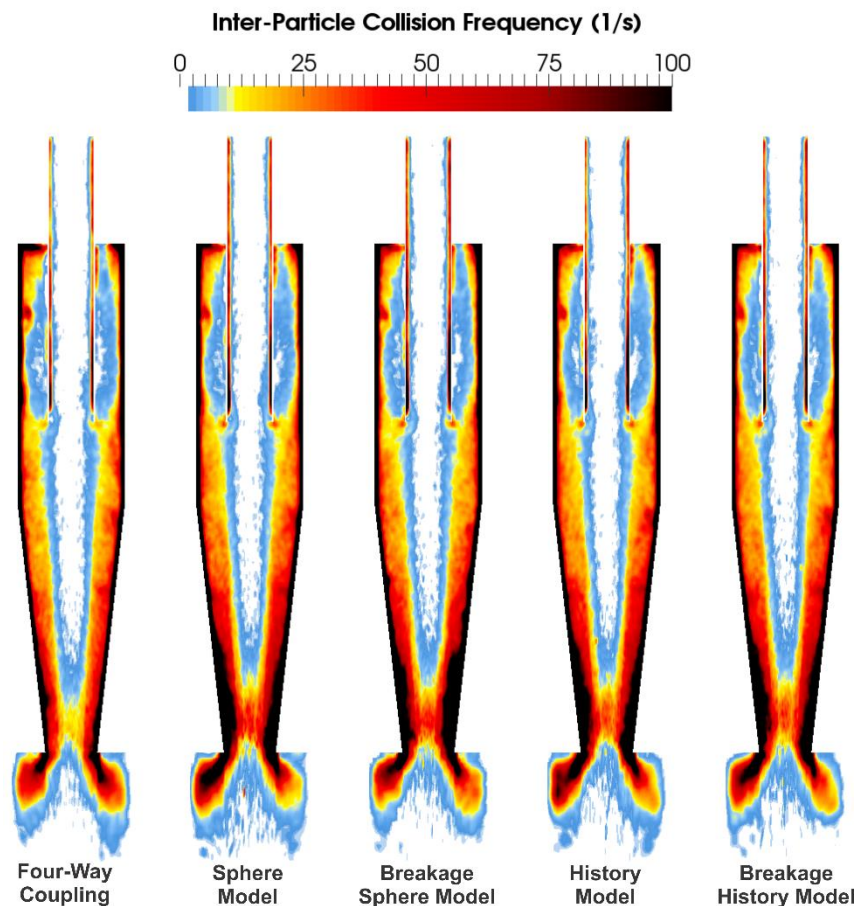


Figure 81. Cross-section of the distribution of averaged inter-particle collision frequency, colour scale shown on top in $[1/\text{s}]$ is based on parcel numbers; $\sim 182,000$ particles/parcel. The averaging process starts at the simulation time of 2 s with a fixed duration of 0.5 s.

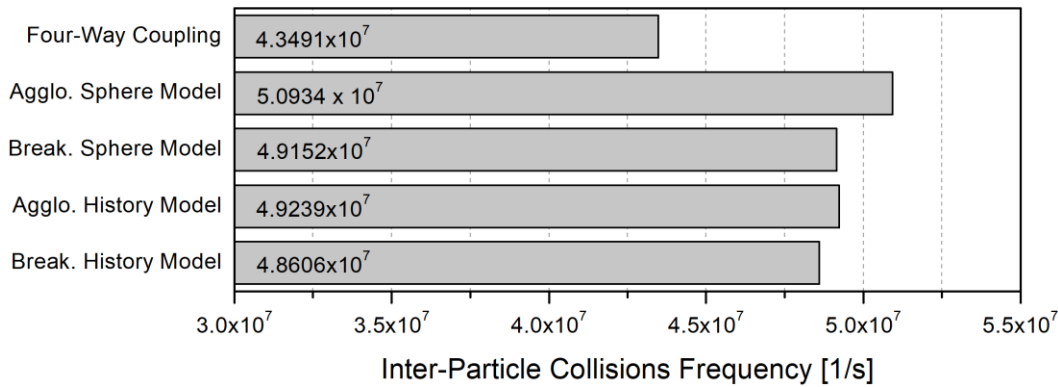


Figure 82. Frequency of averaged inter-particle collisions. Based on parcel numbers; $\sim 182,000$ particles/parcel. The averaging process starts at the simulation time of 2 s with a fixed duration of 0.5 s.

By analysing the absolute values of inter-particle collision frequency (see Figure 82), one can observe that the sphere model presents a higher value in comparison with the history model. Despite its larger size, the porous agglomerate created by the history model yields a higher aerodynamic drag in comparison with the solid agglomerates produced by the sphere model. This difference plays a major role in the overall inter-particle collision frequency, once the larger and porous agglomerate may be easier dragged by the inner vortex and directed towards the centre of the cyclone, where lower particle population is observed. This behaviour is noticeable in the profiles of averaged particle concentration (see Figure 80) at the axial distances of $z = -240$ and -300 mm, where the history model presents the higher particle concentration at the central region of the cyclone. For both agglomeration models, a reduction in the inter-particle collision frequency is observed when the breakage is considered, once the size of the agglomerate is reduced, i.e. the cross-section area of the collision probability is consequently reduced. As expected, the higher agglomeration frequency is observed in the same regions where inter-particle collision frequency is also high, as shown in Figure 83.

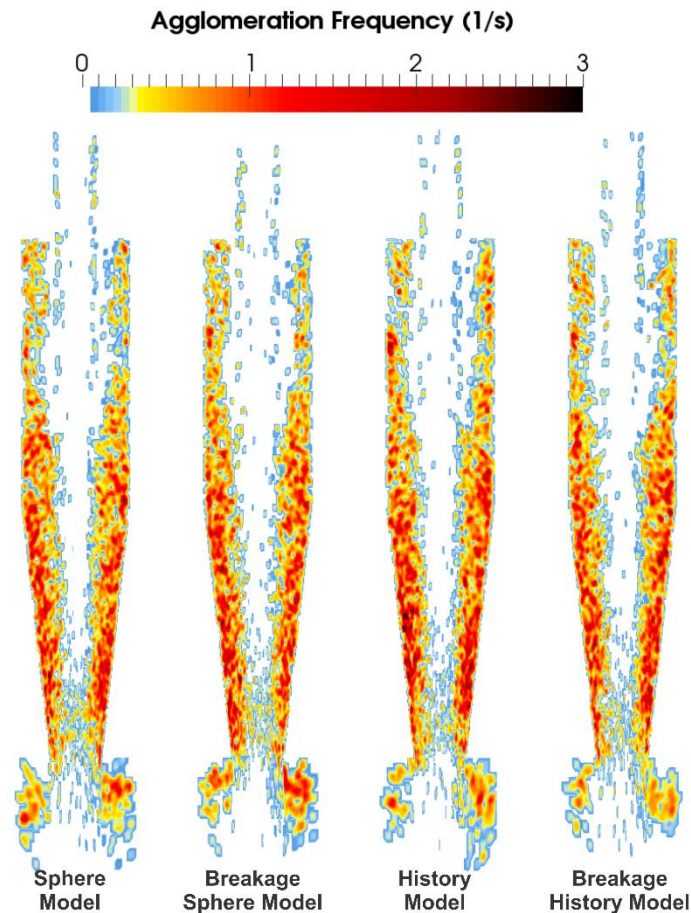


Figure 83. Cross-section of the distribution of averaged agglomeration frequency, colour scale shown on top in [1/s] is based on parcel numbers; $\sim 182,000$ particles/parcel. The averaging process starts at the simulation time of 2 s with a fixed duration of 0.5 s.

When analysing the absolute values of agglomeration frequency (see Figure 84), differences among the agglomeration models appear. The sphere model presents a lower rate of agglomeration when comparing with its agglomerate breakage version. Once the sphere model does not increase substantially the particle size, the increment of particles per parcel created by a breakage increases the collision probability, hence directly increasing the inter-particle collision and agglomeration frequencies. On the other hand, the larger porous agglomerates created by the history model presents the opposite behaviour, where the agglomerate size plays a bigger role in comparison with the number of particles per parcel. Hence, when agglomerate breakage is considered using the history model, a lower agglomeration frequency is observed.

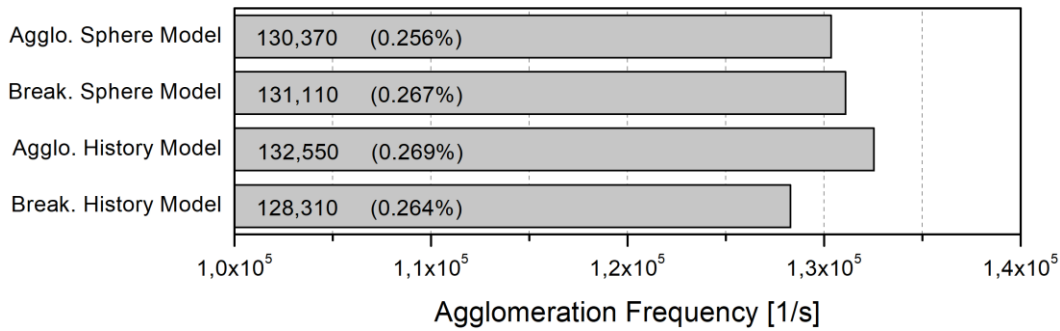


Figure 84. Frequency of averaged agglomerate rate. Based on parcel numbers; $\sim 182,000$ particles/parcel. The percentage indicates the rate of agglomerate per inter-particle collisions. The averaging process starts at the simulation time of 2 s with a fixed duration of 0.5 s.

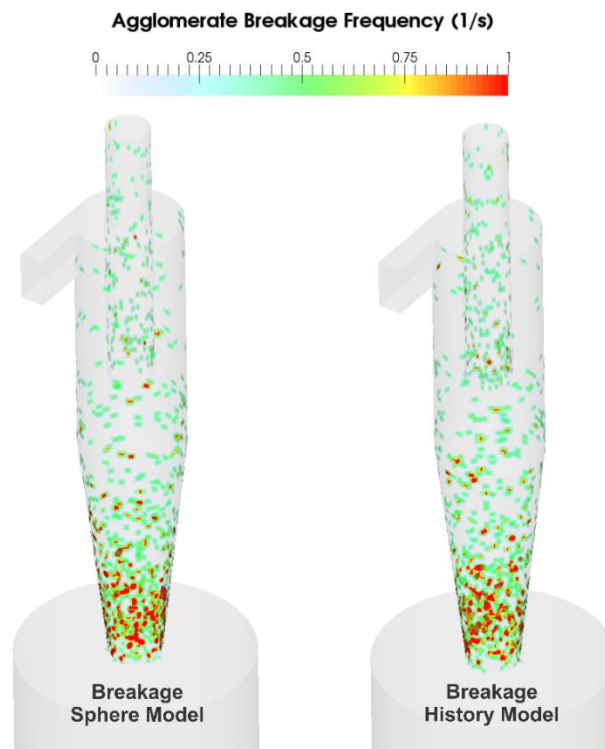


Figure 85. Averaged agglomerate breakage frequency for the sphere (2,807 1/s) and history (2,638 1/s) models. Based on parcel numbers $\sim 182,000$ particles/parcel. The averaging process starts at the simulation time of 2 s with a fixed duration of 0.5 s.

Figure 85 shown the averaged agglomerate breakage frequency for the sphere and history models. Despite both particle-wall and inter-particle impact forces were considered for the agglomerate breakage, only the first presented relevant results, once only a handful of breakage due to inter-particle collision were measured. Although an overall lower frequency of agglomerate breakage is obtained in comparison with agglomeration or inter-particle collision frequencies, it is interesting that this phenomenon has its major occurrence at the bottom of the conical section. This is a region of interest, once this region is related to the collection due to the proximity to the dust collector bin and to the escape, where the inversion of the downwards

outer vortex to the upwards inner vortex happens. Thus, the breakage may be affecting negatively the separation of the cyclone, once smaller particles may be easily dragged by the inner vortex.

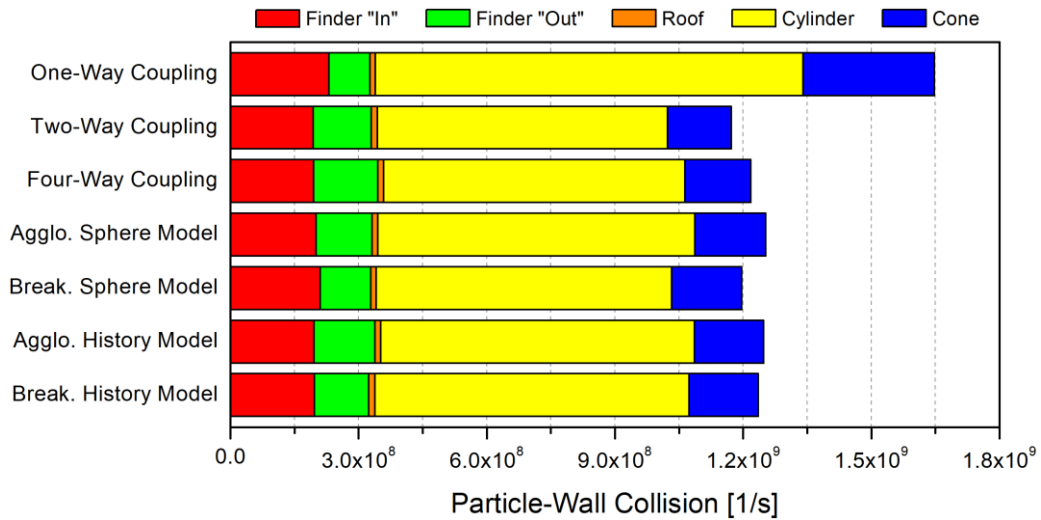


Figure 86. Averaged particle-wall collision frequency divided by five regions. Based on parcel numbers; $\sim 182,000$ particles/parcel. The averaging process starts at the simulation time of 2 s with a fixed duration of 0.5 s.

Still regarding particle-wall collisions, Figure 86 shown the averaged particle-wall collision frequency divided in five different regions of the cyclone: the cylindrical and conical sections; the outer and inner wall of the vortex finder; and the top (roof) of the cyclone. The roof section was measured, once in the first attempts to simulate a cyclone separator, an accumulation of particles in this region was observed. However, with the application of the correct interpolated properties at the particle position the problem was solved. Thus, for all cases no significant difference is observed for this region. At the cylindrical section, the one-way coupling presents the higher frequency among all cases, indicating that despite the dispersed particle concentration profile, a higher concentration of particles closer to the wall due to the higher tangential velocity is observed. The same behaviour is applied for the conical section. Due to the attached distribution of particles on the top of the cyclone, the one-way coupling case presents the smaller frequency for the outer vortex-finder. By comparing the two- and four-way coupling cases, a higher frequency is observed on the last, once the inter-particle collisions may direct particles towards the outer wall of the vortex finder. This effect is also noticeable in the agglomeration and breakage cases, where the broken and less inertial agglomerates are directed towards the cylinder wall due to centrifugal force, hence avoiding contact with the vortex finder wall. Lastly, the inner vortex finder wall collision frequency

indicates that the particles escaping on the one-way coupling are larger and consequently more inertial, hence colliding more frequently with the wall in its way out of the cyclone.

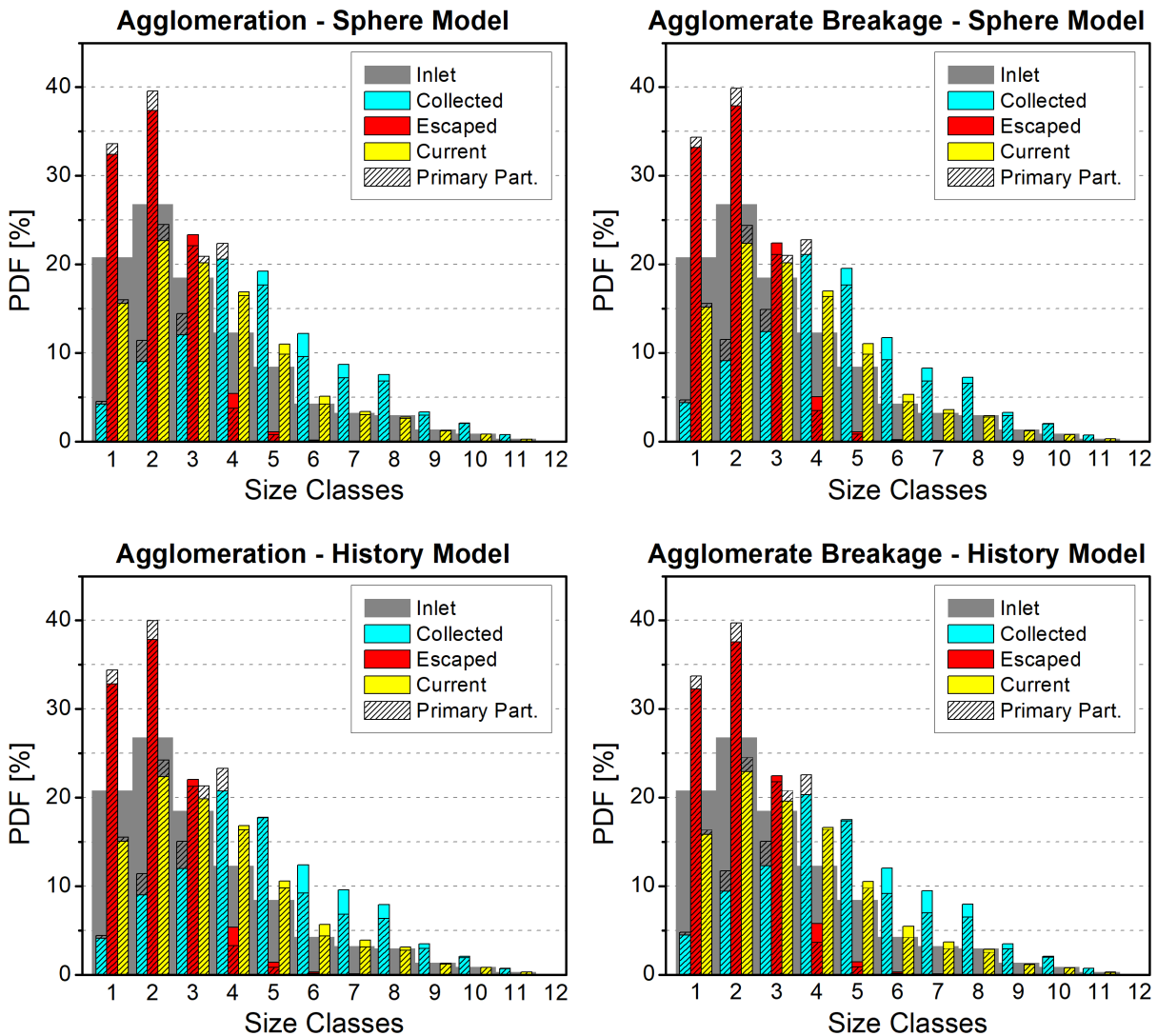


Figure 87. Averaged particle size distribution (number based) for the agglomeration and agglomerate breakage cases. The grey bars represent the distribution at injection, the cyan the collected, the red the escaped and the yellow the current distribution inside the cyclone. The dashed bars indicate the values considering the primary particle size instead of the resultant agglomerate size for every region. The averaged values are calculated during 1 s between the simulation times of 2 and 3 s.

Another interesting analysis is regarding the particle size distribution in the cyclone (Figure 87), where four different regions are measured: the inlet corresponding to the injected distribution; the collected and escaped size distributions; and the current size distribution inside the cyclone. Once agglomeration is considered in the present cases, an additional dashed bar representing the size of the primary particle is plotted over the collected, escaped and current results. Thus, a comparison of the size distributions between the agglomerate and primary particle size is possible. Overall, as observed for the previous cases, the size distribution of the

escaped particles is dislocated to the left, i.e. higher ratio for the smaller particles, while the size distribution of the collected particles is shifted to the centre, indicating that larger particles are easily collected. On the other hand, the size distribution of the current particles inside the cyclone does not follow the inject distribution as observed previously, being for the present cases shifted towards the larger particles. The increase in size due agglomeration may be observed by comparing the size distributions considering the agglomerate and primary particle sizes for the current particles in the system. For the first three size classes (Classes 1 – 3: 0.5 – 1 μm), a higher distribution is observed when considering the primary particle size. This pattern is shifted for larger particles, where a lower distribution is obtained in comparison with the agglomerate size. Therefore, the shift of particle size distribution is attributed to the agglomeration process. The same analysis may be applied to the escape and collect regions, where the agglomeration improves the collected and simultaneously decreases the escaped particle distributions. Consequently, a shift on the collection efficiency is observed, as shown in the Figure 88, where the agglomeration models and its breakage counterparts are compared with the results obtained for the four-way coupling case.

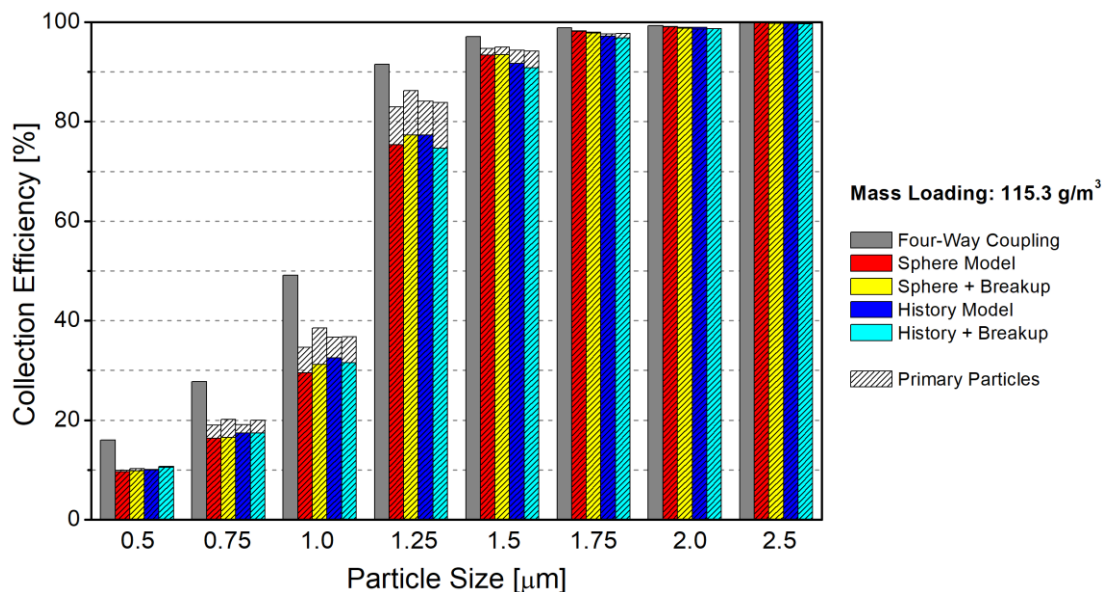


Figure 88. Comparison of the collection efficiency calculated for the four-way coupling and the agglomeration models and its breakage counterparts. Particle sizes bigger than 2.5 μm are not displayed, once a 100% efficiency is obtained. The collection efficiency is calculated during 1 s between the simulation times of 2 and 3 s.

A great difference among the collection efficiency for the four-way coupling and the agglomeration is observed, where the first presents overestimated values for the smaller class sizes. It is also important to point out that, when considering the size of the original primary particle, a higher value of collection efficiency is observed for the agglomeration and

agglomerate breakage cases. Thus, indicating that the agglomeration of these smaller classes improved its separation rate. For the sphere model, a higher collection efficiency is observed when the breakage of agglomerates are considered, indicating that these agglomerates may be breaking close to the collection region, hence improving its value for the smaller classes. On the other hand, the opposite is applied to the history model, where the breakage of agglomerates decrease the collection efficiency for the smaller classes. This difference may indicate that the porous agglomerates are breaking on the way to the escape region, hence decreasing the collection efficiency for the smaller size classes.

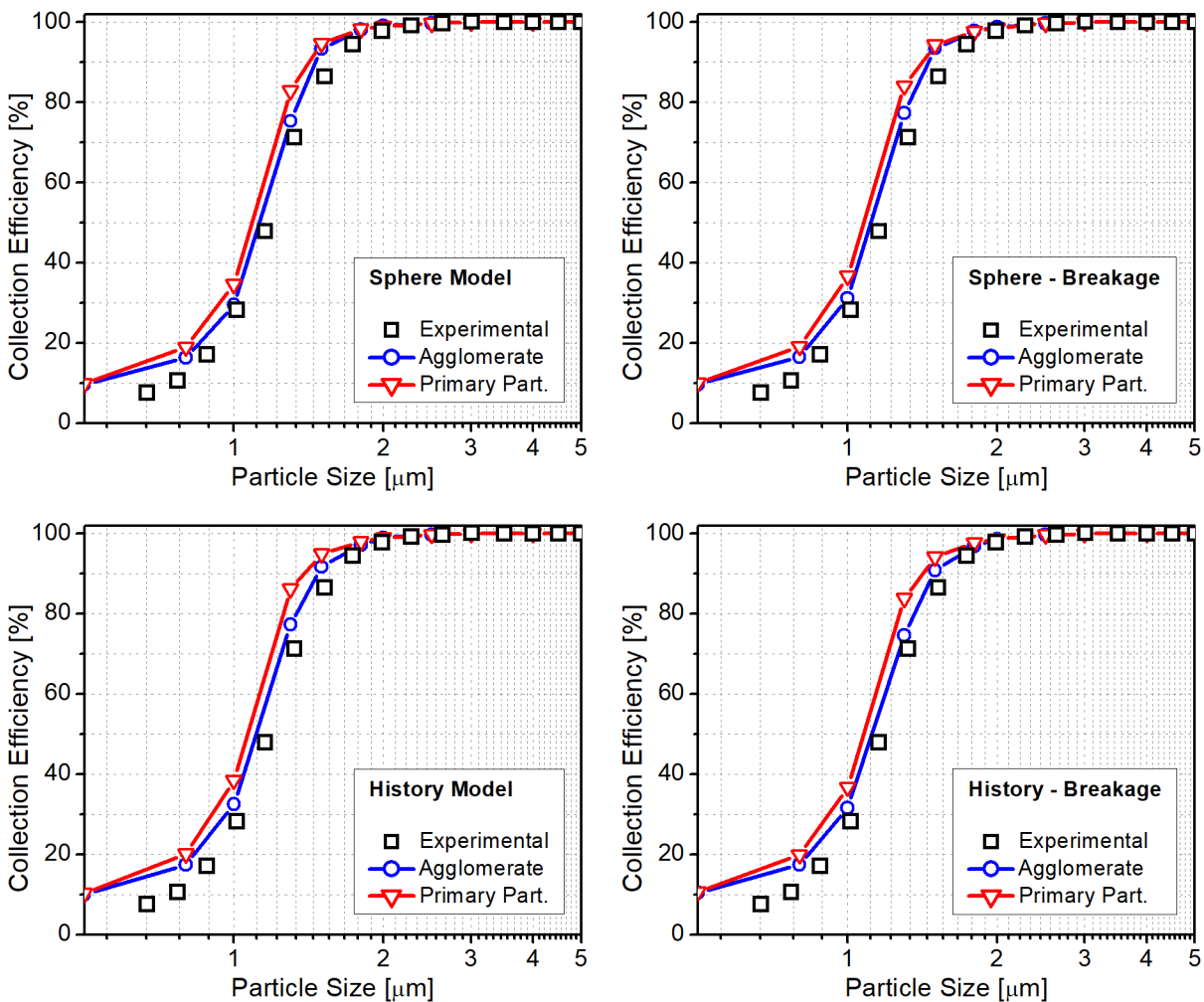


Figure 89. Comparison of the measured collection efficiency (symbols) and the numerical results (lines) agglomeration models and its breakage counterparts. The collection efficiency is calculated during 1 s between the simulation times of 2 and 3 s.

Finally, a comparison of the collection efficiency among the experimental measurements of Huang et al. ^[12] and the cases considering agglomeration and agglomerate breakage are shown in Figure 89. Overall, for both agglomeration models a remarkable agreement regarding the collection efficiency curve is observed, where both the intensity as well as the sigmoid-

shape of the curve are well represented. Compared to the previous one-, two- and four-way coupling calculations, the agreement with the experimental data has been largely improved by the adoption of agglomeration. Although the used particle adhesion properties for calculating the critical impact velocity are based on glass beads properties given by Sommerfeld and Stübing^[38], instead of the Kanto Loan Powders (No. 11, JIZ 8901) particles used by Huang et al.^[12], a satisfactory representation of the separation in the present cyclone is achieved.

Once the modelling of such inter-particle interactions may improve considerably the representation of the separation in gas cyclones, strategies aiming an increment of such phenomena, e.g. agglomeration or agglomerate breakage, may be applied to optimize cyclone's operation. Hence, a modified geometry could be numerically tested in order to improve the collection efficiency through agglomeration. The agglomerate breakage could be also intended, once some processes should avoid agglomerates due to its lower surface area. However, to better represent such phenomena, a more in depth study is demanded, where both agglomeration and agglomerate breakage are the main focus.

5. CONCLUSIONS AND OUTLOOK

For further improving the understanding of particle separation in gas cyclones including the effect of inter-particle collision, agglomeration and agglomerate breakage, numerical calculations based on the coupled Euler/Lagrange approach were conducted using the open source CFD code OpenFOAM 4.1. To consider the effects of particle mass loading on the continuous phase, two-way coupling (i.e. the influence of the particles on the fluid flow field) was accounted for in the momentum equations. Solid particle agglomeration and agglomerate breakage are modelled based on the stochastic inter-particle collision model. In that respect, it was also considered the effect of particle dispersion by SGS turbulence and wall roughness in particle-wall collisions which eventually may also modify the particle tracking.

The first goal of the present work was to implement and validate the necessary models in OpenFOAM 4.1, due to the limitations presented by the previously used CFD code *FASTEST Lag-3D*. Among all models implemented, two models stood out: the particle-wall collision model considering wall roughness and the stochastic inter-particle collision model due to its sheer size and complexity. Over two years were needed before both models were completely implemented and a reasonable agreement with experimental data achieved. However, even after the first positive results, an extensive optimization process was executed, once the sampling process realized by the stochastic inter-particle collision model demanded a considerable amount of computational effort. Thus, with the present version it is possible to execute the validation cases on pneumatic conveying systems considering four-way coupling in a couple of days (2 – 3 days using 12 physical processors of an Intel® Xeon® E5 1.2 GHz), while cases considering only two-way coupling are only slightly faster. Furthermore, the application of the

proposed agglomeration and agglomerate breakage model also do not increase substantially the computational effort needed.

A validation study was performed by the comparison among experimental data, the previous simulations calculated using *FASTEST Lag-3D* and the actual results using OpenFOAM 4.1. The comparison of the present calculations with the experimental data [84, 85, 86, 87] showed a very good agreement for both validation cases. It was demonstrated that particle-wall collisions respecting the wall roughness, as well as the inter-particle collisions have a great impact on particle behaviour. In the horizontal pipe, when neglecting the roughness of the wall and the interaction between particles, the dispersion of the particle concentration could not overcome the gravitational settling, thus creating a higher concentration of particle near the bottom wall. Such effect is avoided by assuming the roughness of the wall and the interaction between particles, having the second a greater relevance for the dispersion of particles in the system. The segregation effects cause by the change of flow direction in the bend and the accumulation of particles at the outer bend wall due to inertial effects and the shielding effect is also observed in the present calculations for the second validation case. A good agreement for the velocity profiles, as well as the mass flux is observed, were the dispersion of particles in the vertical pipe downstream the bend is observed. Thus, based on the good agreement obtained with the calculations performed with OpenFOAM 4.1 for the pneumatic conveying systems, the present code with the implemented models is used to predict the separation in gas cyclones.

The inherent complexity associated with the anisotropic turbulent swirl flow in cyclones, demanded the adoption of LES in combination with a dynamic sub-grid-scale turbulence model for its solution. First a grid independence test is performed, where averaged profiles of tangential and axial velocities with its respective RMS values were compared with experimental data from the literature [13]. Based on the good agreement observed, the coarser mesh, as well as its refinement ratio and blocking structure were used for the further cyclone geometries as a standard. With the methodology for the geometry blocking and grid refinement rate defined, further validations of the gas flow were performed with geometrical variations of the vortex finder of a Stairmand cyclone with different inlet velocities. The overall good agreement showed that the used methodology, as well the turbulence model are adequate for a good prediction of the swirl flow in cyclones.

To verify the appropriate approach for the particle tracking in cyclones and the methodology for the collection efficiency calculation, two different cyclones were studied. The first studied cyclone corresponds to a small scale laboratory-cyclone studied by Xiang et al. [10],

where the influence of the bottom cone diameter D_1 on the performance parameters is investigated. For this case, only one-way coupling calculations are considered, resulting in a simpler configuration to start the two-phase studies. The second cyclone corresponds to the previously studied Stairmand cyclone from Hoekstra^[13] with the three variations of the vortex finder diameter D_s (see Figure 42). Hence, a more complex configuration is explored, where two-way coupling calculations are performed to test the collection efficiency methodology accuracy for different rates of parcels injected in the system. The collection efficiency is a direct product of the particle tracking, once a poor solution of the particle tracking may result in a different route for the particles, hence changing the rate of particles that can be dragged by the upwards inner vortex or collected by the dust collector bin. Therefore, the particle tracking has been solved adequately, once a good agreement with the experimentally measured collection efficiency was observed for both cases.

As a continuation of the previous study, a hypothetical study^[92] is proposed based on the high efficiency Stairmand cyclone to investigate the effects of inter-particle collisions and agglomeration on the performance of a cyclone separator. The results show that the main effects of inter-particle collisions and agglomeration are observed in the conical part of the cyclone. When considering only two-way coupling, the dust rope of higher particle concentration is well defined and spaced, following the swirling flow moving downward the cyclone outer wall towards the dust bin. The same behaviour is not observed in the four-way coupling case, where the dust rope starts to get dispersed in the conical section of the cyclone. This happens because the particles are colliding with each other, resulting in a change of their momentum and trajectory which causes the dispersion of particles out of the initial dense rope regions. However, when the agglomeration models are considered, the dust rope behaviour is partly recovered and its appearance is somewhat between the cases with two- and four-way coupling. Due to the decrease in particle number density through agglomeration, the inter-particle collision probability is reduced, whereby decreasing the particle dispersion effect observed in the four-way coupling case. Also the agglomeration counts are highest in the conical part of the cyclone, where the particles have lower relative velocities. Additionally, the history model predicts slightly higher agglomeration rates especially towards the outlet to the collection bin. Another interesting phenomenon is that for the same particle size, the sphere model yields slightly higher collection efficiency than the more realistic history model for all particle size classes. This is resulting from the smaller agglomerate size (volume equivalent sphere) produced by the sphere model and hence the lower aerodynamic drag. With the history model

effectively larger porous agglomerates are produced yielding higher aerodynamic drag whereby agglomerates may easier escape through the overflow pipe.

Finally, the last test case is based on the experimental data of Huang et al. ^[12], where the impact of the mass loading on the cyclone's performance is studied. With a higher mass loading it is possible to evaluate the influence of inter-particle collisions, agglomeration and agglomerate breakage on the cyclone performance. First, a comparison among one-, two- and four-way coupling is performed, where the inability of the one-way coupling solution is proved by the wrong prediction of the collection efficiency. Despite the presented overestimation of collection efficiency for the smaller particles, the two- and four-way coupling presented a better agreement with the experimental measurements, presenting the same sigmoid-shape as the experiments. The interaction between the gas and the particles is important to a good prediction of the cyclone's performance, once the particle's loss of momentum due to particle-wall and inter-particle collisions may reduce the vortex swirl and consequently reduce the pressure drop. Generally, the size distribution of the escaped particles is dislocated to the left, i.e. higher ratio for the smaller particles, while the size distribution of the collected particles is shifted to the centre, indicating that larger particles are easily collected. For the one-, two- and four way coupling cases, the size distribution of the current particles inside the cyclone follows the distribution of the injection with minor differences due to higher/lower particle residence times. On the other hand, when agglomeration is considered, the size distribution of the current particles inside the cyclone is shifted towards the larger particles. Overall, for both agglomeration models a remarkable agreement regarding the collection efficiency curve is observed, where both the intensity as well as the sigmoid-shape of the curve are well represented. Compared to the previous one-, two- and four-way coupling calculations, the agreement with the experimental data has been largely improved by the adoption of agglomeration, indicating that such phenomenon should be considered for cases with higher mass loading.

Despite advancements made with the present work to improve the understanding of the phenomena involved in the separation process of a gas cyclone, there are still many problems to be addressed and solved. In the present work only binary collisions are allowed, where this condition is satisfied by reducing the Lagrangian time step, i.e. the relevant time scale due to inter-particle collisions is calculated by the inverse of the collision frequency. However, at the dust ropes of high particle concentration a multi-particle collision may take place, hence changing the motion of the involved particles. The used agglomeration and agglomerate breakage models, for example, are simplified versions where the structure of the agglomerate

is not stored, hence a proper selection of the bond that should break is not possible. Even the more sophisticated history model which allows the calculation of agglomerate porosity still considers the agglomerate as a sphere with equivalent diameter, not considering the hydrodynamic effects due to its shape. Naturally such problems are very complex and are mainly still being applied to simplified configurations and geometries, while the present work aims for laboratory scale to industrial cyclones. With the implemented models in OpenFOAM, it is possible to solve an unsteady simulation of a cyclone considering four-way coupling with agglomeration and agglomerate breakage in a week time (using 12 physical processors of an Intel® Xeon® E5 1.2 GHz). Hence, a direct application of the presented models and methodologies may be applied to solve industrial problems and to further optimize cyclones to improve collection efficiency or reduce pressure drop. Lastly, the overall good agreement with experimental data demonstrated in this document shows the reliability of the used methodology and models on the cyclone's separation prediction.

NOMENCLATURE

Latin Symbols

Symbol	Unit	Description
b	m	Cyclone's inlet width
C_D	-	Drag coefficient
$\overline{c_{mol}}$	m s^{-1}	Mean relative velocity between gas molecules
Cu	-	Cunningham correlation
D_c	m	Cyclone's body diameter
D_l	m	Cyclone's bottom cone diameter
D_s	m	Cyclone's vortex finder diameter
D_P	μm	Particle diameter
e	-	Normal coefficient of restitution
$F_{A.W.}$	kg m s^{-2}	Impact force between the agglomerate and the wall
$F_{A.P.}$	kg m s^{-2}	Impact force from an agglomerate-particle collision
F_b	kg m s^{-2}	Adhesive force
f_c	s^{-1}	Inter-particle collision frequency
F_D	kg m s^{-2}	Drag force
F_G	kg m s^{-2}	Gravitational force
F_{LR}	kg m s^{-2}	Slip-rotational lift force

F_{LS}	kg m s^{-2}	Slip-shear lift force
g	m s^{-2}	Gravity
H	J	Hamacker constant
h_{ps}	m	Particle deformation depth
I_P	kg m^2	Moment of inertia
$J_x J_y J_z$	kg m s^{-2}	Impulsive force components
k	$\text{m}^2 \text{s}^{-2}$	turbulent kinetic energy
Kn	-	Knudsen number
k_r	-	Energy restitution ratio
L	m	Lateral displacement
L_a	-	Lateral non-dimensional displacement
L_S	m	Cyclone's vortex finder height
L_C	m	Cyclone's body height under the vortex finder
L_{CO}	m	Cyclone's conical section height
L_e	m	Cyclone's inlet height
L_E	m	Turbulent length scale of turbulence
m_P	kg	Particle mass
n_P	-	Number of particles in the control volume
P	Pa	Pressure of the system
p_c	Pa	Yield pressure
P_{coll}	-	Inter-particle collision probability
Re_P	-	Particle Reynolds number
$R(St)$	-	Correlation function on the Stokes number
St	-	Stokes number
t	s	Time
T_i	$\text{kg m}^2 \text{s}^{-2}$	Torque
T_L	s	Integral Stokesian time scale of turbulence
U	m s^{-1}	Linear velocity
U_{crit}	m s^{-1}	Critical velocity
$u_P v_P w_P$	m s^{-1}	Particle linear velocity components (x,y,z)
U_P	m s^{-1}	Particle velocity
U'_P	m s^{-1}	Particle velocity fluctuation
$\bar{U}_{P,cv}$	m s^{-1}	Local mean velocity in the control volume

u_{R1}	m s^{-1}	Particle velocity in relation to the contact point
$u_R u_{Ry} u_{Rz}$	m s^{-1}	Relative velocity components at the point of contact
V_{cell}	m^3	Volume of the control volume
x_{50}	-	Cut size
Y_c	m	Radial distance of the boundary particle trajectory
z_0	m	Minimum contact distance between the particles

Greek symbols

Symbol	Unit	Description
α	-	Angle between particle and wall
$\Delta\gamma$	-	Roughness angle
ΔP	Pa	Pressure drop
Δt_{cv}	s	Time required for a particle to cross a control volume
Δt_L	s	Lagrangian time step
ε	$\text{m}^2 \text{s}^{-3}$	turbulent dissipation rate
ε_V	-	Porosity of the agglomerate
$\varepsilon_x \varepsilon_z$	-	Factors of velocity proportionality
η	%	Collection efficiency
η_P	-	Impact efficiency
λ	m	Mean free path of the gas molecules
μ	$\text{kg s}^{-1} \text{m}^{-1}$	Fluid dynamic viscosity
μ_T	$\text{kg s}^{-1} \text{m}^{-1}$	Turbulent viscosity
μ_0	-	Static coefficient of friction
μ_d	-	Dynamic coefficient of friction
ν	$\text{m}^2 \text{s}^{-1}$	Kinematic viscosity
ξ	-	Gaussian distribution with zero mean and unit variance
ρ	kg m^{-3}	Density
$\sigma_{P,cv}$	m s^{-1}	Local rms value of the particle velocity in the control volume
τ_P	s	Particle response time
τ_{coll}	s	Average time between binary inter-particle collisions

ϕ	-	Inter-particle collision angle of impact
Ψ	-	Angle of the cross-section of the collision cylinder
ω	s^{-1}	Angular velocity

REFERENCES

- [1] A. C. Hoffmann, L. E. Stein, *Gas Cyclones and Swirl Tubes: Principles, Design and Operation.*, Berlin, Heidelberg, New York: Springer, 2008.
- [2] A. Ogawa, "Mechanical Separation Process and flow patterns of Cyclone Dust Collectors," *Ind. Applied Mech.*, vol. 50, no. 3, p. 33, 1997.
- [3] D. Noriler, A. A. Vegini, A. A. C. Barros, H. F. Meier, M. Mori, "A New Role for Reduction in Pressure Drop in Cyclones Using Computational Fluid Dynamics Techniques," *Brazilian Journal of Chemical Engineering*, vol. 21, pp. 93-101, 2004.
- [4] D. Misiulia, K. Elsayed, A. G. Andersson, "Geometry optimization of a deswirler for cyclone separator in terms of pressure drop using CFD and artificial neural network," *Separation and Purification Technology*, vol. 185, pp. 10-23, 2017.
- [5] C. J. Stairmand, "The design and performance of cyclone separators," *Trans. IChemE*, vol. 29, pp. 409-412, 1951.
- [6] C. E. Lapple, "Gravity and centrifugal separation," *Americal Industrial Hygiene Association Quarterly*, vol. 11, pp. 40-47, 1950.
- [7] J. Dirgo, D. Leith, *Encyclopedia of Fluid Mechanics*, Houston, EUA: Gulf Publishing Company, 1986.
- [8] W. Barth, "Berechnung und Auslegung von Zyklonabscheidern auf Grund neuerer Untersuchungen," *Brennstoff-Wärme-Kraft*, vol. 8, pp. 1-9, 1956.

- [9] P. Rosin, E. Rammler, W. Intelmann, "Principles and limits of cyclone dust removal," *Zeit des Ver. deutscher Ing.*, vol. 76, 1932.
- [10] R. Xiang, S. H. Park, K. W. Lee, "Effects on cone dimension on cyclone performance," *Journal of Aerosol Science*, vol. 32, pp. 549-561, 2001.
- [11] Z. Ji, Z. Xiong, X. Wu, H. Chem, H. Wu, "Experimental investigation on a cyclone separator performance at an extremely low particle concentration," *Powder Technology*, vol. 191, pp. 254-259, 2009.
- [12] A. Huang, K. Ito, T. Fukasawa, K. Fukui, H. Kuo, "Effects of particle mass loading on the hydrodynamics and separation efficiency of a cyclone separator," *Journal of the Taiwan Institute of Chemical Engineers*, vol. 90, pp. 61-67, 2018.
- [13] A.J. Hoekstra, Gas flow field and collection efficiency of cyclone separators, The Netherlands: PhD Thesis - Delft University of Technology, 2000.
- [14] O. L. Sgrott Jr., D. Noriler, V. R. Wiggers, H. F. Meier, "Cyclone optimization by COMPLEX method and CFD simulation," *Powder Technology*, vol. 277, pp. 11-21, 2015.
- [15] R. D. Luciano, B. L. Silva, L. M. Rosa, H. F. Meier, "Multi-objective optimization of cyclone separators in series based on computational fluid dynamics," *Powder Technology*, vol. 325, pp. 452-466, 2018.
- [16] C. J. Stairmand, "Pressure Drop in Cyclone Separators," *Engineering*, vol. 168, pp. 409-412, 1949.
- [17] C. B. Shepherd, C. E. Lapple, "Flow Pattern and Pressure Drop in Cyclone Dust Collectors," *Industrial and Engineering Chemistry*, vol. 1939, pp. 212-222, 1939.
- [18] J. Casal, J. M. Martinez-Benet, "A Better Way to Calculate Cyclone Pressure Drop," *Chemical Engineering*, vol. 90, pp. 99-100, 1983.
- [19] K. Elsayed, C. Lacor, "The effect of cyclone vortex finder dimensions on the flow pattern and performance using LES," *Computers & Fluids*, vol. 30, pp. 224-239, 2013.
- [20] K. S. Lim, H.S. Kim, K.W. Lee, "Characteristics of the collection efficiency for a cyclone with different vortex finder shapes," *Journal of Aerosol Science*, vol. 35, pp. 743-754, 2004.
- [21] F. J. Souza, R. V. Salvo, D. M. Martins, "Effects of the gas outlet duct length and shape on the performance of cyclone separators," *Separation and Purification Technology*, vol. 142, pp. 90-100, 2015.

- [22] E. Balestrin, R. K. Decker, D. Noriler, J. C. S. C. Bastos, H. F. Meier, "An alternative for the collection of small particles in cyclones: Experimental analysis and CFD modeling," *Separation and Purification Technology*, vol. 184, pp. 54-65, 2017.
- [23] K. S. Lim, S.B. Kwon, K.W. Lee, "Characteristics of the collection efficiency for a double inlet cyclone with clean air," *Journal of Aerosol Science*, vol. 34, pp. 1085-1095, 2003.
- [24] S. Bernardo, M. Mori, A. P. Peres, R. P. Dionsio, "3-D computational fluid dynamics for gas and gas-solid flows in a cyclone with different inlet section angles," *Powder Technology*, vol. 162, pp. 190-200, 2006.
- [25] J. Yang, G. Sun, C. Gao, "Effect of the inlet dimensions on the maximum-efficiency cyclone height," *Separation and Purification Technology*, vol. 105, pp. 15-23, 2013.
- [26] K. Elsayed, C. Lacor, "The effect of cyclone inlet dimensions on the flow pattern and performance," *Applied Mathematical Modelling*, vol. 35, pp. 1952-1968, 2011.
- [27] F. J. de Souza, R. V. Salvo, D. A. M. Martins, "Large eddy simulation of the gas-particle flow in cyclone separators," *Separation and purification technology*, no. 94, pp. 61-70, 2012.
- [28] J. W. Lee, H. J. Yang, D. Y. Lee, "Effect of the cylinder shape of a long coned cyclone on the stable flow-field establishment," *Powder Technology*, vol. 165, pp. 30-38, 2006.
- [29] K. Elsayed, C. Lacor, "The effect of the dust outlet geometry on the performance and hydrodynamics of gas cyclones," *Computers & Fluids*, vol. 68, pp. 134-147, 2012.
- [30] K. Elsayed, C. Lacor, "CFD modeling and multi-objective optimization of cyclone geometry using desirability function, artificial neural network and genetic algorithms," *Applied Mathematical Modelling*, vol. 37, pp. 5680-5704, 2013.
- [31] H. Safikhani, M. A. Akhavan-Behabadi, N. Nariman-Zadeh, M. J. M. Abadi, "Modeling and multi-objective optimization of square cyclones separators using CFD and neural networks," *Chemical Engineering Research and Design*, Vols. 301-309, p. 89, 2011.
- [32] O. L. Sgrott Jr., K. K. Costa, D. Noriler, V. R. Wiggers, W. P. Martignoni, H. F. Meier, "Cyclones' Project Optimization by Combination of an Inequality Constrained Problem and Computational Fluid Dynamics Techniques (CFD)," *Chemical Engineering Transactions*, vol. 32, pp. 2011-2016, 2013.
- [33] J. J. Derksen, S. Sundaresan, H. E. A. van den Akker, "Simulation of mass-loading effects in gas-solid cyclone separators," *Powder Technology*, vol. 163, pp. 59-68, 2006.

- [34] A. C. Hoffmann, H. Arends, H. Sie, "An experimental investigation elucidating the nature of the effect of solids loading on cyclone performance," *Filtration & Separation*, vol. 28, no. 3, pp. 188-193, 1991.
- [35] T. A. Sedrez, R. K. Decker, M. K. da Silva, D. Noriler, H. F. Meier, "Experiments and CFD-based erosion modeling for gas-solids flow in cyclones," *Powder Technology*, vol. 311, pp. 120-131, 2017.
- [36] J. Lipowsky, M. Sommerfeld, "Influence of particle agglomeration and agglomerate porosity on the simulation of gas cyclones," in *6th International conference on CFD in Oil & Gas, metallurgical and process industries SINTEF/NTNU*, Trondheim, Norway, 2008.
- [37] C. A. Ho, M. Sommerfeld, "Numerische Berechnung der Staubabscheidung im Gaszyklon unter Berücksichtigung der Partikelagglomeration," *Chemie Ingenieur Technik*, vol. 77, pp. 282-290, 2005.
- [38] M. Sommerfeld, S. Stübing, "A novel Lagrangian agglomerate structure model," *Powder Technology*, vol. 319, pp. 34-52, 2017.
- [39] C. W. Haig, A. Hursthouse, S. McIlwain, D. Sykes, "The effect of particle agglomeration and attrition on the separation efficiency of a Stairmand cyclone," *Powder Technology*, vol. 258, pp. 110-124, 2014.
- [40] G. Gronald, J.J. Derksen, "Simulating turbulent swirling flow in a gas cyclone: A comparison of various modeling approaches," *Powder Technology*, vol. 205, p. 160-171, 2011.
- [41] A. J. Hoekstra, J. J. Derksen, H. E. A. van den Akker, "An experimental and numerical study of turbulent swirling flow in gas cyclones," *Chemical Engineering Science*, vol. 54, p. 2055-2065, 1999.
- [42] F. Kaya, I. Karagoz, "Performance analysis of numerical schemes in highly swirling flows in cyclones," *Current Science*, vol. 94, p. 1273-1278, 2008.
- [43] W. P. Martignoni, S. Bernardo, L. Quintani, "Evaluation of cyclone geometry and its influence on performance parameters by computational fluid dynamics (CFD)," *Brazilian Journal of Chemical Engineering*, vol. 24, pp. 83-94, 2007.
- [44] S. K. Shukla, P. Shukla, P. Ghosh, "Evaluation of numerical schemes for dispersed phase modeling of cyclone separators," *Engineering Applications of Computational Fluid Mechanics*, vol. 5, p. 235-246, 2011.

- [45] G. I. Pisarev, A. C. Hoffmann, W. Peng, H. A. Dijkstra, “Large Eddy Simulation of the vortex end in reverse flow centrifugal separators,” *Applied Mathematics and Computation*, vol. 217, p. 5016–5022, 2011.
- [46] J. J. Derksen, “Separation performance predictions of a stairmand high-efficiency cyclone,” *AIChE Journal*, vol. 49, p. 1359–1371, 2003.
- [47] J. Smagorinsky, “General Circulation Experiments with the Primitive Equations,” *Monthly Weather Review*, vol. 164, pp. 99-164, 1963.
- [48] M. Germano, U. Piomelli, P. Moin, W.H. Cabot, “A dynamic subgrid-scale eddy viscosity model,” *American Institute of Physics 7*, p. 1760–1795, 1990.
- [49] J. H. Ferziger, M. Peric, *Computational methods for fluid dynamics*, Springer-Verlag, 2002.
- [50] D. K. Lilly, “A proposed modification of the Germano subgrid-scale closure method,” *Physics Fluids 4*, p. 633–635, 1992.
- [51] A. Passalacqua, “dynamicSmagorinsky,” April 2014. [Online]. Available: <https://github.com/AlbertoPa/dynamicSmagorinsky>. [Accessed 2019].
- [52] T. Holzmann, *Mathematics, Numerics, Derivations and OpenFOAM(R)*, Leoben: Holzmann CFD, fourth edition, February 2017. URL www.holzmann-cfd.de, 2017.
- [53] F. Liu, “A Thorough Description Of How Wall Functions Are Implemented In OpenFOAM.,” *Proceedings of CFD with OpenSource Software*, 2016.
- [54] G. Kalitzin, G. Medic, G. Iaccarino, P. Durbin, “Near-wall behavior of rans turbulence models and implications for wall functions,” *Computational physics*, no. 204, p. 265{291, 2004.
- [55] M. Sommerfeld, “Numerical Methods for Dispersed Multiphase Flows,” *Particles in Flows*, pp. 327-396, 2017.
- [56] J. Lipowsky, M. Sommerfeld, “LES-Simulation of the formation of particle strands in swirling flows using an unsteady Euler-Lagrange approach,” in *6th International Conference on Multiphase Flow ICMF 2007*, Leipzig, Germany, 2007.
- [57] S. Laín, M. Sommerfeld, “Euler/Lagrange computations of pneumatic conveying in a horizontal channel with different wall roughness,” *Powder Technology*, pp. 76-88, 2008.
- [58] C. T. Crowe, J. D. Schwarzkopf, M. Sommerfeld, Y. Tsuji, *Multiphase flows with droplets and particles*, CRC Press, 2012.

- [59] M. Sommerfeld, B. van Wachem and R. Oliemans, “Best Practice Guidelines for Computational Fluid Dynamics of Dispersed Multiphase Flows,” *ERCOTAC (European Research Community on Flow, Turbulence and Combustion)*, pp. ISBN 978-91-633-3564-8, 2008.
- [60] P.G. Saffman, “The lift on a small sphere in a shear flow,” *Journal of Fluid Mechanics*, vol. 22, pp. 385-400, 1965.
- [61] R. Mei, “An approximate expression for the shear lift force on a spherical particle at finite Reynolds number,” *Int. J. Multiphase Flow*, vol. 18, pp. 145-147, 1992.
- [62] T. B. D. B. Oesterlé, “Experiments on the lift of a spinning sphere in a range of intermediate Reynolds numbers,” *Experiments in Fluids*, vol. 25, no. 1, p. 16–22, 1998.
- [63] S. I. Rubinow, J. B. Keller, “The transverse force on spinning sphere moving in a viscous fluid,” *Journal of Fluid Mechanics*, vol. 11, pp. 447-459, 1961.
- [64] S. C. R. Dennis, S. N. Singh, D. B. Ingham, “The steady flow due to a rotating sphere at low and moderate,” *Journal of Fluid Mechanics*, vol. 101, pp. 257-279, 1980.
- [65] O. Sawatzki, Über den Einfluß der Rotation und der Wandstöße auf die Flugbahn kugeligter Teilchen im, Dissertation, Univ. Karlsruhe, 1961.
- [66] G. K. M. R. M. Sommerfeld, “Some open questions and inconsistencies of lagrangian particle dispersion models,” in *Proceedings of the 9th Symposium on Turbulent Shear Flows*, Kyoto, Japan, 1993.
- [67] T. von Karman, L. Horwarth, “On the statistical theory of isotropic turbulence,” *Proc. Royal Society London*, vol. A164, pp. 192-215, 1938.
- [68] D.K. Lilly, “The representation of small scale turbulence in numerical simulation experiments,” *In Proceedings of the IBM Scientific Computing Symposium on Environmental Sciences*, 1967.
- [69] J.W. Deardorff, “Stratocumulus-capped mixed layer derived from a three dimensional model,” *Boundary-Layer Meteorology*, vol. 18, pp. 495-527, 1980.
- [70] W. H. Snyder, J. L. Lumley, “Some measurements of particle velocity auto-correlation functions,” *Journal of Fluid Mechanics*, no. 48, pp. 41-71, 1971.
- [71] M. Sommerfeld, N. Huber, “Experimental analysis and modelling of particle-wall collisions,” *Multiphase Flow*, vol. 25, pp. 1457-1489, 1999.
- [72] M. Sommerfeld, “Modelling of particle-wall collisions in confined gas-particle flows,” *International Journal of Multiphase Flow*, vol. 18, pp. 905-926, 1992.

- [73] J. Kussin, M. Sommerfeld, "Experimental studies on particle behaviour and turbulence modification in horizontal channel flow with different wall roughness," *Experiments in Fluids*, vol. 33, pp. 143-159, 2002.
- [74] N. A. Konan, O. Kannengieser, O. Simonin, "Stochastic modeling of the multiple rebound effects for particle-rough wall collisions," *International Journal of Multiphase Flow*, vol. 35, pp. 933-945, 2009.
- [75] M. Sommerfeld, "Validation of a stochastic Lagrangian modelling approach for inter-particle collisions in homogeneous isotropic turbulence. International Journal of Multiphase Flows," *International Journal of Multiphase Flows*, vol. 27, pp. 1828-1858, 2001.
- [76] G. Schuch, F. Loeffler, "Ueber die abscheidewahrscheinlichkeit von feststoffpartikeln an tropfen in einer gasstroesung," *Verfahrenstechnik*, vol. 12, pp. 302-306, 1978.
- [77] R.B. Hiller, "Der Einfluß von Partikelstoß und Partrikelhaftung auf die Abscheidung in Faserfiltern," PhD thesis, Universität Karlsruhe, 1981.
- [78] C. A. Ho, M. Sommerfeld, "Modelling of micro-particle agglomeration in turbulent flow," *Chemical Engineering Science*, vol. 57, pp. 3073-3084, 2002.
- [79] M. Breuer, N. Almohammed, "Modeling and simulation of particle agglomeration in turbulent flows using a hard-sphere model with deterministic collision detection and enhanced structure models," *International Journal of Multiphase Flow*, vol. 73, pp. 171-206, 2015.
- [80] N. Almohammed, M. Breuer, "Modeling and simulation of agglomeration in turbulent particle-laden flows: A comparison between energy-based and momentum-based agglomeration models," *Powder Technology*, vol. 294, pp. 373-402, 2016.
- [81] C. A. Ho, M. Sommerfeld, "Analysis and modeling of particle agglomeration in a plane shear layer," in *5th International Conference on Multiphase Flow, ICMF'04*, Yokohama, Japan, 2004.
- [82] S. Stübing, Lagrangesche Berechnung von Agglomeratstrukturen am Beispiel eines Sprühtrockners, Halle (Saale): Dissertation, 2013.
- [83] C. Weiler, M. Wolkenhauer, M. Trunk, P. Langguth, "New model describing the total dispersion of dry powder agglomerates," *Powder Technology*, vol. 203, pp. 248-253, 2010.

- [84] S. Laín, M. Sommerfeld, “Characterization of pneumatic conveying systems using the Euler/Lagrange approach,” *Powder Technology*, vol. 235, pp. 764-782, 2013.
- [85] M. Sommerfeld, S. Laín, “Parameters influencing dilute-phase pneumatic conveying through pipe systems: A computational study by the Euler/Lagrange approach,” *The Canadian Journal of Chemical Engineering*, vol. 93, pp. 1-17, 2015.
- [86] N. Huber, M. Sommerfeld, “Characterization of the cross-sectional particle concentration distribution in pneumatic conveying systems,” *Powder Technology*, vol. 79, pp. 191-210, 1994.
- [87] N. Huber, M. Sommerfeld, “Modelling and numerical calculation of dilute-phase pneumatic conveying in pipe systems,” *Powder Technology*, vol. 99, pp. 90-101, 1998.
- [88] C. J. Freitas, “The issue of numerical uncertainty,” *Applied Mathematical Modelling*, vol. 26, pp. 237-248, 2002.
- [89] P. J. Roache, “Perspective: a method for uniform reporting of grid refinement studies,” *J. Fluids. Eng.*, vol. 116, pp. 405-413, 1994.
- [90] A. Savitzky, M.J.E. Golay, “Smoothing and Differentiation of Data by Simplified Least Squares Procedures,” *Analytical Chemistry*, vol. 36, p. 1627–1639, 1964.
- [91] Origin User Guide, “Origin User Guide,” OriginLab Corporation, 2018. [Online]. Available: <https://www.originlab.com/doc/Origin-Help/Smoothing>. [Accessed 14 12 2018].
- [92] O. L. Sgrott Jr., M. Sommerfeld, “Influence of inter-particle collisions and agglomeration on cyclone performance and collection efficiency,” *Can. J. Chem. Eng.*, vol. 97, pp. 511-522, 2019.
- [93] S. E. Elgobashi, “On predicting particle-laden turbulent flows,” *Applied Scientific Research*, vol. 52, no. 4, pp. 309-329, 1994.